

12. SITE 832¹

Shipboard Scientific Party²

HOLE 832A

Date occupied: 21 November 1990
Date departed: 23 November 1990
Time on hole: 1 day, 20 hr, 45 min
Position: 14°47.78'S, 167°34.35'E
Bottom felt (rig floor; m; drill-pipe measurement): 3100.6
Distance between rig floor and sea level (m): 11.30
Water depth (drill-pipe measurement from sea level, m): 3089.3
Total depth (rig floor; m): 3316.50
Penetration (m): 215.90
Number of cores (including cores with no recovery): 27
Total length of cored section (m): 215.90
Total core recovered (m): 146.26
Core recovery (%): 67.7
Oldest sediment cored:
Depth below seafloor (m): 206.20
Nature: volcanic ash interbedded with clayey volcanic silts
Age: Pleistocene
Measured velocity (km/s): 1.610

HOLE 832B

Date occupied: 23 November 1990
Date departed: 1 December 1990
Time on hole: 8 days, 18 hr, 45 min
Position: 14°47.78'S, 167°34.35'E
Bottom felt (rig floor; m; drill-pipe measurement): 3100.6
Distance between rig floor and sea level (m): 11.30
Water depth (drill-pipe measurement from sea level, m): 3089.3
Total depth (rig floor; m): 4207.30
Penetration (m): 1106.70
Number of cores (including cores with no recovery): 100
Total length of cored section (m): 962.30
Total core recovered (m): 450.95
Core recovery (%): 46.9
Oldest sediment cored:
Depth below seafloor (m): 846.4
Nature: basaltic breccia with sandstone and siltstone
Age: late Miocene
Measured velocity (km/s): 2.350

Principal results: We arrived at Site 832 on 21 November 1990 at 0645 Universal Time Coordinated (UTC). After 10 days and 15.5 hr on site drilling two holes (Holes 832A and 832B) we departed Site 832 at 2215 UTC on 1 December 1990. Because we penetrated into older sedimentary rocks sooner than expected in Hole 832B and were experiencing good core recovery, we requested and received permission to drill past 700 meters below seafloor (mbsf). The early recovery of upper Pliocene or lower Pleistocene sediments at about 550 m suggested that the intra-arc basin of the central New Hebrides Island Arc may have formed earlier than most workers anticipated. We were unable to log Hole 832B as fully as desired because of infilling problems in the upper part of the hole, near the seafloor.

Site 832 (proposed site IAB-1) is located on the flat intra-arc basin floor at 3089.3 meters below sea level (mbsl) in the central part of the North Aoba Basin (NAB), approximately 50 km northeast of the Queiros Peninsula of Espiritu Santo Island and 45 km due south of the smoking volcanic island of Santa Maria (Gaua). The NAB lies between uplifted bedrock masses of Espiritu Santo and Maewo islands and is separated from the northern Vanikolo summit basin by Santa Maria Island and from the South Aoba Basin (SAB) by the active volcanic island of Aoba.

After a brief seismic reflection survey to confirm site location, we began drilling without problems. In Hole 832A we cored 215.9 mbsf and recovered 146.26 m of core for a recovery rate of 67.7%. We drilled Hole 832B to a total depth (TD) of 1106.7 mbsf, coring 962.3 m and recovering 450.95 m of core for a recovery rate of 46.9%.

Seven lithostratigraphic units were identified in the cores collected at Site 832. Lithostratigraphic Unit I (0–206.2 mbsf in Hole 832A; 144.4–385.6 mbsf in Hole 832B) is a 385.6-m-thick series of Pleistocene volcanic clays, silts, and sands, and is subdivided into two subunits (Subunits IA and IB) based on differences in grain size. Subunit IA (0–141.0 mbsf) is a 141-m-thick zone of coarse vitric volcanic ashes interbedded with sandy to clayey volcanic silts. Subunit IB (141.0–206.2 mbsf in Hole 832A; 144.4–385.6 mbsf in Hole 832B) is a 244.6-m-thick unit similar to Subunit IA but with finer vitric ashes. Lithostratigraphic Unit II (385.6–461.5 mbsf) is a 75.9-m-thick Pleistocene sequence of sandstone, siltstone, and claystone largely volcanogenic in the upper part and more calcareous in the lower part. Unit II is a transitional unit between a more volcanic unit above and a more calcareous unit below. Lithostratigraphic Unit III (461.5–625.7 mbsf) is a 164.2-m-thick Pleistocene sequence of chalk, limestone, and calcareous mixed sedimentary rocks interbedded with volcanic siltstone, sandstone, and sed-lithic breccia containing volcanic clasts. The bottom of the unit is late Pliocene or early Pleistocene in age. Lithostratigraphic Unit IV (625.7–702.0 mbsf) is a 76.3-m-thick upper Pliocene or lower Pleistocene sequence of basaltic breccias with subordinate volcanic siltstones and sandstones. Lithostratigraphic Unit V (702.0–865.7 mbsf) is a 163.7-m-thick upper Miocene to upper Pliocene sequence of foraminiferal, nannofossil, calcareous, and silty limestone with some clayey siltstone, mixed sedimentary rocks, and vitric ash layers overlying a 1.5-m-thick basaltic breccia. Lithostratigraphic Unit VI (865.7–952.6 mbsf) is a 86.9-m-thick, middle to upper(?) Miocene lithified volcanic sandstone that grades downward to coarser material. Lithostratigraphic Unit VII (952.6–1106.7 mbsf) is a 154.1-m-thick layer of lithified basaltic breccia with subordinate lithified volcanic sandstone, siltstone, and vitric ash. The top of the unit is latest early to earliest middle Miocene in age.

Foraminifers and nannofossils were the best source of age information. Abundant to common, well-preserved foraminiferal and nannofossil assemblages were recovered between the seafloor

¹ Collot, J.-Y., Greene, H. G., Stokking, L. B., et al., 1992. *Proc. ODP, Init. Repts.*, 134: College Station, TX (Ocean Drilling Program).

² Shipboard Scientific Party is as given in the list of participants preceding the contents.

and 840 mbsf in both Holes 832A and 832B. Below this depth only occasional samples of moderately to poorly preserved foraminifers and nannofossils were reported. Two barren intervals were identified (856–923 mbsf and 972–1106 mbsf). Ages assigned to sediments at Site 832 are as follows: Pleistocene (0 to ~600 mbsf), late Pliocene or early Pleistocene(?) (600–711 mbsf), late Pliocene (711–740 mbsf), early Pliocene to late Miocene (740–856 mbsf), earliest middle Miocene (924–962 mbsf), and latest early Miocene (962 to ~972 mbsf). However, the presence of reworked specimens of the larger benthic foraminifers and calcareous nannofossils in samples below 952 mbsf suggests that the host rock may be younger than early Miocene.

Sediment accumulation rates determined from the biostratigraphic data indicate an important change at ~700 mbsf where the rates vary from less than 100 m/m.y. below this depth to greater than 286 m/m.y. above this depth. Interpretations of seismic reflection profiles and lithostratigraphic examinations of cores from Hole 832B indicate an unconformity at about 700 mbsf, but the biostratigraphic data do not indicate a hiatus that would be longer than about 0.2 m.y. Between the lower Pliocene at 856 mbsf and the lowermost Miocene at 952 mbsf there may be another unconformity.

Correlation between biostratigraphic and paleomagnetic data suggests that the lower boundary of the Olduvai is near 707 mbsf and consequently the Matuyama-Brunhes transition (early Pleistocene) is missing between 640 and 700 mbsf. Several other magnetic reversals that were observed between 707 mbsf and the total depth (TD) of Hole 832B appear to correlate with Pliocene to late Miocene ages. Benthic foraminifers, where found, indicate that sediments of Site 832 were deposited in the lower bathyal zone.

More than 10 volcanic ash layers >3 cm thick and several tens of reworked volcanic ash layers were recovered at Site 832. Fragments of clinopyroxene-phyric basalt or ankaramite were found in the cores between 395 and 1100 mbsf and show vesicular texture and little oxidation, indicating that they underwent little weathering or seawater alteration before burial. Between 1050 and 1100 mbsf, the altered volcanic breccia of lithostratigraphic Unit VII consists of clasts of scoria and lavas within a matrix of chloritized glass, clay minerals, and zeolite. This volcanic breccia was probably derived from submarine volcanism, as suggested by the abundant alteration products contained in the matrix.

Structural studies indicate that deformation observed in cores from Site 832 appears to result from small- to large-scale slumping, normal microfaulting, and compaction processes. Five tectonic units were identified. Tectonic Unit A (0–415 mbsf) includes lithostratigraphic Unit I and the upper part of Unit II and is characterized by subhorizontal bedding, rare slump features, vertical normal microfaults, contorted bedding, and load features that developed in a finely laminated siltstone. Tectonic Unit B (415–626 mbsf) includes the lower part of lithostratigraphic Unit II and all of lithostratigraphic Unit III, which is characterized by abundant slump folds. Tectonic Unit C (696–702 mbsf) corresponds to lithostratigraphic Unit IV, which has laminated siltstone beds dipping 30°–60°, suggesting the presence of slumps. Tectonic Unit D (702–866 mbsf) corresponds to lithostratigraphic Unit V and exhibits mainly horizontal bedding, a few veins filled with gypsum, and normal microfaults with well-developed slickensides. Some sigmoidal features oblique to the bedding are interpreted as forming in response to bedding-parallel extension. Tectonic Unit E (866–1107 mbsf) corresponds to lithostratigraphic Unit VI and VII and is characterized by rarely observable bedding that dips between 20° and 40°; microfaults and an overturned layer are indicative of slumping.

The concentrations of all measured solutes at Site 832 range widely, particularly those of calcium (1.9–215.9 mM), magnesium (0–50.6 mM), sodium (344–501 mM), potassium (2.3–15.2 mM), and chloride (551–742 mM). Each solute exhibits distinct maxima and minima, and the calcium minimum corresponds to the maxima in the concentrations of other solutes. The changes in concentrations probably result from diagenetic alteration of volcanogenic material and from precipitation of authigenic carbonate and phosphate minerals. Sulfate concentration decreases to 0.6 mM in the upper 40 mbsf, but exhibits two maxima at 520.7 mbsf (23.8 mM)

and 802.3 mbsf (22.9 mM), which correspond to the calcium minimum and the sodium, potassium, magnesium, and chloride maxima. Accompanying the decrease in sulfate at approximately 75 mbsf, resulting from sulfate reduction, are maxima of phosphate, ammonia, methane, and alkalinity. These maxima probably reflect organic matter diagenesis and the solutes may provide a source of phosphate and bicarbonate for the authigenic minerals. Organic carbon contents are low, mostly less than 0.5%, but rapid sediment accumulation rates cause high concentrations of the various solutes.

Physical properties measurements at Site 832 were nearly constant from the mudline to below 300 mbsf. This uniformity and consistently low shear strength values (around 50 kPa from 0 to 260 mbsf) indicate underconsolidation, which is typical of an area of rapid sedimentation. Porosity and water content have high values that vary from 50% to 80%. Silty ash layers in lithostratigraphic Unit I are the most porous, least consolidated, and contain the greatest amount of fluid of all material at Site 832. Below 300 mbsf, downhole porosity and water content decrease but maintain relatively high values that rarely fall below 40% and 25%. Bulk density increases from 1.60 to 2.00 Mg/m³ in the upper 300 mbsf of Hole 832B and varies between 2.00 and 2.40 Mg/m³ from 300 to 1103 mbsf. A distinct decrease in porosity (~20%) and an increase in bulk density (>2.50 Mg/m³) are associated with the breccias and coarse sandstones in lithostratigraphic Units II and IV, between 300–400 mbsf and 600–700 mbsf. Sonic velocities are generally low in the upper silty ash of lithostratigraphic Unit I, where they range from 1520 meters per second (m/s) near the seafloor to 1600 m/s at 260 mbsf. Velocity varies between 2000 and 3500 m/s from 260 mbsf to TD of Hole 832B at 1103.3 mbsf. However, the interval between 625 and 702 mbsf exhibits an increase in velocity to over 4000 m/s, which correlates with a sharp bulk density increase and the presence of a volcanic sandstone horizon in lithostratigraphic Unit IV.

Because of deteriorating hole conditions, including bridging and rapid infilling from the upper parts, the complete complement of logging tools could not be used. However, the geophysical string and the formation microscanner were run and produced good data.

Initial heat-flow analyses indicate that a high thermal gradient exists within the intra-arc basin and this, along with porous and fractured volcanoclastic rocks, caused the anomalous alteration and diagenesis reported above. The volcanoclastic rocks encountered at this site are surprisingly un lithified with the exception of isolated layers, as indicated by the high porosity and water content. At one point during the logging operations, high-pressure water flow occurred through the drill string, which is believed to be the result of a highly pressured, highly permeable formational salt-water layer.

BACKGROUND AND OBJECTIVES

Site 832 is the first of two sites (Sites 832 and 833) located within the intra-arc basin of the central New Hebrides Island Arc (Vanuatu). The site is located on the flat basin floor at 3089.3 mbsl in the north central part of the North Aoba Basin (NAB), approximately 50 km northeast of the northern tip of the Queiros Peninsula of Espiritu Santo Island and 45 km due south of the active volcanic island of Santa Maria (Fig. 1).

The NAB is part of a broad arc platform with substantial intra-arc basins, known collectively as the Central Basins of Vanuatu (Fig. 2). The Central Basins lie between the uplifted bedrock masses of Malakula and Espiritu Santo islands (the Western Belt) on one side, and Pentecost and Maewo islands (the Eastern Belt) on the other. The active volcanic island of Aoba divides the basin into two major physiographic and sedimentary basins, the North Aoba Basin, and the South Aoba Basin (SAB) (Katz, 1981) (Fig. 1). The Central Basins are primary depocenters, being filled with detritus transported from the islands and with planktonic biogenic material.

The NAB and SAB were first described as a single inter-arc basin (Karig and Mammerickx, 1972) and then as a late-stage

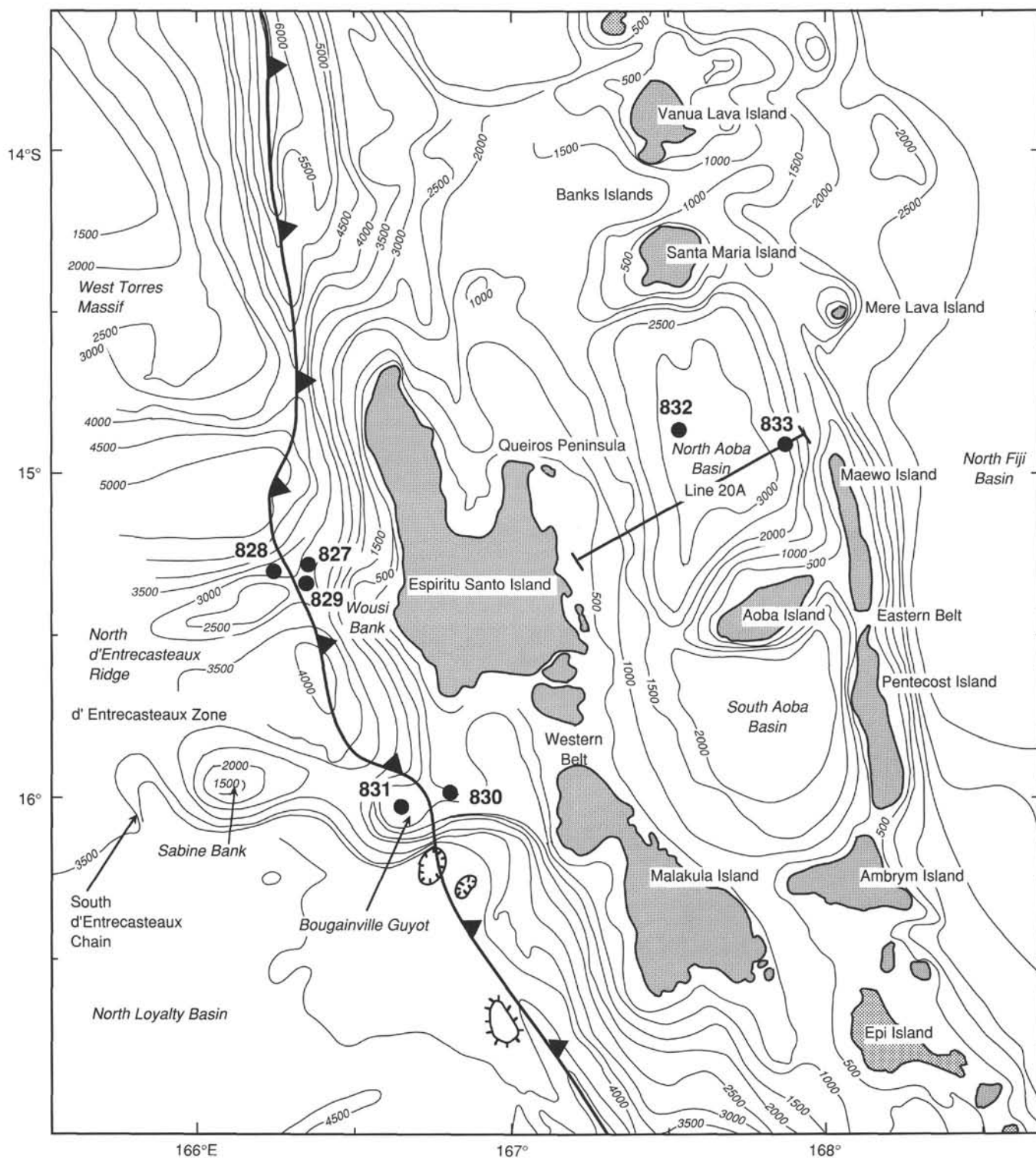


Figure 1. Bathymetric map of intra-arc basin (Central Basins) area of the central New Hebrides Island Arc showing location of Leg 134 sites. Solid line in North Aoba Basin is location of seismic reflection profile, a line drawing of which is shown in Figure 4. Bold line with teeth indicates approximate position of subduction zone; teeth are on upper plate. Bathymetry (in meters) modified after Chase and Seekins (1988).

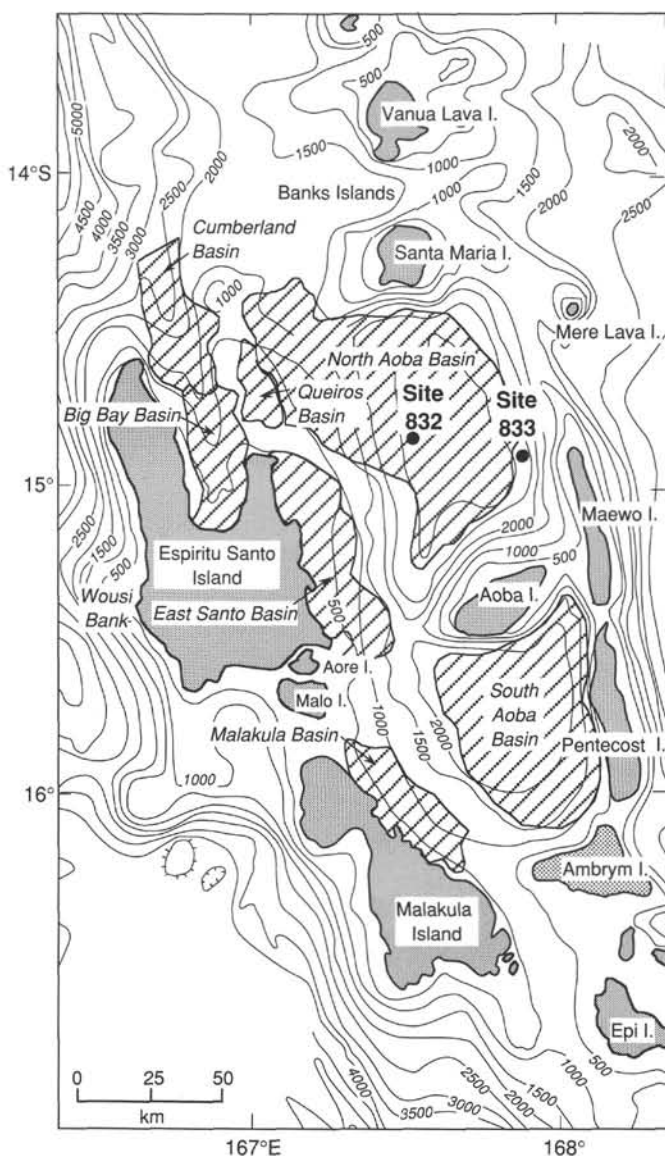


Figure 2. Sedimentary (structural) basins of the central New Hebrides Island Arc (Vanuatu) summit platform area. Modified after Greene and Johnson (1988). Bathymetry in meters.

extensional feature (Luyendyk et al., 1974). Ravenne et al. (1977) considered these basins to be part of a nearly continuous "median sedimentary basin" of the New Hebrides Island Arc. Carney and Macfarlane (1980) described the two basins as an asymmetrical intra-arc basin containing thick deposits of Miocene to Pliocene sediments. Katz (1981) estimates a sedimentary fill more than 2 km thick based on a 1972 geophysical investigation by ORSTOM (France) and suggests that each basin contains different rock types deposited under different sedimentary conditions. Gravity and seismic refraction data indicate that the Central Basins formed on 12- to 13-km-thick crust (Collot and Fisher, 1988). This contrasts with a 25-km-thick crust in the southern part of the arc, and Collot and Fisher (1988) propose this as an explanation for the unusually great depths of the basins. These authors further suggest that the crust of the Central Basins may have originated either as a trapped piece of oceanic crust or from crustal thinning by extension.

Many hypotheses have been set forth to explain the formation of the Central Basins and of the islands and ridges that border them (e.g., Dickinson, 1973; Chase, 1971; Pascal et al., 1973; Falvey, 1975; Coleman and Packham, 1976; Ravenne et al., 1977; Carney and Macfarlane, 1977, 1978, 1980, 1982, 1985; Katz, 1988). One school of thought supposes that a reversal of subduction polarity during the late middle Miocene, from a west-dipping subduction of the Pacific plate along the Vitiav Trench to the present overriding of the Australia-India plate at the New Hebrides Trench, formed the basins (Chase, 1971; Carney and Macfarlane, 1978, 1980; Kroenke, 1984; Macfarlane et al., 1988). Other workers propose that no shift in subduction direction has occurred and that the present arc configuration is the result of a continuous eastward convergence with variation in the steepness of the Benioff zone (Luyendyk et al., 1974; Carney and Macfarlane, 1977; Hanus and Vanek, 1983; Katz, 1988). Hanus and Vanek (1983) conclude, on the basis of the distribution of earthquake focuses along the New Hebrides Benioff zone, that two differently inclined slabs exist at intermediate depths. They argue that these slabs were produced from two consecutive subduction cycles of the same polarity and that these two cycles can explain the formation of the three belts of volcanic islands that make up the New Hebrides Island Arc. In a similar manner, Louat et al. (1988) conclude that only eastward subduction and a steepening Benioff zone are responsible for the formation of the various volcanic belts and of the NAB and SAB.

Collot et al. (1985) used the model of Chung and Kanamori (1978) to explain the uplift of the Western and Eastern belts and the depression of the intra-arc basins. The d'Entrecasteaux Zone (DEZ) collision applied pressure to the western edge of what Chung and Kanamori (1978) would call a semi-infinite elastic plate; upward loading due to the buoyancy of the subducting DEZ caused the buckling of the Central Basins area and the uplift of the Western Belt only. Collot et al. (1985) refined this model to a finite plate by having the Eastern Belt islands break along faults along their eastern flanks, which caused these islands to uplift as well. Geological long-range imaging asdic (GLORIA) data, recently collected by the South Pacific Applied Geosciences Commission (SOPAC), and Seabeam bathymetric data, collected by the Office de la Recherche Scientifique et Technique Outre-Mer (ORSTOM), show thrust sheets along the base of the eastern flank of the Eastern Belt, which suggests that compressional stress is transmitted completely across the arc.

The islands of Vanuatu are divided geologically into three different provinces based on three separate episodes of volcanism: the Western Belt, the Eastern Belt, and the Central Chain. Volcanism took place between the late Oligocene and early middle Miocene in the Western Belt, between the late Miocene and Pliocene in the Eastern Belt, and between the late Miocene and Holocene in the Central Chain (Mitchell and Warden, 1971; Mallick, 1973).

The sequence of Eastern Belt rocks underlies horsts that support Maewo and Pentecost islands (Mallick and Neef, 1974). The older rocks of this belt (Sigotara Group and Tafwutmutu Formation on Maewo) consist of lower to upper Miocene volcanoclastic rocks and conglomerate (Fig. 3). On Maewo, they contain clasts of terrigenous lava with island-arc tholeiitic affinities (Carney and Macfarlane, 1982). Overlying these older sediments are upper Miocene to middle Pliocene island-arc rocks (Maewo Group) of transitional calc-alkaline/tholeiitic composition. On Maewo Island these are both intergradational with and succeeded unconformably by upper Miocene to upper Pliocene *Globigerina* ooze of the Marino Formation. These abyssal rocks were uplifted and eroded

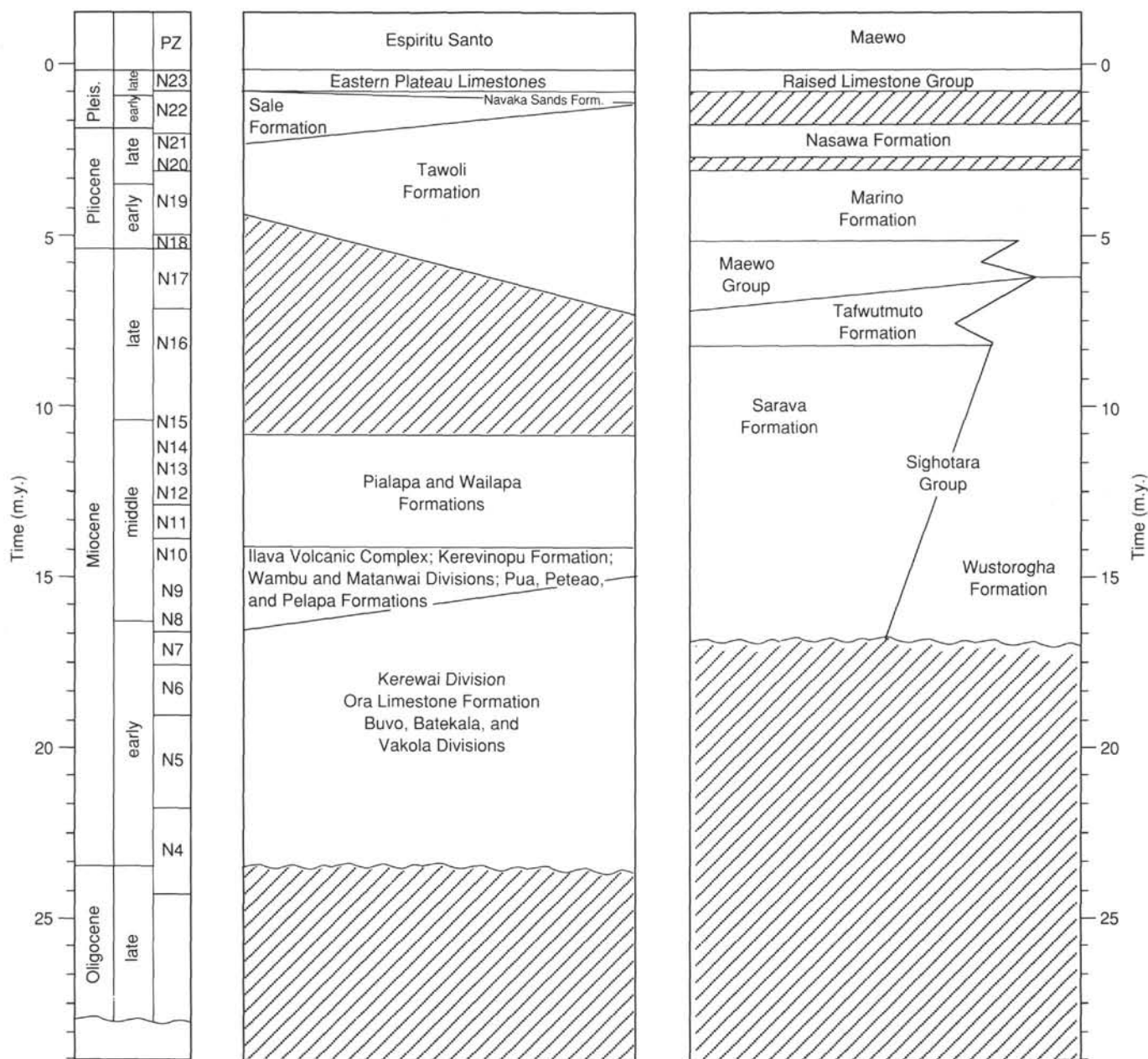


Figure 3. Principal stratigraphic units of Espiritu Santo Island (Western Belt) and Maewo Island (Eastern Belt) with Neogene time scale and planktonic foraminiferal zones (PZ) from Berggren et al. (1985b). Modified after Macfarlane et al. (1988).

during the middle to late Pliocene. Deposition of Nasawa Formation calcarenites and calcilutites followed, and Maewo Island also has a partial cap of Quaternary raised reef limestones (Macfarlane et al., 1988).

The Central Chain is the presently active volcanic arc, which is as old as 5.8 Ma in the southern part of the New Hebrides Island Arc, but Pleistocene in age in the central part (Colley and Ash, 1971; Bellon et al., 1984). Rocks of this chain consist primarily of basalt and andesite with some dacite. These rocks show a varied alkali content ranging from low-potassium tholeiite to high-potassium calc-alkaline rocks (Carney et al., 1985). Ankaramitic and picritic lavas are common on Ambrym and Aoba islands (Gorton, 1974). Carney and Macfarlane (1982) and Macfarlane et al. (1988) conclude from age dates that initial volcanism of the Central Chain was

contemporaneous, at least in part, with volcanism in the Eastern Belt.

The rocks of the Western Belt are exposed on the islands of Malakula and Espiritu Santo islands. Older rocks (volcanic rocks of Espiritu Santo Island) of this belt consist of upper Oligocene to middle Miocene submarine calc-alkaline lava and associated volcanoclastic rocks that are intruded by late-stage gabbro, andesite, and microdiorite stocks. East of the main volcanic axis of the belt, middle Miocene graywacke fills grabens (summit basins) caused by block faulting of these Oligocene and Miocene rocks. A major middle Miocene unconformity truncates these basinal rocks. On Espiritu Santo Island, the Tawoli Formation overlies this unconformity and consists of shallow marine sediments, which include terrigenous clasts that grade upward into deeper water sediments.

Uplifted Quaternary reef limestones cover the older sequences of rocks (Macfarlane et al., 1988).

The North Aoba Basin has been described as a half graben, tilted to the east (Katz, 1988; Fisher et al., 1988), although island structure (Carney and Macfarlane, 1982) and structure mapped along the island shelves and shallow slopes indicate it is a graben. The basin is filled with at least 5 km of sedimentary deposits (Holmes, 1988). In the central part of the basin, seismic reflection profiles (Fisher et al., 1988; Greene and Johnson, 1988) do not show acoustic basement, and the floor of the sedimentary basin cannot be determined from these data (Fig. 4).

On the basis of dredge samples and correlation of acoustical units with island geology, the oldest rocks in NAB appear to be upper Oligocene to lower middle Miocene volcanic rocks that underlie the west slope of the basin (unit E in Fig. 4), and middle Miocene volcanoclastic graywacke and limestone (unit D in Fig. 4) (Greene and Johnson, 1988; Johnson et al., 1988). Unit C in Figure 4 is interpreted as a gently faulted sequence of probable upper Miocene calcarenite more than 1.8 km thick, which laps onto the east and west flanks of the basin. Dredge samples collected along the northwestern flank of Maewo Island where acoustic units D and C crop out (DR-20, Fig. 4) are volcanic sandstone and mudstone, generally composed of vitric and crystal ash with scattered foraminifers and other skeletal debris (Johnson et al., 1988). Foraminifers indicate ages from middle-late Miocene to Pliocene, with some ranging into Pleistocene, thus correlating with the Miocene to Pliocene Marino Formation and Maewo Group on Maewo Island (Fig. 3). Another 0.8 km of uppermost Pliocene and lowermost Pleistocene calcarenite and calcilitute (unit B in Fig. 4) overlie the upper Miocene sedimentary rocks of

acoustic unit C, as indicated by dredge samples from northwestern Maewo that correlate with the late Pliocene and early Pleistocene Nasawa Formation of northern Maewo Island (Johnson et al., 1988). These rocks are, in turn, overlain by 0.8 km of Quaternary volcanic ash and pelagic sediments (unit A in Fig. 4) in the central area of the physiographic basin (Johnson and Greene, 1988). The flanks of the basin are covered by 10–100 m of unstable Quaternary slope sediments (slumps in Fig. 4). This thick sequence of basin fill laps onto the east and west flanks of the basin, and the younger basinal rocks become less extensive through time, indicating either relative elevation of the basin flanks or depletion of sediment input, or both. Thus, the basin's structural relief (deepening) grew contemporaneously with sediment infilling.

As noted by many previous authors (e.g., Mallick, 1975; Carney and Macfarlane, 1977; Carney et al., 1985), the central New Hebrides Island Arc is a product of multiple phases of arc evolution. Seismic reflection profiles (Fisher, et al., 1988; Greene and Johnson, 1988) indicate that the Central Basins are a product of four (numbered 1 through 4 in Fig. 4) tectono-sedimentary phases separated by unconformities, although the relationships tend to be more conformable toward the center of the Central Basins. In addition to the major horsts (Espiritu Santo, Malakula, Maewo, and Pentecost islands) and major grabens (NAB and SAB), smaller subsidiary fault blocks rose and subsided, alternately allowing erosion and deposition. Along the eastern shelf of Espiritu Santo Island a fault block defines East Santo Basin (Fig. 2). This block is downdropped to the east and is separated from NAB by a fault-controlled structural ridge capped by reefs. This block is inferred to be a graben or half graben that accumulated sediments to thicknesses of approximately 2 km.

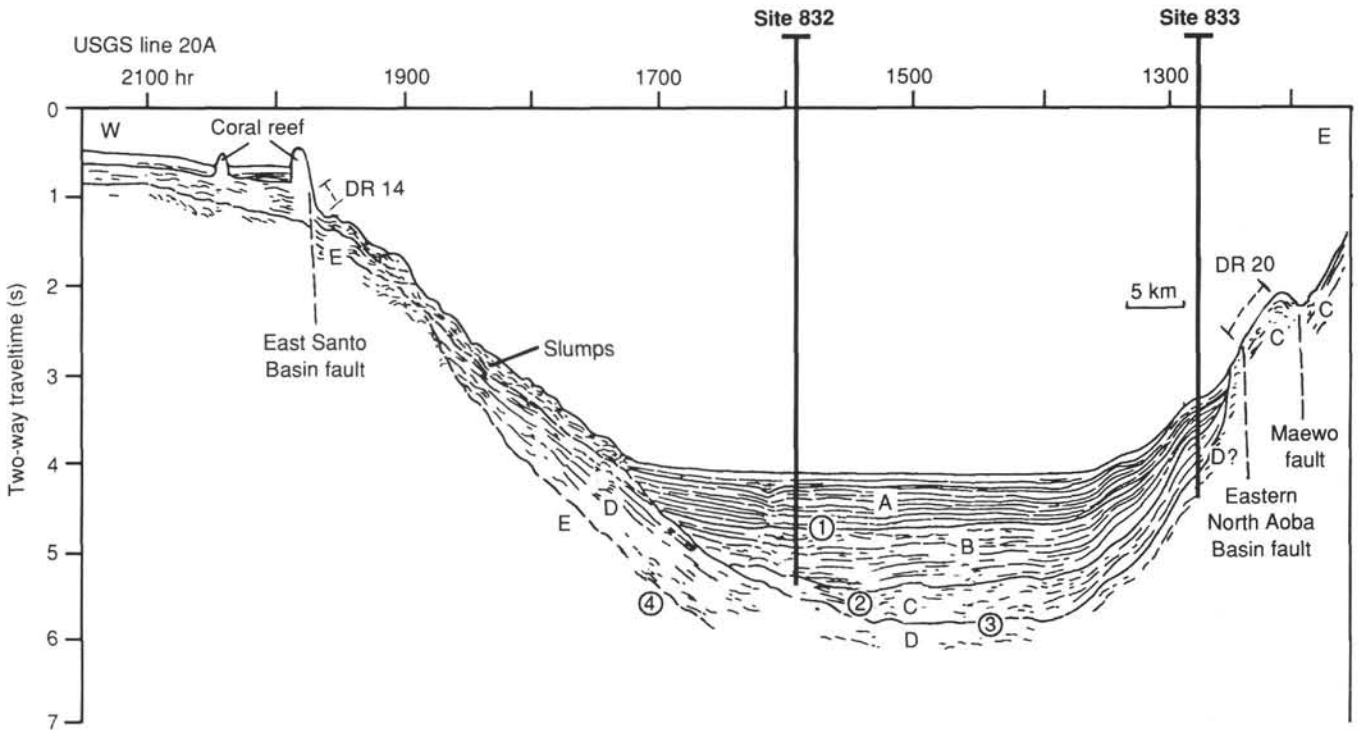


Figure 4. Line drawing of single-channel seismic reflection profile USGS L6-82-SP line 20A showing structure and acoustical stratigraphy of the North Aoba Basin. Letters relate to estimated age of acoustic units: A = Quaternary; B = uppermost Pliocene to lowermost Pleistocene; C = upper Miocene; D = middle Miocene; E = upper Oligocene to middle Miocene. Circled numbers refer to unconformities. Dredge locations are shown as heavy dashed lines with numbers prefixed by DR; numbers refer to dredge samples described by Johnson et al. (1988). Approximate location of Sites 832 and 833 are shown. Location of profile is indicated in Figure 1. Modified after Greene and Johnson (1988).

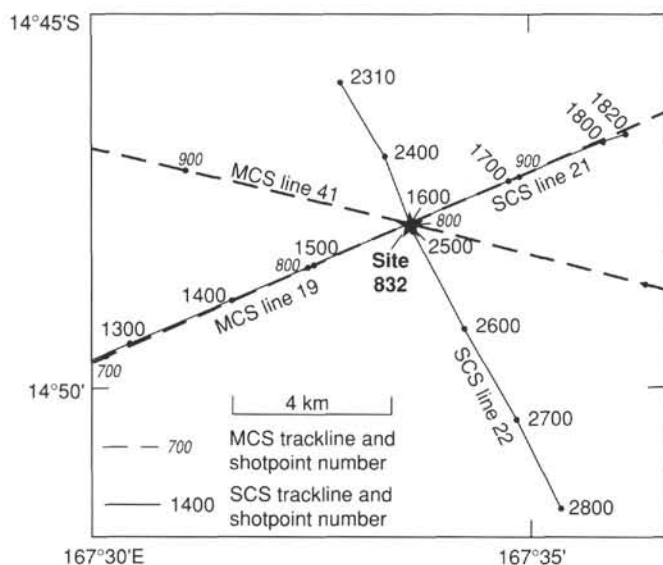


Figure 5. Trackline map showing the locations of Site 832, single-channel seismic lines 21 and 22, as well as migrated multichannel seismic lines 19 (USGS, L5-82-SP) and 41 (French Multipso, C1-87-SP).

The East Santo Basin is likely a subsiding step block; the entire basin fill is layered almost horizontally and the present seabed has a low gradient of 2.5° slope.

The presence of erosional and buttress unconformities in the Central Basins attests that vertical tectonism elevated and depressed local horsts and grabens. In addition to the vertical tectonics, transcurrent motion divided the Central Basins through arc-transverse faulting and extrusion of volcanic rocks at Aoba and Ambrym islands (Greene et al., 1988). This segmentation of the Central Basins appears to be the result of the collision of the DEZ with the New Hebrides Island Arc. Onset of the DEZ collision resulted in the uplift of the Western Belt islands that is reflected in a buttress unconformity within the Central Basins. Unconformity 3 (Fig. 4) is thought to represent the approximate time of collision and thus is the major objective for Site 832.

The principal objectives of drilling at Site 832 are closely related to those of Site 833, as correlation between these two holes is necessary to determine basin-wide sedimentary and tectonic events. These objectives are as follows:

1. To determine if the central New Hebrides Island Arc (Vanuatu) is a product of cyclic arc volcanism and tectonism since the Oligocene, with the axis of volcanism shifting at least three times, from the Western Belt to the Eastern Belt to the Central Chain; and to refine the relationship of the volcanism to changing subduction direction and angles.

2. To determine if the thick sedimentary sequence of the intra-arc basin formed as a result of uplift of the western margin by the end of the middle Miocene and uplift of the eastern margin starting from the middle Pliocene, and to establish whether the basin floor was a sloping platform for most of its history or whether it evolved rapidly into its deep downbowed (graben) form during the Quaternary.

3. To determine the role of extraneous events, such as arc polarity reversals and collision with ridges, in the formation of the intra-arc basin in light of the major differences between this arc-platform complex and other more "standard" volcanic arcs such as Tonga, Kermadec, and the Marianas.

SEISMIC STRATIGRAPHY

Multichannel Seismic Data

Multichannel seismic line 19 crosses east-west over the North Aoba Basin (Fig. 5), and the whole line (not shown here) reveals that the older fill in this basin has been depressed into a broad syncline that trends north-south; the younger, horizontally stratified basin fill laps with an angular unconformity onto the sides of this syncline (Fig. 6). The unconformity, about 700 mbsf at Site 832, reveals abrupt development of relief within the arc-summit areas that flank the basin on the east and west. One explanation for this relief is that the basin began to subside when stress from the collision of the North d'Entrecasteaux Ridge and the arc intensified sufficiently to affect the intra-arc Aoba Basin. This time of heightened stress does not necessarily coincide with the inception of the collision. The rapidity of relief development is apparent from the near absence of offlap sequences along the west basin flank and is borne out by the Pleistocene and Pliocene(?) age of the 700 m of sediment over the unconformity that were recovered at the drill site.

Multichannel seismic sections reveal that the seafloor over the west flank of the basin has locally irregular morphology; this irregularity may signify mass wasting of west-flank rocks that began as a consequence of basin deepening. Mass wasting apparently affects rock bodies that are as thick as 500 m. This mass wasting may explain the origin of the coarse volcanic breccia that was found during drilling to directly overlie the unconformity in the basin.

Water over the drill site is about 3000 m deep; even so, velocity information derived from seismic reflection and seismic refraction data indicate that, in the upper 300 m of the well-bedded basin fill, the acoustic velocity does not differ significantly from that of seawater, indicating very unconsolidated sediment. In fact, many of the volcanic ash-rich layers in the upper 300 m of the hole were unconsolidated and described as "soupy" in core descriptions (see "Lithostratigraphy" section, this chapter).

Multichannel seismic line 19 crosses over Site 832 and reveals the angular bedding intersection at the unconformity that was the main target at this site (Figs. 5 and 6). Strong, parallel reflections from the shallow part of the basin fill lap progressively onto the western basin flank. Below the unconformity is a thin rock body that primarily returns weak reflections, which parallel the seismic events from beds that make up the basin fill below the unconformity. This weakly reflective unit thins toward the basin center. Rocks below the unconformity return mainly weak, discontinuous reflections.

Single-Channel Seismic Data

Single-channel seismic reflection data were collected over Site 832, using two 80-in.³ water guns for the source and a streamer that has a 100-m-long active section. Aboard-ship processing included predictive deconvolution, bandpass filtering, and automatic gain control. Velocity data used to convert depth in the hole to traveltimes come primarily from the sonic log and partly from physical properties measurements, which were used where well logs are not available, from the part of the hole shallower than 275 m.

Site 832 lies just west of the intersection of single-channel seismic lines 21 and 22 that were collected aboard ship (Figs. 5, 7, and 8). These seismic lines show substantially similar acoustic images of the basin fill, but these images differ from that presented by the multichannel seismic section (Fig. 6) in

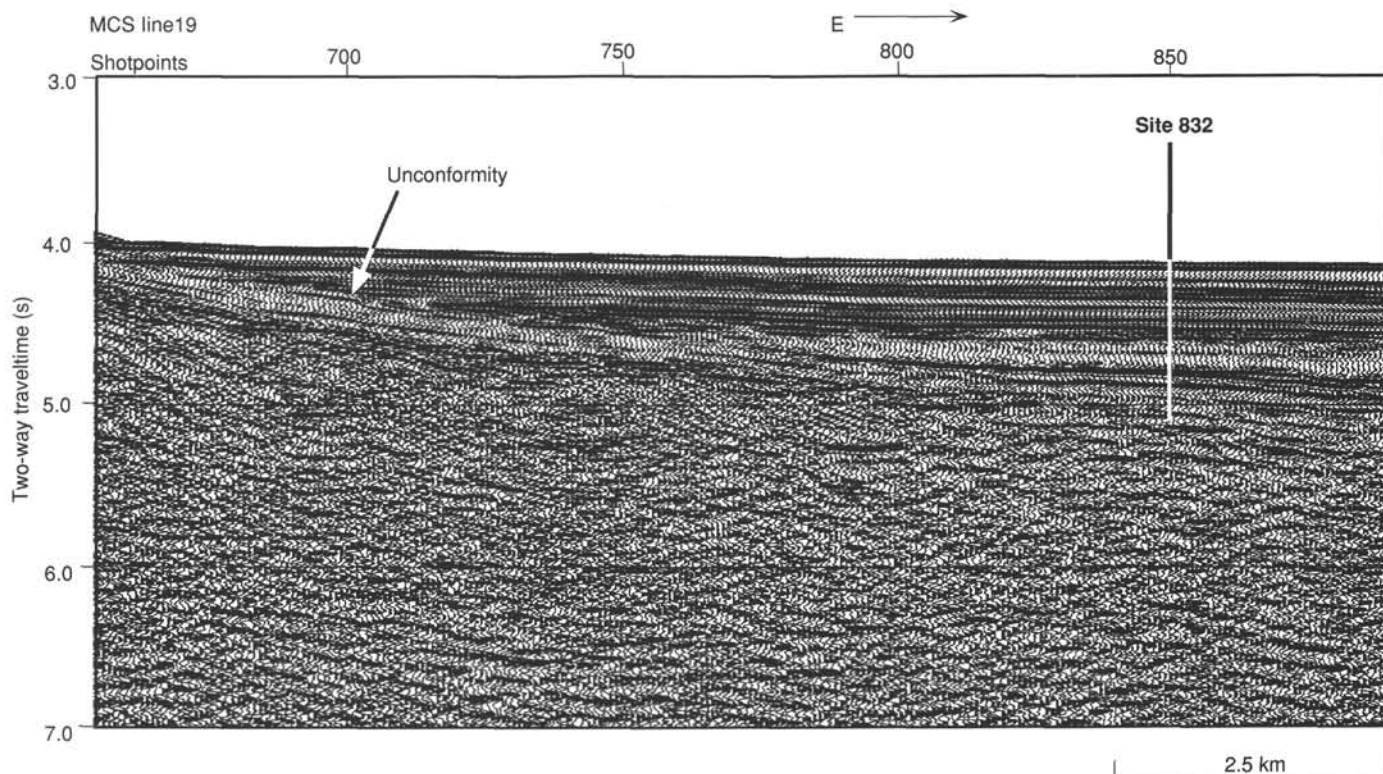


Figure 6. Part of migrated multichannel seismic line 19 (USGS, L5-82-SP) that crosses the arc near Site 832.

that the single-channel image of the unconformity includes mainly discontinuous reflections, whereas the multichannel reflection from the unconformity is strong and continuous. Single-channel seismic section 21 shows parallel, consistent, acoustic layering within 0.5 s of the seafloor. Reflections within the next 0.1 s are poorly reflective, and still-deeper rocks return strong discontinuous reflections.

A preliminary correlation between seismic data and lithostratigraphy (see "Lithostratigraphy" section, this chapter) shows a moderate correspondence between rock-unit boundaries and seismic reflections (Fig. 9). Lithostratigraphic Subunits IA and IB both include volcanic silts, clays, and sands but are distinguished on the basis of the generally coarse sediment that makes up Subunit IA. The contact between these subunits is marked by a strong, three-peaked reflection. The causes for two other continuous reflections, at traveltimes corresponding to 242 and 344 mbsf (Fig. 9), were not identified during core descriptions.

The reflection at 344 mbsf occurs just above the top of lithostratigraphic Unit II, which includes Pleistocene sandstone, siltstone, and claystone, that have a higher degree of consolidation than does the sediment of Unit I. The volcanic fraction of Unit II decreases downward, inversely to an increasing calcareous content.

The contact between lithostratigraphic Units II and III corresponds to a prominent reflection that lies at the base of the continuously parallel-layered basin fill. Unit III consists of Pleistocene and Pliocene(?), highly calcareous volcanic sandstones, siltstones, and breccias. These rocks produce only weak, discontinuous reflections. The weakly reflective zone also includes rocks of Unit IV, an upper Pliocene or Pleistocene basalt breccia with subordinate amounts of volcanic sandstone and siltstone.

The unconformity that was the main target of drilling at this site occurs at the traveltimes of 4.8 s, which corresponds to the base of lithostratigraphic Unit IV (Fig. 9). The unconformity separates the weakly reflective Units III and IV from underlying rocks of Unit V that return strong, discontinuous reflections. Unit V is an upper Miocene, Pliocene, and Pleistocene(?) limestone. The unconformity, therefore, is the contact between a limestone below and a coarse volcanic breccia above.

Reflections from rocks of lithostratigraphic Units V, VI, and VII are indistinguishable. The two deeper units include, in downward succession, a middle to upper Miocene volcanic sandstone and a lower to middle Miocene basalt breccia.

OPERATIONS

Site 832, proposed site IAB-1, is in the North Aoba Basin, located between the islands of Espiritu Santo, Maewo, Aoba, and Santa Maria. The vessel approached the site from the southwest along a reference profile, then conducted a 6-hr preliminary survey (see "Seismic Stratigraphy" section, this chapter) before dropping a positioning beacon at 0645 UTC on 21 November 1990, the third time the site was crossed.

Hole 832A

The first advanced piston coring system (APC) core penetrated the seafloor at 3089.3 mbsl. Oriented APC cores were attempted from 0 to 116 mbsf, although piston strokes were incomplete after the second core. The volcanic sandy and silty sediments were soupy and freely flowed into the core barrel below the cored interval. Unoriented short-stroke APC cores were taken to 151 mbsf, the point of APC refusal. The extended core barrel system (XCB) was then used, but core recovery averaged only 9% (Table 1), and at 215.9 mbsf the

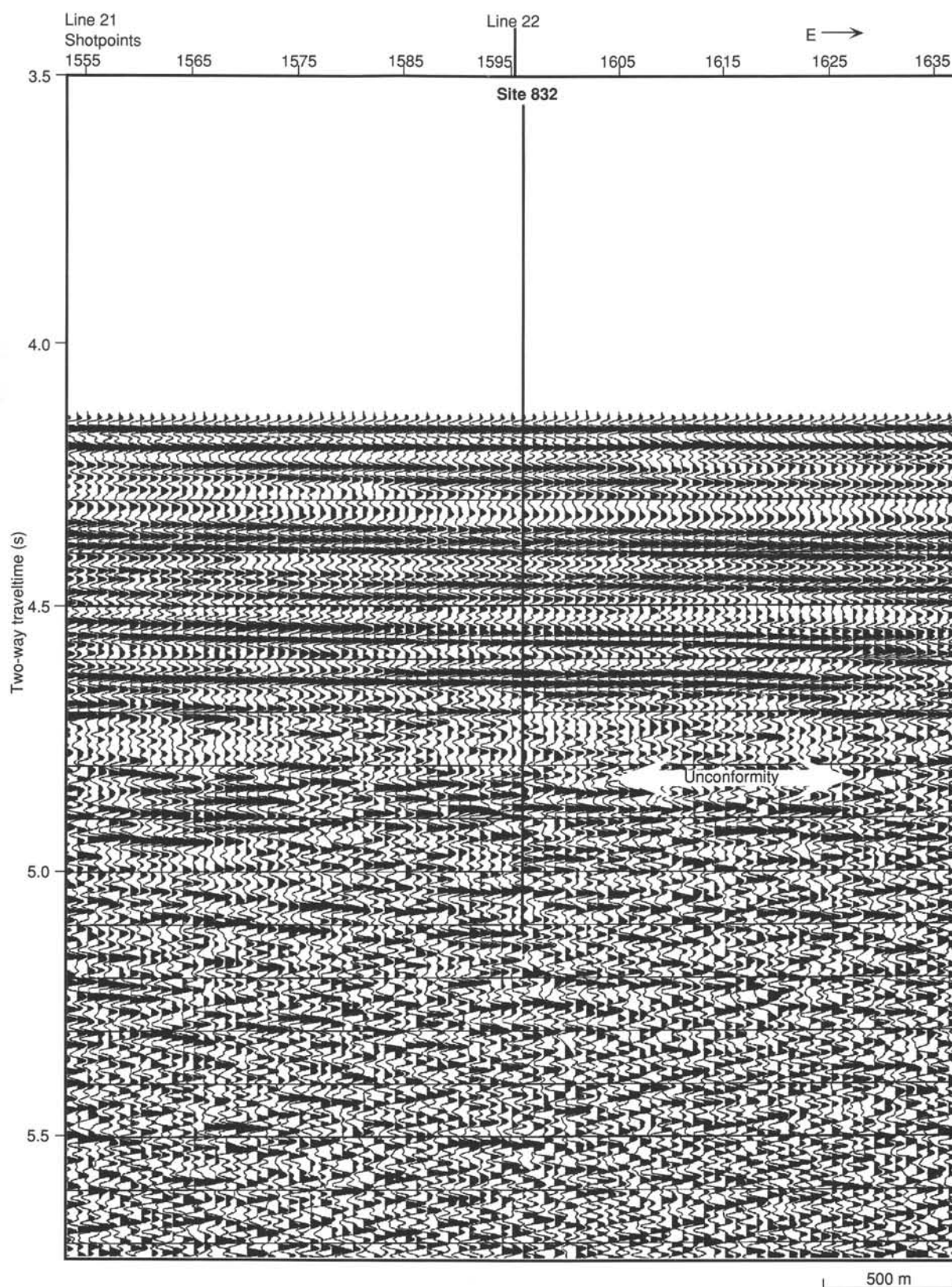


Figure 7. Part of single-channel seismic line 21 that crosses east-west over Site 832.

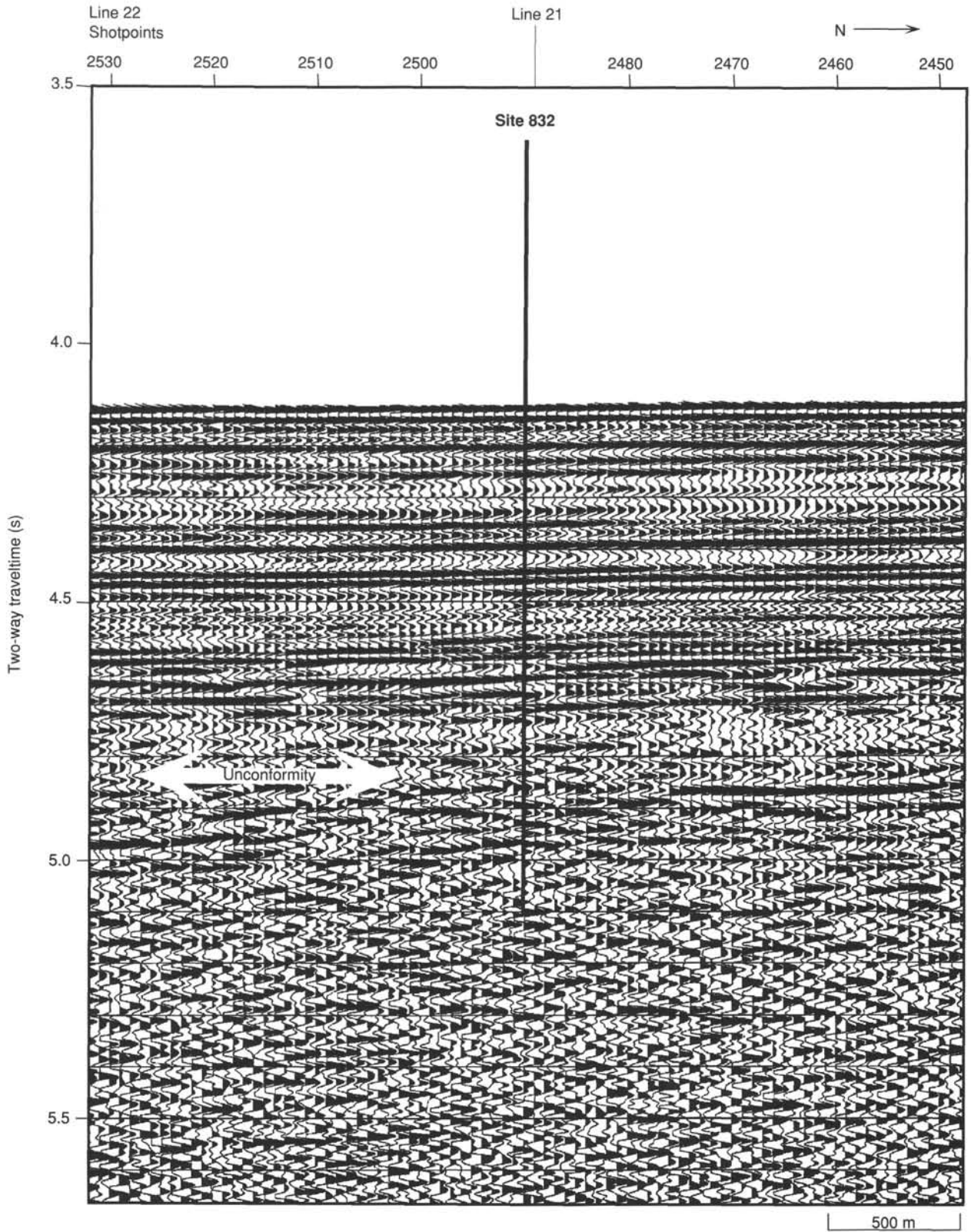


Figure 8. Part of single-channel seismic line 22 that trends north-south over Site 832.

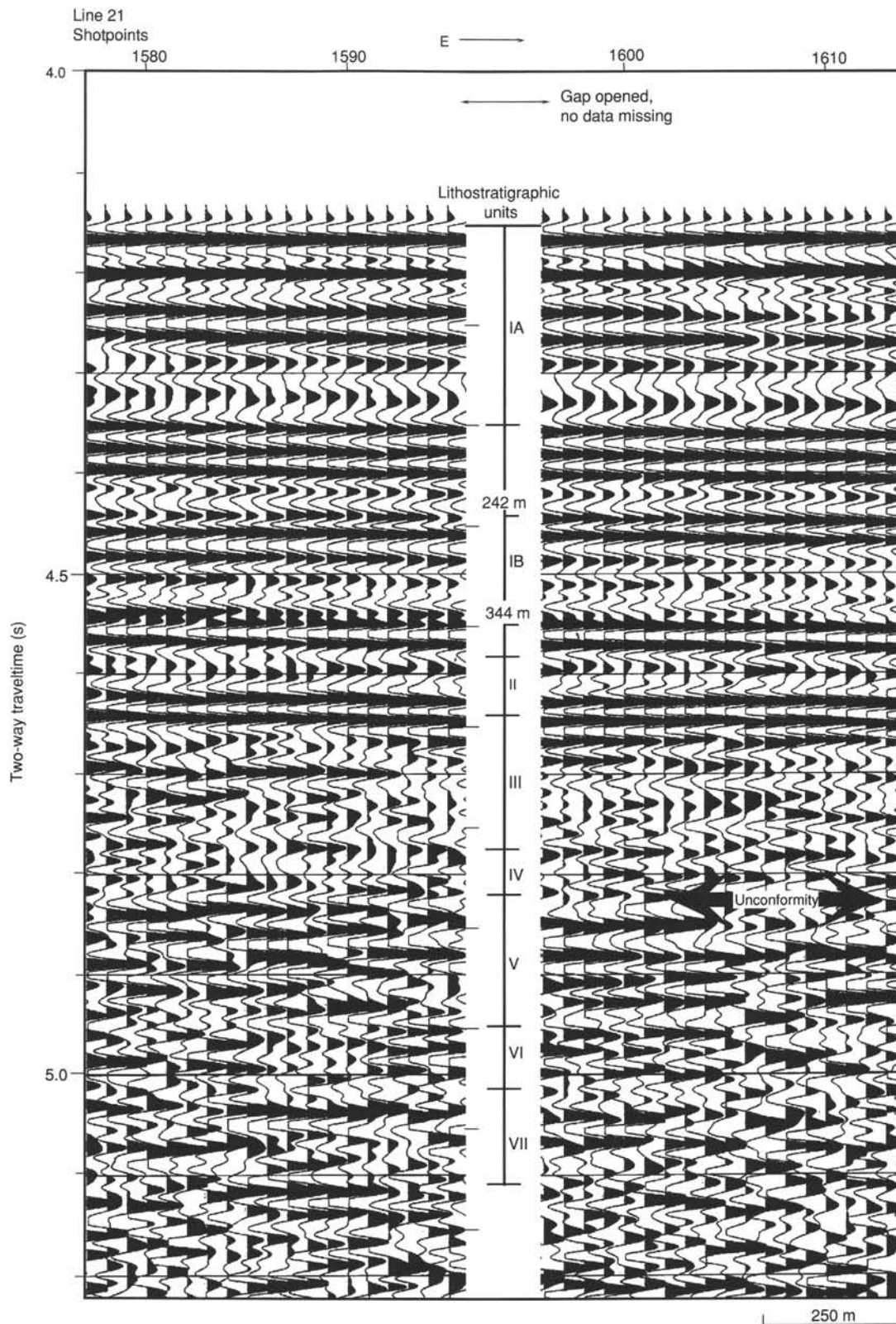


Figure 9. Detailed part of single-channel seismic line 21. Lithostratigraphic units, indicated by Roman numerals in the center of the figure, are explained in the "Lithostratigraphy" section (this chapter). Depths (mbsf) to some prominent reflections are shown along the vertical line in the center of the figure.

Table 1. Coring summary, Holes 832A and 832B.

Core	Date (1990)	Time (UTC)	Depth (mbsf)	Length cored (m)	Length recovered (m)	Recovery (%)	Age
134-832A-							
1H	21 November	1345	0.0–5.9	5.9	5.89	99.8	Pleistocene-Holocene
2H	21 November	1445	5.9–15.4	9.5	9.40	98.9	Pleistocene-Holocene
3H	21 November	1605	15.4–18.5	3.1	3.12	100.0	Pleistocene-Holocene
4H	21 November	1930	18.5–28.0	9.5	9.57	101.0	Pleistocene
5H	21 November	2015	28.0–37.5	9.5	9.64	101.0	Pleistocene
6H	21 November	2100	37.5–47.0	9.5	9.66	101.0	Pleistocene
7H	21 November	2315	47.0–56.5	9.5	9.63	101.0	Pleistocene
8H	22 November	0015	56.5–63.0	6.5	6.51	100.0	Pleistocene
9H	22 November	0100	63.0–72.5	9.5	9.76	103.0	Pleistocene
10H	22 November	0230	72.5–82.0	9.5	9.84	103.0	Pleistocene
11H	22 November	0330	82.0–91.5	9.5	9.87	104.0	Pleistocene
12H	22 November	0415	91.5–101.0	9.5	5.75	60.5	Pleistocene
13H	22 November	0500	101.0–102.0	1.0	4.18	418.0	Pleistocene
14H	22 November	0545	102.0–106.5	4.5	2.60	57.8	Pleistocene
15H	22 November	0700	106.5–116.0	9.5	3.70	38.9	
16H	22 November	0730	116.0–125.5	9.5	9.57	101.0	Pleistocene
17H	22 November	0810	125.5–131.5	6.0	5.58	93.0	Pleistocene
18H	22 November	0855	131.5–141.0	9.5	6.78	71.3	Pleistocene
19H	22 November	1015	141.0–145.0	4.0	2.92	73.0	Pleistocene
20H	22 November	1245	145.0–151.3	6.3	6.31	100.0	Pleistocene
21X	22 November	1400	151.3–158.6	7.3	0.34	4.7	
22X	22 November	1445	158.6–168.1	9.5	0.01	0.1	Pleistocene
23X	22 November	1530	168.1–177.7	9.6	0.00	0.0	Pleistocene
24X	22 November	1615	177.7–187.0	9.3	4.81	51.7	Pleistocene
25X	22 November	1700	187.0–196.7	9.7	0.00	0.0	Pleistocene
26X	22 November	1930	196.7–206.2	9.5	0.82	8.6	Pleistocene
27X	22 November	2015	206.2–215.9	9.7	0.00	0.0	
Coring totals				215.9	146.26	67.7	
134-832B-							
1R	23 November	1450	144.4–154.1	9.7	0.15	1.5	Pleistocene
2R	23 November	1540	154.1–163.8	9.7	0.25	2.6	Pleistocene
3R	23 November	1630	163.8–173.7	9.9	1.10	11.1	Pleistocene
4R	23 November	1830	173.7–183.3	9.6	0.24	2.5	Pleistocene
5R	23 November	1945	183.3–193.0	9.7	0.00	0.0	
6R	23 November	2100	193.0–202.2	9.2	0.00	0.0	
7R	23 November	2145	202.2–211.9	9.7	1.14	11.7	Pleistocene
8R	23 November	2230	211.9–221.4	9.5	1.04	10.9	Pleistocene
9R	23 November	2315	221.4–231.0	9.6	3.12	32.5	Pleistocene
10R	24 November	0100	231.0–240.7	9.7	0.00	0.0	
11R	24 November	0200	240.7–250.4	9.7	0.18	1.9	Pleistocene
12R	24 November	0245	250.4–260.0	9.6	0.00	0.0	
13R	24 November	0330	260.0–269.7	9.7	1.47	15.1	Pleistocene
14R	24 November	0415	269.7–279.4	9.7	1.17	12.0	Pleistocene
15R	24 November	0500	279.4–289.0	9.6	1.56	16.2	Pleistocene
16R	24 November	0545	289.0–298.7	9.7	1.90	19.6	Pleistocene
17R	24 November	0630	298.7–308.4	9.7	2.73	28.1	Pleistocene
18R	24 November	0730	308.4–318.1	9.7	4.20	43.3	Pleistocene
19R	24 November	1000	318.1–327.7	9.6	2.52	26.2	Pleistocene
20R	24 November	1050	327.7–337.4	9.7	3.32	34.2	
21R	24 November	1135	337.4–346.9	9.5	6.85	72.1	
22R	24 November	1255	346.9–356.6	9.7	1.26	13.0	Pleistocene
23R	24 November	1415	356.6–366.3	9.7	2.89	29.8	Pleistocene
24R	24 November	1550	366.3–376.0	9.7	0.00	0.0	Pleistocene
25R	24 November	1700	376.0–385.6	9.6	0.00	0.0	Pleistocene
26R	24 November	1950	385.6–395.3	9.7	1.37	14.1	Pleistocene
27R	24 November	2115	395.3–404.9	9.6	1.96	20.4	Pleistocene
28R	24 November	2230	404.9–414.2	9.3	7.17	77.1	
29R	24 November	2350	414.2–423.6	9.4	7.30	77.6	Pleistocene
30R	25 November	0100	423.6–433.2	9.6	9.28	96.6	Pleistocene
31R	25 November	0210	433.2–442.9	9.7	5.33	54.9	Pleistocene
32R	25 November	0315	442.9–451.9	9.0	5.45	60.5	Pleistocene
33R	25 November	0430	451.9–461.5	9.6	1.56	16.2	Pleistocene
34R	25 November	0540	461.5–471.1	9.6	2.93	30.5	Pleistocene
35R	25 November	0700	471.1–480.8	9.7	3.61	37.2	Pleistocene
36R	25 November	0820	480.8–490.4	9.6	3.37	35.1	Pleistocene
37R	25 November	0930	490.4–500.1	9.7	6.01	61.9	Pleistocene
38R	25 November	1050	500.1–509.8	9.7	2.17	22.4	Pleistocene
39R	25 November	1240	509.8–519.5	9.7	3.73	38.4	
40R	25 November	1355	519.5–529.2	9.7	2.35	24.2	
41R	25 November	1550	529.2–538.9	9.7	2.39	24.6	
42R	25 November	1700	538.9–548.5	9.6	4.25	44.3	
43R	25 November	1840	548.5–558.2	9.7	4.19	43.2	late Pliocene

Table 1 (continued).

Core	Date (1990)	Time (UTC)	Depth (mbsf)	Length cored (m)	Length recovered (m)	Recovery (%)	Age
44R	25 November	2030	558.2–567.7	9.5	1.77	18.6	late Pliocene
45R	25 November	2140	567.7–577.4	9.7	3.93	40.5	late Pliocene
46R	25 November	2250	577.4–587.0	9.6	3.67	38.2	late Pliocene
47R	26 November	0030	587.0–596.7	9.7	3.76	38.7	late Pliocene
48R	26 November	0145	596.7–606.4	9.7	1.53	15.8	late Pliocene
49R	26 November	0300	606.4–616.1	9.7	4.80	49.5	late Pliocene
50R	26 November	0415	616.1–625.7	9.6	5.44	56.6	
51R	26 November	0530	625.7–635.3	9.6	6.71	69.9	
52R	26 November	0715	635.3–645.0	9.7	8.20	84.5	
53R	26 November	0850	645.0–654.7	9.7	9.84	101.0	
54R	26 November	1050	654.7–664.4	9.7	5.80	59.8	
55R	26 November	1240	664.4–673.0	8.6	7.42	86.3	late Pliocene
56R	26 November	1500	673.0–682.7	9.7	6.34	65.3	
57R	26 November	1730	682.7–692.3	9.6	7.52	78.3	
58R	26 November	1915	692.3–702.0	9.7	2.38	24.5	
59R	26 November	2045	702.0–711.6	9.6	9.20	95.8	late Pliocene
60R	26 November	2200	711.6–720.8	9.2	7.69	83.6	late Pliocene
61R	26 November	2345	720.8–730.5	9.7	9.20	94.8	late Pliocene
62R	27 November	0120	730.5–739.8	9.3	4.97	53.4	late Pliocene
63R	27 November	0245	739.8–749.5	9.7	9.84	101.0	early Pliocene
64R	27 November	0400	749.5–759.2	9.7	7.73	79.7	early Pliocene
65R	27 November	0520	759.2–768.8	9.6	9.27	96.5	
66R	27 November	0655	768.8–778.6	9.8	5.32	54.3	
67R	27 November	0820	778.6–788.2	9.6	3.36	35.0	
68R	27 November	0930	788.2–797.8	9.6	0.41	4.3	
69R	27 November	1100	797.8–807.7	9.9	8.70	87.9	
70R	27 November	1215	807.7–817.4	9.7	9.91	102.0	late Miocene
71R	27 November	1405	817.4–827.0	9.6	7.56	78.7	late Miocene
72R	27 November	1540	827.0–836.7	9.7	7.96	82.0	
73R	27 November	1700	836.7–846.4	9.7	7.30	75.2	late Miocene
74R	27 November	1815	846.4–856.1	9.7	4.75	48.9	
75R	27 November	1930	856.1–865.7	9.6	0.00	0.0	
76R	27 November	2115	865.7–875.3	9.6	0.08	0.8	
77R	27 November	2230	875.3–885.0	9.7	0.26	2.7	
78R	28 November	0000	885.0–894.7	9.7	9.55	98.4	
79R	28 November	0130	894.7–904.4	9.7	7.51	77.4	
80R	28 November	0250	904.4–914.0	9.6	5.81	60.5	
81R	28 November	0415	914.0–923.7	9.7	4.67	48.1	
82R	28 November	0545	923.7–933.3	9.6	8.15	84.9	
83R	28 November	0705	933.3–942.9	9.6	4.92	51.2	
84R	28 November	0830	942.9–952.6	9.7	3.47	35.8	
85R	28 November	1000	952.6–962.2	9.6	7.33	76.3	
86R	28 November	1120	962.2–971.8	9.6	4.52	47.1	
87R	28 November	1335	971.8–981.1	9.3	4.77	51.3	
88R	28 November	1520	981.1–990.8	9.7	5.08	52.4	
89R	28 November	1720	990.8–1000.5	9.7	9.46	97.5	
90R	28 November	1900	1000.5–1010.1	9.6	9.86	103.0	
91R	28 November	2040	1010.1–1019.7	9.6	2.99	31.1	
92R	28 November	0210	1019.7–1029.3	9.6	2.38	24.8	
93R	29 November	0000	1029.3–1039.0	9.7	7.83	80.7	
94R	29 November	0200	1039.0–1048.6	9.6	4.52	47.1	
95R	29 November	0430	1048.6–1058.3	9.7	5.27	54.3	
96R	29 November	0640	1058.3–1068.0	9.7	7.01	72.2	
97R	29 November	0800	1068.0–1077.7	9.7	9.29	95.8	
98R	29 November	0930	1077.7–1087.3	9.6	8.71	90.7	
99R	29 November	1100	1087.3–1097.0	9.7	7.38	76.1	
100R	29 November	1315	1097.0–1106.7	9.7	6.34	65.3	
Coring totals				962.3	450.95	46.9	

hole was terminated. Five downhole temperature measurements were attempted in Hole 832A, but only two produced usable data.

Hole 832B

The ship was offset 25 m north of Hole 832A to drill Hole 832B. The hole was washed (drilled without coring) from 0 to 144.4 mbsf, then cored with the rotary core barrel system (RCB). From 144.4 to 327.7 mbsf, recovery averaged only 12% (see Table 1). Downhole temperature runs were made at 174 and 319 mbsf, and indicated that the geothermal gradient

in this part of the North Aoba Basin is relatively high (see "Downhole Measurements" section, this chapter).

Core recovery improved with depth as induration of the volcanoclastic sediments and the amount of clay and carbonate increased (see "Lithostratigraphy" section, this chapter). Hole conditions and rate of penetration (ROP) remained good as the target depth of 700 mbsf was approached. Because the sediments were younger than expected (see "Biostratigraphy" section, this chapter), clearance was requested and received to continue coring first to 1000 mbsf and subsequently to a maximum of 1200 mbsf. Although hole conditions

and ROP remained favorable, near 1020 mbsf the lithology changed to unfossiliferous basaltic breccia. At 1107 mbsf, coring was discontinued at the request of the co-chief scientists. A total of 962.3 m were cored for a recovery rate of 46.9% (Table 1).

A wiper trip made in preparation for logging encountered considerable resistance between about 250 and 154 mbsf and a substantial bridge at about 890 mbsf. Although these intervals were cleaned, logging was done in stages because of potential bridging problems (see "Downhole Measurements" section, this chapter). The end of the pipe was pulled up from the total depth (TD) of 1106.7 to 902 mbsf for the first logging tool runs. The geophysical tool string, consisting of the dual induction tool (DIT), the long-spaced sonic tool (LSS), the lithodensity tool (HLDT), and the LDGO temperature tool (TLT), was run successfully from 25 m above TD to 902 mbsf. While logging tools were being assembled for the second run, the pipe began to stick. The logging plan was revised to place the end of the pipe at 250 mbsf, the bottom of the upper interval in which resistance was encountered during the wiper trip, to run the remainder of the logs from as deep as possible to 250 mbsf. The hole then was cleaned out to TD and the pipe was pulled to 277 mbsf, where it became stuck.

When the pipe could not be freed after 2.5 hr of pulling, the logging program resumed, using the stuck pipe as surface casing. The seismic stratigraphy tool string (DIT, LSS, and TLT) was successfully deployed in the hole. This second run overlapped the first and the upper part of the hole was logged. The formation microscanner (FMS) was deployed to within 23 m of total depth and successfully recorded data up to about 520 mbsf, where it became stuck. It was freed and recovered without any further attempt at logging. A third logging run was made with the magnetic susceptibility tool string, but was aborted when the tool would not pass completely out of the drill string. Because of deteriorating logging conditions, the remaining scheduled logs were canceled. The drill string was worked free and recovered. After retrieving the positioning beacon, the *JOIDES Resolution* departed for the final site.

LITHOSTRATIGRAPHY

Sedimentary Units

On the basis of smear slides made from samples representative of visually distinct lithologies, and coulometric determinations of carbonate content, the stratigraphic succession at Site 832 is divided into seven lithologic units (Figs. 10, 11, and Table 2). The uppermost unit is subdivided into two subunits.

Because deep-sea drilling procedures do not cover the entire sediment sequence at any site, lithologies must be extrapolated across gaps in the recovery if the sum of the thicknesses of lithologic units is to equal the length of the drilled section. Where a compositional change occurs between recovered intervals, we have arbitrarily chosen to place the lithologic boundary at the top of the lower core. In effect, we assume for this purpose that the missing interval has the same composition as the bottom of the upper core. In Table 2 the entries in the columns for "interval," "depth," and "thickness" reflect this convention of extrapolation.

Lithostratigraphic Unit I (385.6 m thick, Pleistocene) comprises mainly sandy to clayey volcanic silts with interbedded volcanic ash layers, coarser in Subunit IA than in Subunit IB. Sandstones, siltstones, and claystones, largely volcanic in the upper part and more calcareous below, constitute lithostratigraphic Unit II (75.9 m thick, Pleistocene). Lithostratigraphic Unit III consists mainly of chalks, limestones, and mixed

sedimentary rocks, with interbedded volcanic sandstones and breccias (164.2 m thick, Pleistocene and possibly late Pliocene). Basaltic breccias, with subordinate volcanic sandstones and siltstones, constitute lithostratigraphic Unit IV (76.3 m thick, late Pliocene and/or Pleistocene). Below an abrupt transition, lithostratigraphic Unit V is composed predominantly of limestones (foraminiferal, nannofossil, and silty) and siltstones (163.7 m thick, mostly Pliocene with some Miocene). These are underlain by the volcanic sandstones, gradually coarsening downward, of lithostratigraphic Unit VI (86.9 m thick, middle to late Miocene). Basaltic breccias, with subordinate volcanic sandstones and siltstones, constitute lithostratigraphic Unit VII (154.1 m thick to the bottom of the hole, early to middle Miocene in the upper part, indeterminate below).

Lithostratigraphic Unit I

Depth: 0–206.2 mbsf (Hole 832A) and 144.4–385.6 mbsf (Hole 832B)

Interval: Sections 134-832A-1H-1, 0 cm, to 134-832A-26X-CC, 10 cm, and Sections 134-832B-1R-CC, 0 cm, to 134-832B-23R-CC, 22 cm

Thickness: 385.6 m (thickness in Hole 832A—206.2 m; in Hole 832B—241.2 m)

Age: Pleistocene

Unit I comprises a thick series of rapidly accumulated volcanic clays, silts, and sands, divided into two subunits on the basis of grain size: the upper beds are generally coarser than those below.

Subunit IA

Depth: 0–141.0 mbsf (Hole 832A)

Interval: Sections 134-832A-1H-1, 0 cm, to 134-832A-19H-1, 0 cm

Thickness: 141.0 m

Age: Pleistocene

The main constituents of Subunit IA are unlithified, very dark gray to black (5Y 3/1 to 2.5/1) coarse vitric volcanic ash layers within gray to dark gray (5Y 5/1 to 4/1), sandy to clayey volcanic silts (Fig. 12). These lithologies alternate usually on scales of a few centimeters to a few decimeters. Notably thicker beds are 2 m of vitric volcanic ash at 57–59 mbsf (Sections 134-832A-8H-1 and -8H-2), and almost 20 m of silty volcanic clay at 72–92 mbsf (Cores 134-832A-10H and -11H). Thick beds of coarse vitric volcanic ash may be represented by soupy recoveries of this lithology at, for example, 101–105 mbsf and 131–138 mbsf (Cores 134-832A-13H to -14H, and -18H).

Volcanic lapilli occur at 32–37, 47, 48, and 73 mbsf (Sections 134-832A-5H-4 to -5H-7; Section 134-832A-7H-1, 0–39 cm, and 120–150 cm; and Section 134-832A-10H-1, 0–24 cm). Pumice clasts occur at 103–105 and 107–109 mbsf (Sections 134-832A-13H-3 and -13H-CC, and Sections 134-832A-15H-1 and -15H-2). Wood fragments are noted at 86 mbsf (Section 134-832A-11H-3, 60–80 cm). Calcareous nannofossils, and usually foraminifers, occur in all but the coarsest beds. Section 134-832A-16H-1, 0–18 cm (116 mbsf), contains gravel-sized fragments of corals, bivalves, and pumice.

Subunit IB

Depth: 141.0–206.2 mbsf (Hole 832A) and 144.4–385.6 mbsf (Hole 832B)

Interval: Sections 134-832A-19H-1, 0 cm, to 134-832A-26X-CC, 12 cm, and Sections 134-832B-1R-CC, 0 cm, to 134-832B-26R-1, 0 cm

Thickness: 244.6 m (thickness in Hole 832A—65.2 m; in Hole 832B—241.2 m)

Age: Pleistocene

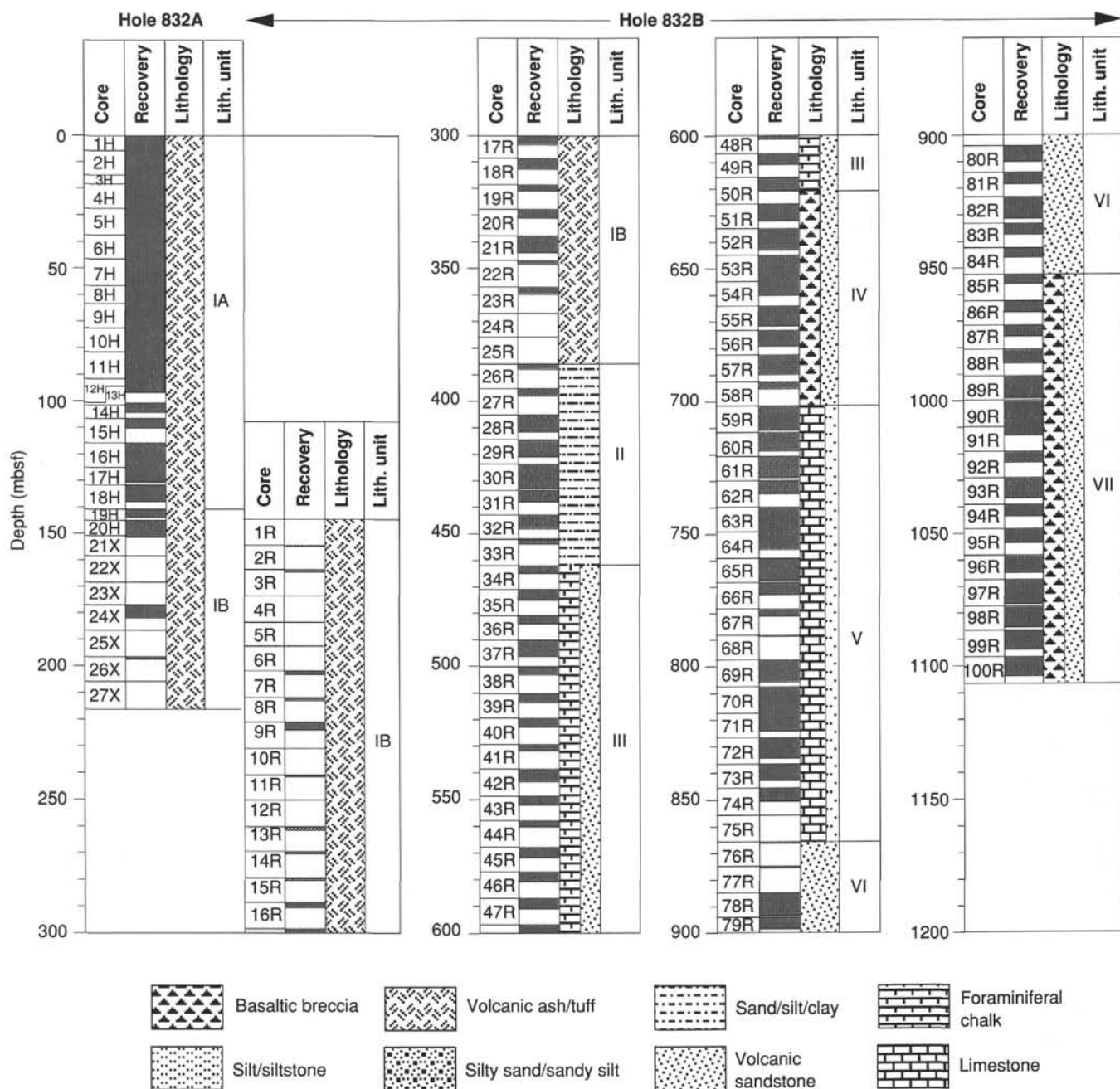


Figure 10. Lithostratigraphy at Site 832.

The main recovered constituents of Subunit IB are gray to very dark gray (5Y 5/1 to 3/1) silty volcanic clay and clayey volcanic silt with foraminifers and calcareous nannofossils. The upper part of the subunit is unlithified, but below 281 mbsf (Core 134-832B-15R) most of the recovery is of claystones, siltstones, and partially lithified, fine vitric volcanic ash. There is substantially more carbonate, in the form of calcareous volcanic siltstone and chalk, below 285 mbsf than there is above.

Scoriaceous rock fragments occur at 164 mbsf (Section 134-832B-3R-1, 15–20 cm). Two chalk beds were sampled between 310 and 321 mbsf (Section 134-832B-18R-2, 57–80 cm, and Sections 134-832B-19R-1, 110 cm, to -19R-CC); the upper limit of the latter is shown in Figure 13. Contorted beds, small-scale slumps, load features, and clastic dikes are re-

markably well developed in the finely laminated silty claystone of Core 134-832B-21R at 337–344 mbsf (Figs. 14 and 15).

It is not clear to what extent the finer texture of this subunit may represent a real *in-situ* difference from the coarser subunit above, as opposed to its being a result of poor recovery of coarse, poorly consolidated sediments by the rotary drilling method employed (see discussion under the "Remarks" subheading below).

Lithostratigraphic Unit II

Depth: 385.6–461.5 mbsf (Hole 832B)
 Interval: Sections 134-832B-26R-1, 0 cm, to 134-832B-34R-1, 0 cm
 Thickness: 75.9 m
 Age: Pleistocene

Table 2. Lithostratigraphic units, Site 832.

Interval	Unit	Subunit	Depth (mbsf)	Thickness (m)	Age
Sections 134-832A-1H-1, 0 cm, to 134-832B-26R-1, 0 cm	I		0-206.2 (Hole 832A) 144.4-385.6 (Hole 832B)	385.6	Pleistocene
Sections 134-832A-1H-1, 0 cm, to 134-832A-19H-1, 0 cm		IA	0-141.0	141.0	Pleistocene
Sections 134-832A-19H-1, 0 cm, to 134-832B-26R-1, 0 cm		IB	141.0-206.2 (Hole 832A) 144.4-385.6 (Hole 832B)	244.6	Pleistocene
Sections 134-832B-26R-1, 0 cm, to 134-832B-34R-1, 0 cm	II		385.6-461.5	75.9	Pleistocene
Sections 134-832B-34R-1, 0 cm, to 134-832B-51R-1, 0 cm	III		461.5-625.7	164.2	Pleistocene and Pliocene(?)
Sections 134-832B-51R-1, 0 cm, to 134-832B-59R-1, 0 cm	IV		625.7-702.0	76.3	Pleistocene and/or Pliocene
Sections 134-832B-59R-1, 0 cm, to 134-832B-76R-CC, 0 cm	V		702.0-865.7	163.7	mostly Pliocene and some Miocene
Sections 134-832B-76R-CC, 0 cm, to 134-832B-85R-1, 0 cm	VI		865.7-952.6	86.9	middle to late Miocene
Sections 134-832B-85R-1, 0 cm, to 134-832B-100R-CC, 15 cm	VII		952.6-1106.7	154.1	Miocene and indeterminate

Unit II consists predominantly of sandstones, siltstones, and claystones, with substantial volcanic contributions in its upper part and calcareous components in its lower part. It is thus transitional between the more pyroclastic unit above and the more calcareous one below.

The upper volcanic claystones to coarse-grained sandstones range in color from light gray to black (5Y 6/1 to 2.5/1) and show occasional laminae and burrow traces (see, for example, Fig. 16). A few wood fragments occur at about 405-412 mbsf (Core 134-832B-28R). The lower calcareous silty sandstones to silty claystones range in color from gray to very dark gray (5Y 5/1 to 3/1) and contain varying amounts of foraminifers and calcareous nannofossils. Contorted lenses and laminae occur at 406-409 mbsf (Sections 134-832B-28R-2 and -28R-3), and a large slump seems to have emplaced the bottom 20 cm of Section 134-832B-31R-2 and the top 30 cm of Section 134-832B-31R-3, at 436 mbsf.

The bottom 50 cm of Core 134-832B-26R and most of Core 134-832B-27R is a gray (5Y 5/1) sed-igneous breccia. A very dark gray (5Y 3/1) basaltic breccia constitutes the top 124 cm of Core 134-832B-28R. There is a 59-cm calcareous sed-lithic breccia in Section 134-832B-30R-2 (Fig. 17), and 130 cm of basaltic breccia with a matrix of calcareous sandy siltstone constitutes most of Core 134-832B-33R (452-453 mbsf).

Lithostratigraphic Unit III

Depth: Hole 832B, 461.5-625.7 mbsf
Interval: Sections 134-832B-34R-1, 0 cm, to 134-832B-51R-1, 0 cm
Thickness: 164.2 m
Age: Pleistocene, and possibly late Pliocene below about 600 mbsf

The distinguishing feature of Unit III is its highly calcareous character relative to adjacent units: about 40% of it comprises chalks, limestones, and calcareous mixed sedimentary rocks. The remainder comprises volcanic sandstones, siltstones, and breccias, the finer-grained varieties slightly predominating. Beds of the different lithologies are commonly decimeters to a few meters in thickness, the thinner ones occurring notably at about 500, 551, and 597 mbsf (Sections 134-832B-38R-1, -43R-2, -43R-3, and -48R-1). One of the

limestone/breccia contacts is shown in Figure 18. The chalks and limestones are gray to greenish gray (5Y 5/1 to 5GY 5/1), foraminiferal and calcareous (in the sense of containing a high proportion of calcareous grains of indeterminate origin), often with substantial amounts of calcareous nannofossils and volcanic grains.

Interbedded volcanic sandstones and mixed sedimentary rocks are commonly gray (5Y 5/1) and contain some foraminifers and calcareous nannofossils, pebbles of pumice and basalt, and altered volcanic glass. These sandstones and mixed sedimentary rocks, as well as the chalks and limestones, exhibit faults, steeply dipping beds, and slump structures. The breccias are gray to greenish gray (5Y 5/1 to 5G0Y 5/1), with angular to subrounded clasts of basalt, volcanic sandstone, and occasionally limestone, and a matrix of volcanic sand or silt with calcareous grains.

Lithostratigraphic Unit IV

Depth: Hole 832B, 625.7-702.0 mbsf
Interval: Sections 134-832B-51R-1, 0 cm, to 134-832B-59R-1, 0 cm
Thickness: 76.3 m
Age: Pleistocene and/or Pliocene

The upper limit of this unit is arbitrarily placed between two successive cores, as its transition to the one above is gradual. Approximately 60% of Unit IV consists of basaltic breccia and approximately 40% is volcanic sandstone and siltstone. Most of the breccias and finer-grained beds in the upper part of the unit are 50 cm to 2 m thick, but below 659 mbsf (Section 134-832B-54R-3) the beds of breccia are thicker. The breccia is lithified, usually black (5Y 2.5/1), occasionally very dark gray (5Y 3/1) or greenish gray (10Y 4/1), and usually matrix-supported. Most clasts are vesicular basalt fragments, usually 2-10 cm in size but occasionally much larger; two pieces of basalt extend over 67 cm and 45 cm in Section 134-832B-57R-2 (684-686 mbsf). In addition, there are clasts of limestone, corals, and bioclastic limestone with moldic porosity resulting from the removal of bivalves. The matrix is a sandstone similar in composition to the volcanic

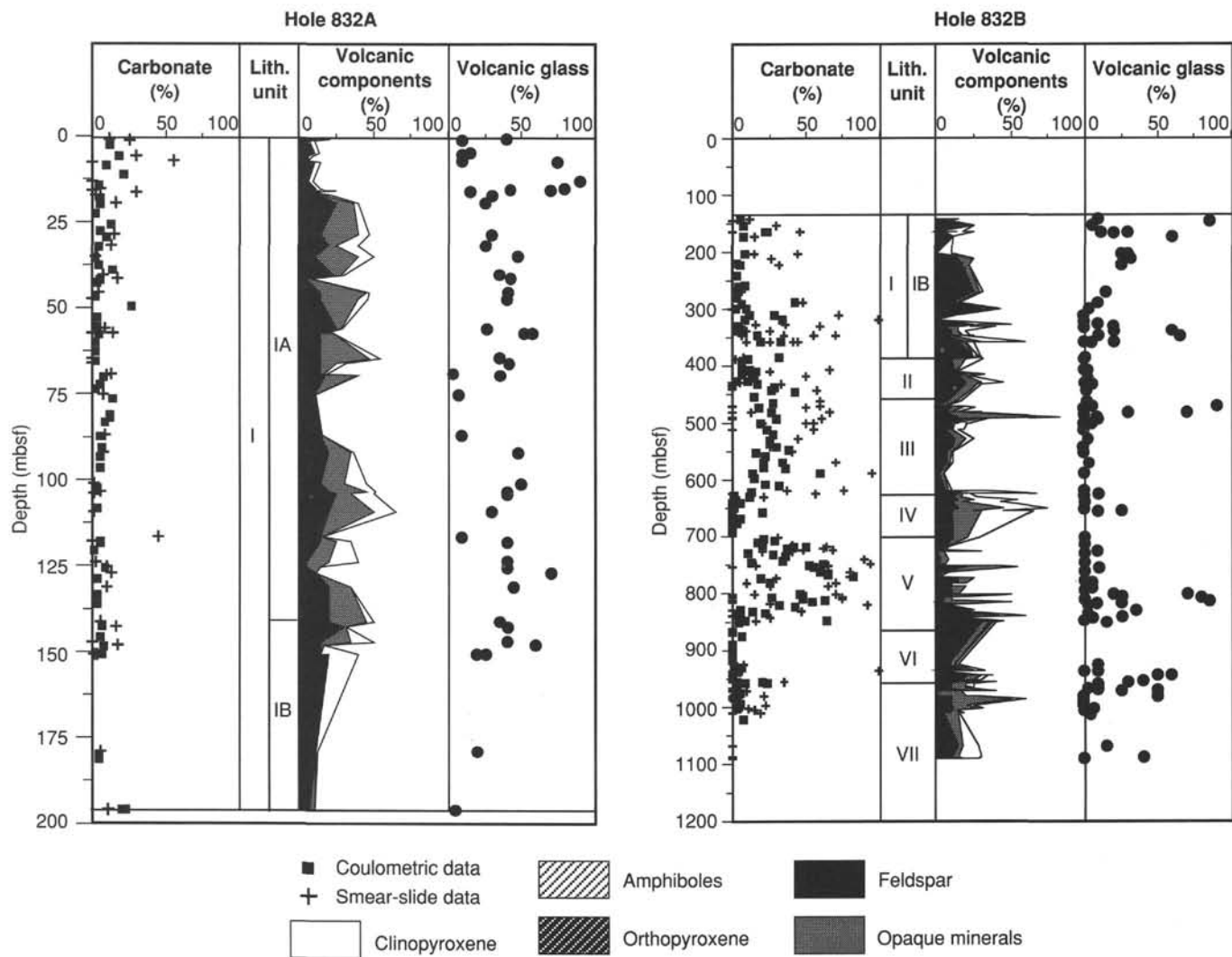


Figure 11. Variation in carbonate content and volcanogenic minerals with depth in Holes 832A and 832B. Carbonate content was determined by both coulometric and smear-slide analyses; percentage of volcanic components was estimated from smear slides.

sandstone that constitutes the subdominant lithology of this unit.

The volcanic sandstone is lithified, black to greenish gray (5Y 2.5/1 to 5G 4/1), and usually coarse-grained. Prominent constituents are basaltic grains, palagonite, pyroxene, foraminifers, and calcareous grains. Interbedded with the sandstone at about 650 mbsf (Core 134-832B-53R) is a lithified, very dark gray (5Y 3/1) volcanic siltstone. This siltstone and some of the sandstones exhibit faulting, convoluted slumped beds, fractures, and wavy laminae (Fig. 19).

Lithostratigraphic Unit V

Depth: 702.0–865.7 mbsf (Hole 832B)

Interval: Sections 134-832B-59R-1, 0 cm, to 134-832B-76R-CC, 0 cm

Thickness: 163.7 m

Age: Pliocene to late Miocene

Sharply demarcated from the coarser Unit IV above, Unit V consists predominantly of light gray to dark greenish gray (5Y 6/1 to 5GY 4/1) limestone (variously described as foraminiferal, nannofossil, calcareous, or silty according to its high percentage of foraminifers, calcareous nannofossils, calcareous grains of uncertain origin, or silt-sized nonbiogenic grains, respectively), and siltstone. [Coulometric de-

terminations of carbonate in samples from this unit are often lower than the estimates from smear slides, indicating that some of these "limestones" might more correctly though clumsily be recorded as "mixed sedimentary rocks." It is also possible that the criteria applied in choosing samples for analysis of physical properties, and subsequent coulometry, are different from those applied in selecting levels for preparation of smear slides.] Gray to greenish gray (5Y 5/1 to 5GY 6/1), calcareous clayey siltstone and mixed sedimentary rock occur in Cores 134-832B-59R, -60R, and -72R (702–720 and 827–835 mbsf), the latter containing shell fragments. Gray to dark greenish gray (5Y 5/1 to 5GY 4/1) calcareous volcanic siltstones to silty volcanic sandstones occur at about 725 and 769–788 mbsf (Cores 134-832B-61R and -66R to -68R). Very dark gray to dark greenish gray (5Y 3/1 to 5GY 4/1) vitric ash layers, 1–15 cm thick, are present at about 725, 750–768, and 798–835 mbsf (Cores 134-832B-61R, -64R, -65R, and -69R to -72R). Slickensides are common at 740–757 mbsf (Cores 134-832B-63R and -64R). Pieces of wood up to 1 × 10 mm occur in intervals 134-832B-67R-1, 83–84 cm, 134-832B-67R-CC, 35–36 cm, and 134-832B-68R-CC, 22–23 cm (779, 782, and 788 mbsf). At 820 mbsf (Section 134-832B-71R-2, 60–70 cm), a white to light gray (10YR 8/1 to 5Y 6/1) waxy vein of gypsum (by

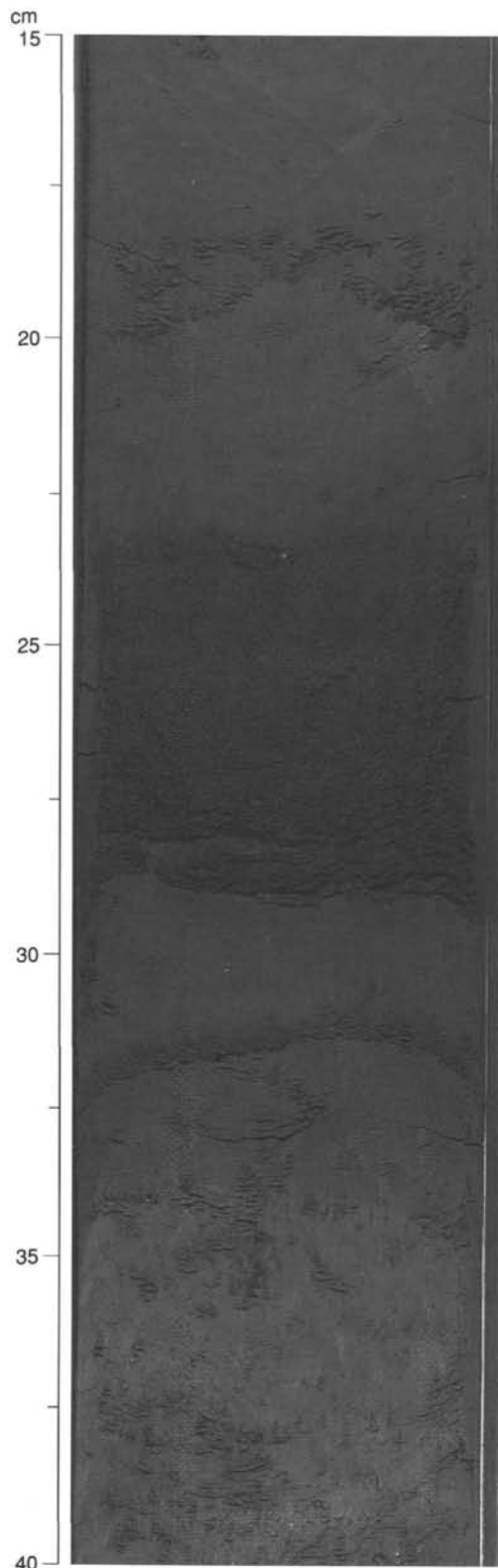


Figure 12. Layers of vitric ash within clayey volcanic silt in interval 134-832A-9H-3, 15–40 cm. There is no burrow-mottling such as is often evident in the upper parts of ash layers and turbidites.

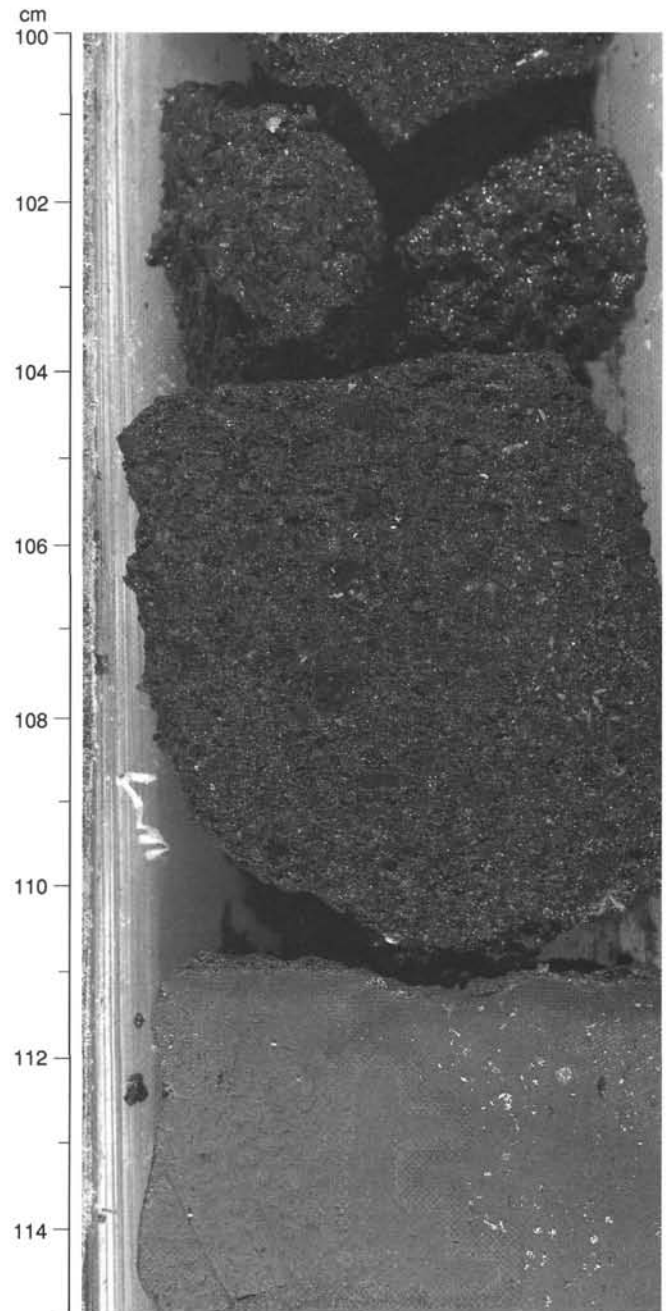


Figure 13. Contact between the chalk bed that extends from Section 134-832B-19R-1, 110 cm, to Section 134-832B-19R-CC, and overlying volcanic sandstone found in lithostratigraphic Subunit IB.

X-ray diffraction) several centimeters thick fills a fracture that cuts the core at an angle of 55° to the vertical. Throughout the unit, bioturbation is commonly intense, but it is only slight at 808–818 mbsf in Core 134-832B-70R.

Near the base of this unit, at 837–838 mbsf (interval 134-832B-73R-1, 0 cm, to -73R-2, 23 cm), is a partially lithified, black (5Y 2.5/1) basaltic breccia containing a few neritic carbonate clasts. At the base of the unit, in interval 134-832B-74R-3, 73 cm, to -74R-CC is a very dark gray (5Y 3/1) clayey volcanic siltstone with a convoluted interval in Section 134-832B-74R-3 73–100 cm, underlain by inclined beds at 100–125 cm with a slump at their base.

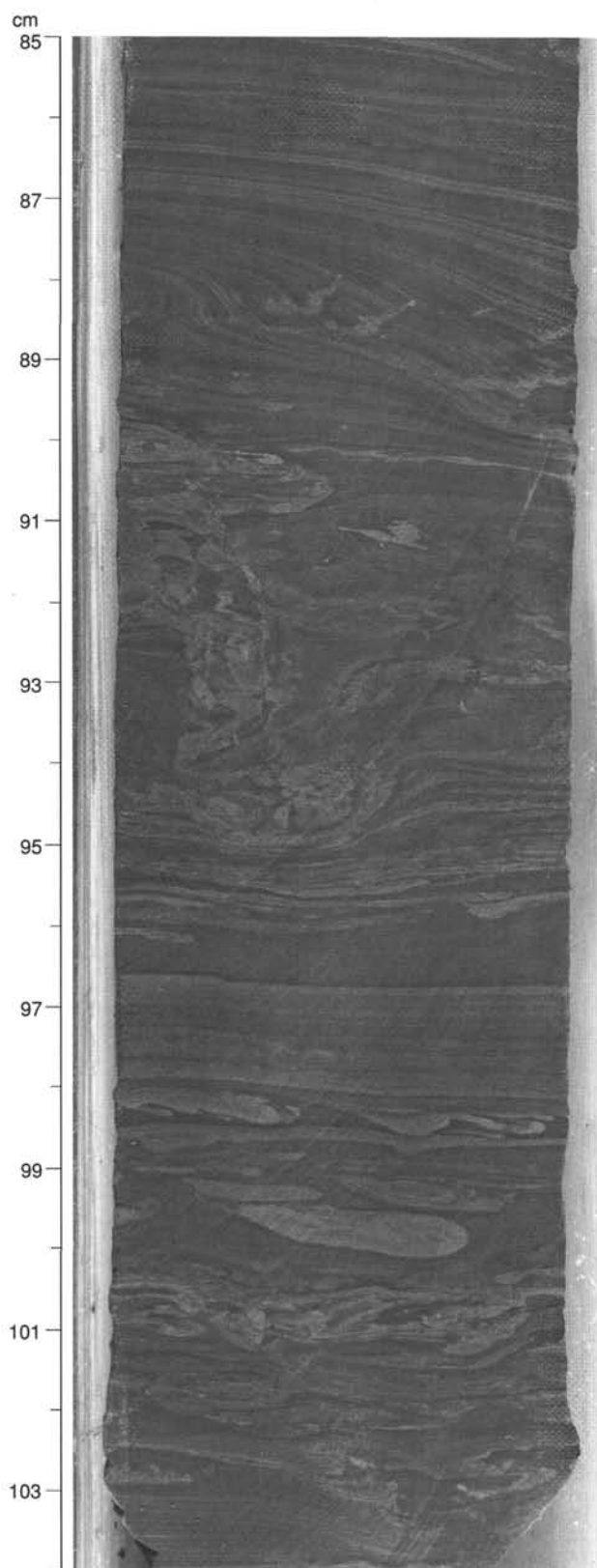


Figure 14. Wet-sediment deformation in the finely laminated silty claystone of interval 134-832B-21R-3, 85–104 cm, in lithostratigraphic Subunit IB.

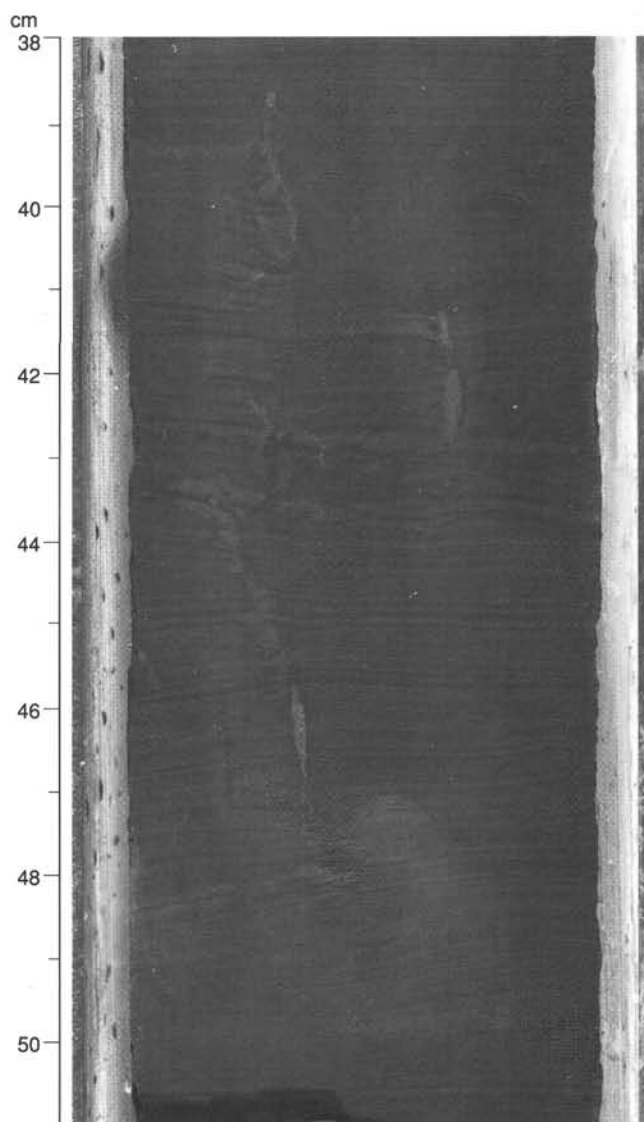


Figure 15. Clastic dike in the laminated silty claystone of interval 134-832B-21R-4, 38–51 cm, in lithostratigraphic Subunit IB.

Lithostratigraphic Unit VI

Depth: 865.7–952.6 mbsf (Hole 832B)

Interval: Sections 134-832B-76R-CC, 0 cm, to 134-832B-85R-1, 0 cm

Thickness: 86.9 m

Age: middle to late Miocene

Unit VI consists of lithified, dark greenish gray to black (5Y 4/1 to 5Y 2.5/1) volcanic sandstone. Cores 134-832B-76R and -77R (865–885 mbsf) recovered only a few cobbles of this material as core-catcher samples. The unit shows a general coarsening from the top downward, but within it are graded beds that fine upward and occasionally downward. Granule- to pebble-sized clasts of pumice, basalt, and mud occur sporadically throughout, and two 8-cm basalt cobbles occur in Section 134-832B-78R-1, 0–15 cm, at 885 mbsf (perhaps washed from the poorly recovered interval above). Grains of neritic carbonate occur at about 930–938 mbsf (lower part of Cores 134-832B-82R through -83R). Small fractures and faults are observed at 892, 894, and 916 mbsf (Sections 134-832B-78R-5, 70–80 cm; 134-832B-78R-7, 10–19 cm, and 40–46 cm; and 134-832B-81R-2, 36–49 cm). Fractures are filled with calcite at about 930 and

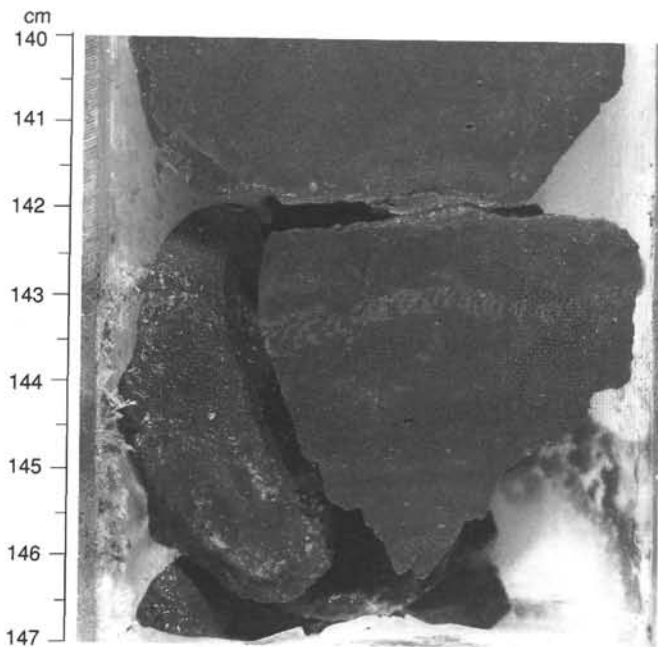


Figure 16. Burrow trace within clayey siltstone of lithostratigraphic Unit II at interval 134-832B-28R-4, 140–147 cm. The third-dimensional extension of the trace is visible at the subvertical fracture at 143 cm.

933–938 mbsf (Sections 134-832B-82R-5 and -83R-1 through -83R-4). Pyrite occurs in the intervals 134-832B-84R-1, 56–66 cm, and 113–116 cm, at 943–944 mbsf.

Lithostratigraphic Unit VII

Depth: 952.6–1106.7 mbsf (Hole 832B)
 Interval: Sections 134-832B-85R-1, 0 cm, to 134-832B-100R-CC, 15 cm
 Thickness: 154.1 m
 Age: early to middle Miocene down to about 970 mbsf; indeterminate below

Unit VII consists of about 60% lithified basaltic breccia and conglomerate, and about 40% lithified volcanic sandstone and siltstone. Most of the coarser and finer beds range in thickness from a few decimeters to a few meters; it is not always clear whether a particular sandstone or siltstone interval represents a large clast within the breccia, or an interbed.

Clasts in the breccias and conglomerates are commonly 5 mm to 2 cm in size, but occasionally larger than 10 cm (Fig. 20). They are principally of basalt and pumice, accompanied down to 1010 mbsf (Section 134-832B-91R-CC) by neritic calcareous grains including coral and algal fragments and large foraminifers. At 972–977 mbsf (Core 134-832B-87R) is an igneous conglomerate in which most of the clasts are fragments of light grayish brown to grayish brown (10YR 4/2 to 5/2) pumice, and vesicular basalt with clinopyroxene phenocrysts and pumiceous rims (possibly volcanic bombs). Many of the vesicles and veins in the basalts are filled with zeolites. The lithified, dark gray to black (5Y 4/1 to 2.5/1) matrices of the breccias vary from clayey volcanic sand to vitric volcanic silty sand.

The volcanic sandstones and siltstones in this unit are dark gray to dark greenish gray (5Y 4/1 to 5GY 4/1), with vitric ash which is generally undergoing devitrification toward the bottom of the section. Slumps, microfaults, graded and cross-laminated beds, and steeply inclined bedding planes are common. Beds at 975–976 mbsf (Sections 134-832B-85R-3 and -85R-4) show evidence of folding and overturning.

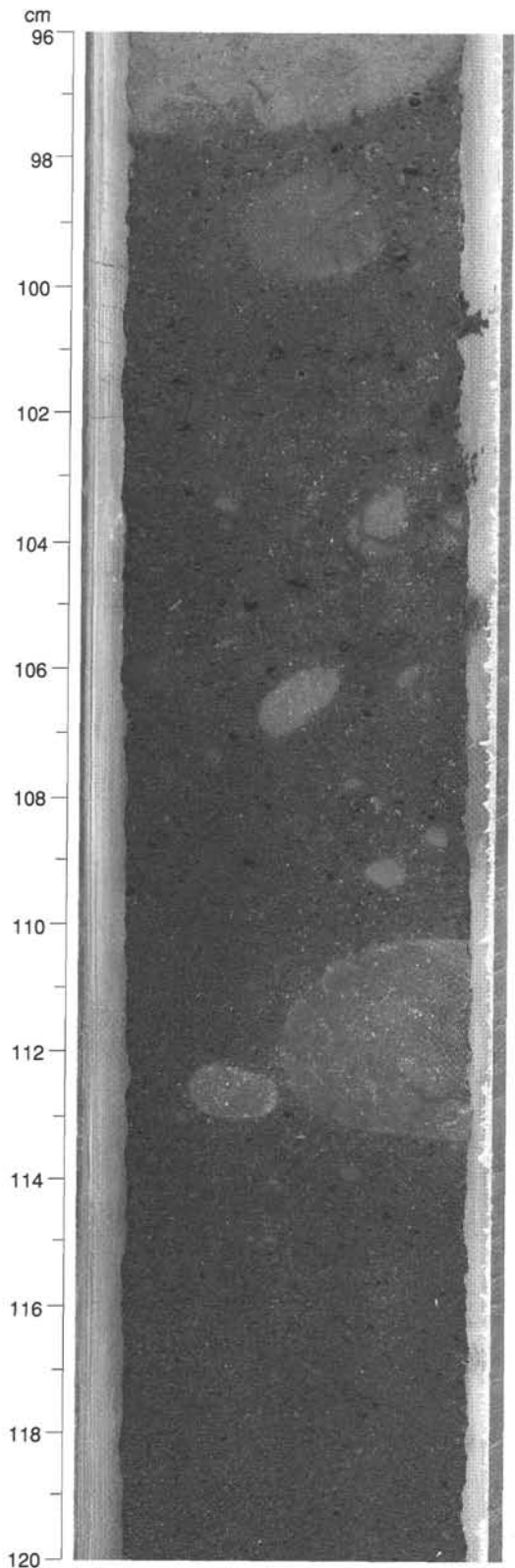


Figure 17. Cobbles of silty chalk within the volcanic sandstone of lithostratigraphic Unit II at interval 134-832B-30R-2, 96–120 cm.

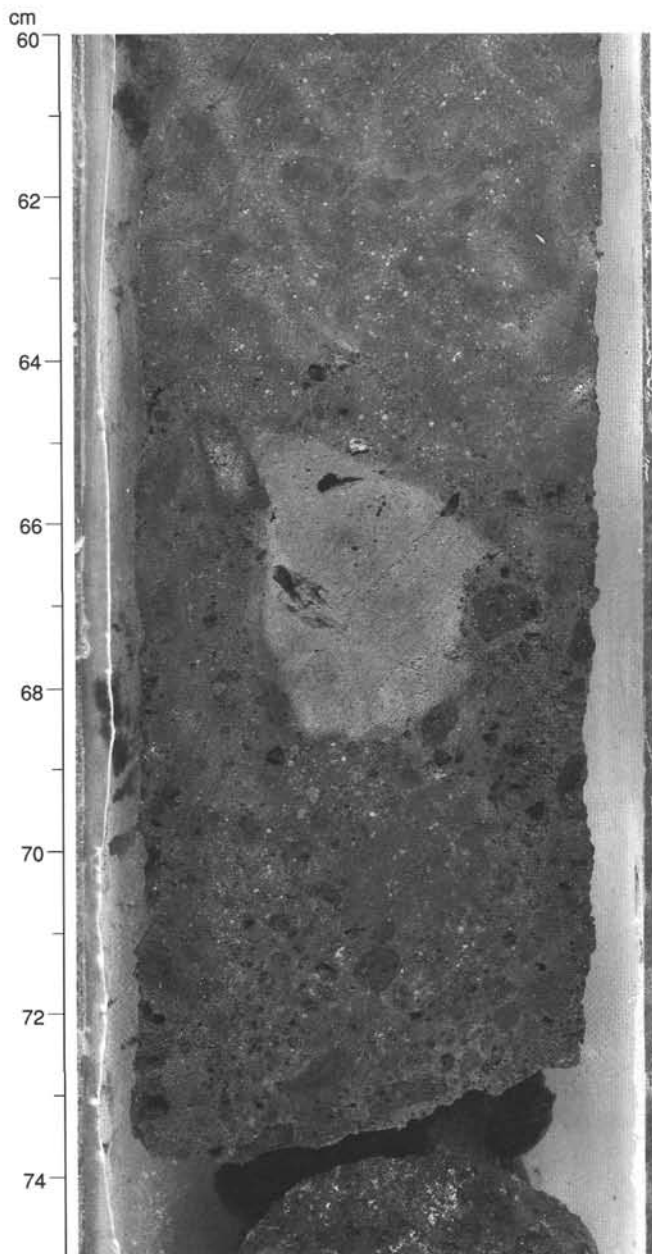


Figure 18. Contact between basaltic breccia and limestone with foraminifers in lithostratigraphic Unit III at 65 cm in interval 134-832B-47R-1, 60–75 cm.

Remarks

Influence of Coring Technique on Lithologies Recovered

Hole 832A was drilled using the hydraulic piston corer (HPC) and the XCB until the sediments became so lithified that recovery dropped to an unacceptable level, at about 200 mbsf. The RCB was then used to drill Hole 832B, from about 150 to 1100 mbsf. The uppermost sedimentary unit at this site, lithostratigraphic Unit I, a 360-m-thick sequence of vitric volcanic ash layers within sandy to clayey volcanic silts, is divided into two subunits at about the level at which poor core recovery with the XCB motivated the change to RCB coring. Subunit (IA) is distinguished from Subunit IB on the basis of the former being characterized by coarser vitric ash than the latter. This distinction is apparently partly real, since unlithi-

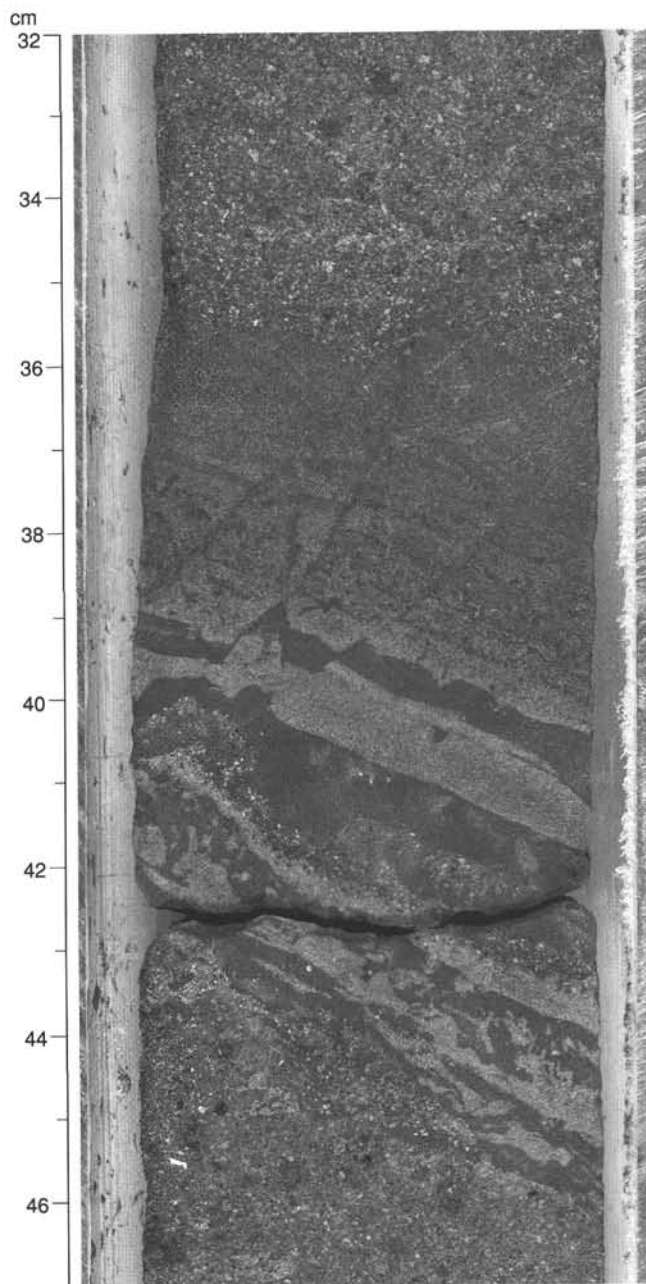


Figure 19. Microfaulted and contorted siltstone within coarse-grained volcanic sandstone of lithostratigraphic Unit IV in interval 134-832B-53R-4, 32–47 cm.

fied sediments in Cores 134-832A-21X and -24X, in the 50 m of overlap of Holes 832A and 832B, are volcanic silt and fine vitric volcanic ash, but it is probably artificially exaggerated as a result of the fact that rotary coring does not recover unconsolidated sands as well as does the hydraulic piston corer.

Though evidence for such selective recovery was not noted in the cores representing Subunit IB, there is clear evidence for this process occurring on a small scale in Unit V, at about 750–770 mbsf (Cores 134-832B-64R and -65R). In this interval, at some breaks in the limestone core, the surface below the break has a thin veneer of very coarse volcanic sand, and immediately above the break is much finer sediment, darker than the limestone and burrow-mottled in the manner characteristic of the upper parts of graded sand layers. Obviously,

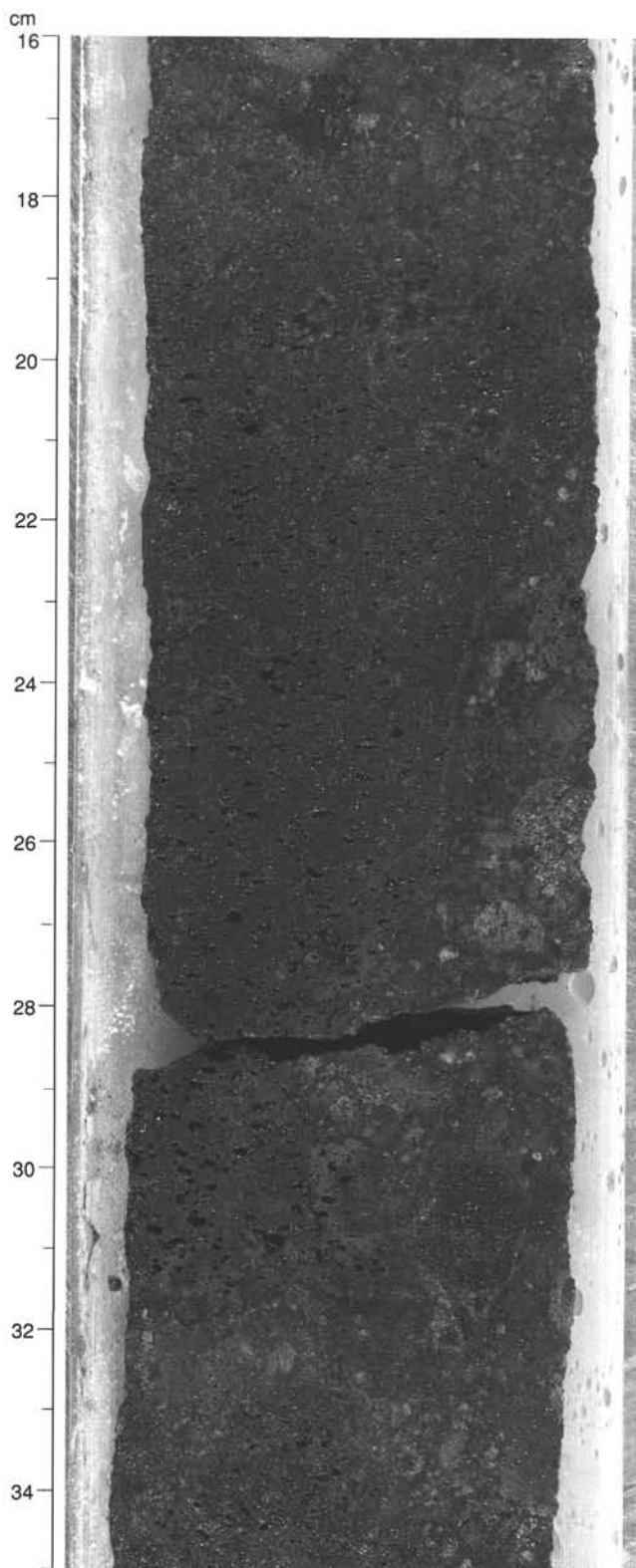


Figure 20. A large and a smaller clast (at 19.5–32 cm and 32.5–35 cm) of vesicular basalt within the breccia of lithostratigraphic Unit VII in interval 134-832B-100R-3, 16–35 cm.

the greater part of the less coherent volcanic sand of intermediate grain sizes has been lost. Instances were noted in Sections 134-832B-64R-1, 5–8 cm; -65R-2, 25–39 cm; and -65R-4, 115–118 cm.

Nonvolcanogenic Components of the Sediments

At many localities on the seafloor, where layers of volcanic ash or turbidites constitute a substantial part of the sediment sequences, it is nevertheless possible to identify some nonvolcanogenic, nonturbiditic intervals that can be considered as the normal, background sediments at those places. Candidates for such “normal” intervals were not found in the Quaternary part of the sequence at Site 832, and possible reasons for this were sought in a comparison with Deep Sea Drilling Project (DSDP) sequences from this general region. There are few nearby DSDP sites, and only two of them are not strongly influenced by the influx of Quaternary volcanic ash or turbidites. At Site 209 (15°56'S, 152°11'E, in a water depth of 1428 m; Burns, Andrews, et al., 1973) the Quaternary foraminiferal-nannofossil oozes are 24 m thick, and at Site 587 (21°11'S, 161°20'E, in a water depth of 1101 m; Kennett, von der Borch, et al., 1986) similar oozes are about 31 m thick. The component of that “normal” lithology would constitute only 3%–5% of the 600–700 m of Quaternary deposits at Site 832. That small proportion (and more) is accounted for by the calcareous microfossils in the volcanic silts and clays.

The only DSDP sequence in this region with a complete, nonvolcanogenic, nonturbiditic Pliocene sequence is at Site 587, where foraminiferal-nannofossil oozes of that epoch are 56 m thick. This is to be compared with the 100–200 m of Pliocene at Site 832, represented largely by the limestones and siltstones of Unit V.

The middle to late Miocene sequence of nannofossil-bearing ashes and tuffs at DSDP Site 205 (25°31'S, 177°54'E, in a water depth of 4320 m; Burns, Andrews, et al., 1973) is 252 m thick, and thus accumulated more rapidly than the approximately 150 m of sediments of this age at Site 832.

Connotations of the Term “Reworked”

The collaboration of a number of geologists with diverse backgrounds in describing the sediments from Site 832 revealed two distinct senses in which the term “reworked” is used. Igneous petrologists characterize volcanic ash as being “reworked” when there is evidence of its having been moved from its original site of deposition to its present location, without regard to the mechanism or context of the transport, or relative age (though there will always be some difference in age, however slight, between the original emplacement of autochthonous and transported grains). An association of fresh shards with partially devitrified ones is taken as evidence of probable reworking of the latter, as, for example, in the description of Core 134-832A-13H. Discrete ash layers occurring within sediments also containing dispersed ash is interpreted as indicating that the dispersed shards are reworked (in Core 134-832A-8H).

In the paleontological literature, the term “reworked” is applied practically exclusively to fossils that are considerably older than the associated sediment or *in-situ* assemblage (i.e., the stratigraphic ranges of the reworked species do not overlap the age that can be assigned to the containing sediment on the basis of other evidence). The difference in age between the reworked elements and the autochthonous assemblage has to be substantial in order for the reworking to be recognized unambiguously. In the case of the mixing of fossils from different water-depth habitats, but of approximately the same age (a situation analogous to some of the petrologists' usages), the terms “downslope transport” or “displacement”

are usually used (see discussion by Boltovskoy and Wright, 1976, pp. 376–377, for example). Thus, igneous petrologists use the term “reworked” in a wider sense than do paleontologists, and an understanding of the different usages can facilitate effective communication.

BIOSTRATIGRAPHY

Calcareous Nannofossils

The calcareous nannofossil biostratigraphy in Holes 832A and 832B is typified by moderately to well-preserved assemblages, indicating a discontinuous geologic sequence ranging in age from late Pleistocene or Holocene to possibly latest early Miocene (Fig. 21). Biostratigraphic interpretation is hindered by dilution from volcanoclastic sediments that results in nannofossil abundances fluctuating between common and rare. Further complications result from the presence of barren samples in Sections 134-832B-53R-CC (702.0 mbsf) through -59R-CC (711.6 mbsf), and Sections 134-832B-74R-CC (856.1 mbsf) through -83R-CC (942.9 mbsf). The absence of nannofossils across these intervals prevents the precise determination of the Pleistocene-Pliocene boundary and of the ages of most of the upper and middle Miocene sequences. The occurrence of mass wasting and associated downslope processes are manifested in an erratic record, containing reworked assemblages that hinder the biostratigraphic utility of several last occurrence datums, particularly in the upper parts of Holes 832A and 832B.

Pleistocene

Samples 134-832A-1H-CC through -6H-CC (47.0 mbsf) contain an assemblage typified by the presence of *Gephyrocapsa oceanica*, *Gephyrocapsa caribbeanica*, *Helicosphaera kamptneri*, *Calcidiscus leptoporus*, and the late Pleistocene zonal marker *Emiliana huxleyi* (Zone CN14). Neogene specimens of *Discoaster brouweri*, *Calcidiscus macintyreii*, and *Discoaster variabilis* are often present as reworked components.

In Samples 134-832A-7H-CC (56.5 mbsf) through -27X-CC (215.9 mbsf), the nannofossil assemblage is dominated by *G. oceanica*, *G. caribbeanica*, *Rhabdosphaera claviger*, *H. kamptneri*, and *C. leptoporus*. Neogene and possibly Paleogene nannofossils occur as sporadic reworked specimens, as evidenced by the presence of *D. brouweri*, *D. variabilis*, *Sphenolithus abies*, *Discoaster pentaradiatus*, and *Cyclicargolithus floridanus*.

From Samples 134-832B-26R-CC (395.3 mbsf) through -53R-CC (654.7 mbsf) the nannofossil data are inconsistent because of fluctuating abundances of the marker species *G. oceanica* and *G. caribbeanica*. The difficulty in determining the first occurrence of *G. oceanica* centers upon the general decrease in the placolith size ($<4 \mu\text{m}$) concomitant with a decrease in the birefringence of the cross-bar in *gephyrocapsids* below Sample 134-832B-26R-CC. Common specimens of *G. oceanica* are recognized above this sample, whereas below it distinctive specimens of *G. oceanica* occur only sporadically. Because the significance placed upon the abundance of this species directly affects the placement of the CN14/CN13 zonal boundary in this hole, no precise interpretation is made at this time. These samples are referred to herein as Zone CN14/CN13 until a less subjective evaluation can be made as a result of more extensive, shore-based studies.

Pliocene

The presence of *D. brouweri* and the absence of *gephyrocapsids* in Samples 134-832B-59R-CC (711.6 mbsf) to -62R-CC (739.8 mbsf) indicate deposition during the latest

Pliocene. The accompanying assemblage comprises *C. macintyreii*, *H. kamptneri*, *Calcidiscus leptoporus*, and small reticulofenestrids ($<5 \mu\text{m}$). There is no evidence for reworking in these samples. The presence of *Sphenolithus abies* in Samples 134-832B-63R-CC (749.5 mbsf) to -65R-CC (768.8 mbsf) indicates that these sediments are no younger than late early Pliocene (Zone CN11). Also found in these samples were *Sphenolithus neoabies*, *D. brouweri*, *D. variabilis*, *H. kamptneri*, *C. leptoporus*, and small reticulofenestrids ($<5 \mu\text{m}$). These samples display no evidence of reworking.

Miocene

Samples with nannofossil assemblages indicative of the late Miocene were found in Samples 134-832B-66R-CC (778.6 mbsf) through -74R-CC (856.1 mbsf). The presence of *Discoaster quinquerramus* in association with *D. brouweri*, *H. kamptneri*, *D. variabilis*, *C. macintyreii*, *Dictyococcites* sp. ($<5 \mu\text{m}$), and *Reticulofenestra* sp. ($<5 \mu\text{m}$) suggests that these samples are from Zone CN9. There is no evidence for reworking in these samples and the preservational state is moderate. Abundances vary from common to rare.

Early Miocene(?)

It is difficult to determine the ages of Samples 134-832B-84R-CC (952.6 mbsf) through -92R-CC (1029.3 mbsf) because of the paucity of nannofossils. Most samples from this interval contain varying proportions of *Sphenolithus heteromorphus* and *C. floridanus*, indicating deposition during the early Miocene (Zone CN4). Some samples contain what appear to be discoasters that would suggest a younger origin. Samples 134-832B-85R-2, 62–63 cm, and 134-832B-90R-CC contain discoasters that resemble *D. brouweri* and *D. quinquerramus*. The occurrence of *D. brouweri* would indicate that these samples are no older than middle Miocene, whereas the presence of *D. quinquerramus* would further constrain the age to within the uppermost Miocene Zone CN9. The presence of two distinct nannofossil assemblages suggests that most of the specimens interpreted as lower Miocene are displaced. Despite conflicting data, these samples have tentatively been assigned to the early Miocene Zone CN4; however, further shore-based analysis of additional data should clarify the significance of the enigmatic discoasters.

Planktonic Foraminifers

Abundance and preservation of planktonic foraminifers in Holes 832A and 832B vary greatly because of dilution by volcanoclastic sediments and progressive lithification downhole. Good preservation and abundant assemblages were found in Cores 134-832A-1H to -74R (0–856.1 mbsf), whereas below 856 mbsf preservation varies from moderate to poor, specimens are few, and samples are commonly barren. Although sedimentological information (turbidites, slumps, etc.; see “Lithostratigraphy” section, this chapter) suggests intensive reworking, this is only readily apparent within some core sections and in a few core-catcher samples that contain shallow-water larger benthic foraminifers (see core description forms near the back of this volume). The planktonic foraminiferal assemblage shows fairly little evidence of reworking, usually in sediments from the preceding biostratigraphic age.

A continuous foraminiferal biostratigraphy from the Holocene to latest late Miocene is recognized between the interval from the seafloor to 856.1 mbsf, followed by an interval with no data (between 865.7 and 923.7 mbsf). Continuing down in Hole 832B, the first indication of earliest middle Miocene is recorded from 933.3 to 962.2 mbsf and is followed subsequently by an uppermost lower Miocene assemblage noted from Samples 134-832B-88R-CC and 134-832B-90R-CC (between 990.8 and

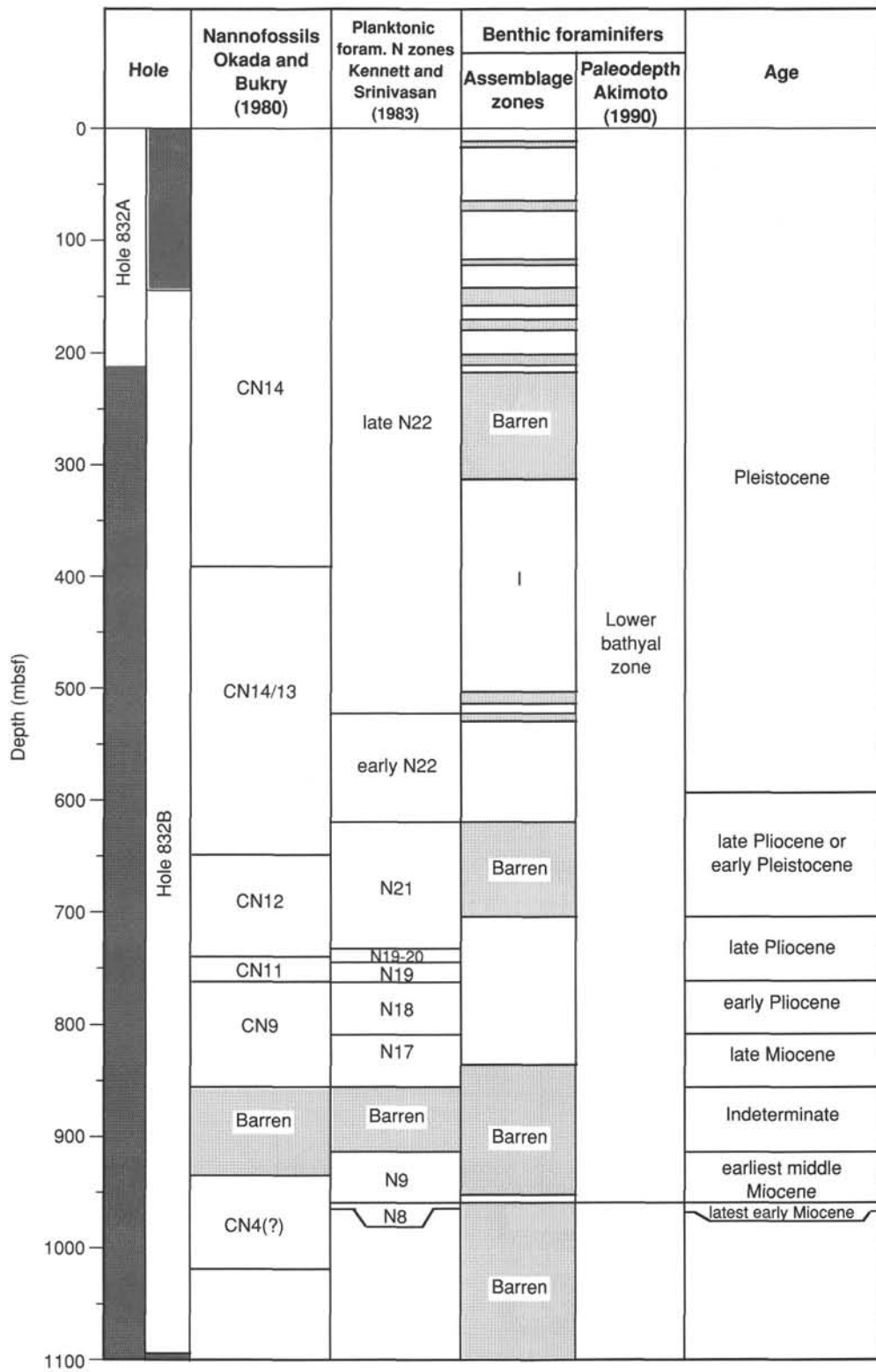


Figure 21. Biostratigraphic summary of Site 832.

1010.1 mbsf). The age of sediments between the interval from 1029.3 to 1106.7 mbsf in Hole 832B cannot be determined because of the lack of age-diagnostic species and the general absence of planktonic foraminifers.

Within Zone N22 we distinguished informally the late Pleistocene to Holocene and the early Pleistocene. The former assemblage zone is characterized by the occurrence of *Globorotalia truncatulinoides* and the latter by the co-occurrence of *G. truncatulinoides* and *Globorotalia tosaensis*. Planktonic foraminiferal Zone N18 is adopted here as early Pliocene following the work of Berggren et al. (1985a, 1985b). Major discrepancies within the Neogene planktonic foraminiferal datum levels have been discussed by Haig and Perembo (1990), who have placed Zone N18 of Kennett and Srinivasan (1983) in the early Pliocene. We use here the term Zone N17 (late Miocene) because of the sampling spacing and absence of index species to distinguish Zone N17B from N17A.

Late Pleistocene to Holocene

The late Pleistocene to Holocene (Zone N22) is represented by the interval from the seafloor to 308.4 mbsf (Samples 134-832A-1H-CC to -27X-CC; 134-832B-1R-CC to -17R-CC) at Site 832. Foraminiferal assemblages in this interval are composed predominantly of *Globorotalia truncatulinoides*, *Globorotalia menardii*, *Globorotalia tumida*, *Globorotalia unguolata*, *Globorotalia crassaformis*, *Pulleniatina obliquiloculata*, *Neogloboquadrina dutertrei*, *Candeina nitida*, *Globigerinoides conglobatus*, and *Sphaeroidinella dehiscens*, among others.

Early Pleistocene

Samples between 318.1 and 529.2 mbsf (Samples 134-832B-18R-CC to -40R-CC) from Hole 832B are assigned to the early Pleistocene (Zone N22), based on the co-occurrence of *Globorotalia truncatulinoides* and *Globorotalia tosaensis*. Planktonic assemblages in this interval are very similar to those described for the late Pleistocene to Holocene. Uncertainty in the first occurrence of *G. truncatulinoides* is recorded between 529.2 and 625.7 mbsf (Samples 134-832B-40R-CC to -50R-CC), as this species is distinguished from its ancestral *G. tosaensis* by the presence of a well-defined keel in the last chamber (cf. Kennett and Srinivasan, 1983). This morphological trait is poorly defined in this stratigraphic interval.

Late Pliocene

The samples between 625.7 and 739.8 mbsf (Samples 134-832B-50R-CC to -62R-CC) in Hole 832B are assigned to the late Pliocene (Zone N21), based on the presence of *G. tosaensis* and the absence of *G. truncatulinoides*. Some species that predominate in this interval include *S. dehiscens*, *Globorotalia* cf. *multicamerata*, *G. menardii*, *G. tumida*, *G. tumida* cf. *flexuosa*, *G. crassaformis*, *Globigerinoides fistulosus*, *Pulleniatina praecursor*, and *P. obliquiloculata*.

Early Pliocene

Sample 134-832B-63R-CC at 749.5 mbsf represents the early Pliocene (Zones N19–N20), based on the presence of *G. crassaformis*, in addition to *Dentoglobigerina altispira*, *Sphaeroidinellopsis kochi*, *Globorotalia tumida flexuosa*, and *Pulleniatina praecursor*, among others. The interval from 759.2 to 768.8 mbsf (Samples 134-832B-64R-CC to -65R-CC) is assigned to Zone N19, also of early Pliocene age, based on the presence of *G. tumida* and the absence of *G. crassaformis*. Common species in this interval include *D. altispira*, *G. tumida tumida*, *S. seminulina seminulina*, and *S. paenedehiscens*. In addition, the interval from 778.6 to 817.4 mbsf (Samples 134-832B-66R-CC to -70R-CC) is assigned to the earliest Pliocene (Zone N18). Foraminiferal species present throughout this interval include *Pulleniatina primalis*, *D. altispira*, *S. kochi*, *S. paenedehiscens*, *S.*

seminulina seminulina, *G. tumida*, *P. praecursor*, *Globigerinoides conglobatus*, and *Globorotalia janaei* to *G. margaritae primitiva*.

Late Miocene(?)

The interval from 817.4 to 856.1 mbsf (Samples 134-832B-71R-CC to -74R-CC) is assigned to the late Miocene(?) (Zone N17), based on the occurrence of *Globorotalia plesiotumida*, *S. paenedehiscens*, *Globoquadrina baraemoensis*, and the absence of typical Pliocene fauna occurring in the overlying interval.

Middle and Early Miocene

The basal part of middle Miocene (Zone N9) was recorded in Sample 134-832B-85R-2, 29–32 cm (954 mbsf), based on the presence of *Orbulina universa* and *Orbulina suturalis* associated with *Sphaeroidinellopsis disjuncta* and *D. altispira*. The latest early Miocene (Zone N8) was noted in Sample 134-832B-86R-CC at 971.8 mbsf based on the co-occurrence of *Globigerinoides sicanus* and *G. triloba*; also present are *Globigerinoides altiapertura* and *Globigerinoides immaturus*.

A reworked larger benthic foraminifer *Lepidocyclina (Nephrolepidina) sumatrensis* occurs in Sample 134-832B-89R-1, 25–28 cm, and indicates the early Miocene (T-letter stage Te5; planktonic Zones N4 to N5). This species was previously recorded (cf. Carney, 1986) in the lower Miocene (Upper e = Te5) Sarava Formation on Maewo Island.

Radiolarians

Rare, well- to moderately preserved radiolarians occur in the first 11 cores of Hole 832A. Well-preserved fragments occur also in the highly indurated silt of Sample 134-832B-86R-CC. Careful preparation of samples from around this level may yield a fauna sufficient to make a contribution to the determination of the age of these silts.

Benthic Foraminifers

Rare to few benthic foraminifers occur in core-catcher samples examined from Site 832. Preservation is generally moderate to good in the samples from the seafloor to 778.6 mbsf (Samples 134-832A-1H-CC to 134-832B-66R-CC), but becomes poor below this depth. No benthic foraminifers are found in samples in the intervals from 13.4 to 18.5 mbsf, 72.5 to 82.0 mbsf, 116.0 to 125.5 mbsf and below 206.2 mbsf in Hole 832A, or from 144.4 to 163.8 mbsf, 173.7 to 183.3 mbsf, 221.4 to 318.1 mbsf, 509.8 to 519.5 mbsf, 529.2 to 538.9 mbsf, 625.7 to 711.6 mbsf, 846.4 to 962.2 mbsf, and below 971.8 mbsf in Hole 832B.

The assemblages recognized in the Neogene sequence at Site 832 mainly consist of several species such as *Cibicides wuellerstrofi*, *Melonis barleeanus*, *M. pacificus*, *M. sphaeroides*, *Pyrgo murrhina*, and *Uvigerina hispidocostata*. The occurrence of *Melonis sphaeroides* and the constancy of faunal components indicate that the Neogene strata at Site 832 were deposited in the lower bathyal zone under normal oceanic conditions.

Sublittoral species such as *Amphistegina radiata* and *Elphidium advena* also occur in coarse-grained volcanic samples in the intervals from 28.0 to 47.0 mbsf, 91.5 to 106.5 mbsf, and 131.5 to 141.0 mbsf in Hole 832A, and 962.2 to 971.8 mbsf in Hole 832B. The presence of these specimens indicates that the volcanic clasts were derived from the sublittoral zone.

Summary

The sediments at Site 832 were deposited during the following times: Pleistocene (0 to around 600 mbsf), late Pliocene or early Pleistocene(?) (600 to 711 mbsf), late Pliocene (711 to 769 mbsf), early Pliocene (769 to 856 mbsf), (possibly late Miocene at 817 to 856 m), earliest middle Miocene (924 to 962 mbsf), and latest early Miocene (962 to

972 mbsf). The occurrence of *Melonis sphaeroides* in sequences from Holes 832A and 832B indicates that sediments were deposited in the lower bathyal zone.

A plot of sediment accumulation rate (Fig. 49) shows a change in slope near 700 mbsf, above which rates are >100 m/m.y. and below which rates vary from about 50 m/m.y. Although the presence of a hiatus at this depth is implied by a change in lithology (see "Lithostratigraphy" section, this chapter) and in seismic reflection profile (see "Seismic Stratigraphy" section, this chapter), biostratigraphic data do not indicate any missing section. Any hiatus within this interval must be of very short duration (<200,000 yr). Between the lower Pliocene at 856 mbsf and the lowermost middle Miocene at 952 mbsf is another possible unconformity. The presence of reworked specimens of larger benthic foraminifers and calcareous nannofossils in samples below 924 mbsf suggests that all of these samples are reworked and therefore younger than early Miocene.

IGNEOUS PETROLOGY

Numerous volcanic ash layers containing unaltered glass, plagioclase, and clinopyroxene were found in the cores recovered from Hole 832A and the upper part of Hole 832B, between 0.15 and 840 mbsf. Fragments of volcanic rocks, mainly clinopyroxene-phyric basalts ("ankaramite") and their associated rocks, were recovered between 395 and 1100 mbsf. The lowermost part of the core, between 1050 and 1100 mbsf, consists of altered volcanic breccia, in which volcanic clasts of scoria and lavas are set in a matrix of chloritized glass, clay minerals, and zeolite. In this discussion, the petrological descriptions are divided into two parts: volcanic ash and lava clasts found in volcanic breccias.

Volcanic Ash

More than 10 volcanic ash layers thicker than 10 cm were found, mostly above 150 mbsf. The number of ash layers thinner than 10 cm is quite high, probably over 100 when smears of ash are included. Most of these thin layers are found in the intervals 0–213 mbsf (in lithostratigraphic Unit I), 471–481 mbsf (in lithostratigraphic Unit III), and 802–840 mbsf (in lithostratigraphic Unit V). The volcanic ash is mostly within the range of sand size, varying from fine-grained to coarse-grained, although lapilli and pieces of pumice up to 2 cm are also observed. The color of the ash varies from black (5Y 2.5/1), gray (5Y 5/1), to dusky yellowish brown (10YR 3/2), probably reflecting the compositional trend from basaltic to dacitic. The ash layers always include crystals of clinopyroxene and plagioclase as well as unaltered vesicular brown glass. Vesicles are generally subrounded, but in grains of ash that are light brown in color, vesicles are elongated subparallel to the walls of stretched glass. Some glass fragments show contraction cracks on their surface. Additional constituents of the ash are opaque minerals and

crystals of either olivine or orthopyroxene. In two volcanic ash samples (Samples 134-832A-18H-1, 42–44 cm, and 134-832A-18H-4, 89–91 cm) there are fragments of both very light-colored glass and dark brown glass, indicating the existence of two magmatic liquids with different compositions. There are no fragments of intermediate color or banded varieties, which seems to suggest that the two types of glass came together only at the depositional stage.

Several reworked volcanic ash layers are also found: these contain foraminifers and altered volcanic glass or volcanic groundmass in addition to unaltered glass. The glass fragments in these reworked ash layers lack vesicles and cusped margins. Also, the proportion of glass is usually small, and the reworked layers are often graded, with grains becoming finer toward the top. In contrast, volcanic ash layers show little grading and are wet when interbedded with less permeable silt.

In addition to volcanic ash, gray (5Y 5/1) to olive gray (5Y 4/1) pumice fragments, 1 cm or less in diameter, are found in the volcanic breccia between 957 and 994 mbsf (in lithostratigraphic Unit VII). Occasionally scoriae of similar size are found in the volcanic sandstone.

Seven volcanic ash samples were collected between 5.08 and 145.76 mbsf (in lithostratigraphic Unit I) and were separated for onboard chemical analyses (see "Igneous Geochemistry" section, this chapter, for analytical results). Smear slide descriptions of these volcanic ash samples are listed in Table 3 and show mineral assemblages of plagioclase + clinopyroxene ± olivine. Orthopyroxene was not found in the volcanic ash layers in lithostratigraphic Unit I. Smear slide data for selected ash layers from all the horizons, however, show that orthopyroxene is also absent in the volcanic ash layers of lithostratigraphic Unit III, but that it appears again in ash layers of lithostratigraphic Unit V. This change in mineral assemblage will be further discussed in the following part, which discusses lava clasts.

Volcanic Clasts

Clasts of mostly basaltic composition are found in a matrix of volcanic sandstone, which is mainly composed of rock fragments that have undergone varying degrees of alteration and have colors ranging from dark gray, oxidized brown, to chloritized green. This lithology is repeated several times throughout the core, and is referred to as "basaltic breccia" in the "Lithostratigraphy" section (this chapter). The basaltic clasts, subrounded or subangular, are mostly pebble-sized (1–3 cm) but occasionally exceed 10 cm. Dark gray (5Y 4/1) to dark greenish gray (5GY 4/1) basaltic breccias are especially abundant in the lower parts of the core, which correspond to lithostratigraphic Units IV and VII.

Table 4 lists modal compositions of phenocryst phases, vesicles, and alteration products such as zeolite, palagonite,

Table 3. Modal analyses (vol%) of volcanic ash from Hole 832A derived from smear-slide descriptions.

Core, section, interval (cm)	Depth (mbsf)	Unit	Dark brown glass	Transparent or pale brown glass	Plagioclase	Clinopyroxene	Olivine	Rock fragment
134-832A-								
1H-4, 58–60	5.08	I	30	0	12	17	1	40
2H-5, 82–87	12.72	I	40	0	10	5	0	45
4H-3, 28–34	21.78	I	0	55	10	5	0	30
7H-1, 26–28	47.26	I	25	0	10	20	5	40
18H-1, 42–44	131.92	I	25	37	15	5	0	18
18H-4, 89–91	136.89	I	36	10	20	4	tr	30
20H-1, 76–80	145.76	I	30	0	tr	12	3	55

Note: tr = trace amount. Modal analysis was carried out for the coarse fraction (38–125 μ m, except for Sample 134-832A-7H-1, 26–28 cm, which is 63–125 μ m) separated for chemical analyses.

chlorite, and clay minerals for lava clasts recovered from Site 832. Most of the lava clasts are highly vesicular and have been altered; those recovered from the lower levels are especially highly altered. Oxidation is hardly observed at all among the lava clasts recovered from Site 832. As shown in Table 4, the phenocryst assemblage of the clasts varies with depth. Thus, in the following descriptions the volcanic clasts are divided into three groups, each representing different levels of core and different phenocryst assemblages.

1. Clinopyroxene (10%–35%) and plagioclase (0%–25%) are the dominant phases with opaque minerals always appearing as minor phases in the lava clasts occurring between 396 and 617 mbsf (within lithostratigraphic Units II and III). Euhedral to subhedral clinopyroxenes of augite composition are characteristically large, generally varying in size between 1 and 6 mm. Plagioclase is smaller than clinopyroxene with a usual size range of 0.2 to 1 mm. It is euhedral to subhedral, and almost all samples contains inclusions of brown glass. In two instances (Samples 134-832B-38R-1, 18–19 cm, and 134-832B-41R-1, 22–23 cm), phenocryst-size plagioclase is absent. In Sample 134-832B-43R-3, 23–26 cm, amphibole is found as a phenocryst phase in addition to clinopyroxene, plagioclase, and opaque minerals. Amphibole is anhedral and has reaction rims 0.02 mm thick of opaque minerals, pyroxenes, and plagioclase. This is the only case of a hydrous mineral occurring as a phenocryst phase in volcanic rocks recovered from the cores drilled in the central New Hebrides Island Arc. Opaque minerals, probably titanomagnetite, are of microphe-nocryst size (mostly from 0.1 to 0.4 mm); they are usually subrounded and often euhedral. They appear as discrete grains in the groundmass but are also included in clinopyroxene phenocrysts. The groundmass is composed of fine-grained plagioclase, clinopyroxene, opaque minerals, and very dark brown glass. The exception is the amphibole-bearing basaltic andesite (Sample 134-832B-43R-3, 23–26 cm), which shows intersertal texture with brown glass, plagioclase, orthopyroxene, clinopyroxene, and opaque minerals.

2. The phenocryst assemblage changes to clinopyroxene, plagioclase, and olivine in the lava clasts occurring between 631 and 686 mbsf (within lithostratigraphic Unit IV). Olivine phenocrysts are euhedral to subhedral, varying in size from 0.2 to 2 mm. They are generally fresh but olivine in three samples is partly altered to iddingsite. Other than olivine, phenocrysts are the same as described from lithostratigraphic

Units II and III with the following exceptions. Clinopyroxene often shows zoning with an inner core having a different extinction angle. Dusty plagioclase is pervasive in Sample 134-832B-56R-2, 55–56 cm. The groundmass minerals, showing intergranular texture, are more coarse-grained than in the lava clasts at higher levels except in Sample 134-832B-55R-4, 127–128 cm. The average groundmass mineral size reaches 0.1 mm in Sample 134-832B-57R-2, 124–125 cm.

3. Orthopyroxene joins the phenocryst phases of clinopyroxene, plagioclase, and olivine, but either plagioclase or olivine may be absent from lava clasts occurring below 983 mbsf (within lithostratigraphic Unit VII). Orthopyroxene is euhedral to subhedral and ranges in size between 0.2 and 2 mm. Unlike olivine, in which rims are often altered to iddingsite and chlorite, the orthopyroxene is fresh. Clinopyroxene is not usually as large as in other samples described above. The absence of microphe-nocryst-sized opaque minerals is also noteworthy. As a result, the texture of lavas recovered from this level is completely different from those of lithostratigraphic Units II, III, and IV. Sample 134-832B-100R-4, 7–8 cm, is an unusually fresh two-pyroxene andesite having unaltered brown glass that occupies 45% volume of the rock. This probably represents one of the most siliceous of the lavas recovered from Site 832.

The overall petrological trends observed among recovered lava clasts indicate a definite change upward from two-pyroxene andesite or olivine-bearing two-pyroxene basalt to ankaramite, distinctive basaltic lava in which clinopyroxene is the dominant phase. The descriptions of the mineralogy of ash layers show that orthopyroxene is present in lithostratigraphic Unit V but absent from lithostratigraphic Units I and III, a trend consistent with that observed in the lava clasts. These trends suggest a change of magmatism from a mature island-arc type volcanism to a rifting-type volcanism (e.g., Barsdell et al., 1982).

Potential sources of these volcanic clasts are the islands of Aoba, Santa Maria, Mere Lava, Maewo, and Espiritu Santo, all of which are located about equal distance from Site 832. General petrological descriptions by Carmichael et al. (1974) indicate that the lavas of Aoba Island, built up above sea level during the late Pliocene, are picrite basalts and ankaramites. The former contains more than 35% olivine phenocrysts with less abundant augite and no plagioclase. The latter contains 30% to 40% augite phenocrysts and only rarely plagioclase. Lavas with less abundant olivine and pyroxene phenocrysts are also found. Occur-

Table 4. Modal analyses of phenocryst assemblages for lavas from Hole 832B.

Core, section, interval (cm)	Unit	Clinopyroxene	Plagioclase	Olivine	Orthopyroxene	Opaque minerals	Amphibole	Vesicles	Alteration products
134-832B-									
27R-1, 54–56	II	35	15	—	—	5	—	10	8
28R-1, 1–3	II	30	10	—	—	1	—	18	8
31R-2, 9–11	II	20	15	—	—	3	—	15	4
38R-1, 18–19	III	10	—	—	—	2	—	30	3
41R-1, 22–23	III	25	—	—	—	3	—	15	15
43R-3, 23–26	III	10	25	—	—	6	8	7	—
50R-2, 46–48	III	15	7	—	—	3	—	5	—
51R-5, 7–8	IV	15	20	8	—	1	—	—	—
55R-4, 125–126	IV	20	4	tr	—	1	—	10	22
55R-4, 127–128	IV	15	20	5	—	5	—	8	45
56R-2, 55–56	IV	20	10	3	—	—	—	35	36
57R-2, 124–125	IV	25	35	4	—	—	—	—	10
88R-2, 105–109	VII	7	20	2	4	—	—	40	17
94R-2, 107–109	VII	12	16	6	3	—	—	20	44
100R-3, 146–147	VII	10	—	17	3	—	—	3	19
100R-4, 7–8	VII	5	18	—	7	—	—	—	—

Note: tr = trace amount; — = not observed.

rences of picrite and ankaramite were also reported from Maewo Island, though from upper Miocene to upper Pliocene formations (Macfarlane et al., 1988). Pleistocene to Holocene volcanism at Santa Maria Island includes outpourings of olivine basalt and andesite lavas and extensive ash eruptions (Macfarlane et al., 1988). Lavas occurring on Espiritu Santo Island are porphyritic basalts with dominant plagioclase, erupted during the Miocene (Mallick and Greenbaum, 1977; Robinson, 1969). The occurrence of orthopyroxene phenocrysts has been reported only from the Miocene volcanic rocks of Espiritu Santo Island and from Maewo Island. Similarly, amphibole phenocrysts are reported only from the Miocene volcanic rocks of Espiritu Santo Island (Mallick and Greenbaum, 1977; Robinson, 1969; Carney, 1986).

Thus, clinopyroxene-phyric basalts recovered from the upper part of the succession, in cores belonging to lithostratigraphic Units II, III, and IV, may have been derived from either Aoba Island or Maewo Island, but not from Espiritu Santo Island or Santa Maria Island. Maewo Island represents the most likely source for the older lavas. Although some differences are recognized between the lavas recovered from lithostratigraphic Units II and IV, picrite and ankaramite, lacking plagioclase, are found only in two samples from Site 832. Most of the lavas are more evolved types containing plagioclase. In contrast, lavas recovered from cores belonging to lithostratigraphic Unit VII are likely to have been derived from Espiritu Santo Island or Maewo Island, where orthopyroxene phenocrysts are found in the basalts and andesites. In addition, amphibole-bearing basaltic andesite recovered from lithostratigraphic Unit III has probably been derived from Espiritu Santo Island. The volcanic ash in lithostratigraphic Unit I may have originated from any of the islands of the Central Chain of the New Hebrides Island Arc. Extensive ash deposits from Santa Maria Island are likely to be found in the upper part of the cores recovered from Site 832.

The breccias of the lowest layers, especially below 1050 mbsf, were probably the product of submarine volcanism because they contain a matrix with abundant alteration products such as palagonite, chlorite, clay minerals, and zeolite. However, drilling ended far above the basement, as the total depth of 1106.7 m is much less than the thickness of horizontal sedimentary layers (>3 km) inferred from the seismic reflection data (see "Seismic Stratigraphy" section, this chapter). All the volcanic rocks recovered from Site 832 were probably derived from nearby islands or submarine volcanic centers since the Miocene.

IGNEOUS GEOCHEMISTRY

Numerous ash layers and many lava clasts were encountered during drilling at Site 832 in the North Aoba Basin. Their mineralogical and petrographic characteristics are described in the "Igneous Petrology" section (this chapter). From these, seven ash layers and seven volcanic fragments were chosen for X-ray fluorescence analyses on board (see "Explanatory Notes" chapter, this volume). The results are reported in Table 5. Before crushing, the pyroclastic material was treated with 1-N HCl in an ultrasonic bath to remove calcite and organic matter.

Ashes

The volcanic ash deposits from Hole 832A represent a considerable compositional range. SiO₂ varies between 51.36 and 58.02 weight percent (wt%), and the magnesium number (Mg# = MgO/[MgO + FeO_{total}] mol%) ranges from 0.59 to 0.36. As pointed out in the "Igneous Petrology" section (this chapter), crystals and glass do not appear to have undergone significant alteration. This is reflected in the low value of loss on ignition

(LOI; Table 5), which ranges from 0.72 to 1.94, averaging around 1%. The total alkali content varies between 3.60 and 8.71 (Table 5) and the Na₂O/K₂O ratio ranges from 2.10 to 1.15, indicating a relatively potassic affinity for the parental magma.

On the K₂O-SiO₂ diagram (Fig. 22) ash compositions plot either in the calc-alkaline or in the high-potassium calc-alkaline fields, except for Samples 134-832A-2H-5, 82–87 cm, and 134-832A-4H-3, 28–34 cm, which lie in the shoshonitic field. They range from basalts (Samples 134-832A-7H-1, 26–28 cm, and 134-832A-20H-1, 76–80 cm) to basaltic andesites (Samples 134-832A-1H-4, 58–60 cm, 134-832A-2H-5, 82–87 cm, and 134-832A-18H-4, 89–91 cm) and andesites (Samples 134-832A-4H-3, 28–34 cm, and 134-832A-18H-4, 89–91 cm). This diagram does not reveal any covariation between SiO₂ and K₂O in the different ashes, but a strong correlation is apparent in the K₂O vs. Zr plot (Fig. 23). Similarly, a positive correlation exists between Zr and other elements such as Ba, Rb, and Nb (Fig. 23). These trends are consistent with a common origin via crystal fractionation from a single parental magma, though varying proportions of crystals and glass in the samples will also have influenced the plots.

Figure 22 also shows the field for lava compositions of several islands in the New Hebrides Central Chain (data from Gorton, 1974; Dupuy et al., 1982; Barsdell et al., 1982; Marcelot et al., 1983; Briquieu, 1984). The great majority of the lavas fall in the calc-alkaline field, and only a few samples from Santa Maria and one from Ambrym show K₂O contents in excess of 2% and plot in or close to the shoshonitic field. In Figure 24 the compositional range of the ashes is displayed in a mid-ocean ridge basalt (MORB)-normalized incompatible element diagram (normalizing values from Pearce, 1982). The high contents of the trace elements in the analyzed samples (up to 30× MORB) are comparable with the sample from Santa Maria, though, Ba, Ce, and Nb analyses are not available for the latter. In this diagram the slightly positive Zr anomaly in the ashes is also significant, because only Santa Maria among the neighboring islands has erupted lavas with a Zr content greater than MORB (i.e., >1 in the normalized plot [Briquieu, 1984]). All these features point to the nearby island of Santa Maria as the most probable source of the ash layers encountered in the upper part of Site 832.

Lavas

The compositions of the lava clasts from Hole 832B (Table 5) fall well within the calc-alkaline field (Fig. 22) and show a narrower chemical range than that of the ashes previously described. All except one are basalts (SiO₂ between 47.3 and 50.01 wt%; Mg# from 0.62 to 0.55). Sample 134-832B-43R-3, 22–26 cm, is more differentiated (SiO₂ 54.46 wt%; Mg# 0.51) and is a basaltic andesite. The latter is the only sample that bears abundant amphibole crystals (8%; see "Igneous Petrology" section, this chapter). Variation diagrams suggest two groups of clasts, particularly apparent on the plots of Nb and Y vs. Zr (Fig. 23). Samples 134-832B-27R-1, 51–54 cm, 134-832B-31R-1, 126–128 cm, 134-832B-41R-1, 17–21 cm, and 134-832B-55R-5, 47–50 cm, tend to have lower SiO₂, K₂O, Ba, Rb, and Sr, and higher Nb and Y concentration than the other lavas (Samples 134-832B-43R-3, 22–26 cm, 134-832B-51R-4, 123–125 cm, and 134-832B-57R-2, 122–124 cm). The distinction is even more evident in the Ti-Zr diagram of Figure 25 where all but one of the samples plot in the calc-alkaline field. However, Samples 134-832B-27R-1, 51–54 cm, 134-832B-31R-1, 126–128 cm, 134-832B-41R-1, 17–21 cm, and 134-832B-55R-5, 47–50 cm, form a distinct group, more enriched in TiO₂ and plotting toward the MORB field. A similar calc-alkaline affinity is apparent from the Ti-Zr-Y

Table 5. Major and trace element analyses of ashes (numbers 1–7) and lava clasts (numbers 8–14) recovered from Site 832.

Number ^a	1	2	3	4	5	6	7	8	9	10	11	12	13	14
Hole, core, section	832A-1H-4	832A-2H-5	832A-4H-3	832A-7H-1	832A-18H-1	832A-18H-4	832A-20H-1	832B-27R-1	832B-31R-1	832B-41R-1	832B-43R-3	832B-51R-4	832B-55R-5	832B-57R-2
Sample interval (cm)	58–60	82–87	28–34	26–28	42–44	89–91	76–80	51–54	126–128	17–21	22–26	123–125	47–50	122–124
Rock type ^b	HK-BA	Sh-BA	Sh-A	HK-B	CA-A	CA-BA	CA-B	CA-B	CA-B	CA-B	CA-BA	CA-B	CA-B	CA-B
Depth (mbsf)	5.08	12.72	21.78	47.26	131.92	136.89	145.76	395.81	434.46	529.37	551.72	631.37	670.87	685.36
Major elements (wt%)														
SiO ₂	54.69	55.33	58.02	51.53	57.99	55.61	51.36	48.76	48.83	47.34	54.46	49.91	47.91	50.01
TiO ₂	0.82	0.89	0.63	0.84	0.74	0.76	0.80	1.09	1.21	1.43	0.71	0.77	1.14	0.76
Al ₂ O ₃	16.31	16.54	17.30	15.52	16.28	16.54	13.53	14.02	14.38	14.19	17.12	12.94	14.79	14.80
Fe ₂ O ₃ (t)	8.29	9.27	6.04	10.59	8.37	8.88	11.01	10.92	11.78	11.53	8.20	10.15	11.20	10.65
MnO	0.18	0.21	0.20	0.19	0.17	0.17	0.18	0.17	0.20	0.19	0.16	0.16	0.21	0.17
MgO	4.09	2.72	1.75	5.03	3.22	3.93	8.01	7.18	7.29	7.34	4.33	8.25	7.83	6.75
CaO	8.15	6.33	4.46	9.25	7.32	8.26	11.14	14.09	12.38	13.47	8.93	12.85	13.00	11.69
Na ₂ O	3.13	4.14	4.67	2.93	3.11	2.86	2.19	1.95	2.05	2.18	3.01	1.67	2.15	2.27
K ₂ O	2.13	3.18	4.05	2.18	1.74	1.36	1.42	0.74	0.77	0.79	1.52	1.29	0.74	0.97
P ₂ O ₅	0.26	0.42	0.26	0.24	0.19	0.18	0.20	0.21	0.24	0.28	0.26	0.33	0.23	0.17
Total	98.02	99.00	97.36	98.27	99.11	98.52	99.82	99.12	99.11	98.72	98.68	98.29	99.17	98.22
LOI	1.14	0.72	1.94	0.89	1.55	0.97	1.07	0.96	0.86	1.45	0.85	1.79	2.62	0.94
Mg#	0.49	0.37	0.36	0.48	0.43	0.47	0.59	0.57	0.55	0.56	0.51	0.62	0.58	0.56
Na ₂ O/K ₂ O	1.47	1.30	1.15	1.34	1.79	2.10	1.54	2.64	2.66	2.75	1.99	1.30	2.92	2.35
Na ₂ O + K ₂ O	5.26	7.31	8.71	5.10	4.85	4.22	3.60	2.69	2.82	2.97	4.53	2.96	2.88	3.24
Trace elements (ppm)														
Ti	4886	5336	3747	5036	4406	4526	4796	6535	7254	8543	4256	4586	6804	4526
Ni	33	10	4	40	18	23	87	50	64	55	20	85	55	38
Cr	91	11	6	87	40	58	314	192	213	181	34	336	170	117
V	238	257	111	303	202	231	309	331	324	349	272	322	348	317
Cu	121	185	94	154	94	96	152	86	108	94	83	133	139	83
Zn	79	106	110	96	86	80	71	73	78	84	52	64	78	55
Sr	612	759	669	814	410	420	749	416	540	457	627	621	466	533
Rb	35	52	67	34	29	22	21	5	7	8	27	14	9	12
Ce	30	50	64	29	25	24	29	30	25	29	33	41	28	20
Ba	562	745	872	548	515	432	364	178	177	209	352	238	221	271
Nb	4	4	6	3	4	3	2	5	6	9	3	2	5	1
Zr	175	220	247	187	146	135	162	114	152	148	163	152	132	117
Y	20	24	22	17	25	22	11	22	26	26	18	20	24	18

Note: LOI = loss on ignition; Mg# = MgO/(MgO + FeO_{total}) mol%.

^a See Figures 22 through 27.

^b Rock-type abbreviations: HK = high-potassium calc-alkaline series; Sh = shoshonitic series; CA = calc-alkaline series; B = basalt; BA = basaltic andesite; A = andesite.

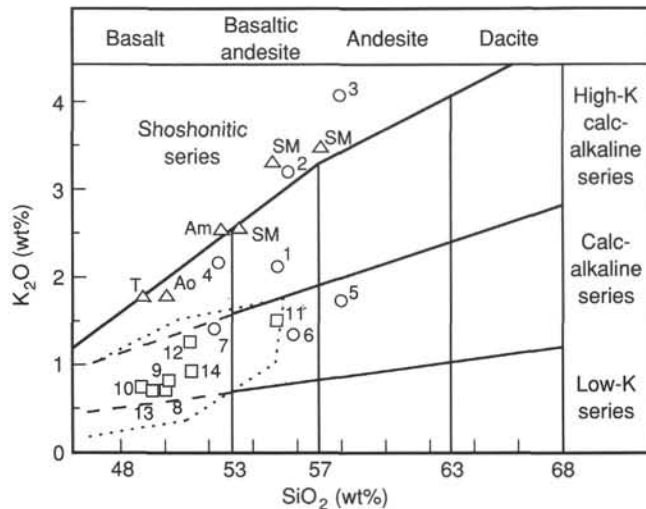


Figure 22. K_2O - SiO_2 diagram for ashes (circles) and basaltic clasts (squares) drilled at Site 832, North Aoba Basin. Numbers correspond to those in Table 5. Dotted line encloses compositions of lavas from several islands of the Central Chain of the New Hebrides Island Arc. Triangles refer to more alkali-rich magmas erupted at Tongoa (T), Aoba (Ao), Ambrym (Am), and Santa Maria (SM) islands. Field boundaries from Wilson (1989).

diagram (Fig. 26), although the same four basalts are displaced toward the MORB-island arc tholeiite (IAT) field.

When the two groups of lavas are plotted on a MORB-normalized incompatible element diagram (Fig. 27) it is evident that Samples 134-832B-43R-3, 22-26 cm, 134-832B-51R-4, 123-125 cm, and 134-832B-57R-2, 122-124 cm, are lower in Ti, Y, and Nb, and higher in K, Rb, Ba, and Sr (i.e., have more obvious calc-alkaline features compared with the other samples). From the petrographic observations (see "Igneous Petrology" section, this chapter), three groups of lavas with different parageneses were identified. Unfortunately, we do not have analyses of lava fragments from deeper in Hole 832B than Core 134-832B-57R (690 mbsf), and only four of the seven samples recovered from higher than this were sufficiently large for chemical analysis. Despite this, the different trends observed suggest there may be some compositional variations with depth in the stratigraphic sequence. However, we are dealing entirely with reworked material, which might represent an inversion of the sequence of material actually erupted. A progression from MORB-IAT upward to more calc-alkaline rocks in the original volcanic pile might, on erosion, give a dominance of calc-alkaline rocks at the base.

SEDIMENT AND FLUID GEOCHEMISTRY

The principal objective for measuring pore-fluid chemistry at Site 832 was to observe diagenesis in undeformed intra-arc sediment in order to compare with diagenesis in the deformed forearc sediment. The pore-fluid chemistry at Sites 827, 829, and 830 reflects much diagenesis that may have resulted partly from processes associated with the collision of the d'Entrecasteaux Zone with the New Hebrides Island Arc. A secondary objective was to determine if meteoric water from the surrounding islands mixes with the fluids in the Aoba Basin. Such mixing apparently occurs along continental margins such as the coasts of Oman (Prell, Niitsuma, et al., 1989) and Peru (Kastner et al., 1990). The Aoba Basin contains a thick sedimentary section (see "Background and Objectives" section, this chapter) that may contain large amounts of organic

matter shed off of the surrounding islands. An additional geochemical objective, therefore, was to measure the organic carbon contents of the sediments and to assess the hydrocarbon potential of the basin.

Results

A total of 30 fluid samples were collected from whole-round sections of cores at the two holes drilled at Site 832 (Table 6). Seven samples were obtained using the APC and one sample using the XCB at Hole 832A. The remaining samples were obtained with the RCB at Hole 832B. As usual, the parts of the samples that had been contaminated with drilling mud were removed prior to squeezing. The degree of contamination is difficult to determine; sulfate concentrations increase in the deepest samples, but other solute concentrations indicate that this sulfate is not from contamination (Fig. 28).

Samples were taken approximately every 20 m, except within hard, well-lithified units, and through zones with limited core recovery. Because such units occur at several horizons, the sample density is lower between ~180 and 280 mbsf and between 611 and 706 mbsf. Below 740 mbsf, samples were taken approximately every 30 m because samples 20 cm long were required to obtain sufficient quantities of fluid. No pore-fluid samples were taken below 832.8 mbsf because the sediment appeared hard and well cemented and thus probably contained little fluid.

Where samples were taken, however, the volume of water obtained was greater at comparable depths than at the forearc sites (Fig. 29). Only one sample (Sample 134-832B-51R-1, 130-150 cm) provided no fluid although it was squeezed for several hours at 35,000 psi. This sample was taken from the well-cemented, coarse graywacke at 627.0 mbsf and is characterized by low porosity and water content (see "Physical Properties" section, this chapter).

Chloride and Salinity

The chloride concentration and salinity exhibit similar overall trends (Fig. 28). The chloride concentration gradient increases slightly to 622 mM at 280.0 mbsf and increases sharply to a maximum of 700 mM (~25% seawater concentration) at a depth of 341.8 mbsf. A second maximum of 742 mM (~34% seawater concentration) occurs at a depth of 611.2 mbsf. These chloride maxima correspond to maxima in salinity of 46.3‰ and 50.6‰.

Sodium, Potassium, Calcium, and Magnesium

The concentration gradients of sodium, potassium, calcium, and magnesium exhibit small but significant changes above 280 mbsf and extraordinarily large variations below this depth (Fig. 28). Between the sediment-water interface and ~280 mbsf, the potassium and magnesium concentrations decrease continuously, and the calcium concentration also initially decreases to 1.9 mM at 42 mbsf, but increases slightly to 4.7 mM at 222.9 mbsf (Fig. 30). The sodium concentration increases steadily to a maximum of 501 mM at 280 mbsf. Below 280 mbsf, the pore-fluid gradients exhibit several maxima and minima with large gradients between the extremes (Fig. 28). The calcium maxima and the potassium, sodium, and magnesium minima correspond to the chloride and salinity maxima. The sodium and calcium profiles are mirror images (Fig. 31) but the potassium profile differs slightly from the smooth sodium and calcium profiles; it exhibits a sharp maximum of 15.2 mM at a depth of 280 mbsf and only a slight gradient below 700 mbsf. No measurable magnesium exists in the fluid sampled between 341.8 and 428.0 mbsf and the deepest sample at 832.8 mbsf. Between 428.0 and 802.3 mbsf the magnesium concentrations are low, generally <10 mM.

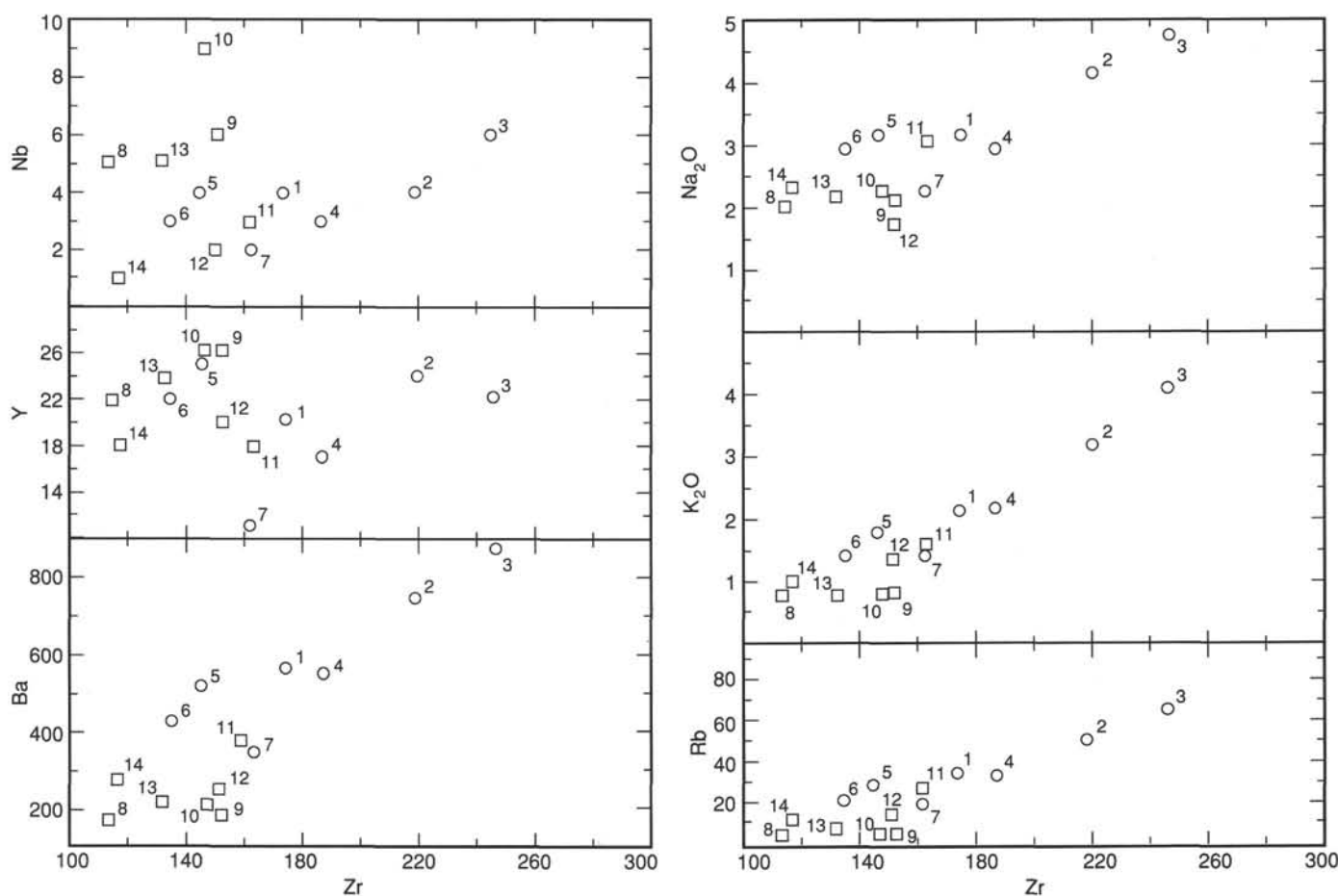


Figure 23. Plots of selected major and trace elements against Zr for volcanic ash deposits (circles) and lava clasts (squares) from Site 832, North Aoba Basin. Na_2O and K_2O are in weight percent; Rb, Nb, Y, Ba, and Zr in parts per million. Numbers correspond to those in Table 5.

Alkalinity, Phosphate, Ammonia, Sulfate, Methane, and Silica

The profiles of alkalinity, phosphate, ammonia, and methane are similar: all are characterized by sharp, distinct maxima around 77 mbsf (Figs. 28 and 32). The maxima in alkalinity (30.0 mM), phosphate (119.8 μM), and ammonia (2307 μM) are higher than values measured in the forearc sites. The maximum methane concentration is 28,211 parts per million (ppm) at 77 mbsf and 11,511 ppm at 164.7 mbsf; otherwise, the methane concentration is <10,000 ppm in both holes. Below the maxima, alkalinity, phosphate, and methane concentrations decrease to near-zero values at a depth of 280 mbsf and remain near zero to 832.8 mbsf, the deepest sample measured. The ammonia profile exhibits some variations but is characterized by two small but distinct maxima at 462.9 and 723.6 mbsf. Close to the depths of the chloride minima (Table 6).

The sulfate concentration decreases rapidly to a minimum of 0.6 mM at 42 mbsf (Fig. 28). The sulfate concentration remains low, although not zero (Table 6) to 280.0 mbsf, below which depth it exhibits a broad but distinct maximum from 428.0 to 588.3 mbsf and a smaller and more distinct maximum at 802.3 mbsf. These depths also correspond to the potassium, sodium, and magnesium minima and the chloride and calcium maxima.

The silica concentration is variable, but averages $\sim 500 \mu\text{M}$ from the sediment-water interface to a depth of ~ 400 mbsf. From this depth, silica decreases to 150 μM in the deepest sample at 832.8 mbsf. The silica concentration does not

appear to correspond to maxima or minima in any other solute concentration.

Sedimentary Carbon

All of the carbon data are reported in Table 7. The CaCO_3 contents are plotted against depth in the "Lithostratigraphy" section (this chapter) and the total organic carbon contents are plotted vs. depth in Figure 33. The organic carbon content is low typically <0.5%.

Discussion

Diagenesis apparently controls the solute concentrations at Site 832. Above 250 mbsf, the maxima of ammonia, phosphate, alkalinity, and methane concentrations probably relate to the bacterially mediated, coupled oxidation of organic matter and reduction of sulfate (e.g., Claypool and Kaplan, 1974). This interval is characterized by rapid sedimentation rates (see "Sediment Accumulation Rates" section, this chapter). The pore fluids are thus quickly cut off from diffusive exchange with the overlying seawater, which causes an increase in concentration of the regenerated solutes. Where the sulfate concentrations are high in the deeper section of the site, however, alkalinity, phosphate, and methane concentrations remain low and the ammonia maxima are much smaller than in the shallower section even though the sediments contain roughly the same organic carbon concentrations as in the shallow sediments (Fig. 33).

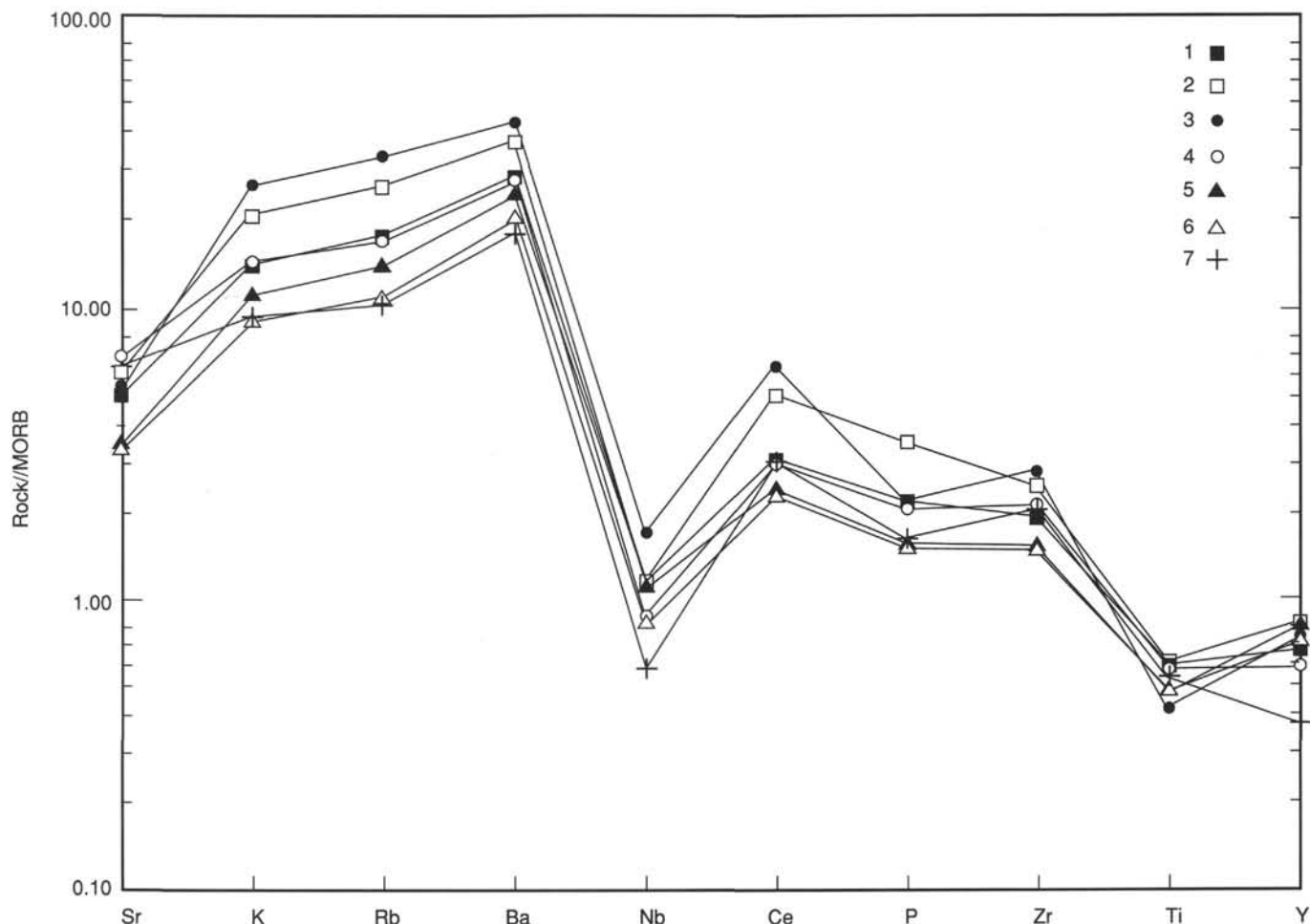


Figure 24. MORB-normalized incompatible element patterns for seven ash layers recovered at Site 832, North Aoba Basin (normalizing values from Pearce, 1982). Numbers refer to samples in Table 5.

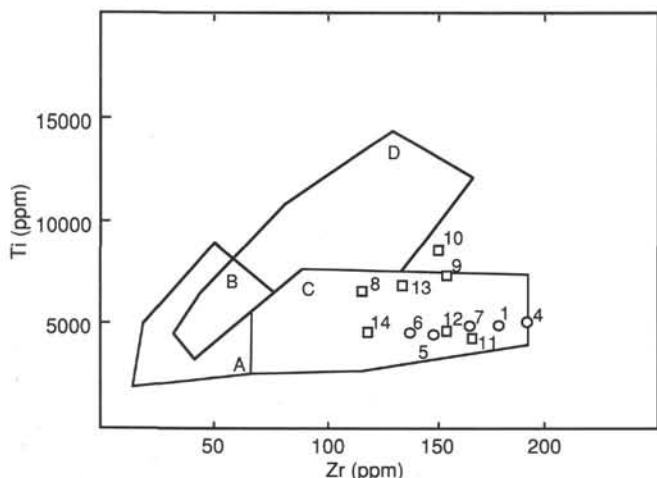


Figure 25. Ti-Zr tectono-magmatic discrimination diagram (Pearce and Cann, 1973) for ashes and basaltic rocks drilled at Site 832. A and B = island-arc basalts, C = calc-alkaline basalts, and D = mid-ocean ridge basalts. Symbols and numbers as in Figure 22.

Within the sediments above 250 mbsf, changes in calcium and magnesium concentrations (Fig. 31) are consistent with the precipitation of authigenic carbonate or phosphate minerals, particularly calcite, dolomite, and apatite. The high alkalinity may provide a source of bicarbonate for the carbonate mineral precipitation reactions and the high phosphate concentrations may provide phosphate for the precipitation of apatite. No authigenic calcite, dolomite, or apatite were observed in the sediments, however (see "Lithostratigraphy" section, this chapter), which suggests that these minerals constitute a small fraction of the sediment.

In addition to the carbonate and organic matter diagenesis, diagenesis of volcanogenic material appears to be important in controlling magnesium, calcium, potassium, sodium, and chloride concentrations (Fig. 31). The maxima in chloride and calcium concentrations, and the minimum in sodium concentration correspond to the tops of lithostratigraphic Units II and IV, which are characterized by a greater concentration of volcanogenic material (see "Lithostratigraphy" section, this chapter). Similar changes in concentrations of magnesium and calcium are attributed to alteration of volcanic ash and basaltic basement in DSDP sites (Gieskes, 1981; Lawrence and Gieskes, 1981).

Summary

The overall control of the pore-fluid gradients at Site 832 appears to be diagenesis—in particular, oxidation of organic matter, precipitation of authigenic carbonate and phosphate

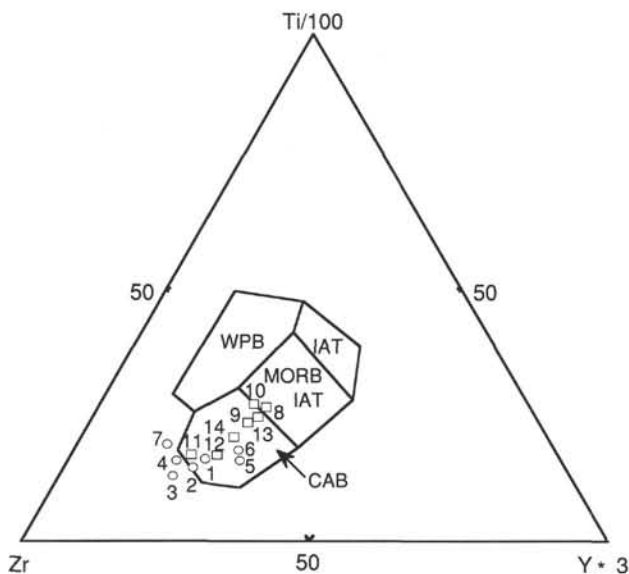


Figure 26. Ti-Zr-Y tectono-magmatic discrimination diagram (Pearce and Cann, 1973) for volcanic ashes (including more differentiated samples) and lava clasts recovered at Site 832, North Aoba Basin. WPB = within-plate basalts, IAT = island-arc tholeiites, CAB = calc-alkaline basalts, and MORB = mid-ocean ridge basalts. Symbols and numbers as in Figure 22.

minerals, and alteration of volcanogenic sediments. The pore fluids show no evidence of flow of meteoric water from the surrounding islands, perhaps because Site 832 is located near the geographic center of the Aoba Basin. The lack of hydrologic flow implies that if hydrocarbons are generated they will not be flushed from the sediments, but the low organic carbon contents suggest that the sediment penetrated at Site 832 may not contain large volumes of hydrocarbon source material.

STRUCTURAL STUDIES

All deformational structures observed at Site 832 result from small- to large-scale slumping, normal microfaulting, and compaction processes. Structural features observed in Hole 832B (144–1107 mbsf) are illustrated in Figure 34. Attitude of bedding planes and distribution of deformational structure types allow us to distinguish five structural units (A through E) that are described below from top to the base of the hole. Boundaries between these structural units are poorly defined because they are never outlined by tectonic features. These structural units often correspond to lithostratigraphic units (see "Lithostratigraphy" section, this chapter).

Structural Unit A spans the interval from 0 to about 415 mbsf (from Core 134-832A-1H to top of Core 134-832B-29R). Vitric ashes and sandy to clayey volcanic silts of lithostratigraphic Unit I (see "Lithostratigraphy" section, this chapter) and the upper part of the sandstones, siltstones, and claystones of lithostratigraphic Unit II are the dominant sediment types of Unit A. Structural Unit A is primarily characterized by horizontal to subhorizontal bedding surfaces and rare deformational structures. Above 270 mbsf (Core 134-832B-14R), the presence of unconsolidated sediments and soupy vitric ash layers complicates the interpretation of the observed features in the cores. However, almost vertical or steeply inclined beds bounded above and below by subhorizontal layers at 15 mbsf (interval 134-832A-2H-6, 120–150 cm) and at 76–80 mbsf (from Section 134-832A-10H-3 to Section 134-832B-2H-5) are interpreted as slump induced. Steeply dipping or vertical microfaults with small normal displacement (few millimeters to 1 cm) are noted at 10 mbsf (interval 134-832A-

2H-3, 100–105 cm), 14 mbsf (interval 134-832A-2H-6, 20–25 cm), and 74 mbsf (interval 134-832A-10H-2, 57–60 cm). Below 270 mbsf, sediments are partially lithified. Some subvertical faults occur between 312 and 320 mbsf (Cores 134-832B-18R and -19R).

Structural Unit B spans the interval from 415 to 626 mbsf (from the top of Core 134-832B-29R to the top of Core 134-832B-51R), and is composed of sandstones, siltstones, and claystones of the lower part of lithostratigraphic Unit II, and chinks and calcareous volcanic mixed sedimentary rocks interbedded with volcanic sandstones and breccias of lithostratigraphic Unit III. This structural unit is characterized by extreme variations in bedding plane dip angles (e.g., horizontal to vertical) (Fig. 34). These attitudes are attributed to the presence of abundant slump folds. Slump-fold hinges were recovered in the intervals Section 134-832B-31R-2, 130 cm, to Section 134-832-31R-3, 50 cm; Section 134-832B-32R-3, 25–70 cm; Section 134-832B-35R-2, 87–95 cm; Section 134-832B-36R-2, 5–25 cm; Section 134-832B-39R-2, 45–55 cm; and Section 134-832B-45R-2, 110–135 cm. One of the best examples of slump-fold hinges is shown in the Figure 35. Some microfaults with a normal (interval 134-832B-36R-2, 5–10 cm) or reverse (interval 134-832B-32R-3, 25–30 cm) sense of movement are locally associated with the slump structures.

Structural Unit C spans the interval from 626 to 702 mbsf (from the top of Core 134-832B-51R to the top of Core 134-832B-59R) and corresponds to lithostratigraphic Unit IV, which is composed of basaltic breccia and volcanic sandstone and siltstone. In this unit bedding planes are only observed in the intervals of laminated siltstones with dips of 30° to 65° (from Section 134-832B-51R-2 to the top of Core 134-832B-53R). Large variations in the dip of bedding planes and the presence of a flat shear plane at the base of a steeply dipping bed in Section 134-832B-53R-5 suggest that the observed bedding attitudes may result from slumping. Structural Unit C is also characterized by the occurrence of tilted conjugate normal faults. The best examples of these structures are observed in the laminated siltstones of intervals 134-832B-53R-4, 35–45 cm, and 134-832B-53R-6, 12–37 cm (Fig. 36). The faults at interval 134-832B-53R-4, 35–45 cm, can be divided into two conjugate sets: one set dips steeply (80° to vertical) and shows dip slip motion, whereas the other set dips gently (30°–45°), showing a normal sense of movement. When bedding is restored to horizontal, both sets of faults represent a normal displacement and dip steeply in the opposite direction. These structures indicate that the siltstones of Unit C were affected by normal faulting prior to tilting.

Structural Unit D spans the interval from 702 to 866 mbsf (from the top of Core 134-832B-59R to the top of Core 134-832B-76R) and corresponds to lithostratigraphic Unit V, which predominantly consists of silty limestone with calcareous volcanic siltstone and vitric ash. This structural unit is characterized by the presence of vein structures (tension gash arrays; Fig. 37), normal microfaults with very well-developed slickensides on the fault planes (Fig. 38), and horizontal bedding except in its basal part where slumps occur (Core 134-832B-74R). Moreover, in interval 134-832B-71R-2, 56–68 cm, a gypsum vein (1 to 1.5 cm wide) occurs (Fig. 39). Microfaults occur from Core 134-832B-63R to Core 134-832B-74R, but are especially abundant from 740 to 769 mbsf (Core 134-832B-63R to Core 134-832B-65R). Most fault planes dip 30° to 50° although some are shallower (up to 10°) and steeper (up to vertical). Well-developed slickensides can be observed on most of the fault planes (Fig. 38). Offsets of bedding or steps on the thin mineralizations that coat the fault planes always indicate a normal sense of motion. Displacements are only of small magnitude, ranging from 1 to 5 mm. Vein structures have been observed at different levels between 750 and 846 mbsf (intervals 134-832B-64R-1, 45–55 cm; 134-832B-65R-1, 115–125

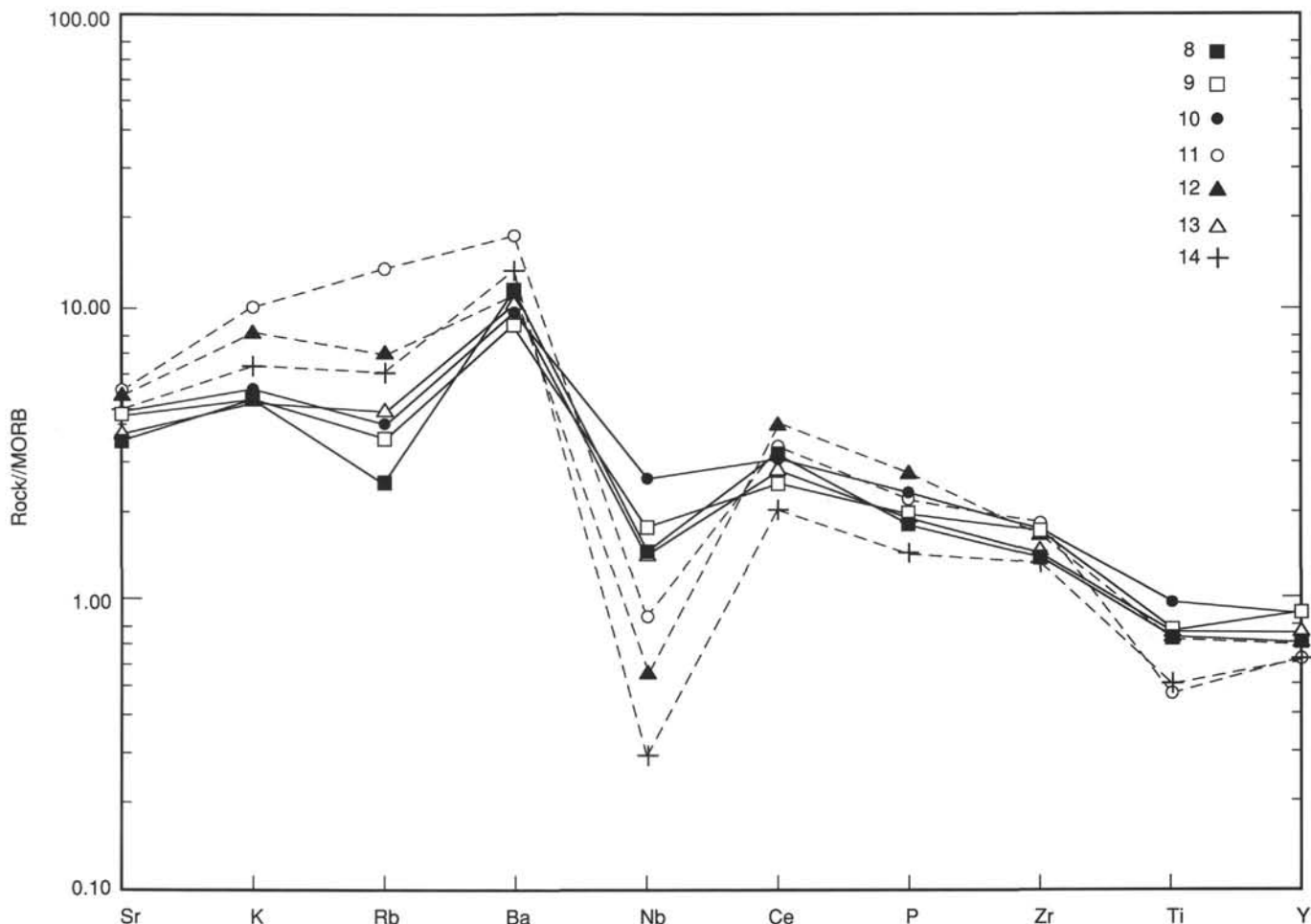


Figure 27. MORB-normalized incompatible element patterns for basaltic clasts encountered at Site 832, North Aoba Basin (normalizing values from Pearce, 1982). Dashed lines emphasize samples with more distinct calc-alkaline geochemical affinities (see text for explanation). Numbers refer to samples in Table 5.

cm; 134-832B-65R-2, 30–35 cm; 134-832B-70R-6, 23–24 cm; 134-832B-71R-5, 25–35 cm; 134-832B-72R-5, 62–67 cm; and 134-832B-73R-3, 105–120 cm). These small-scale (1–6 cm) veins are vertical to oblique with respect to the bedding and show a planar to sigmoidal trace on the core face. The sigmoidal feature of Figure 37 is composed of tension gashes associated with normal microfaults. Similar structures have been found in several DSDP cores and are interpreted as a response to bedding-parallel extension (Lundberg and Moore, 1986).

Structural Unit E spans the interval from 866 to 1107 mbsf (from the top of Core 134-832B-75R to the base of Core 134-832B-100R), and corresponds to lithostratigraphic Units VI and VII, which consist predominantly of volcanic sandstone and basaltic breccia. In this structural unit bedding generally is poorly defined. However, when it can be observed in the fine-grained layers, the dip angles range between 20° to 40°, which is remarkably different from structural unit D, in which bedding is almost horizontal. Locally the bedding is vertical (Section 134-832B-84R-1) and even overturned (intervals 134-832B-85R, 30 cm, to -85R-4, 65 cm, and in the top of Section 134-832B-86R-3). This attitude of bedding results from slumps as indicated by the slump fold-hinge recovered in the interval 134-832B-85R-4, 55–85 cm, and located below a 2-m-thick overturned sequence. Reverse and left lateral strike slip microfaults are associated with these slump structures. In Section 134-

832B-87R-1, tilted conjugate normal microfaults indicate that sediments at the base of Hole 832B were affected by normal faulting prior to tilting.

PALEOMAGNETISM

The natural remanent magnetization (NRM) and the magnetization after alternating field (AF) demagnetization using a peak field intensity of 10 mT were measured in archive halves of APC and selected XCB and RCB cores at 5-cm intervals using the cryogenic magnetometer. A pilot set of 144 discrete samples taken from the working halves of cores (32 samples from Hole 832A and 112 samples from Hole 832B) was progressively demagnetized using the Schonstedt AF demagnetizer and measured with the Molspin spinner magnetometer. Cores 134-832A-2H to -11H were oriented using the multishot orientation technique. Magnetic susceptibility was measured at 5-cm intervals on all cores from Holes 832A and 832B.

Paleomagnetic Results at Hole 832A

Most sediments recovered at Hole 832A are unlithified sandy to clayey volcanic silts. Remanent magnetizations in Cores 134-832A-2H to -11H (0–91.5 mbsf) after AF demagnetization at 10 mT are of normal polarity (Fig. 40). The observed scatter in inclination and declination is best explained by incomplete removal of a strong drilling-induced

Table 6. Pore-fluid chemistry, Site 832.

Core, section, interval (cm)	Depth (mbsf)	pH	Salinity (‰)	Chloride (mM)	Sodium (mM)	Potassium (mM)	Magnesium (mM)	Calcium (mM)	Sulfate (mM)	Alkalinity (mM)	Phosphate (μ M)	Ammonia (μ M)	Silica (μ M)
134-832A-													
1H-3, 145-150	4.5	7.9	34.5	551	477	12.10	50.60	9.29	26.1	4.9	12.0	71	396
4H-3, 145-150	23.0	7.8	35.1	560	486	11.73	46.10	3.01	4.5	23.0	75.0	1336	425
6H-3, 145-150	42.0	8.0	34.0	566	483	10.80	47.27	1.93	0.6	28.0	99.7	1680	437
8H-2, 144-150	59.5	8.1	34.0	568	484	10.86	46.71	2.32	0.7	30.0	104.5	1973	425
10H-3, 143-150	77.0	8.1	34.0	566	489	10.32	43.79	2.17	0.8	30.0	119.8	2307	542
16H-3, 145-150	117.5	7.8	34.0	573	489	9.57	42.30	2.28	0.8	27.3	89.3	2291	484
19H-1, 145-150	142.5	8.0	34.0	577	490	9.74	42.55	2.53	1.2	26.3	86.4	2246	530
24X-2, 145-150	180.7	7.8	34.5	583	495	9.24	42.69	3.35	2.4	21.7	42.5	1897	501
134-832B-													
9R-2, 140-150	222.9	8.0	34.2	596	499	10.82	35.47	4.66	0.6	11.0	14.8	2054	458
15R-2, 58-68	280.0	8.2	36.0	622	501	15.24	14.24	30.59	2.9	0.7	1.0	1599	316
17R-1, 10-20	300.3	7.9	38.0	642	484	12.55	15.71	54.48	4.8	0.5	0.7	1159	389
19R-1, 140-150	319.5	7.8	41.0	673	443	9.11	12.05	102.27	7.9	0.5	0.7	693	446
21R-3, 140-150	341.8		45.0	700	392	4.43	0	168.30	12.8			203	473
23R-2, 16-31	358.2	8.1	45.0	692	363	3.86	0	177.33	13.8	0.4	0.5	168	511
28R-2, 135-150	407.8	8.9	46.3	674	344	2.33	0	192.44	17.0	0.9	0.5	46	121
30R-4, 138-150	428.0	8.5	43.2	653	410	4.77	0	140.78	21.5	0.5	0.5	142	389
32R-2, 135-150	445.8	8.3	42.2	645	441	6.80	2.90	116.67	22.0	0.3	0.5	261	477
34R-1, 135-150	462.9	8.3	42.0	645	477	8.91	2.52	97.41	22.0	0.3	0.5	429	379
37R-3, 130-150	494.7	8.1	41.0	637	488	8.26	3.33	90.51	22.0	0.3	0.5	386	404
40R-1, 123-135	520.7		44.0	655	488	7.89	7.84	85.08	23.8			323	358
42R-2, 0-13	540.4	8.1	42.5	674	481	6.38	2.69	110.25	23.4	0.4	0.5	261	429
45R-1, 130-150	569.0	6.7	46.2	698	447	5.67	0.90	148.43	21.3	0.3	0.5	301	439
47R-1, 130-150	588.3	7.7	48.0	719	415	5.11	3.33	166.78	20.4	0.4	0.5	203	282
49R-CC, 0-20	611.2	8.0	50.6	742	344	3.96	0.54	215.93	16.5	0.3	0.5	145	408
59R-3, 130-150	706.3	7.9	48.5	708	374	4.34	3.23	180.15	14.5	0.1	0.5	272	586
61R-2, 130-150	723.6	8.2	45.1	682	401	4.20	3.86	150.59	14.6	0.3		349	270
63R-6, 0-20	747.3		44.2	678	431	4.05			14.4				
66R-3, 130-150	773.1		40.0	631	448	4.20	9.23	98.37	19.9			298	156
69R-4, 0-20	802.3		44.0	680	462	3.87	10.08	122.78	22.9			352	230
72R-4, 127-146	832.8		46.0	704	450	3.63	0	147.03	20.8			207	150

component of magnetization and by drilling disturbance. Several layers of unconsolidated sands are interbedded in the clayey volcanic silt. This type of lithology usually gives poorer recovery and is easily disturbed during drilling.

Intensities of remanent magnetization of the Pleistocene sediments after demagnetization at 10 mT are about 0.1 to 0.3 A/m, similar to intensities of Pleistocene sediments observed at Sites 827, 828, 829, and 830. Characteristic magnetizations of discrete samples of the Pleistocene sediments (Fig. 41) were easily identified from the orthogonal demagnetization diagrams and secondary magnetizations are generally removed by demagnetization at 20 mT. Although recovery was poor in Cores 134-832-12H to -26X (91.5-206.2 mbsf), paleomagnetic results suggest that these sediments were deposited within the Brunhes Chron.

Paleomagnetic Results at Hole 832B

Paleomagnetic results at Hole 832B reflect lithologic variation. Hence, discussion of the paleomagnetic data from Hole 832B is organized according to the major lithologic changes observed in the cores. Seven lithostratigraphic units were identified at Site 832 (see "Lithostratigraphy" section, this chapter for a description of the units). Paleomagnetic data from Cores 134-832B-2R through -50R (154.1-625.7 mbsf; lithostratigraphic Subunit IB and Units II and III) are summarized in Figure 42. Inclinations, although scattered, are predominantly negative, indicating a normal polarity for these cores. However, stepwise AF demagnetizations performed on some discrete samples taken from these cores revealed complicated demagnetization behavior. As shown in Figure 43, several samples from Core 134-832B-43R (548.5-558.2 mbsf) exhibited demagnetization curves that missed the origin of the vector plots, indicating that some components of magnetization were not removed from the samples. This demagnetiza-

tion behavior seems to coincide with cores that displayed slump structures.

The basaltic breccias (lithostratigraphic Unit IV, Core 134-832B-51R to -58R, 625.7-702.0 mbsf), also exhibit distinctive magnetic behavior. As shown in Figure 42, NRM intensities of the basaltic breccias are higher than those from the overlying sediments of lithostratigraphic Unit III, as are magnetic susceptibilities. AF demagnetization of 15 discrete samples of the basaltic breccias yielded a stable characteristic component of magnetization after removal of a soft drilling-induced component of magnetization. However, the fact that this magnetic signature is well behaved does not ensure that the magnetization is of primary origin. For example, volcanic siltstones and sandstones from Core 134-832B-53R exhibit faulting, convoluted slumped beds, and steeply dipping beds. Results of AF demagnetization of five samples taken from this core indicate that the magnetization might postdate all the observed sedimentary structures and tectonic activities. A more detailed study of additional discrete samples is required for further interpretations of the paleomagnetic data.

A major change in lithology occurs at the top of Core 134-832B-59R near 700 mbsf (see "Lithostratigraphy" section, this chapter). The sediments below this depth consist predominantly of light gray to dark greenish gray limestone and volcanic sandstones (lithostratigraphic Unit V). The NRM intensities and magnetic susceptibilities of this unit are lower than those of the overlying volcanic sandstone and basaltic breccia of lithostratigraphic Unit IV and the sedimentary rocks of lithostratigraphic Units I-III discussed above. Pass-through cryogenic magnetometer measurements revealed several intervals of magnetic polarity changes (Fig. 44) throughout this unit, which were later confirmed by detailed AF demagnetization measurements of 27 corresponding discrete samples. The determination of polarity change is based pri-

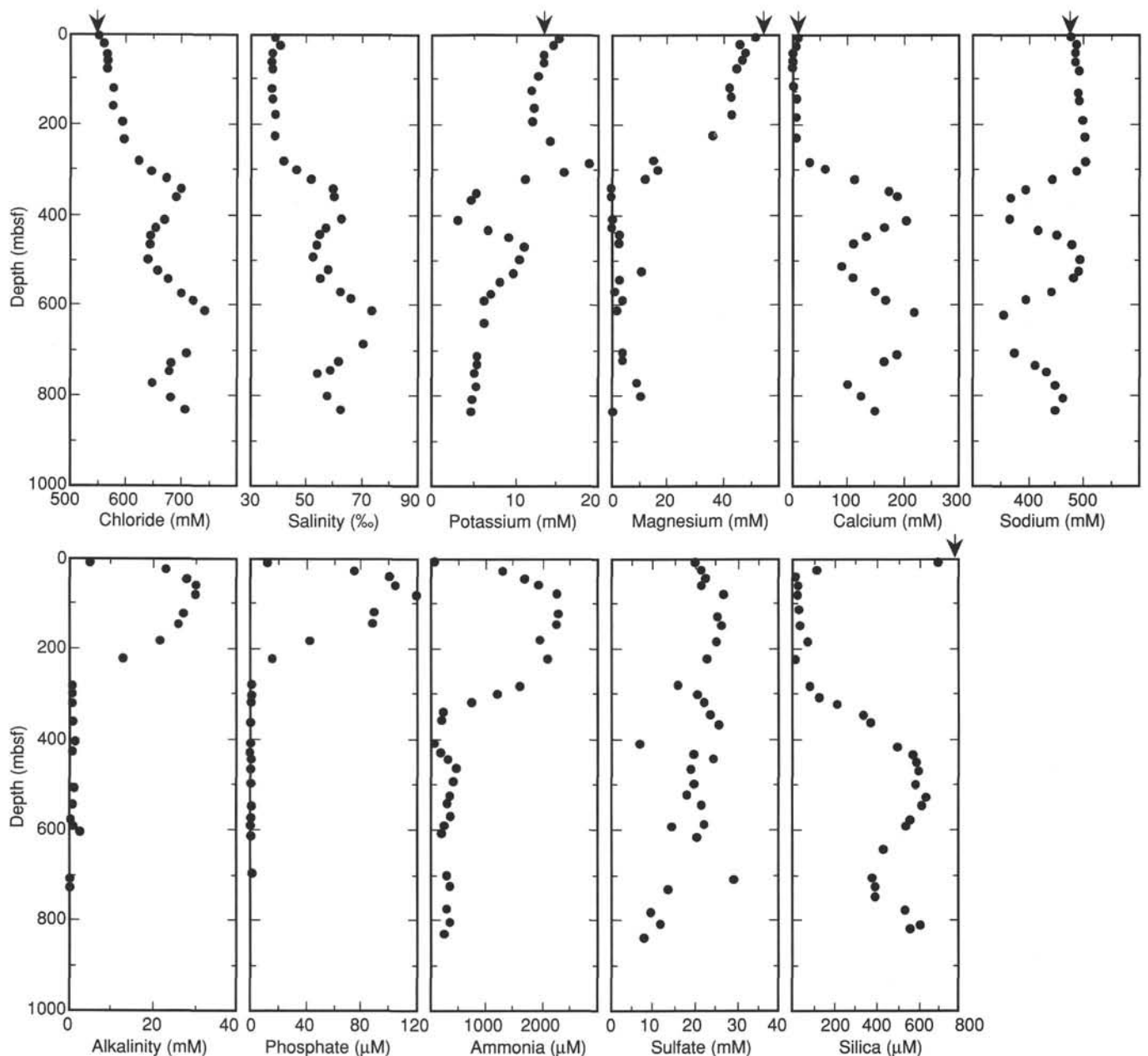


Figure 28. Pore-fluid gradients, Site 832. The arrows indicate seawater concentrations.

marily on the change in sign of the inclination. However, when cores contain long, continuous pieces, changes in inclination may sometimes be correlated with near- 180° variation in declination. An example is given by the two discrete samples taken from the same piece of core at the bottom of Section 134-832B-70R-6 (Fig. 45), from which negative and positive inclinations, as well as nearly antiparallel declinations, are observed.

Cores 134-832B-78R to -84R (870–950 mbsf) recovered mainly volcanic sandstones of lithostratigraphic Unit VI. Demagnetization of these cores at 10 mT revealed only positive inclinations (Fig. 46).

The deepest rocks recovered at Site 832, from Cores 134-832B-84 to -100R (942.9–1106.7 mbsf), consist mainly of basaltic breccia and conglomerate (lithostratigraphic Unit VII). The NRM intensities (Fig. 46) and magnetic susceptibil-

ities (Fig. 47) of this unit are significantly lower than those of the overlying units, probably reflecting an increase in the amount of alteration (see “Igneous Petrography” section, this chapter).

Magnetostratigraphy

The first polarity reversal was found in Core 134-832B-59R at a depth of 707 mbsf. However, biostratigraphic data suggest that sediments below this depth may be of late Pliocene age and that the last occurrence of the foraminifer *Globorotalia tosaensis*, which became extinct at approximately 0.6 Ma ago, was in Core 134-832B-18R (308.4–318.1 mbsf). This information suggests that sediments from about 400 to 700 mbsf were deposited during the early Pleistocene, corresponding mostly to a period of reversed polarity (Matuyama Chron). Apart from a short piece of core (about 30 cm long) from the top of

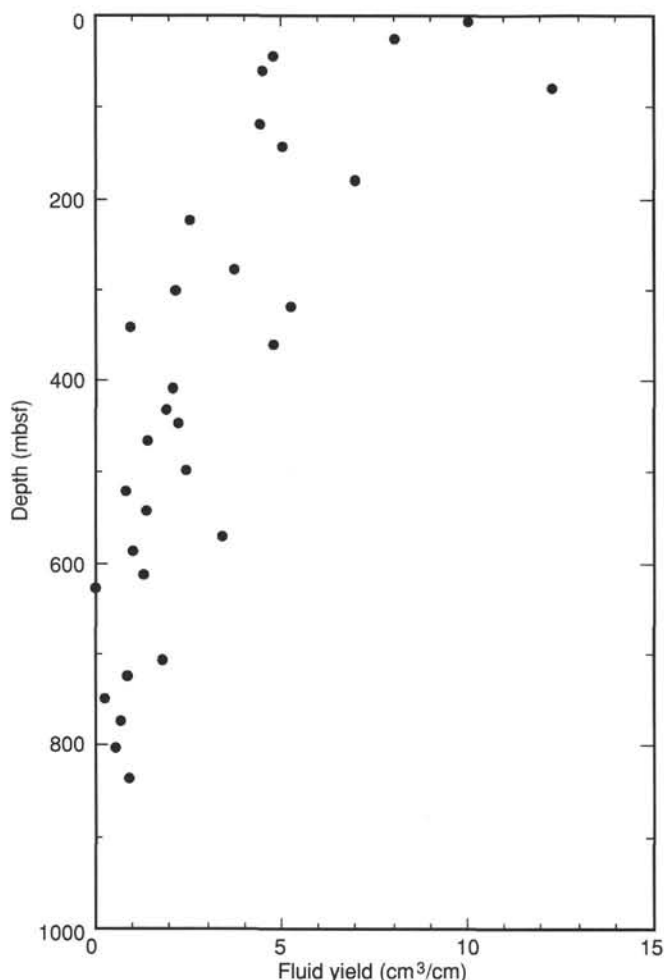


Figure 29. The yield of fluid per centimeter of core that was squeezed, Site 832. This value is only a qualitative measure of the water contained in the sample because some variable amount of the sample was removed from each sample prior to squeezing.

Core 134-832B-26R (385.6 mbsf) that recorded a positive inclination (confirmed by progressive AF demagnetization of one discrete sample), there is no evidence for reversed polarity interval from Core 134-832B-1R to -58R (160–707 mbsf). Unfortunately, we cannot dismiss the possibility that the reversed interval in Core 134-832B-26R has been displaced by slumps. Assuming that the biostratigraphic ages are correct, the failure to recognize the Brunhes/Matuyama boundary from cores recovered at Site 832 may result from an unrecognized sedimentary hiatus or by a possible large magnetic normal overprint during the Brunhes Chron.

Both cryogenic magnetometer measurements and AF demagnetizations of discrete samples identified several magnetic reversals from 700 to 850 mbsf. Key biostratigraphic markers permitted the tentative correlation of some polarity intervals found at Site 832 with the geomagnetic time scale (Berggren et al., 1985a, 1985b; see Fig. 48). On the basis of foraminiferal and nannofossil assemblages, the age of Core 134-832B-59R is placed at the Pliocene-Pleistocene boundary. Thus, the first magnetic polarity shift from normal to reversed may correspond to the bottom of the Olduvai event. The Matuyama-Gauss boundary may correspond to the reversal recorded in Core 134-832B-61R at a depth of 724.7 mbsf. Preliminary biostratigraphic evidence also sug-

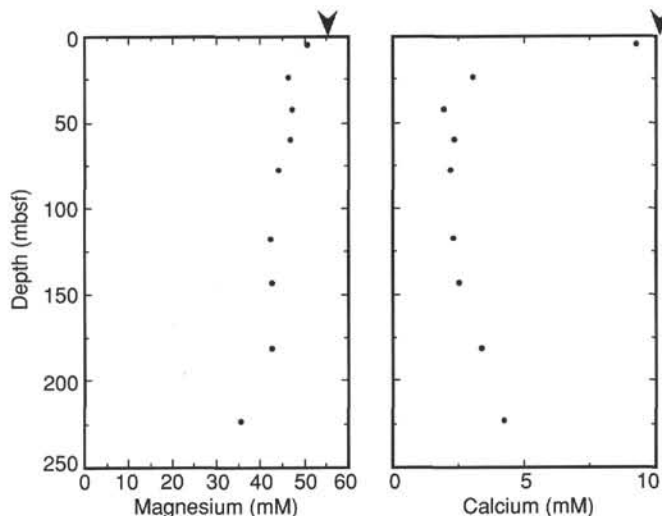


Figure 30. Calcium and magnesium pore-fluid concentrations from 0 to 250 mbsf plotted vs. depth. Arrows indicate seawater concentrations.

gests that the reversal in Core 134-832B-64R at a depth of 750 mbsf may represent the boundary between the Gauss and Gilbert chrons. Furthermore, the reversal at 808.7 mbsf (Core 134-832B-69R) is placed at the bottom of Gilbert Chron on the basis of nannofossil ages in sediments from Core 134-832B-69R.

Short polarity intervals may be correlated with geomagnetic subchrons, assuming that these age determinations and the major corresponding boundaries have been correctly recognized. The short normal polarity interval from 713.2 to 713.7 mbsf may correspond to the Reunion event in the Matuyama Chron at about 2.1 Ma. If we assume that the top of the Gilbert Chron is found at 750 mbsf, we do not observe the reversed polarity intervals delimiting the Kaena and Mammoth events at the base of the Gauss Chron. However, the correlation of the three normal polarity intervals (753.5–755.2 mbsf; 760.2–762 mbsf; 763.3–766.5 mbsf) with the Cochiti, Nunivak, and Sidufjall events within the Gilbert Chron (Fig. 48) is questionable.

The poor recovery in Cores 134-832B-67R and -68R (778.6–797.8 mbsf) introduces a gap in the magnetostratigraphic record. Although progressive AF demagnetization at 50 mT of two discrete samples from Cores 134-832B-66R and -67R revealed positive inclinations, no stable endpoints were reached for the magnetizations. A similar situation was also found in Cores 134-832B-78R to -100R (885.0–1106.7 mbsf). In addition, several discrete samples from these cores exhibited steep negative inclinations even after AF demagnetization at 80 mT, indicating incomplete removal of a strong normal magnetic overprint. We therefore consider these paleomagnetic results to be uncertain (shaded areas in Figs. 44 and 48). The normal polarity intervals (808.7–816.6 mbsf; 819.7–830.5 mbsf) in Figure 48 may correspond to Chron 5 (or anomaly 3A).

The magnetic polarity sequence is often not well defined by measurements using the cryogenic magnetometer because the applied AF fields of 10–15 mT are usually not sufficient to isolate the primary magnetization. Much more detailed work on the remaining discrete samples from Site 832 is needed to refine these correlations.

Magnetic Susceptibility

Magnetic susceptibilities of sediments and igneous rocks recovered at Site 832 exhibit large variations, sometimes even

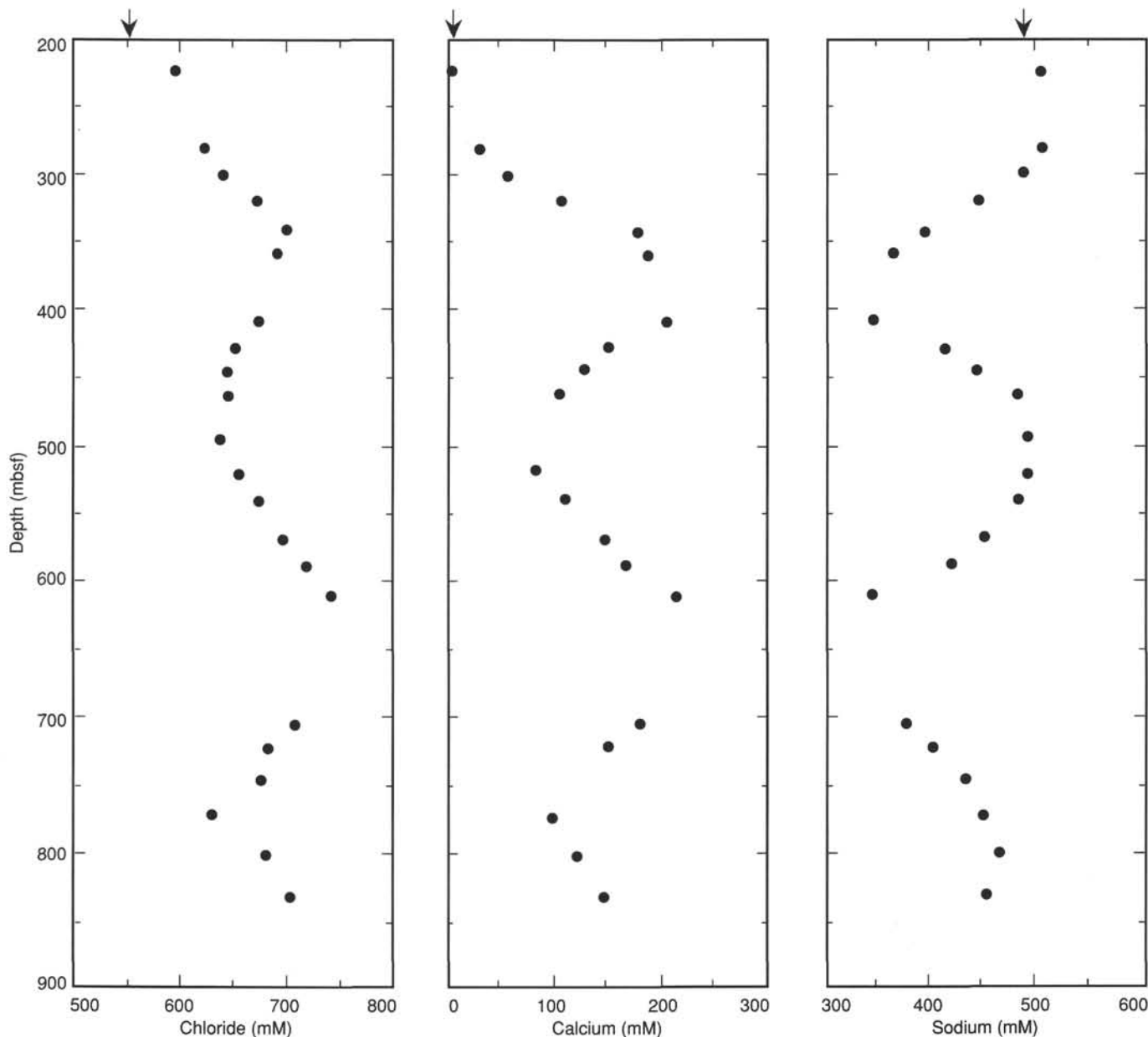


Figure 31. Chloride, calcium, and sodium pore-fluid concentrations from 200 to 900 mbsf plotted vs. depth. Arrows indicate seawater concentrations.

within a single core, because of the variability in the amount of volcanic material present (Fig. 47). Magnetic susceptibilities of the volcanic silt and sandstone in lithostratigraphic Units I–III (from 0 to 625.7 mbsf) average about 0.01 SI units. The basaltic breccia of lithostratigraphic Unit IV (from 625.7 to 702.0 mbsf) is easily distinguished by its much higher magnetic susceptibility values, typically of about 0.02 to 0.04 SI units. A major stratigraphic unconformity that corresponds to a lithological transition from the basaltic breccia to the underlying silty limestones of lithostratigraphic Unit V is also revealed by the susceptibility data with values from about 0.005 to 0.01 SI units. The rather high susceptibilities in the silty limestones may reflect the abundance of volcanic material in the limestones. The susceptibilities of the underlying volcanic sandstone of lithostratigraphic Unit VI are even lower than those of the limestones. The susceptibilities of the basaltic breccia in lithostratigraphic Unit VII (from 952.6 to 1106.7 mbsf) are

generally less than 0.01 SI units. The lowest susceptibilities recorded at Site 832 occur from about 1040 to 1100 mbsf, corresponding to a zone in which the matrix of the basaltic breccia is rich in alteration minerals including palagonite, chlorite, clay, and zeolite (see “Igneous Petrography” section, this chapter).

SEDIMENT ACCUMULATION RATES

The sediment accumulation rates at Site 832 are estimated from lines constructed by the extrapolation of points representing observed nannofossil and foraminiferal datums (Fig. 49). As with the biostratigraphy, the sediment accumulation rate interpretations at Site 832 are limited by the discontinuous nature of the microfossil record resulting from extensive barren intervals.

The estimated rate of accumulation in the interval from Section 134-832A-1X-CC to 134-832B-22R-CC (0–356 mbsf)

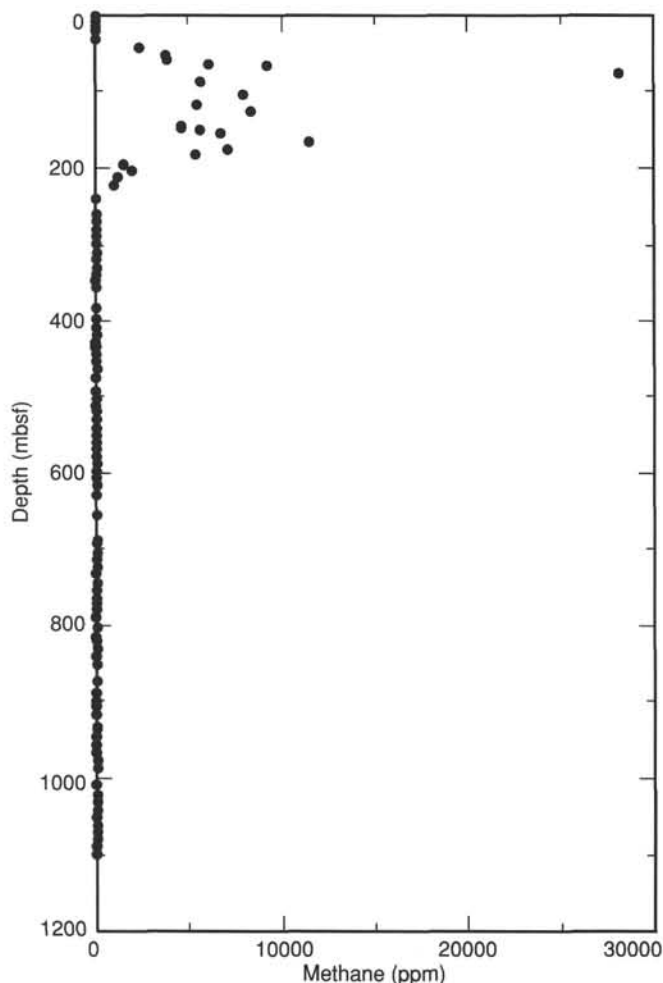


Figure 32. Methane concentrations in the headspace samples.

is 356 m/m.y. The estimated rate of accumulation decreased to 286 m/m.y. over the interval from Section 134-832B-22R-CC to 134-832B-59R-CC (356–711 mbsf); however, because the rate across this interval relies upon the placement of the first occurrence of the *Globorotalia truncatulinoides*, some uncertainty exists for this rate.

Unlike the other datums used in determining sediment accumulation rates at Site 832, the first occurrence of *G. truncatulinoides* is represented by two error bars. The vertical error bar represents the uncertainty in the first clear appearance of a keel in the last chamber of *Globorotalia tosaensis* (the ancestral species of *G. truncatulinoides*), which occurs in the interval between Samples 134-832B-40R-CC and -50R-CC (519–625 mbsf). The horizontal error bar indicates the uncertainty in age for this datum, which has been shown to occur between 1.9 and 2.7 m.y. (Hills and Thierstein, 1989). The midpoint of the resulting rectangle created by the two error bars is the point from which sediment accumulation rates are calculated in this study. Considering the degree of possible variation in the *G. truncatulinoides* datum, it is reasonable to accept a generalized sediment accumulation rate greater than 250 m/m.y. for the interval from Section 134-832A-1X-CC to 134-832B-59-CC (0–711 mbsf).

A change in the sediment accumulation rate occurs between Samples 134-832B-59R-CC and 134-832B-76R-CC (711–875 mbsf). Although a possible short hiatus within the upper Pliocene or lower Pleistocene complicates the estimation of rates across this interval (see “Biostratigraphy” sec-

tion, this chapter), the microfossil datums suggest that the rate is less than 100 m/m.y. This slower rate of deposition, relative to the overlying cores, is also supported by a lithologic change as evidenced by the presence of fine-grained, hemipelagic sediments below Sample 134-832B-59R-CC (711 mbsf).

The nanofossil and foraminiferal datums in Samples 134-832B-84R-CC (952 mbsf) and 134-832B-85R-CC (962 mbsf) suggest that a second unconformity exists somewhere within the barren interval above Sample 134-832B-84R-CC (952 mbsf). Due to the lack of datums below Sample 134-832B-85R-CC (962 mbsf), no further estimates for the remainder of Hole 832B can be made on the basis of microfossils.

PHYSICAL PROPERTIES

Measurements of index properties and Hamilton Frame sonic velocities were completed on sediments and rocks at Site 832. Full APC and XCB cores from Hole 832A were measured using the gamma-ray attenuation porosity evaluator (GRAPE) and the *P*-wave logger (PWL) on the multisensor track. Undrained shear strength measurements were completed on the APC/XCB cores of Hole 832A (2.35–196.8 mbsf) and on the undisturbed upper cores of Hole 832B (164.2–260.5 mbsf). All measurements at Site 832 were made according to the procedures described in the “Explanatory Notes” chapter (this volume).

Index Properties

Values of porosity (wet and dry), water content (wet and dry), and bulk density (wet-, dry-, and grain) for Site 832 are listed in Table 8. Figure 50 illustrates the variation of porosity, water content, and bulk density as a function of depth below seafloor. Bulk density trends often mirror those of porosity and water content; therefore, bulk density and porosity are plotted against depth along with the lithostratigraphic units in Figure 51.

At Site 832, porosity ranges from 9.2% to 80.3%, water content ranges from 3.4% to 85.5%, and bulk density ranges from 1.45 to 3.31 Mg/m³. The index properties data can be separated into three distinct zones. The zones are closely associated with the lithostratigraphic division at the site, with exception of the lithostratigraphic Unit I/Unit II boundary. The zones are associated with the lithostratigraphic units as follows:

Index Zone 1 = 0–312.4 mbsf in lithostratigraphic Unit I, Unit III (Hole 832B, 461.5–625.7 mbsf), Unit V (Hole 832B, 702.0–865.7 mbsf), Unit VI (Hole 832B, 865.7–952.6 mbsf), and Unit VII (Hole 832B, 952.6–1106.7 mbsf);

Index Zone 2 = 312.4–385.6 mbsf in lithostratigraphic Unit I, and Unit II (Hole 832B, 385.6–461.5 mbsf); and

Index Zone 3 = lithostratigraphic Unit IV (Hole 832B, 625.7–702.0 mbsf).

Index Zone 1 (0–312.4, 461.5–625.7, and 702.0–1106.7 mbsf) includes most of the total depth and is composed of several lithologies (see “Lithostratigraphy” section, this chapter). Zone 1 is characterized by porosity and water content values which decrease very slowly with depth. In the upper part of the zone, particularly from 0 mbsf to about 160 mbsf, water content values are high and somewhat scattered (Fig. 50). The near-vertical gradient suggests that the sediments are underconsolidated, possibly as deep as 300 mbsf. Between the surface (at 2.3 mbsf) and 1099.8 mbsf, porosity and water content decrease from 78.3% to 35.3% and from 85.9% to 18.6%, respectively (Table 8). The bulk density also increases slowly within index Zone 1, from 1.74 Mg/m³ at 2.3 mbsf to 2.31 Mg/m³ at 1099.8 mbsf. Index Zone 2 (312.4–461.5 mbsf) is an interval which is composed of sed-lithic- and basaltic-breccia, volcanic clay, silt, and sand. This zone is characterized by index property values which are

Table 7. Sediment carbon contents, Site 832.

Core, section, interval (cm)	Depth (mbsf)	Total carbon (wt%)	Inorganic carbon (wt%)	TOC (wt%)	CaCO ₃ (wt%)
134-832A-					
1H-2, 80-83	2.30	1.59	1.4	0.19	11.2
1H-4, 80-83	5.30		2.2		18.0
2H-2, 80-83	8.20	1.35	1.1	0.25	9.2
2H-4, 77-80	11.17		2.5		21.2
2H-6, 81-84	14.21		0.5		3.8
3H-2, 80-83	17.70	0.76	0.6	0.16	4.8
4H-1, 130-133	19.80		0.7		5.5
4H-3, 115-118	22.65	0.33	0.3	0.03	2.3
4H-5, 117-120	25.67		1.5		12.3
4H-6, 147-150	27.47		0.7		5.7
5H-1, 130-133	29.30		1.1		9.4
5H-3, 130-133	32.30	0.66	0.6	0.06	4.7
5H-5, 130-133	35.30		0.3		2.2
5H-7, 50-53	37.50		0.5		3.8
6H-1, 127-130	38.77		1.7		14.0
6H-3, 132-135	41.82	0.79	0.6	0.19	5.1
6H-4, 75-78	42.75		0.3		2.8
6H-7, 40-43	46.90		0.2		1.7
7H-2, 117-120	49.67		3.2		26.3
7H-4, 117-120	52.67	0.48	0.4	0.08	3.2
7H-6, 117-120	55.67		0.4		3.3
8H-1, 120-123	57.70		0.6		4.6
8H-3, 65-68	60.15	0.27	0.3	0.00	2.1
8H-5, 29-32	62.79		0.2		1.9
9H-2, 104-106	65.54	0.33	0.3	0.03	2.3
9H-5, 103-106	70.03		0.9		7.3
9H-74, 53-56	72.53		0.7		5.8
10H-1, 140-143	73.90	0.37	0.3	0.07	2.3
10H-3, 127-130	76.77		1.6		13.7
10H-6, 140-143	81.40		1.4		11.3
11H-1, 130-133	83.30		1.1		8.9
11H-4, 130-133	87.80	0.88	0.7	0.18	5.8
11H-6, 130-133	90.80		0.7		5.9
12H-2, 77-80	93.77	0.69	0.6	0.09	5.0
12H-4, 78-79	96.78		0.6		5.2
13H-2, 79-80	102.80	0.38	0.4	0.00	3.2
14H-2, 79-80	103.80	0.47	0.4	0.07	3.5
15H-2, 73-80	108.70	0.40	0.4	0.00	3.0
16H-2, 80-83	118.30	0.81	0.7	0.11	5.7
16H-2, 127-130	118.80		0.6		4.9
16H-4, 78-89	121.30		0.1		0.9
17H-1, 77-80	126.30	1.35	1.1	0.25	8.7
17H-3, 78-90	129.30		0.4		3.3
18H-2, 79-80	133.80	0.44	0.4	0.04	3.4
18H-4, 78-79	136.80		0.4		3.1
19H-2, 77-80	143.30	0.92	0.7	0.22	6.1
20H-1, 145-148	146.50		0.7		5.7
20H-3, 130-133	149.30	1.13	0.9	0.23	7.7
21X-CC, 7-8	151.30	0.83	0.7	0.13	6.2
24X-2, 131-135	180.50	0.65	0.5	0.15	4.5
24X-4, 7-8	182.30		0.5		4.1
26X-1, 9-12	196.80	2.72	2.5	0.22	20.7
134-832B-					
1R-CC, 4-6	144.44	0.80	0.7	0.12	5.7
2R-CC, 18-19	154.28	1.12	0.9	0.25	7.2
3R-1, 54-55	164.34	2.97	2.8	0.22	22.9
3R-CC, 14-15	164.85	1.16	2.7	0.00	22.2
4R-CC, 18-19	173.88		0.9		7.7
7R-1, 60-63	202.80	1.09	1.0	0.13	8.0
8R-1, 85-88	212.75	1.72			
9R-1, 6-8	221.45	1.18	0.4	0.74	3.7
9R-2, 100-103	223.90		0.7		5.7
11R-CC, 7-10	240.77	0.43	0.4	0.05	3.2
13R-1, 10-13	260.10	1.05	1.0	0.09	8.0
13R-1, 125-128	261.25		0.6		4.6
14R-1, 87-90	270.57	0.47	0.3	0.13	2.8
15R-2, 5-7	280.12	0.36	0.3	0.04	2.7
16R-1, 45-47	289.45		5.1		42.8
16R-2, 16-18	290.66	1.06	0.8	0.26	6.7
17R-1, 17-20	298.87		1.2		10.1
17R-3, 71-73	300.91	0.22	0.2	0.03	1.6
18R-2, 72-75	310.62		3.4		28.7
18R-3, 117-120	312.41	1.55	1.4	0.17	11.5

Table 7 (continued).

Core, section, interval (cm)	Depth (mbsf)	Total carbon (wt%)	Inorganic carbon (wt%)	TOC (wt%)	CaCO ₃ (wt%)
19R-1, 105-108	319.15		1.0		8.4
19R-2, 87-88	320.47	4.66	4.1	0.52	34.5
20R-3, 26-28	330.89	0.49	0.4	0.05	3.7
21R-1, 105-107	338.45		0.4		3.7
21R-3, 106-108	341.46	1.06	0.9	0.21	7.1
22R-1, 57-59	347.47	2.38	2.0	0.38	16.7
23R-1, 87-89	357.47		2.3		18.7
23R-3, 68-70	359.09	4.44	4.0	0.47	33.1
26R-1, 65-68	386.25	4.20	3.8	0.37	31.9
26R-1, 114-116	386.74		1.3		10.9
27R-1, 101-103	396.31	0.79	0.7	0.08	5.9
28R-1, 17-20	405.07		0.8		6.7
28R-2, 80-83	407.20		1.4		11.7
28R-3, 70-72	408.60	2.05	1.9	0.16	15.7
28R-3, 147-150	409.37		0.9		7.2
29R-1, 37-39	414.57		0.8		6.8
29R-3, 38-40	417.58	2.03	1.8	0.20	15.2
29R-5, 38-40	420.58		1.7		14.2
30R-2, 83-84	425.93	1.35	1.3	0.07	10.7
30R-3, 88-90	427.48		0.4		3.2
30R-6, 92-95	432.02		2.1		17.4
31R-1, 127-130	434.47	0.09	0.1	0.03	0.5
31R-3, 127-130	437.47	3.58	3.4	0.18	28.3
32R-1, 137-140	444.27		3.3		27.1
32R-3, 137-140	447.27	5.34	5.1	0.20	42.8
33R-1, 122-125	453.12	1.88	1.8	0.07	15.1
34R-2, 60-63	463.60	3.53	3.4	0.16	28.1
35R-2, 110-112	473.70	2.41	2.2	0.18	18.6
36R-2, 75-78	483.06	3.38	3.2	0.17	26.7
37R-2, 96-98	492.86	3.83	3.6	0.20	30.2
38R-1, 84-86	500.94	2.48	2.3	0.15	19.4
39R-2, 85-87	512.15	2.96	2.8	0.15	23.4
40R-1, 94-97	520.44	3.50	3.3	0.17	27.7
41R-1, 93-96	530.13	3.26	3.1	0.16	25.8
42R-2, 81-84	541.21	3.79	3.6	0.18	30.1
43R-1, 47-50	548.97	4.89	4.6	0.27	38.5
43R-3, 44-47	551.94		1.9		15.8
44R-1, 117-120	559.37	2.79	2.7	0.12	22.2
45R-1, 107-110	568.77		4.1		34.4
45R-3, 72-75	571.42	2.67	2.5	0.13	21.2
46R-1, 37-39	577.77		2.6		21.6
46R-3, 32-35	580.72	4.53	4.3	0.23	35.8
47R-1, 70-73	587.70		1.6		13.4
47R-2, 87-90	589.37	7.47	7.2	0.32	59.6
48R-1, 100-103	597.70	2.15	1.8	0.31	15.3
49R-1, 100-103	607.40	2.87	2.7	0.15	22.7
49R-3, 100-103	610.40		3.9		32.3
50R-2, 63-66	617.27	4.21			
50R-4, 100-103	620.62		1.6		13.1
51R-2, 27-29	627.47		0.1		0.6
51R-4, 75-77	630.89	1.41	1.3	0.07	11.2
52R-2, 85-87	637.46		0.2		1.6
52R-4, 85-87	640.19	0.73	0.7	0.03	5.8
52R-6, 85-87	643.13		0.1		0.5
53R-2, 88-90	647.38		0.1		0.5
53R-4, 88-90	650.38	0.09	0.1	0.01	0.7
53R-6, 88-90	653.38		0.1		0.5
54R-2, 80-83	657.00		2.5		20.7
54R-4, 79-81	660.01	0.04	0.0	0.00	0.3
55R-2, 140-143	667.30		0.1		0.4
55R-4, 140-143	670.30	0.67	0.6	0.03	5.3
56R-2, 137-140	675.87		0.4		3.5
56R-4, 137-140	678.84	0.04	0.0	0.02	0.2
57R-2, 67-69	684.81	0.03	0.0	0.00	0.2
57R-4, 97-99	687.97		0.1		0.4
58R-2, 37-40	694.17	0.04	0.0	0.00	0.3
59R-2, 120-123	704.70		2.6		21.4
59R-4, 120-123	707.71	3.63	3.5	0.14	29.1
59R-6, 120-123	710.71		2.0		16.7
60R-2, 140-143	714.50		2.4		19.9
60R-4, 140-143	717.50	5.25	4.9	0.31	41.2
60R-5, 127-130	718.87		6.0		49.6
61R-1, 147-148	722.27		4.5		37.5
61R-3, 147-150	725.25	4.81	4.5	0.28	37.7
61R-6, 147-150	729.73		1.3		10.7
62R-2, 25-28	732.25	3.47	3.3	0.19	27.3

Table 7 (continued).

Core, section, interval (cm)	Depth (mbsf)	Total carbon (wt%)	Inorganic carbon (wt%)	TOC (wt%)	CaCO ₃ (wt%)
62R-4, 25-28	735.25		4.3		35.7
63R-2, 23-25	741.53		4.0		33.7
63R-4, 23-25	744.53	1.63	1.6	0.08	12.9
63R-6, 21-23	747.51		7.4		62.0
64R-2, 90-92	751.90		6.2		51.6
64R-4, 92-94	754.92	7.02	6.6	0.38	55.3
65R-2, 123-125	761.93		7.1		59.3
65R-4, 124-126	764.94	8.23	7.8	0.45	64.8
65R-6, 124-126	767.94		7.7		64.4
66R-1, 118-120	769.98		9.8		81.4
66R-3, 119-121	772.79	2.74	2.3	0.42	19.3
67R-2, 112-114	781.22	3.40	3.1	0.29	25.9
69R-2, 122-124	800.52		5.5		45.7
69R-4, 145-147	803.75	6.08	5.7	0.34	47.8
69R-6, 45-47	805.75		3.2		26.7
70R-1, 149-150	809.19		5.8		47.9
70R-3, 146-148	812.16	7.97	7.5	0.49	62.3
70R-5, 145-147	815.15		6.5		54.0
71R-2, 125-128	820.15		3.8		31.9
71R-5, 104-107	824.44	5.38	5.1	0.31	42.2
72R-2, 21-23	828.71	0.35	0.6		5.3
72R-4, 30-31	831.81		1.6		13.6
72R-6, 22-25	834.69		2.7		22.3
73R-1, 10-13	836.80		0.7		5.6
73R-2, 11-14	838.31	0.21	0.2	0.00	1.8
73R-4, 122-124	842.23		0.7		5.6
74R-1, 143-146	847.83		1.0		8.3
74R-2, 140-143	849.30	8.11	7.6	0.49	63.5
74R-3, 140-143	850.80		0.5		4.2
76R-CC, 0-8	865.70	0.08	0.0	0.06	0.2
77R-CC, 20-23	875.50	0.89	0.8	0.07	6.8
78R-2, 127-130	887.77		0.1		0.5
78R-4, 122-125	890.72	0.06	0.1	0.01	0.4
78R-6, 120-123	893.63		0.1		0.4
79R-2, 115-118	897.35		0.1		0.4
79R-4, 109-112	900.29		0.0		0.2
80R-2, 103-106	906.95		0.0		0.3
80R-4, 99-102	909.91	0.05	0.1	0.00	0.4
81R-2, 137-140	916.81	0.06	0.1	0.01	0.4
82R-2, 137-140	926.57	0.09	0.1	0.00	0.7
82R-5, 137-140	930.90		0.8		6.7
83R-1, 123-125	934.53	0.61	0.6	0.04	4.7
83R-3, 123-125	937.53		0.4		3.0
84R-2, 42-44	944.82	0.26	0.1	0.20	0.5
85R-1, 91-92	953.51	0.37	0.4	0.02	2.9
85R-2, 80-83	954.90		2.4		19.9
85R-3, 123-124	956.83		1.0		8.5
85R-4, 88-90	957.98		2.8		23.7
85R-5, 90-92	959.50		0.4		3.7
86R-1, 72-74	962.92	0.45	0.4	0.03	3.5
86R-3, 71-73	965.91		0.3		2.3
87R-1, 117-120	972.97	0.65	0.6	0.02	5.2
87R-3, 117-120	975.97		0.5		4.2
88R-1, 135-137	982.45		0.1		0.8
88R-2, 130-133	983.84	0.34	0.4	0.00	2.9
88R-3, 131-133	985.33		0.4		3.1
89R-2, 130-132	993.60	0.71	0.7	0.03	5.7
89R-4, 130-132	996.51		0.5		4.0
89R-6, 134-136	999.55		0.6		4.7
90R-2, 122-124	1003.10	0.38	0.3	0.04	2.8
92R-2, 52-54	1021.50	0.94	0.9	0.04	7.5
93R-2, 15-18	1031.00	0.30	0.3	0.04	2.2
93R-5, 15-18	1035.00		0.4		2.9
94R-2, 82-84	1041.00	0.11	0.1	0.03	0.7
95R-2, 132-135	1051.00	0.10	0.1	0.03	0.6
96R-2, 137-140	1061.00	0.11	0.1	0.05	0.5
96R-4, 137-140	1064.00		0.1		0.5
97R-2, 133-136	1071.00	0.09	0.1	0.02	0.6
97R-4, 123-126	1074.00		0.1		0.7
97R-6, 127-130	1077.00		0.1		0.5
98R-2, 120-123	1080.00	0.07	0.1	0.01	0.5
98R-5, 120-123	1085.00		0.1		0.7
99R-2, 120-122	1090.00	0.12	0.1	0.03	0.7
99R-4, 118-120	1093.00		0.1		0.7
100R-2, 131-134	1100.00	0.09	0.0	0.05	0.3
100R-4, 131-134	1103.00		0.1		0.7

Note: TOC = total organic carbon.

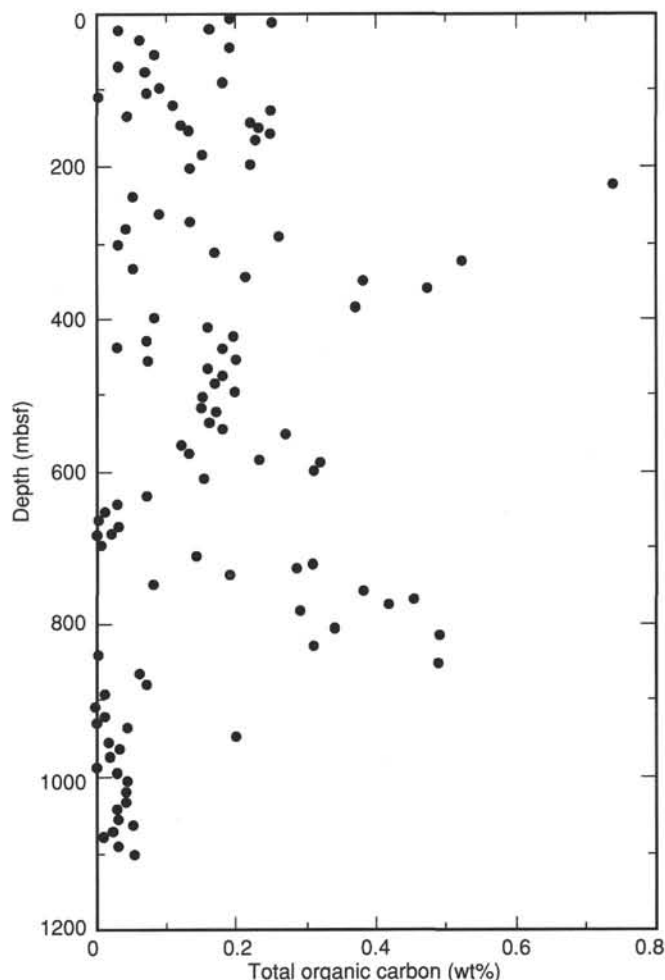


Figure 33. Total organic carbon content of sediments at Site 832 plotted vs. depth.

more scattered than measurements in index Zones 1 and 3. Porosity ranges from 30.4% to 80.3%, water content ranges from 14.0% to 63.7%, and bulk density ranges from 1.83 to 2.92 Mg/m³. Index Zone 3 (625.7–702.0 mbsf) is a similar interval, which is composed of basaltic breccia and coarse-grained volcanic sandstone. Porosity decreases sharply from 38.8% at 627.5 mbsf to 9.2% at 684.8 mbsf, and water content decreases within the same interval from 22.0% to 3.4%. Bulk density values are scattered in index Zone 3 and vary from 2.21 to 3.31 Mg/m³.

Sonic Velocity

Sonic velocities were measured using the PWL and the Hamilton Frame in Hole 832A. In Hole 832B, the PWL collected velocities down to 182.2 mbsf, while measurements were taken with the Hamilton Frame throughout the hole. Hamilton Frame velocities are listed in Table 9, and the variation in velocity with depth for Hamilton Frame is shown in Figure 50. The discussion concerning the velocities at Site 832 focuses on Hamilton Frame data since PWL data was collected only down to 182.2 mbsf, and since this data agrees well with Hamilton Frame data within the measured interval.

At Site 832, vertical velocity ranges from 1502 to 5282 m/s and horizontal velocity ranges from 1522 to 5337 m/s. The velocity data generally divides into three zones, which correlate with the index zones and the lithostratigraphic units as discussed above in "Index Properties" (this section). The vertical and horizontal

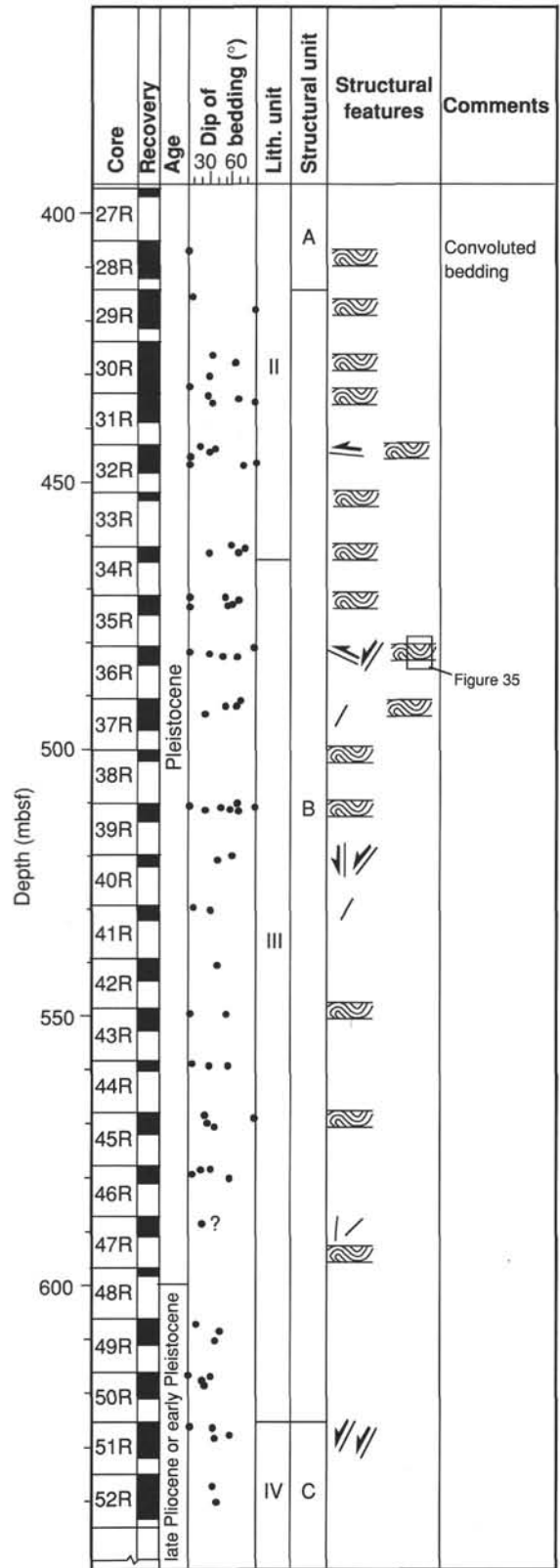
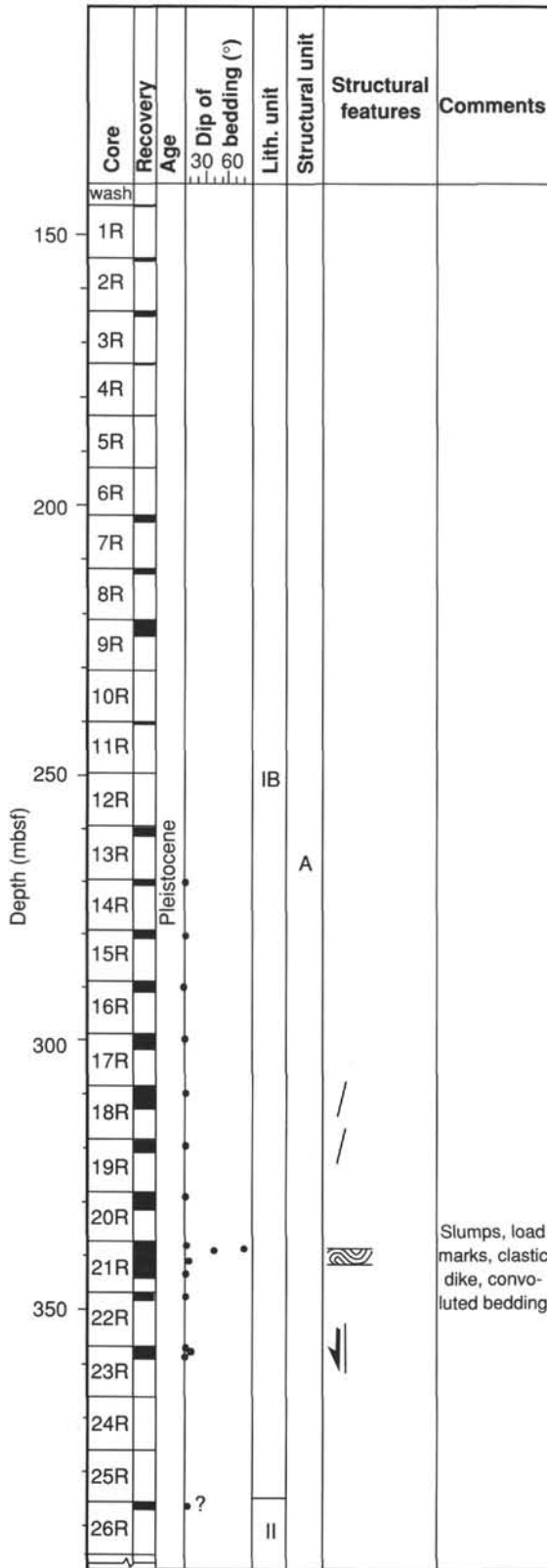


Figure 34. Structural log of Hole 832B. Hole 832A (0–216 mbsf) is not shown because no identifiable structures were observed.

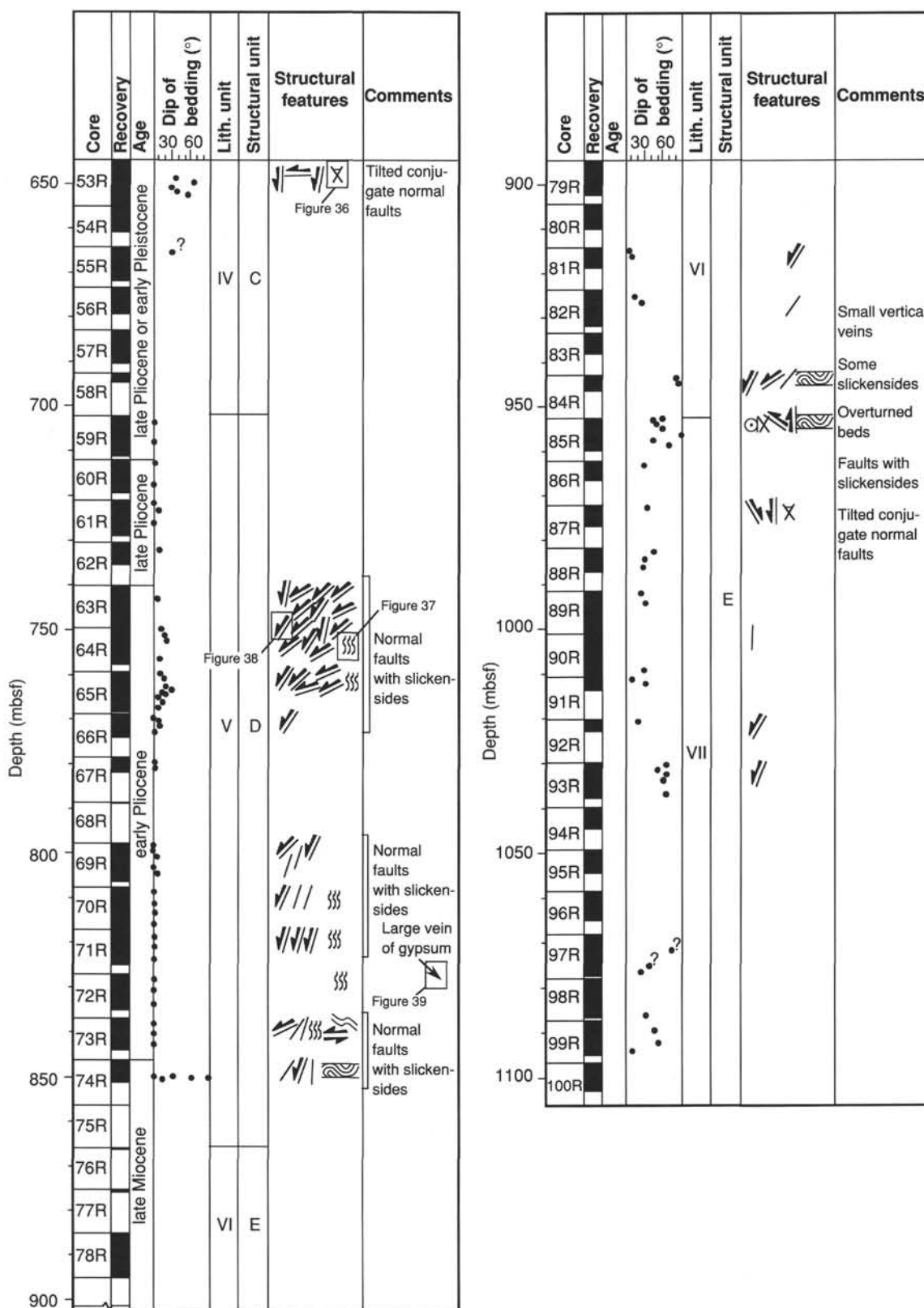


Figure 34 (continued).

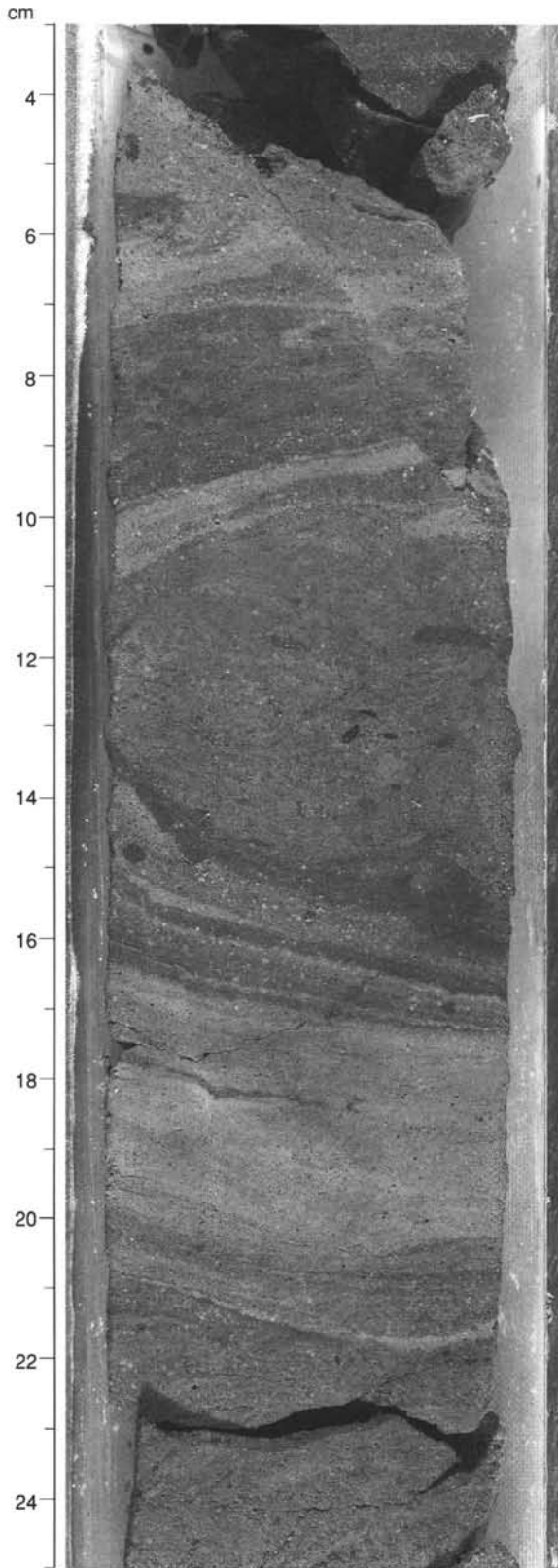


Figure 35. Photograph of a slump fold observed in interval 134-832B-36R-2, 3–25 cm. The location is indicated in Figure 34.

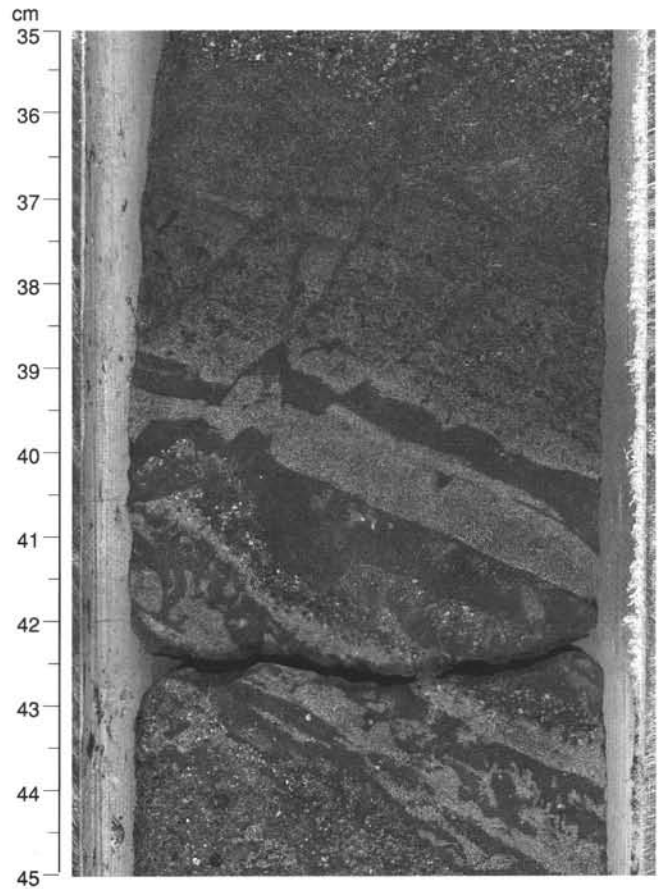


Figure 36. Photograph of tilted conjugate normal faults observed in interval 134-832B-53R-4, 35–45 cm. The location is indicated in Figure 34.

velocities are essentially isotropic at Site 832; therefore, only vertical velocity values are discussed.

The vertical velocity steadily increases within velocity index Zone 1 from 1510 m/s at 5.3 mbsf to 3608 m/s at 1090.0 mbsf. A subzone exists within Zone 1 in which vertical velocity increases from 2395 to 2701 m/s between 473.7 and 620.6 mbsf (index Zone 1/lithostratigraphic Unit III). The velocities in this subzone of mixed volcanic and calcareous rocks increase at the same rate as in the rest of Zone 1, but the velocities are generally higher. In velocity zone 2, vertical velocities increase sharply and are scattered. The velocity values range from 1738 to 3364 m/s and probably reflect varying lithology of volcanic clay, silt, sand, and matrix of sed-lithic breccia. One extreme value for Site 832 of 5082 m/s was measured in a breccia layer at 434.5 mbsf, and this value may be the velocity of a breccia clast. Most velocity values (15 of 17) in velocity Zone 3 range from 3440 to 4757 m/s and correlate with the coarse-grained sandstone and matrix of breccia of lithostratigraphic Unit IV (625.7–702.0 mbsf). Two high values, 5282 m/s and 4882 m/s, at 660.0 and 684.8 mbsf, may also be the velocities of breccia clasts.

Shear Strength

Shear strength data for Site 832 are listed in Table 10. Shear-strength measurements were made only in the unconsolidated volcanic silt of lithostratigraphic Unit I. Data within the measured interval (0–260.5 mbsf) are steady but scattered. The values were low, reflecting the unconsolidated nature of

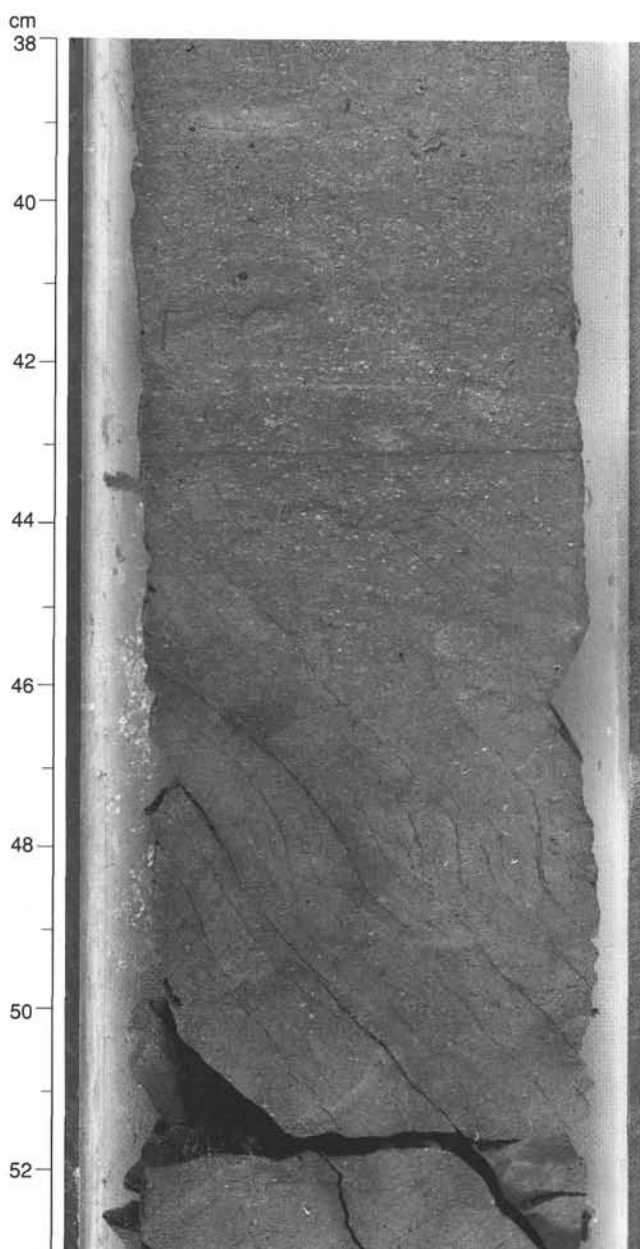


Figure 37. Photograph of an array of sigmoidal tension gashes observed in interval 134-832B-64R-1, 38–53 cm. The location is indicated in Figure 34.

numerous wet ash layers, and varied from 12.5 to 73.3 kPa (Fig. 52), an average of about 50 kPa.

Thermal Conductivity

At Site 832 thermal conductivity was measured to a depth of 181.5 mbsf in Hole 832A using the soft sediment “full-space method,” and from 642.8 to 1071.5 mbsf in Hole 832B using the hard-rock “half-space method.” Details of these thermal conductivity measurement procedures are given in the “Explanatory Notes” chapter (this volume). No thermal conductivity measurements could be completed from 181.5 to 642.8 mbsf because the state of lithification of the cores in that interval fell between the capabilities of both measurement methods.

From 0 to 181.5 mbsf in Hole 832A, thermal conductivity values hovered around 0.9 W/(m · K), ranging from 0.75 to

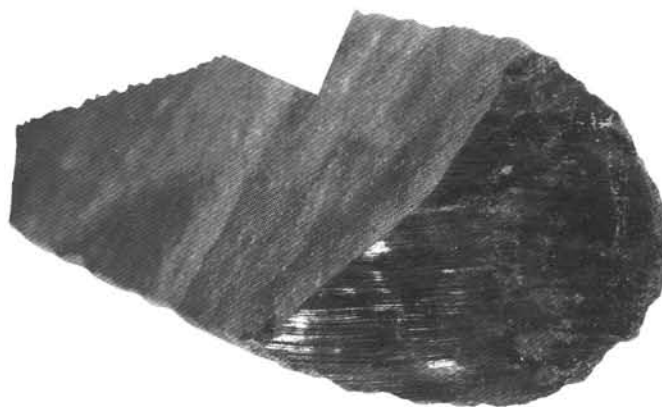


Figure 38. Photograph of a fault surface with slickensides indicating a normal sense of movement along the fault. The structure was observed in interval 134-832B-64R-2, 105–110 cm. The location is indicated in Figure 34.

1.13 W/(m · K) (Table 11). These relatively low thermal conductivity values are consistent with the wet, unconsolidated nature of the sediments from 0 to 200 mbsf, as indicated by other physical properties data (Fig. 50). The highest thermal conductivity value was recorded in the interval from 600 to 800 mbsf, where most values are above 1.20 W/(m · K) (Fig. 53). These data points also correlate with other physical properties in that interval, corresponding to sharp decreases in water content and sharp increases in bulk density and velocity in the basaltic breccia of lithostratigraphic Unit IV. A pore-water sample taken in this interval (627.0 mbsf) provided absolutely no fluid, although it was squeezed for several hours at high pressure (see “Sediment and Fluid Geochemistry” section, this chapter).

Summary

Physical properties at Site 832 varied only slightly from the mudline to below 300 mbsf in sediments which consisted largely of unconsolidated silty ash. This is probably the result of the extremely rapid sedimentation rate at this site during the Pleistocene (see “Sediment Accumulation Rates” section, this chapter) associated with rapid tectonic subsidence of the Aoba Basin. Porosity and water content have high values, consistently the highest in the upper section of any of the seven sites drilled on Leg 134. From 300 mbsf downward, porosity and water content decrease slowly but continued to have relatively high values. Bulk density displays a similar trend over the total depth of the hole. A sharp decrease in porosity and water content and concomitant increase in bulk density at the top of lithostratigraphic Unit IV (625.7 mbsf) is associated with well-cemented sandstones and breccia within this unit. Maximum sonic velocities for Site 832 are also measured within this interval. A similar but less obvious trend occurs in lithostratigraphic Unit II (385.6–461.5 mbsf), suggesting that Unit II, which also consists of sandstone and breccia, may be a less mature version of Unit IV.

DOWNHOLE MEASUREMENTS

Logging Operations

Logging operations in Hole 832B began at 1430 local time (L) on 30 November 1990 after several wiper trips down to the total hole depth of 1107 mbsf. A solid bridge that barred the hole at 890 mbsf had to be cleared, and to prevent hole



Figure 39. Photograph of a large gypsum vein, observed in interval 134-832B-71R-2, 53–73 cm. The location is indicated in Figure 34.

collapse, the bottom of the drill pipe remained at 907 mbsf for the first logging effort. The 1087–907 mbsf depth interval was logged with the geophysical tool string: long-spaced sonic, lithodensity, natural gamma-ray spectrometry, dual induction resistivity, and the Lamont temperature probe.

After this initial logging run, the drill pipe stuck for a short time and a strong backflow of water jeopardized logging of the entire hole, so the end of the drill pipe was positioned at 250 mbsf to stabilize the borehole wall. However, after another wiper trip to clear the hole to 1107 mbsf, the drill pipe stuck fast with its end at 277 mbsf, where it remained for the duration of the logging. The second logging run also used the geophysical tool string and logged the 939–277 mbsf depth interval. The data from the two logging runs correlate well in the zone of overlap. Because of the hole problems, the second logging run was done without the lithodensity tool, which contains a radioactive source, so no bulk density data is available above 907 mbsf.

The formation microscanner, combined with natural gamma-ray spectrometry and Lamont temperature probe, was used during the third logging run. The log was run for 1088–591 mbsf, where problems were encountered. After the logging runs were finished, it became apparent that part of the bit release mechanism had fallen down around the logging cable. We were fortunate that the tool string was not lost.

The susceptibility tool was lowered but it failed to exit from the bottom of the drill pipe, and to avoid damaging or losing this tool, logging operations ceased at 2300 L on 1 December 1990 after 32.5 hr. Logs obtained in Hole 832B are of good quality, as shown in the Log Summary at the end of this chapter.

Comparison of Well-Log Data to Core Lithology

In this section the well-log data (see Log Summary) are compared to the lithostratigraphy. Well-log data were collected only below 277 mbsf, beginning within lithostratigraphic Unit I (0–385.6 mbsf), which includes Pleistocene volcanic sand, silt, and clay. The shapes of the well-log curves in the lower part of Unit I are indistinguishable from those in lithostratigraphic Unit II (385.6–461.5 mbsf). Unit II also consists of Pleistocene volcanic sand, silt, and clay but contains an increasing amount of calcareous material downhole. The signature of the resistivity log over Units I and II includes sharp peaks that reveal alternating high and low resistivity beds. The high resistivity beds also tend to have relatively high velocity values (low transit times) and low gamma-ray readings. The gamma-ray log shows a gradual, linear decrease downward across the upper two units; this gamma-ray decrease may result from the increased calcareous content in Unit II.

The shapes of well-log curves over lithostratigraphic Units I and II contrast with those from the underlying Unit III (461.5–625.7 mbsf), which includes Pliocene(?) and Pleistocene chinks, limestones, and calcareous volcanic sandstones, siltstones, and breccias. Throughout Unit III the resistivity log shows generally low values with subdued peaks that are much lower than those of the overlying Unit II. The sonic log shows less variation than it does over Units I and II. The gamma-ray log decreases gradually in Unit III, reaching a minimum value at about 600 mbsf, and then the values increase gradually, indicating a greater clay content downward toward the underlying breccia of Unit IV.

Unit IV (625.7–702.0 mbsf) is an upper Pliocene and Pleistocene basalt breccia, having a transitional upper contact through which the grain size increases gradually. The resistivity- and sonic-log readings support the concept of a transitional upper contact, in that both logs increase over the depth

interval 620–642 mbsf. The lower part of the basaltic breccia has the highest resistivities and velocities of any rocks penetrated at Site 832. The lower contact with the limestone of lithostratigraphic Unit V is abrupt in all logs, for over a short depth interval (2 to 3 m), resistivity decreases to some of the lowest values obtained at this site, and the velocity and gamma-ray logs drop precipitously. The large decrease in the sonic log should produce a strong reflection, and such a reflection is evident in the multichannel seismic data but not in single-channel data. This discontinuity in logs correlates with an angular unconformity evident on seismic sections (see “Seismic Stratigraphy” section, this chapter).

Upper Miocene and Pliocene limestone of Unit V (702.0–865.7) underlies the basaltic breccia of Unit IV. Log readings over the limestone are subdued, and in this respect are similar to readings over the calcareous rocks of Unit III. The gamma-ray log increases gradually with depth through Unit V, indicating progressively more clay, and this increase parallels a gradually increasing rock resistivity. From core descriptions, the base of this limestone has been placed at 865.7 mbsf, within an interval of little to no core recovery. A large discontinuity in the resistivity log and a small one in the sonic log occur deeper, at about 887 mbsf, where core recovery increases dramatically.

Unit VI (865.7–952.6 mbsf) is a possibly middle Miocene volcanic sandstone. The unit is distinguished from the overlying one on the basis of a much higher resistivity and a slightly higher velocity. The bottom of this unit is marked in log readings by a very low-resistivity, low-velocity interval that is about 7 m thick. Bulk density also drops dramatically in this interval while the caliper indicates a much smaller hole diameter.

Unit VII (952.6–1106.7 mbsf) is a possibly lower Miocene basaltic breccia. Sonic-log values from this unit differ little from readings obtained from the lower part of Unit VI, but both sonic and resistivity and bulk density logs increase suddenly deep within this unit, at 1042 mbsf. This abrupt increase corresponds to the presence of basaltic breccia and volcanic sandstones (see core description forms near the back of this volume). The increased density and sonic velocity is also observed in measurements on core samples (see “Physical Properties” section, this chapter).

FMS Logging

FMS data were recorded at Hole 832B between 630 and 1090 mbsf. Difficulty in moving the tool when it was above 630 mbsf resulted in a decision to make only one logging pass. Except in a few depth zones (782–785 mbsf, 865–870 mbsf, and 950–955 mbsf), the small diameter of the hole (between 10 and 14 in.) provided good contact between the pads and the borehole wall, and excellent data were obtained. FMS data were processed aboard the *JOIDES Resolution*, and the processed data are presented on microfiche at the back of this volume. Data processing available aboard ship includes the automatic computation of dip and dip azimuth of planar features—mainly bedding, faults, fractures, and veins—that intersect the borehole. The dip and dip azimuth of steeply dipping features (more than 60°) had to be measured by hand on the images and are therefore imprecise.

Faults, fractures, and bedding planes are described below (see summary in Fig. 54) from FMS images and compared to observations reported from core descriptions (see “Structural Studies” section, this chapter). The shallowest usable FMS data were collected at 630 mbsf, within lithostratigraphic Unit IV, which is composed of basaltic breccia and interbeds of volcanic sandstone. The FMS image of the basaltic breccia exhibits high contrast between small, irregular resistive fea-

tures that are embedded within a more conductive matrix. Sequences of volcanic sandstone or siltstone produce images having less contrast and finely laminated bedding. In lithostratigraphic Unit IV dips show no predominant value but range from 0° to 60°. In the sandstone sequences of this unit, vertical fractures (Fig. 55) parallel the borehole, perpendicular to the bedding. Those fractures are apparently drilling-induced fractures (Serra, 1989) which would not be present in cores. The fractures are observed in only one plane (i.e., for opposite pads of the FMS). Oblique fractures that dip from 70° to 85° are also evident in lithostratigraphic Unit IV at 674–676 mbsf, 694–700 mbsf, and 703–706 mbsf. These fractures are discontinuous, irregular, spaced apart by about 50 cm, and they have a constant orientation (Fig. 56). Like vertical fractures, oblique fractures are evident on opposite sides of the borehole, but the two types of fractures do not appear within the same depth intervals.

Lithostratigraphic Unit V (702–865.7 mbsf) consists of foraminiferal limestone with layers of volcanic siltstone and vitric ash. The FMS images indicate that these rocks are very finely laminated and show clearly that bedding planes are generally horizontal or dip slightly at 10° to 20° with a dip azimuth of 100–130°. Sequences of more resistive siltstones and vitric ashes contrast with the more conductive limestones. Highly conductive faults that cross the borehole in the interval between 742 and 774 mbsf dip 50° to 60° and dip azimuthally 340° to 10° (Fig. 57). Where faults are present, observations from both cores (see “Structural Studies” section, this chapter) and FMS data indicate a slight increase in the dip of bedding planes, from 0°–5° to 10°–20°. Faults in the interval from 608 to 821 mbsf are thick (10–15 cm) and have a dip azimuth of 150°.

Lithostratigraphic Unit VI, a basaltic breccia with volcanic sandstone, begins at 853 mbsf and is marked by alternating pebbly beds and fine laminations. In the volcanic sandstones, the beds dip 10° to 40° and have a dip azimuth of 50° to 100° (Fig. 58).

The transition between lithostratigraphic Unit VI and VII is apparent in FMS images from between 948 and 953 mbsf by a sudden increase in the hole diameter from about 30 cm to more than 40 cm over a depth interval of less than 20 cm. The increased hole diameter renders FMS data much less useful since the pads are often not in contact with the borehole wall. FMS images of lithostratigraphic Unit VII are generally similar to those of Unit VI, except that the bedding planes in the volcanic siltstone of Unit VII, which appear to be more steeply inclined (30°–70°; Fig. 59) than are those of Unit VI (less than 40°).

Vertical drilling-induced fractures are present in breccia and volcanic sandstones in the bottom part of lithostratigraphic Unit VI, as well as in Unit VII. The fracture orientation is consistent in Units IV, VI, and VII (Fig. 54). The direction of the principal stress, parallel to the direction of the vertical fractures, ranges from 50° to 80°. Few oblique fractures are evident in these units (Fig. 54), and their interpretation is less obvious than for the vertical fractures. The oblique ones may be fractures enhanced by drilling (Serra, 1989); if so, they would parallel the direction of the principal stress. The dip azimuth of oblique fractures is locally constant at 10°–30° in the lower part of Unit IV, at 130°–150° in Unit VI, and at 320°–360° in Unit VII (Fig. 54), but these orientations do not agree with those of the vertical fractures.

Heat Flow

Eight runs of the water sampler temperature probe (WSTP) temperature tool were performed at Site 832, only three of which were successful. This low rate of success was due to the

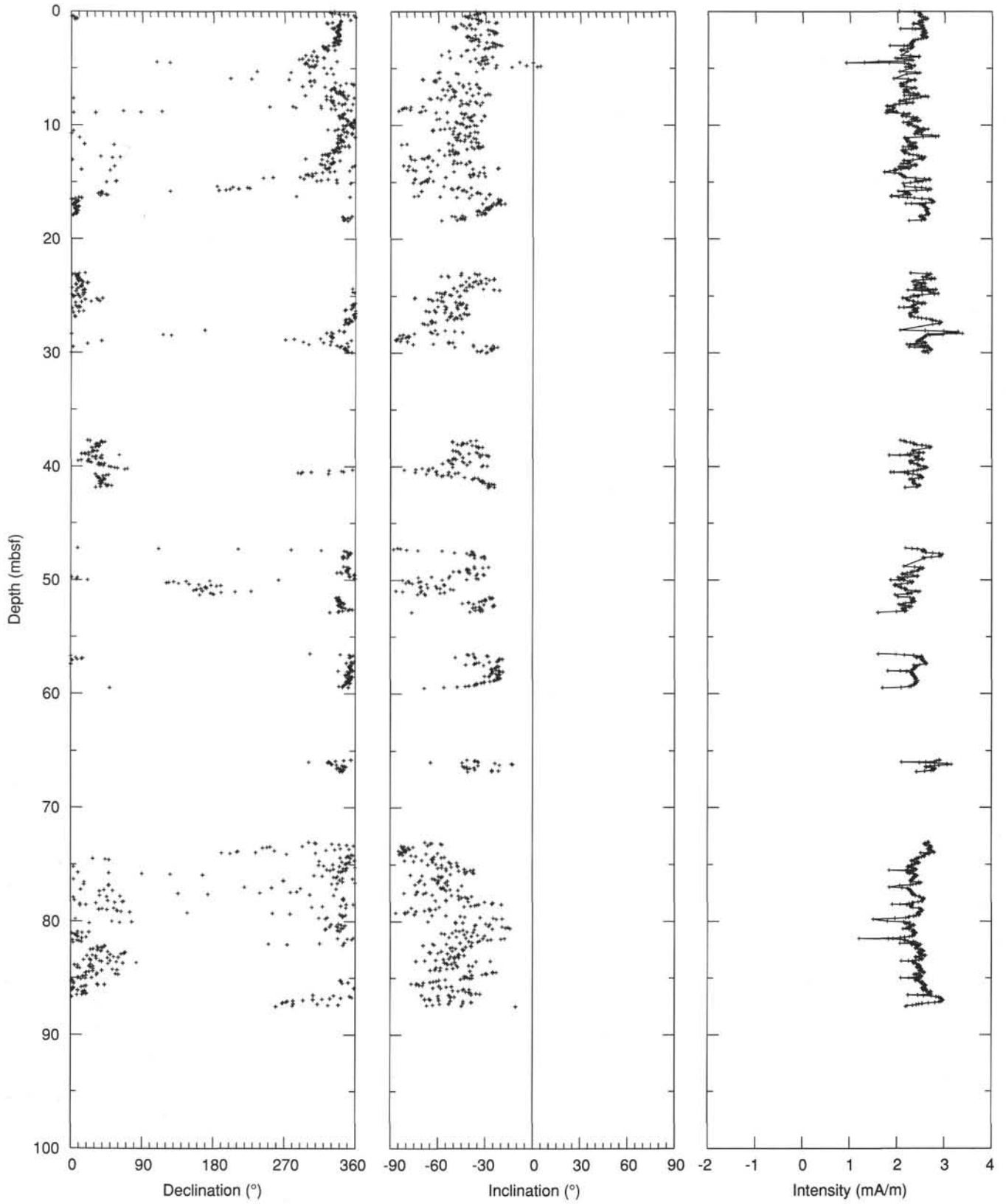


Figure 40. Depth plot of stable magnetization (after AF demagnetization at 10 mT) for cores in Hole 832A.

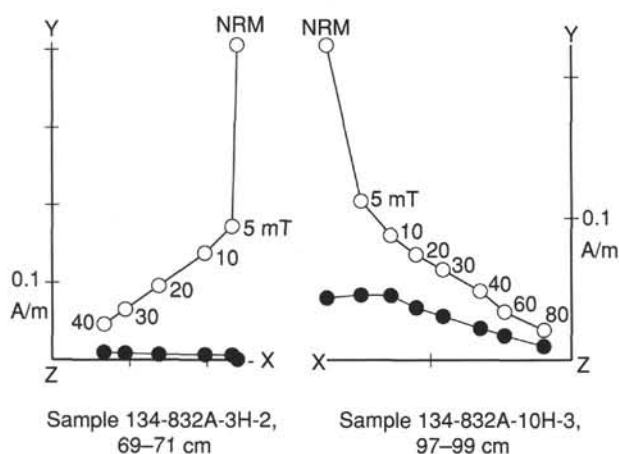


Figure 41. Representative orthogonal demagnetization plots of discrete samples from APC cores in Hole 832A. Open circles represent vector endpoints projected onto the vertical plane; solid circles, endpoints projected onto the horizontal plane. NRM = natural remanent magnetization.

presence of extensive ash layers in the sediments, which prevented the probe from being properly inserted into the sediment below the drill bit. The data reduction techniques used at this site were the same as those used at other Leg 134 sites. The thermal conductivity values are given in the "Physical Properties" section (this chapter) (Table 11 and Fig. 53).

Run 4H in Hole 832A (18.5 mbsf; Fig. 60) was successful, and its reduction to equilibrium temperature is plotted in Figure 61. Run 7H in Hole 832A (Fig. 62) at a depth of 47.0 mbsf was unsuccessful as the probe did not fully penetrate the sediment. Run 20H in Hole 832A (Fig. 63) at a depth of 145.0 mbsf was also unsuccessful; the probe was pulled out of the sediment just after penetration. Run 27X in Hole 832A (Fig. 64) at a depth of 196.7 mbsf was unsuccessful because again the probe did not fully penetrate the sediment. Run 28X in Hole 832A (215.9 mbsf; Fig. 65) was successful. However, the probe was slowly raised upward after only a few minutes in the bottom, so only the beginning of the penetration record is used to calculate the equilibrium temperature (Fig. 66). Run 4R in Hole 832B (Fig. 67) at 173.3 mbsf was successful with no disturbance. The reduction to equilibrium temperature is given in Figure 68. Run 10R in Hole 832B (Fig. 69) at 231.0 mbsf was unsuccessful, as the probe hit a hard ash layer and did not fully penetrate the bottom. The final temperature run, 19R in Hole 832B (318.1 mbsf; Fig. 70), struck an extremely hard layer. Frictional heating from penetration increased the probe temperature to 56°C, and invalidates some of the assumptions used in the 1/time approximation of the temperature probe decay curve (Fig. 71), resulting in an invalid estimated equilibrium temperature. More detailed numerical analysis may determine a valid equilibrium temperature for this measurement.

The three valid sub-bottom temperature measurements and the seafloor water temperature are plotted vs. the integrated thermal resistivity in Figure 72. The surficial heat flow at this site is 41.8 mW/m², higher than was expected for the intra-arc basin sites. The high sedimentation rate in the North Aoba Basin will reduce the surficial heat flow such that it is less than the heat flow at depth. The exact amount that the heat flow is reduced depends not only on the sedimentation rate but also upon the duration of the sedimentation. An idea of the amount that the heat flow is reduced is given by the calculations of Hobart and Weissel

(1987) for sedimentation in the New Georgia Sound basin of the Solomon Islands. If the thermal diffusivity of the sediment is taken as 10⁻⁶ m²/s, a typical value, then 1 km of sediment deposited uniformly over 1 m.y. would depress the surficial heat flow by 19% and the heat flow at depth is 1.23 times the value at the surface. If this rate continues for 5 m.y. (i.e., 5 km in 5 m.y.), then the surficial heat flow would be depressed by 38% and the value at depth would be 1.61 times the surface value. Basement temperatures as a function of time may also be calculated once a sedimentation rate history has been determined.

SUMMARY AND CONCLUSIONS

Site 832 is located at 14°47.78'S, 167°34.35'E in water depth of 3089.3 mbsl. This site is located on the flat intra-arc North Aoba Basin (NAB) floor, approximately 50 km northeast of the Queiros Peninsula of Espiritu Santo Island and 45 km due south of the active volcanic island of Santa Maria. The NAB is surrounded by several islands, including the uplifted horst block islands of Maewo and Espiritu Santo and the active or recently active volcanoes of Aoba, Mere Lava, and Santa Maria.

Two holes were drilled at Site 832. Hole 832A was drilled and cored to 215.9 mbsf and recovered 146.26 m of core for a recovery rate of 67.7%. Hole 832B was washed down to 144.4 mbsf, then drilled to a total depth (TD) of 1106.7 mbsf, and cored 962.3 m, from which 450.95 m of core were recovered for a recovery rate of 46.9%.

Seven lithostratigraphic units were identified in the cores obtained at Site 832 (Fig. 73). Lithostratigraphic Unit I (0–206.2 mbsf in Hole 832A and 144.4–385.6 mbsf in Hole 832B) is a 385.6-m-thick Pleistocene sequence of sandy to clayey volcanic silts with interbedded volcanic ash layers. This unit is divided into two subunits. Lithostratigraphic Subunit IA (0–141.0, Hole 832A) is a 141.0-m-thick Pleistocene sequence of coarse-grained vitric volcanic ash layers with sandy to clayey volcanic silt interbed. The subunit is very soupy and contains volcanic lapilli, pumice clasts, and gravel-sized corals and wood fragments. Subunit IB (141.0–385.6 mbsf) is a 244.6-m-thick Pleistocene sequence of silty volcanic clay to clayey volcanic silts with foraminiferal and calcareous nannofossils. Below 281 mbsf lithification occurs within the claystones and siltstones, and partial lithification occurs in the fine vitric volcanic ash, with substantially more carbonate components below 285 mbsf.

Lithostratigraphic Unit II (385.6–461.5 mbsf) is a 75.9-m-thick Pleistocene sandstone, siltstone, and claystone sequence with substantial volcanic material in the upper burrowed part and significantly more carbonate material near the lowermost of the unit. The bottom 50 cm contain sed-igneous (basaltic) breccia. Lithostratigraphic Unit III (461.5–625.7 mbsf) is a 164.2-m-thick Pleistocene highly calcareous sequence composed of 40% chalks, limestones, and calcareous mixed sediments, with the remaining 60% composed of volcanic sandstones, siltstones, and breccias. The bottom of the unit is late Pliocene or early Pleistocene in age. Lithostratigraphic Unit IV (625.7–702.0 mbsf) is a 76.3-m-thick lower Pleistocene or upper Pliocene(?) breccia that is composed of about 60% lithified basaltic breccia which also contains limestone and coral clasts in a sandstone matrix and 40% volcanic sandstone and siltstone. Lithostratigraphic Unit V (702–865.7 mbsf) is a 163.7-m-thick upper Miocene to upper Pliocene limestone comprised of layers of foraminiferal, nannofossil, calcareous, or silty limestone with occasional layers of vitric ash. Intense bioturbation is common and some wood is present. A sharp upper contact occurs with the overlying Unit IV and a basal breccia occurs which contains a few neritic carbonate fragments overlying clayey volcanic siltstone.

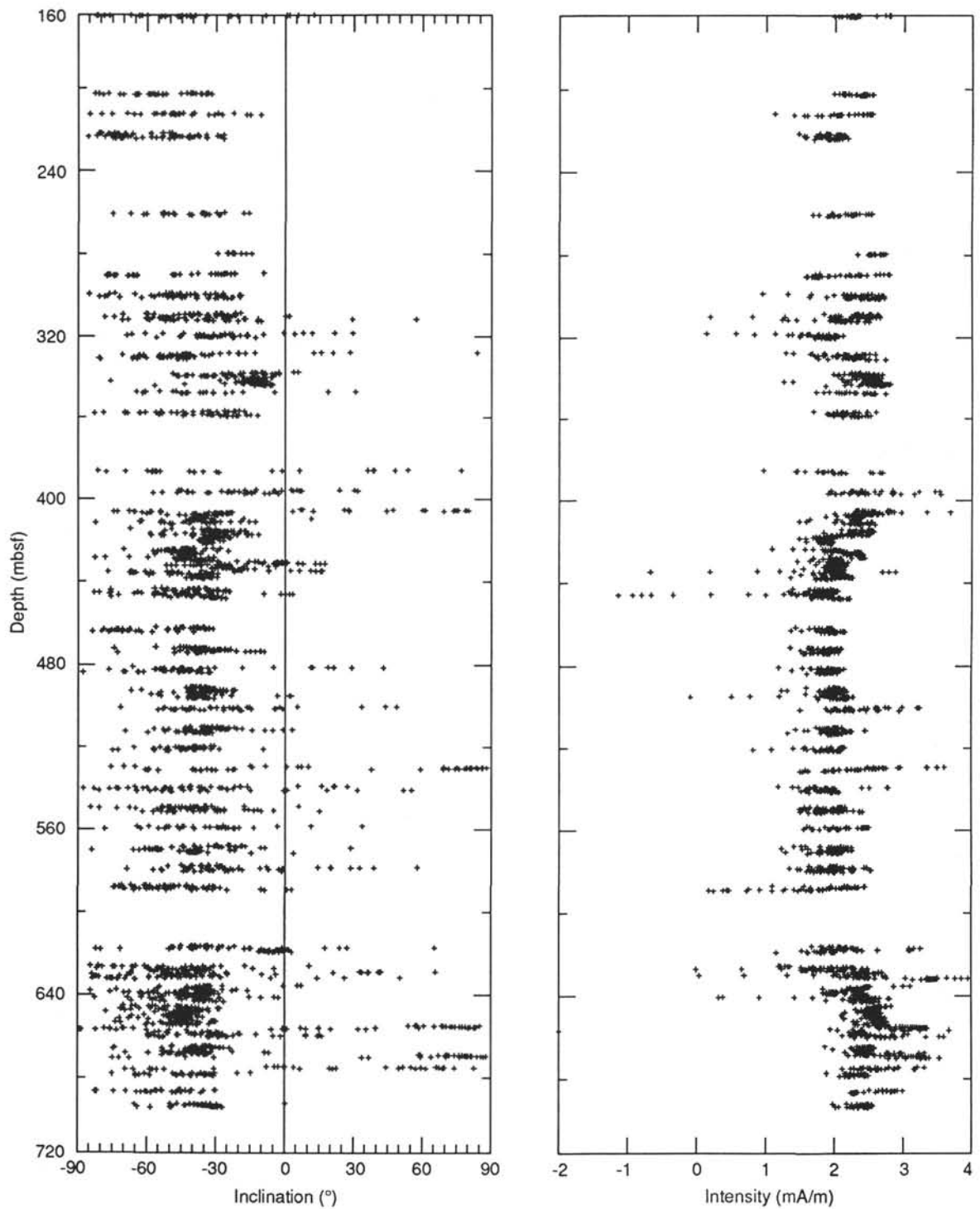


Figure 42. Variation of inclination and intensity after demagnetization at 10 mT with depth (from 160 to 720 mbsf) in Hole 832B.

Lithostratigraphic Unit VI (865.7–952.6 mbsf) is an 86.9-m-thick middle to upper(?) Miocene lithified volcanic sandstone that becomes coarser-grained from top to bottom and has graded beds. Rare pyrite occurs. Lithostratigraphic Unit VII (952.6–1106.7 mbsf) is a 154.1-m-thick breccia composed of 60% lithified basaltic breccia and 40% lithified volcanic sandstone and siltstone, which contains neritic calcareous grains, including corals, algae fragments, large foraminifers, and

occasional basaltic scoriae. The top of this Unit is early to middle Miocene in age.

Foraminifers and nannofossils were the best source of age information. Ages determined range from Pleistocene or Holocene to latest early Miocene(?), with the foraminifers giving the first indication of earliest middle Miocene fauna at 954.4 mbsf and a latest early Miocene fauna at 971.8 mbsf. Biostratigraphic ages range as follows: late Pleistocene to Holocene, 0–308.4

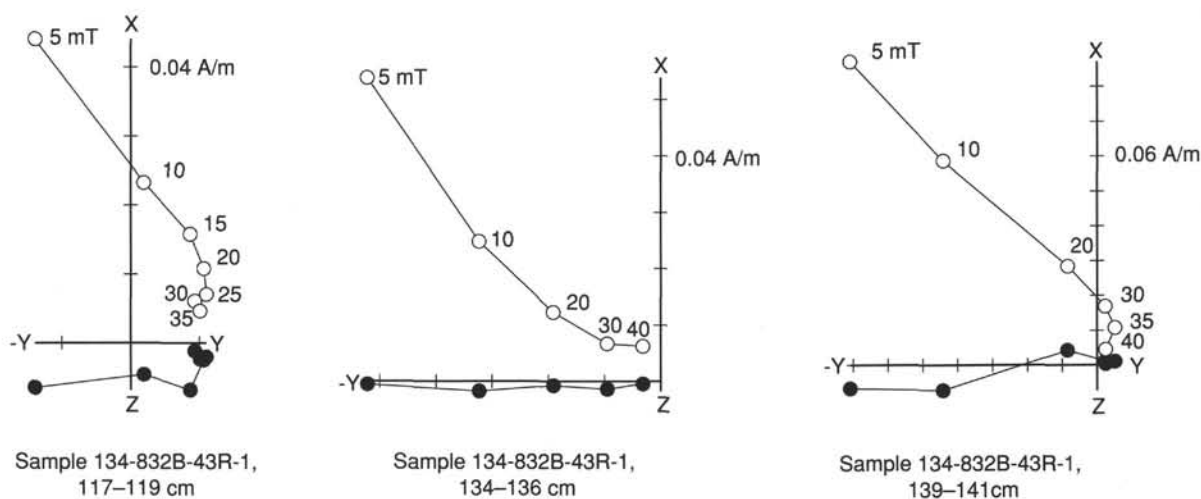


Figure 43. Representative orthogonal demagnetization plots of discrete samples from Core 134-832B-43R. Open circles represent vector endpoints projected onto the vertical plane; solid circles, endpoints projected onto the horizontal plane.

mbsf; early Pleistocene, 308.4–600 mbsf; late Pliocene or early Pleistocene, 600–711 mbsf; late Pliocene, 711–768.8 mbsf; early Pliocene, 768.8–817.4 mbsf; possible late Miocene, 817.4–856.1 mbsf; and middle to early Miocene, 924–972 mbsf. Benthic foraminifers indicate a depositional environment of lower bathyal for most all the sediments found at Site 832.

Biostratigraphic analyses were used to estimate the sediment accumulation rate for the deposits cored at Site 832. Generally, a sediment accumulation rate of 286 m/m.y. or greater was estimated for the interval of 0–711 mbsf. At 711 mbsf a major change in sedimentation rate appears to have occurred with the sediments beneath this level (711–875 mbsf) having been deposited at less than 100 m/m.y., as supported by the presence of hemipelagic sediments.

More than 10 volcanic ash layers greater than 10 cm thick and several tens of reworked volcanic ash layers were recovered at Site 832. Chemistry of these ashes suggests that they have a related origin from a fairly potassic parental magma. These ashes share a common chemistry with the volcanic rocks of Santa Maria Island and are most likely derived from there. Fragments of clinopyroxene-phyric basalt or ankaramite were found in the cores between 395 and 1100 mbsf and show vesicular texture and little oxidation, indicating that they underwent little weathering or seawater alteration before burial. Clinopyroxene-phyric basalts recovered from breccias within lithostratigraphic Units II, III, and IV may have been derived from either Aoba or Maewo islands. Lavas recovered from the lower part of lithostratigraphic Unit VII appear to have resulted from submarine volcanism and contained orthopyroxene phenocrysts, which suggests that these rocks were derived from Maewo or Espiritu Santo islands. Generally, these volcanic rocks varied in composition with depth, with the upper Pliocene rocks being of MORB-like or IAT composition and the upper Miocene rocks being calc-alkaline; however, a stratigraphic inversion may have resulted from reworking.

In addition to the lithostratigraphic units, four structural units were identified on the basis of deformation observed in the sedimentary rocks. Structural Unit A (0–415 mbsf) corresponds to lithostratigraphic Unit I and the upper part of Unit II and is relatively (relative to the other structural units) devoid of deformation structures, with the exception of a few isolated vertical or steeply inclined beds that appear to be slump induced. Structural Unit B (415–626 mbsf), corre-

sponding to the lower part of lithostratigraphic Unit II and all of Unit III, shows extreme variations in dip angles of bedding with good examples of slump fold hinges; abundant slump structures are present. Structural Unit C (626–702 mbsf) corresponds to lithostratigraphic Unit IV and exhibits bedding planes with a 30°–65° dip with flat shear planes that suggest downslope sediment creep; normal faulting appears to have occurred before tilting. Structural Unit D (702–866 mbsf), corresponding to lithostratigraphic Unit V, is defined on the basis of abundant microfaults with 30°–50° dips and slickensides, especially concentrated at interval 740–769 mbsf, and slump structure illustrated by tension gash arrays and horizontal bedding that defines the base of slumps. Bedding-parallel extension appears to have occurred in this unit. Structural Unit E (866–1107 mbsf) corresponds to lithostratigraphic Units VI and VII and shows poorly defined bedding, which presently dips 20°–40° and are considerably differently oriented than the beds of the overlying structural unit. Locally, bedding is vertical or overturned, resulting from slumping, and reverse and left-lateral strike-slip microfaults are present. At the base of structural Unit E tilted conjugate normal microfaults indicate that the sedimentary rocks at this level were normally faulted before tilting.

Analyses made of the pore fluids at Site 832 indicate that the concentration gradients of sodium, potassium, calcium, and magnesium have extraordinary variations below 280 mbsf. Above 250 mbsf the maxima of ammonia, phosphate, alkalinity, and methane concentrations appear to relate to bacterially mediated, coupled oxidation of organic matter and reduction of sulfate. In the deeper parts of the drilled sequence, below 280 mbsf, sulfate concentrations are high; however, alkalinity, phosphate, and methane concentrations are low. Concentration of organic carbon is low (<0.5%) throughout the sequence. Diagenesis appears to be the result of oxidation of organic matter, precipitation of authigenic carbonate and phosphate minerals, and alteration of volcanogenic sediments. The cause of the intense diagenesis is not known, but may relate to the specific mineralogical or chemical composition of the volcanic materials that compose the central New Hebrides Island Arc. Pore fluids show no evidence of meteoric water flow from the surrounding islands. This lack of hydrologic flow implies that any hydrocarbons generated will not be flushed from the sediments, but the low organic carbon contents suggest that the sedimentary rocks penetrated may

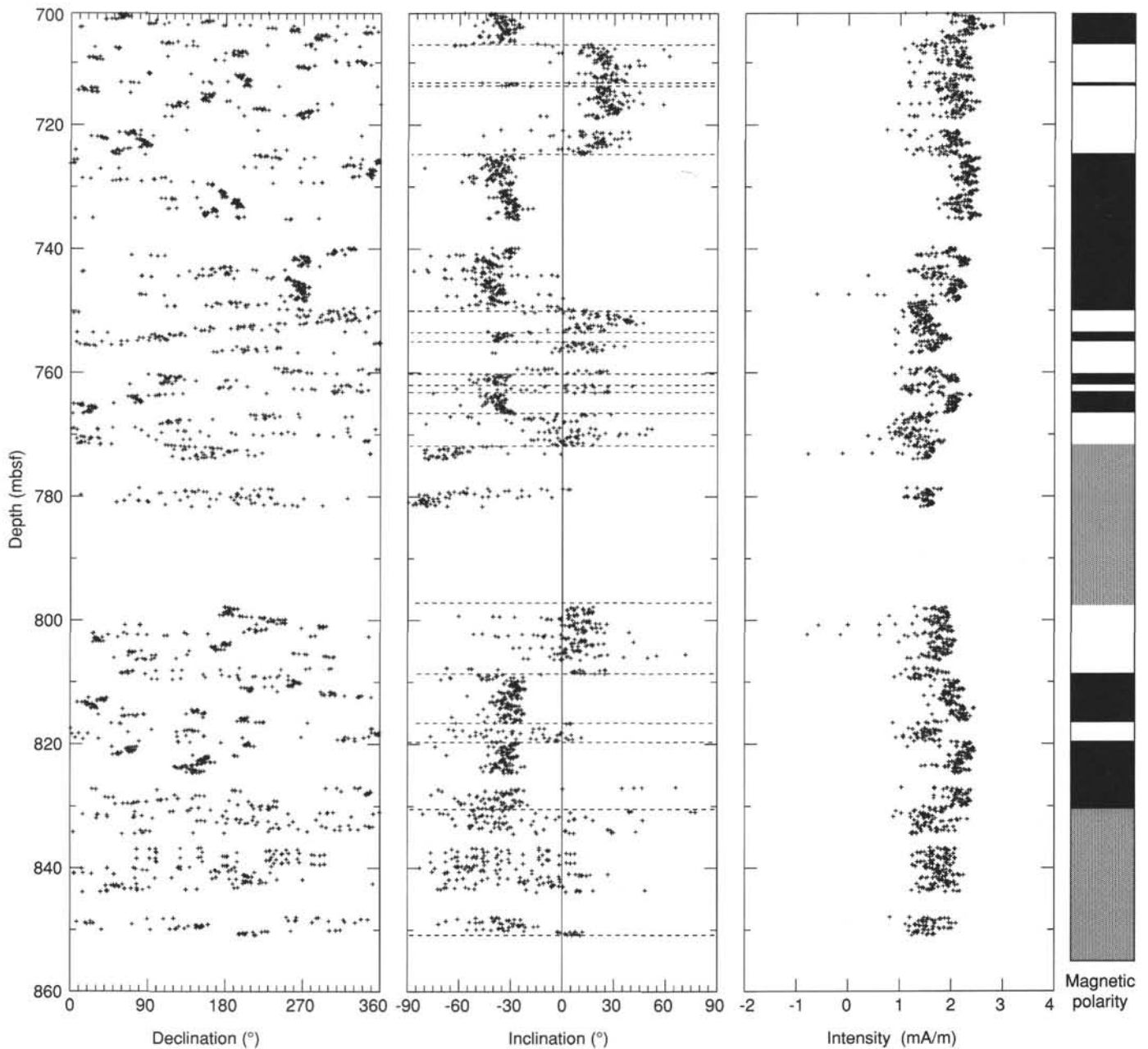


Figure 44. Declination, inclination, intensity, and magnetic polarity after demagnetization at 10 mT plotted against depth (from 700 to 860 mbsf) in Hole 832B. Black indicates normal polarity; white, reversed polarity; and shaded area, uncertain polarity.

not contain large volumes of source material. At approximately 800 mbsf the organic carbon content is about 0.5 wt%.

Physical properties at Site 832 varied only slightly from the mudline to below 300 mbsf in sediments which consisted largely of unconsolidated silty ash. This is probably the result of the extremely rapid sedimentation rate at this site during the Pleistocene, associated with rapid tectonic subsidence of the Aoba Basin. Porosity and water content have high values, consistently the highest in the upper section of any of the seven sites drilled on Leg 134. From 300 mbsf downward, porosity and water content decrease slowly but continue to have relatively high values. Bulk density displays a similar trend over the total depth of the hole. A sharp decrease in porosity and water content and a concomitant increase in bulk density at the top of lithostratigraphic

Unit IV (625.7 mbsf) is associated with well-cemented sandstones and breccia in that unit.

Initial interpretations of the drilling results at Site 832 indicate that basin formation is the product of island-arc volcanism and tectonic deformation. The unconformity at about 700 mbsf appears to represent the time uplift of the central part of the Western Belt occurred in response to the collision of the DEZ. The existence of clayey foraminiferal and nannofossil limestones interbedded with ash and silty volcanic sandstones of lithostratigraphic Unit V beneath the unconformity suggests relatively (relative to the overlying unit) quiet water sediment deposition devoid of volcanic and terrestrially derived material. In contrast, the coarser-grained basaltic breccias of the overlying lithostratigraphic Unit IV

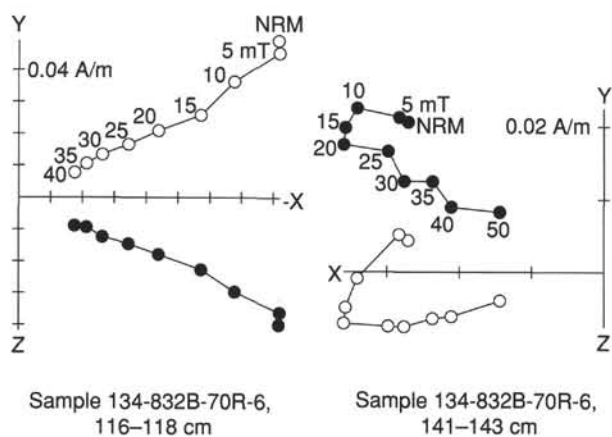


Figure 45. Representative vector endpoint diagrams showing the results of AF demagnetization of samples from Core 134-832B-70R. Open circles represent vector endpoints projected onto the vertical plane; solid circles represent endpoints projected onto the horizontal plane.

suggest uplift of a volcanic province close to Site 832 that supplied the breccia. Central Chain volcanoes, either Aoba or Santa Maria islands, are the likely source of these materials. Timing of the uplift and formation of the unconformity is not well constrained, but biostratigraphic analyses indicate that it appears to be close to the late Pliocene–early Pleistocene boundary. In contrast, the basaltic breccia encountered at the bottom of Hole 832A (lithostratigraphic Unit VII) appears to represent submarine eruptions associated with the volcanic formation of Espiritu Santo Island. The upper 385 mbsf (lithostratigraphic Unit I) represents recent (Pleistocene) basin filling from the effusive products of the Central Chain volcanoes, specifically from Aoba, Santa Maria, and Mere Lava islands. Structural analyses of the cores indicated that there have been several tectonic events that changed the inclination of the NAB's flanks, thereby dislodging sediments and forming slumps. These events appear to have been particularly active during the earliest middle Miocene, middle Miocene, late Miocene to early Pliocene, and latest early Pliocene to earliest late Pliocene. Many of the lithostratigraphic units identified at Site 832 can be correlated with the lithostratigraphic units of Site 833.

REFERENCES

Akimoto, K., 1990. Distribution of Recent benthic foraminiferal faunas in the Pacific off Southwest Japan and around Hachijojima Island. *Sci. Rep. Tohoku Univ.*, Ser. 2, 60:139–223.

Barsdell, M., Smith, I.E.M., and Sporli, K. B., 1982. The origin of reversed geochemical zoning in the Northern New Hebrides Volcanic Arc. *Contrib. Mineral. Petrol.*, 81:148–155.

Bellon, H., Marcelot, G., Lefevre, C., and Maillot, P., 1984. Le volcan de l'île d'Erromango (République de Vanuatu): calendrier de l'activité (données ^{40}K - ^{40}Ar). *C. R. Acad. Sci. Ser. 2*, 299:257–262.

Berggren, W. A., Kent, D. V., Flynn, J. J., and Van Couvering, J. A., 1985a. Cenozoic geochronology. *Geol. Soc. Am. Bull.*, 96:1407–1418.

Berggren, W. A., Kent, D. V., and Van Couvering, J. A., 1985b. The Neogene: Part 2. Neogene geochronology and chronostratigraphy. In Snelling, N. J. (Ed.), *The Chronology of the Geological Record*. *Geol. Soc. London Mem.*, 10:211–260.

Boltovskoy, E., and Wright, R., 1976. *Recent Foraminifera*: The Hague (W. Junk).

Briqueu, L., 1984. Etude du magmatisme associé aux zones de subduction à l'aide de traceurs géochimiques multiples: éléments traces et rapports isotopiques $^{87}\text{Sr}/^{86}\text{Sr}$ et $^{143}\text{Nd}/^{144}\text{Nd}$. [Thèse]. Univ. Montpellier, Documents et Travaux du Centre de Géologie et de Géophysique, No. 5.

Burns, R. E., Andrews, J. E., et al., 1973. *Init. Repts. DSDP*, 21: Washington (U.S. Govt. Printing Office).

Carmichael, I.S.E., Turner, F. J., and Verhoogen J., 1974. *Igneous Petrology*: New York (McGraw Hill).

Carney, J. N., 1986. *Geology of Maewo*. Regional Rept.—Vanuatu Dep. Geol., Mines and Rural Water Supplies.

Carney, J. N., and Macfarlane, A., 1977. Volcano-tectonic events and pre-Pliocene crustal extension in the New Hebrides. *Int. Symp. on Geodynamics in South-west Pacific, Noumea, New Caledonia, 1976*. Paris (Editions Technip), 91–104.

_____, 1978. Lower to middle Miocene sediments on Maewo, New Hebrides, and their relevance to the development of the Outer-Melanesian Arc system. *Australas. Soc. Explor. Geophys. Bull.* 9:123–130.

_____, 1980. A sedimentary basin in the central New Hebrides Arc. *Tech. Bull.—U. N. Econ. Soc. Comm. Asia Pac., Comm. Co-ord. Jt. Prospect Miner. Resour. South Pac. Offshore Areas*, 3:109–120.

_____, 1982. Geological evidence bearing on the Miocene to Recent structural evolution of the New Hebrides Arc. *Tectonophysics*, 87:147–175.

_____, 1985. Geology and mineralisation of the Cumberland Peninsula, north Espiritu Santo. *Vanuatu Dept. of Geol., Mines and Rural Water Suppl. Rep.*

Carney, J. N., Macfarlane, A., and Mallick, D.I.J., 1985. The Vanuatu island arc—an outline of the stratigraphy, structure, and petrology. In Nairn, A.E.M., Stehli, F. G., and Uyeda, S. (Eds.), *The Ocean Basins and Margins* (Vol. 7): New York (Plenum), 685–718.

Chase, C. G., 1971. Tectonic history of the Fiji Plateau. *Geol. Soc. Am. Bull.*, 82:3087–3110.

Chase, T. E., and Seekins, B. A., 1988. Submarine topography of the Vanuatu and southeastern Solomon Islands regions. In Greene, H. G., and Wong, F. L. (Eds.), *Geology and Offshore Resources of Pacific Island Arcs—Vanuatu Region*. Circum-Pac. Council. Energy and Miner. Resour., Earth Sci. Ser., 8:201–224.

Chung, W. Y., and Kanamori, H., 1978. A mechanical model for plate deformation associated with aseismic ridge subduction in the New Hebrides arc. *Tectonophysics*, 50:29–40.

Claypool, G. E., and Kaplan, I. R., 1974. The origin and distribution of methane in marine sediments. In Kaplan, I. R. (Ed.), *Natural Gases in Marine Sediments*: New York (Plenum), 99–140.

Coleman, P. J., and Packham, G. H., 1976. The Melanesian borderlands and India-Pacific plate boundaries. *Earth-Sci. Rev.*, 12:197–233.

Colley, H., and Ash, R. P., 1971. *The Geology of Erromango*. Regional Rept.—New Hebrides Geol. Surv.

Collot, J.-Y., Daniel, J., and Burne, R. V., 1985. Recent tectonics associated with the subduction/collision of the d'Entrecasteaux zone in the central New Hebrides. *Tectonophysics*, 112:325–356.

Collot, J.-Y., and Fisher, M. A., 1988. Crustal structure, from gravity data, of a collision zone in the central New Hebrides Island Arc. In Greene, H. G., and Wong, F. L. (Eds.), *Geology and Offshore Resources of Pacific Island Arcs—Vanuatu Region*. Circum-Pac. Council. Energy and Miner. Resour., Earth Sci. Ser., 8:125–140.

Dickinson, W. R., 1973. Reconstruction of past arc-trench systems from petrotectonic assemblages in the island arcs of the western Pacific. In Coleman, P. J. (Ed.), *The Western Pacific: Island Arcs, Marginal Seas, Geochemistry*: Perth (Univ. of Western Australia Press), 569–601.

Dupuy, C., Dostal, J., Marcellot, G., Bougault, H., Joron, J. L., and Treuil, M., 1982. Geochemistry of basalts from central and southern New Hebrides arc: implication for their source rock composition. *Earth Planet. Sci. Lett.*, 60:207–225.

Falvey, D. A., 1975. Arc reversals, and a tectonic model for the North Fiji Basin. *Australas. Soc. Explor. Geophys. Bull.*, 6:47–49.

Fisher, M. A., Falvey, D. A., and Smith, G. L., 1988. Seismic stratigraphy of the summit basins of the New Hebrides Island Arc. In Greene, H. G., and Wong, F. L. (Eds.), *Geology and Offshore Resources of Pacific Island Arcs—Vanuatu Region*. Circum-Pac. Council. Energy and Miner. Resour., Earth Sci. Ser., 8:201–224.

Gieskes, J. M., 1981. Deep-sea drilling interstitial water studies: implications for chemical alteration of the oceanic crust, layers I and II. In Warme, J. E., Douglas, R. G., and Winterer, E. L. (Eds.), *The Deep Sea Drilling Project: A Decade of Progress*. Soc. Econ. Paleontol. Mineral. Spec. Publ., 32:149–167.

- Gorton, M. P., 1974. The geochemistry and geochronology of the New Hebrides [Ph.D. dissert.]. Australian National Univ., Canberra.
- , 1977. The geochemistry and origin of Quaternary volcanism in the New Hebrides. *Geochim. Cosmochim. Acta*, 41:1257–1270.
- Greene, H. G., and Johnson, D. P., 1988. Geology of the Central Basin region of the New Hebrides Arc inferred from single-channel seismic-reflection data. In Greene, H. G., and Wong, F. L. (Eds.), *Geology and Offshore Resources of Pacific Island Arcs—Vanuatu Region*. Circum-Pac. Council. Energy and Miner. Resour., Earth Sci. Ser., 8:177–200.
- Greene, H. G., Macfarlane, A., Johnson, D. A., and Crawford, A. J., 1988. Structure and tectonics of the central New Hebrides Arc. In Greene, H. G., and Wong, F. L. (Eds.), *Geology and Offshore Resources of Pacific Island Arcs—Vanuatu Region*. Circum-Pac. Council. Energy and Miner. Resour., Earth Sci. Ser., 8:377–412.
- Haig, D. W., and Perembo, R.C.B., 1990. Foraminifera as stratigraphic guides for Papua New Guinea. In Carmen, G. J., and Carmen, Z. (Eds.), *Petroleum Exploration in Papua New Guinea: Proceedings of the First PNG Petroleum Convention*. Port Moresby.
- Hanus, V., and Vanek, J., 1983. Deep structure of the Vanuatu (New Hebrides) islands arc: intermediate depth collision of subducted lithospheric plates. *N. Z. J. Geol. Geophys.*, 26:133–154.
- Hills, S. J., and Thierstein, H. R., 1989. Plio-Pleistocene calcareous plankton biochronology. *Mar. Micropaleontol.*, 14:67–96.
- Hobart, M. A., and Weissel, J. K., 1987. Geothermal surveys in the Solomon Islands—Woodlark Basin Region. In Taylor, B., and Exon, N. F. (Eds.), *Marine Geology, Geophysics, and Geochemistry of the Woodlark Basin-Solomon Islands*. Circum-Pac. Council. Energy and Miner. Resour., Earth Sci. Ser., 7:49–66.
- Holmes, M. L., 1988. Seismic refraction measurements in the summit basins of the New Hebrides Arc. In Greene, H. G., and Wong, F. L. (Eds.), *Geology and Offshore Resources of Pacific Island Arcs—Vanuatu Region*. Circum-Pac. Council. Energy and Miner. Resour., Earth Sci. Ser., 8:163–176.
- Johnson, D. P., Belford, D. J., Carter, A. N., and Crawford, A. J., 1988. Petrology and age of dredge samples collected in the Central Basin, Vanuatu. In Greene, H. G., and Wong, F. L. (Eds.), *Geology and Offshore Resources of Pacific Island Arcs—Vanuatu Region*. Circum-Pac. Council. Energy and Miner. Resour., Earth Sci. Ser., 8:141–162.
- Johnson, D. P., and Greene, H. G., 1988. Modern depositional regimes, offshore Vanuatu. In Greene, H. G., and Wong, F. L. (Eds.), *Geology and Offshore Resources of Pacific Island Arcs—Vanuatu Region*. Circum-Pac. Council. Energy and Miner. Resour., Earth Sci. Ser., 8:287–300.
- Karig, D. E., and Mammerickx, J., 1972. Tectonic framework of the New Hebrides island arc. *Mar. Geol.*, 12:187–205.
- Kastner, M., Elderfield, H., Martin, J. B., Suess, E., Kvenvolden, K. A., and Garrison, R. E., 1990. Diagenesis and interstitial-water chemistry at the Peruvian continental margin—major constituents and strontium isotopes. In Suess, E., von Huene, R., et al., *Proc. ODP, Sci. Results*, 112: College Station, TX (Ocean Drilling Program), 413–440.
- Katz, H. R., 1981. Report on interpretation of seismic profiling data collected on the Vauban cruise in Vanuatu waters. *Tech. Bull.—U. N. Econ. Soc. Comm. Asia Pac., Comm. Co-ord. Jt. Prospect Miner. Resour. South Pac. Offshore Areas*, No. 12.
- , 1988. Offshore geology of Vanuatu-previous work. In Greene, H. G., and Wong, F. L. (Eds.), *Geology and Offshore Resources of Pacific Island Arcs—Vanuatu Region*. Circum-Pac. Council. Energy and Miner. Resour., Earth Sci. Ser., 8:93–124.
- Kennett, J. P., and Srinivasan, M. S., 1983. *Neogene Planktonic Foraminifera: A Phylogenetic Atlas*. Stroudsburg, PA (Hutchinson Ross).
- Kennett, J. P., von der Borch, C. C., et al., 1986. *Init. Repts. DSDP*, 90: Washington (U.S. Govt. Printing Office).
- Kroenke, L. W., 1984. Cenozoic tectonic development of the southwest Pacific. *Tech. Bull.—U. N. Econ. Soc. Comm. Asia Pac., Comm. Co-ord. Jt. Prospect Miner. Resour. South Pac. Offshore Areas*, No. 6.
- Lawrence, J. R., and Gieskes, J. M., 1981. Constraints on water transport and alteration in the oceanic crust from the isotopic composition of pore water. *J. Geophys. Res.*, 86:7924–7934.
- Louat, R., Hamburger, M., and Monzier, M., 1988. Shallow and intermediate-depth seismicity in the New Hebrides Arc: constraints on the subduction process. In Greene, H. G., and Wong, F. L. (Eds.), *Geology and Offshore Resources of Pacific Island Arcs—Vanuatu Region*. Circum-Pac. Council. Energy and Miner. Resour., Earth Sci. Ser., 8:329–356.
- Lundberg, N., and Moore, J. C., 1986. Macroscopic structural features in Deep Sea Drilling Project cores from forearc regions. In Moore, J. C. (Ed.), *Structural Fabrics Preserved in Deep Sea Drilling Project Cores From Forearcs*: Mem. Geol. Soc. Am., 166:13–44.
- Luyendyk, B. P., Bryan, W. B., and Jezek, P. A., 1974. Shallow structure of the New Hebrides island arc. *Geol. Soc. Am. Bull.*, 85:1287–1300.
- Macfarlane, A., Carney, J. N., Crawford, A. J., and Greene, H. G., 1988. Vanuatu—a review of the onshore geology. In Greene, H. G., and Wong, F. L. (Eds.), *Geology and Offshore Resources of Pacific Island Arcs—Vanuatu Region*. Circum-Pac. Council. Energy and Miner. Resour., Earth Sci. Ser., 8:45–92.
- Mallick, D.I.J., 1973. Some petrological and structural variations in the New Hebrides. In Coleman, P. J. (Ed.), *The Western Pacific: Island Arcs, Marginal Seas, Geochemistry*: Perth (Univ. of Western Australia Press), 193–211.
- , 1975. Development of the New Hebrides Archipelago. *Philos. Trans. R. Soc. London, B*, 272:277–285.
- Mallick, D.I.J., and Greenbaum, D., 1977. *Geology of Southern Santo*. Regional Rept.—New Hebrides Geol. Surv.
- Mallick, D.I.J., and Neef, G., 1974. *Geology of Pentecost*. Regional Rept.—New Hebrides Geol. Surv.
- Marcelot, G., Maury, R. C., and Lefevre, C., 1983. Mineralogy of Erromango lavas (New Hebrides): evidence of an early stage of fractionation in island arc basalts. *Lithos*, 16:135–151.
- Mitchell, A.H.G., and Warden, A. J., 1971. Geological evolution of the New Hebrides island arc. *J. Geol. Soc. London*, 127:501–529.
- Okada, H., and Bukry, D., 1980. Supplementary modification and introduction of code numbers to the low-latitude coccolith biostratigraphic zonation (Bukry, 1973; 1975). *Mar. Micropaleontol.*, 5:321–325.
- Pascal, G., Dubois, J., Barazangi, M., Isacks, B. L., and Oliver, J., 1973. Seismic velocity anomalies beneath the New Hebrides island arc: evidence for a detached slab in the upper mantle. *J. Geophys. Res.*, 78:6998–7004.
- Pearce, J. A., 1982. Trace element characteristics of lavas from destructive plate boundaries. In Thorpe, R. S. (Ed.), *Andesites: Orogenic Andesites and Related Rocks*: New York (Wiley), 525–548.
- Pearce, J. A., and Cann, J. R., 1973. Tectonic setting of basic volcanic rocks determined using trace element analysis. *Earth Planet. Sci. Lett.*, 24:419–426.
- Prell, W. L., Niitsuma, N., et al., 1989. *Proc. ODP, Init. Repts.*, 117: College Station, TX (Ocean Drilling Program).
- Ravenne, C., Pascal, G., Dubois, J., Dugas, F., and Montadert, L., 1977. Model of young intra-oceanic arc: the New Hebrides island arc. In *Int. Symp. on Geodynamics in South-west Pacific, Noumea, New Caledonia, 1976*. Paris (Editions Technip), 63–78.
- Robinson, G. P., 1969. *The Geology of North Santo*. Regional Rept.—New Hebrides Geol. Surv.
- Serra, O., 1989. *Formation Microscanner Image Interpretation*: Houston (Schlumberger Educational Services).
- Wilson, M., 1989. *Igneous Petrogenesis: A Global Tectonic Approach*: London (Unwin Hyman).

Ms 134A-112

NOTE: All core description forms (“barrel sheets”) and core photographs have been printed on coated paper and bound as Section 4, near the back of this volume, beginning on page 581.

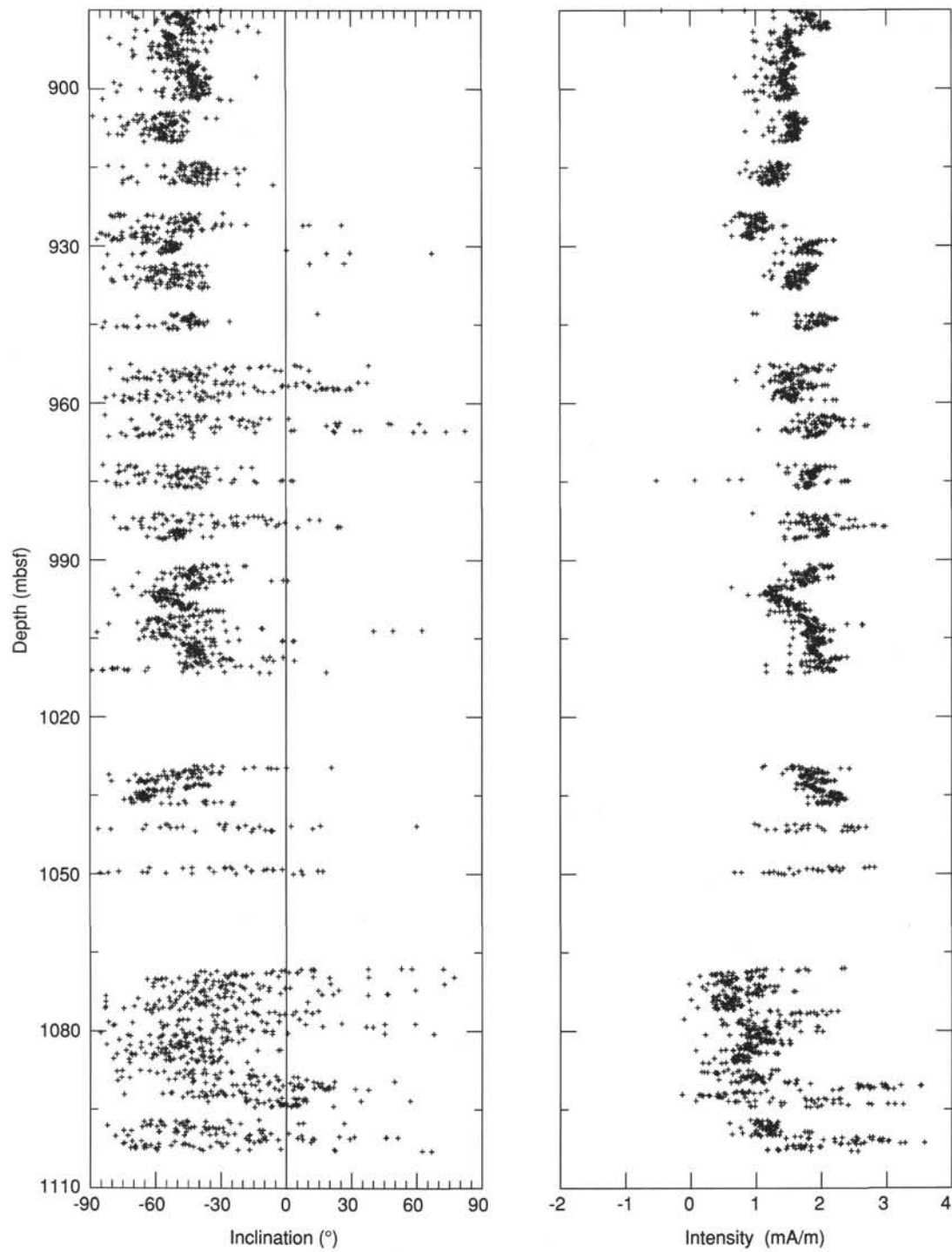


Figure 46. Variation of inclination and intensity after demagnetization at 10 mT with depth (from 870 to 1100 mbsf) in Hole 832B.

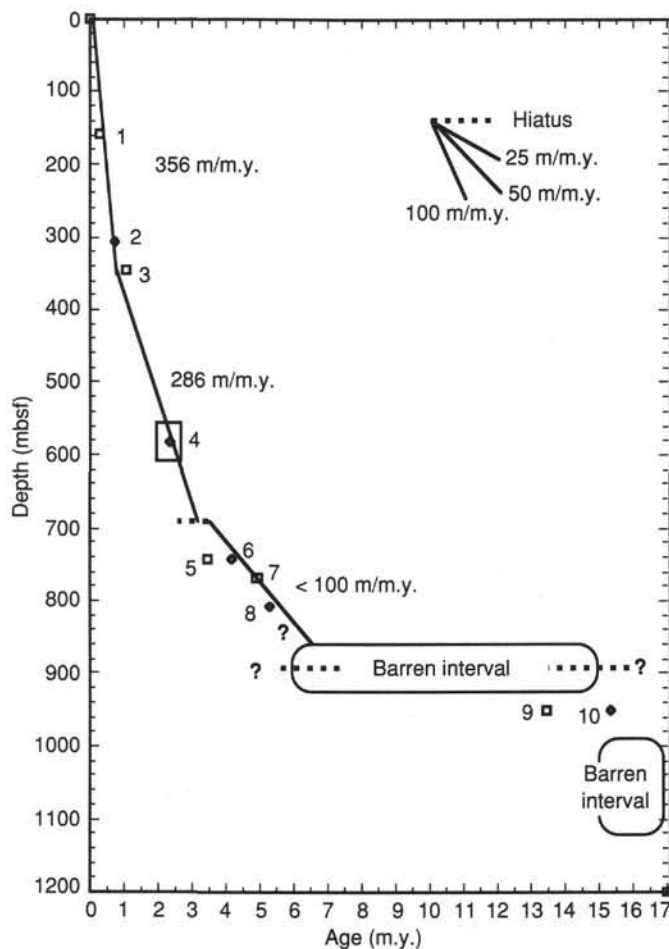


Figure 49. Sediment accumulation rates for Site 832. The following first appearance and last appearance datums (FAD, LAD) were used to compile this plot: 1 = FAD *Emiliana huxleyi* at 0.28 Ma from Sample 134-832A-6H-CC; 2 = LAD *Globorotalia tosaensis* at 0.60 Ma from Sample 134-832B-18R-CC, 21-25 cm; 3 = FAD large *Gephyrocapsa* at 1.36 Ma from Sample 134-832B-22R-CC; 4 = FAD *Globorotalia truncatulinoides* at 5.90-2.70 Ma from between Samples 134-832B-40R-CC and 134-832B-50R-CC; 5 = FAD *Sphenolithus abies* at 3.47 Ma from Sample 134-832B-63R-CC; 6 = FAD *Globorotalia crassaformis* at 4.30 Ma from Sample 134-832B-63R-CC; 7 = LAD *Discoaster quinqueramus* at 5.00 Ma from Sample 134-832B-66R-CC; 8 = FAD *Globigerinoides conglobatus* at 5.30 Ma from Sample 134-832B-70R-CC; 9 = LAD *Sphenolithus heteromorphus* at 13.60 Ma from Sample 134-832B-84R-CC; 10 = FAD *Orbulina* spp. at 15.20 Ma from Sample 134-832B-85R-2, 29-32 cm.

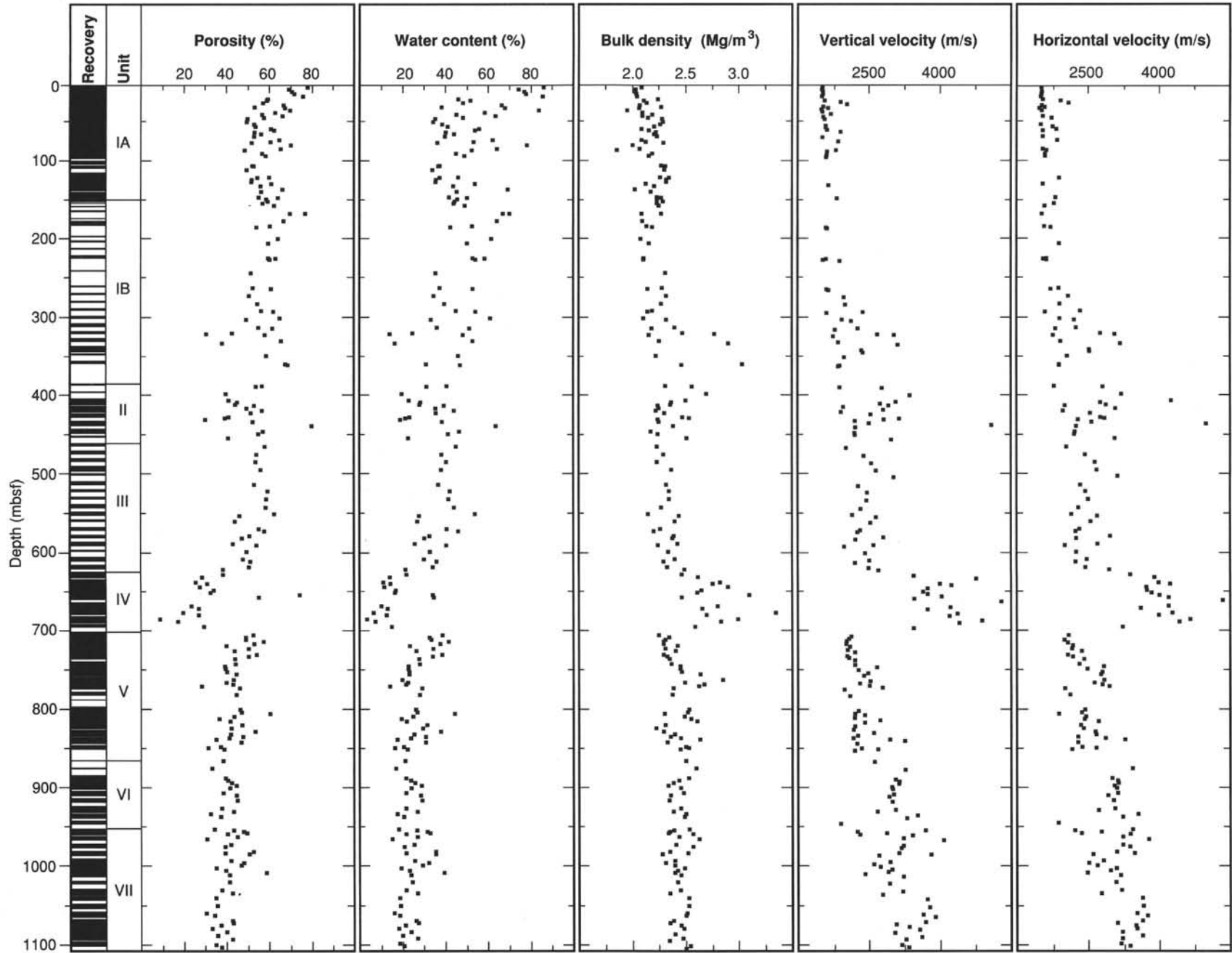


Figure 50. Porosity, water content, bulk density, and sonic velocity vs. depth, Site 832.

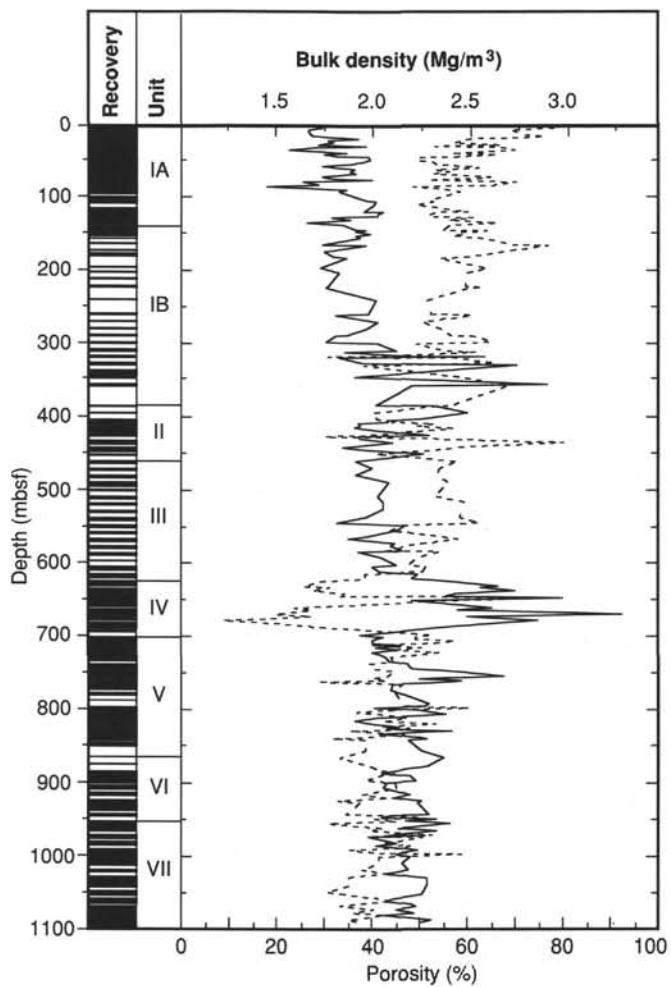


Figure 51. Bulk density (solid line) and porosity (dashed line) vs. depth, Site 832.

Table 8. Index properties data, Site 832.

Sample (cm)	Depth (mbsf)	Unit	Wet-bulk density (Mg/m ³)	Dry-bulk density (Mg/m ³)	Grain density (Mg/m ³)	Porosity		Water content	
						Wet (%)	Dry (%)	Wet (%)	Dry (%)
134-832A-									
1H-2, 80	2.30	IA	1.74	0.93	2.93	78.3	71.4	46.2	85.9
1H-4, 80	5.30	IA	1.67	0.96	2.58	69.2	65.4	42.6	74.2
2H-2, 77	8.17	IA	1.67	0.94	2.60	70.9	66.4	43.5	76.9
2H-4, 77	11.17	IA	1.68	0.95	2.70	72.0	67.5	43.8	77.9
2H-6, 80	14.20	IA	1.69	0.91	2.48	76.2	67.8	46.1	85.5
3H-2, 80	17.70	IA	1.93	1.32	2.82	59.4	56.2	31.5	46.1
4H-1, 130	19.80	IA	1.77	1.17	2.62	59.2	57.3	34.2	51.9
4H-3, 115	22.65	IA	1.80	1.22	2.73	57.4	56.5	32.6	48.4
4H-5, 117	25.67	IA	1.72	1.03	2.74	67.0	64.3	39.9	66.4
4H-6, 147	27.47	IA	1.97	1.42	2.79	53.4	51.4	27.8	38.4
5H-1, 130	29.30	IA	1.71	1.02	2.79	67.6	65.2	40.5	68.0
5H-3, 130	32.30	IA	1.57	0.86	2.71	70.1	69.2	45.6	83.8
5H-5, 130	35.30	IA	1.75	1.10	2.74	63.0	61.4	37.0	58.7
5H-7, 50	37.50	IA	1.87	1.28	2.78	56.9	55.5	31.2	45.4
6H-1, 127	38.77	IA	1.75	1.07	2.80	66.5	63.8	38.9	63.6
6H-3, 132	41.82	IA	1.82	1.23	2.65	57.7	55.7	32.5	48.2
6H-4, 75	42.75	IA	1.98	1.46	2.65	50.3	47.9	26.0	35.2
6H-7, 40	46.90	IA	1.99	1.48	2.67	49.6	47.5	25.6	34.4
7H-2, 117	49.67	IA	1.96	1.41	2.78	53.2	51.5	27.9	38.6
7H-4, 117	52.67	IA	1.89	1.34	2.68	53.7	52.1	29.2	41.2
7H-6, 117	55.67	IA	1.74	1.11	2.60	61.0	59.0	35.9	56.1
8H-1, 120	57.70	IA	1.83	1.19	2.72	62.6	59.3	35.1	54.1
8H-3, 65	60.15	IA	1.91	1.36	2.64	53.5	51.1	28.6	40.2
8H-5, 30	62.80	IA	1.89	1.31	2.71	56.4	54.1	30.6	44.1
9H-2, 103	65.53	IA	1.92	1.37	2.69	53.3	51.3	28.5	39.8
9H-5, 103	70.03	IA	1.74	1.07	2.76	65.0	62.9	38.3	62.2
9H-7, 50	72.50	IA	1.79	1.16	2.70	60.8	58.8	34.9	53.5
10H-1, 140	73.90	IA	2.00	1.47	2.85	52.1	50.4	26.6	36.3
10H-3, 127	76.77	IA	1.64	0.92	2.71	70.4	67.7	43.9	78.2
10H-6, 140	81.40	IA	1.72	1.05	2.66	65.6	62.8	39.1	64.2
11H-1, 130	83.30	IA	1.45	0.95	2.73	48.9	58.6	34.4	52.5
11H-4, 130	87.80	IA	1.87	1.29	2.75	56.8	55.1	31.1	45.2
11H-6, 130	90.80	IA	1.83	1.23	2.73	58.6	56.9	32.9	49.0
13H-2, 79	102.81	IA	1.97	1.43	2.84	52.3	51.1	27.2	37.3
14H-2, 79	103.81	IA	2.02	1.47	2.81	53.0	50.5	27.0	36.9
15H-2, 79	108.79	IA	2.01	1.50	2.85	49.6	48.8	25.3	33.9
16H-2, 80	118.30	IA	1.96	1.34	2.87	60.3	56.6	31.5	46.1
16H-2, 127	118.77	IA	2.06	1.49	2.86	54.8	51.4	27.3	37.5
16H-4, 78	121.28	IA	2.03	1.50	2.85	52.1	50.0	26.3	35.7
16H-6, 78	124.28	IA	2.03	1.50	2.87	52.0	50.2	26.3	35.6
17H-1, 77	126.27	IA	1.79	1.16	2.62	61.3	58.3	35.1	54.1
17H-3, 78	129.28	IA	1.89	1.32	2.67	56.3	53.5	30.4	43.8
18H-2, 78	133.78	IA	1.66	0.98	2.58	66.5	63.9	40.9	69.3
18H-4, 78	136.78	IA	1.85	1.27	2.76	56.4	55.3	31.3	45.5
19H-2, 77	143.27	IB	1.92	1.35	2.67	55.3	52.5	29.5	41.9
20H-1, 141	146.41	IB	1.92	1.32	2.76	58.9	55.5	31.4	45.7
20H-3, 130	149.30	IB	1.99	1.38	2.74	59.6	54.6	30.7	44.4
21X-CC, 4	151.34	IB	1.92	1.33	2.80	57.1	54.8	30.5	44.0
24X-2, 132	180.52	IB	1.80	1.18	2.56	60.5	57.1	34.5	52.7
24X-4, 7	182.27	IB	1.87	1.31	2.61	54.4	52.3	29.9	42.6
26X-1, 9	196.79	IB	1.73	1.07	2.64	64.3	61.6	38.1	61.6
134-832B-									
1R-CC, 4	144.44	IB	1.97	1.31	2.89	64.3	59.0	33.5	50.4
2R-CC, 17	154.27	IB	1.94	1.30	2.74	62.7	57.2	33.1	49.4
3R-1, 27	164.07	IB	1.74	1.02	2.72	70.0	65.4	41.2	70.2
3R-CC, 14	164.85	IB	1.97	1.18	2.89	77.1	65.7	40.2	67.2
4R-CC, 18	173.88	IB	1.75	1.07	2.55	67.0	61.9	39.2	64.4
7R-1, 60	202.80	IB	1.83	1.22	2.64	59.8	56.8	33.5	50.4
9R-1, 5	221.45	IB	1.77	1.16	2.57	59.8	57.3	34.6	52.9
9R-1, 122	222.62	IB	1.76	1.11	2.69	63.3	60.8	36.9	58.5
9R-2, 100	223.90	IB	1.76	1.14	2.59	60.4	58.1	35.1	54.2
11R-CC, 7	240.77	IB	2.02	1.49	2.76	51.8	49.2	26.3	35.6
13R-1, 10	260.10	IB	1.98	1.44	2.71	52.6	50.0	27.2	37.4
13R-1, 125	261.25	IB	1.81	1.18	2.54	61.1	57.1	34.6	53.0
14R-1, 87	270.57	IB	2.03	1.51	2.77	50.9	48.6	25.7	34.6
15R-2, 4	280.12	IB	1.97	1.41	2.75	54.7	51.9	28.4	39.7
16R-1, 45	289.45	IB	1.87	1.29	2.64	56.6	54.0	31.1	45.1
16R-2, 16	290.66	IB	1.81	1.18	2.56	62.2	57.8	35.2	54.2
17R-1, 17	298.87	IB	1.76	1.09	2.72	65.1	62.1	37.9	61.1
17R-3, 70	300.90	IB	2.03	1.53	2.74	49.5	47.3	24.9	33.2
18R-2, 72	310.62	IB	2.13	1.56	3.09	55.1	52.3	26.5	36.1
18R-3, 117	312.41	IB	1.86	1.23	2.73	61.7	58.2	34.0	51.5
19R-1, 4	318.14	IB	2.22	1.78	2.83	43.1	40.9	19.9	24.9
19R-1, 105	319.15	IB	2.59	2.28	2.88	31.0	28.4	12.3	14.0
19R-2, 87	320.47	IB	1.83	1.24	2.65	58.3	55.9	32.6	48.4

Table 8 (continued).

Sample (cm)	Depth (mbsf)	Unit	Wet-bulk density (Mg/m ³)	Dry-bulk density (Mg/m ³)	Grain density (Mg/m ³)	Porosity		Water content	
						Wet (%)	Dry (%)	Wet (%)	Dry (%)
20R-1, 42	328.12	IB	1.95	1.27	2.84	65.9	59.7	34.6	53.0
20R-3, 26	330.89	IB	2.76	2.37	2.88	38.5	32.1	14.3	16.7
22R-1, 58	347.48	IB	1.91	1.31	2.61	59.0	54.4	31.6	46.3
23R-1, 87	357.47	IB	2.92	2.23	4.36	67.7	57.2	23.7	31.1
23R-3, 68	359.09	IB	2.21	1.50	2.75	68.8	56.0	32.0	47.0
26R-1, 66	386.26	II	2.02	1.43	2.73	56.9	52.3	28.9	40.7
26R-1, 114	386.74	II	2.33	1.77	2.59	54.1	44.4	23.8	31.3
27R-1, 102	396.32	II	2.50	2.09	2.72	40.1	34.5	16.4	19.7
28R-1, 17	405.07	II	2.26	1.83	2.82	41.3	39.1	18.8	23.1
28R-2, 50	406.90	II	2.09	1.62	2.68	45.3	43.0	22.2	28.6
28R-3, 147	409.37	II	2.08	1.62	2.43	44.4	40.2	21.9	28.0
28R-5, 70	411.57	II	1.93	1.38	2.72	53.2	51.4	28.3	39.5
29R-1, 37	414.57	II	1.94	1.43	2.48	49.7	46.6	26.3	35.6
29R-3, 37	417.57	II	1.91	1.33	2.74	57.0	54.4	30.6	44.1
29R-5, 37	420.57	II	2.01	1.48	2.77	51.6	49.3	26.3	35.7
30R-2, 83	425.93	II	2.22	1.80	2.80	41.3	39.3	19.0	23.5
30R-3, 88	427.48	II	2.30	1.89	2.78	39.8	37.1	17.7	21.6
30R-4, 92	429.02	II	1.93	1.62	3.03	30.4	36.4	16.1	19.2
30R-6, 92	432.02	II	1.94	1.40	2.65	52.6	50.2	27.8	38.6
31R-3, 127	437.47	II	2.11	1.29	2.77	80.3	63.5	38.9	63.7
32R-1, 137	444.27	II	1.85	1.26	2.71	57.4	55.5	31.8	46.7
32R-3, 137	447.27	II	1.93	1.36	2.70	55.1	52.4	29.3	41.4
33R-1, 122	453.12	II	2.27	1.85	2.86	41.2	39.1	18.6	22.8
34R-2, 60	463.60	III	1.92	1.32	2.73	58.2	54.8	31.1	45.1
35R-2, 110	473.70	III	2.00	1.44	2.67	54.3	50.4	27.8	38.5
36R-2, 75	483.06	III	1.92	1.36	2.76	53.9	52.4	28.8	40.5
37R-2, 96	492.86	III	2.09	1.51	2.82	56.3	51.4	27.6	38.1
39R-2, 85	512.15	III	2.03	1.48	2.75	53.3	49.9	26.9	36.8
40R-1, 95	520.45	III	2.06	1.45	2.74	59.6	53.3	29.7	42.2
41R-1, 94	530.14	III	2.06	1.45	2.66	59.0	52.1	29.3	41.5
42R-2, 84	541.24	III	1.97	1.36	2.72	58.7	54.2	30.6	44.1
43R-1, 47	548.97	III	1.82	1.18	2.73	62.6	59.4	35.1	54.1
43R-3, 44	551.94	III	2.18	1.70	2.82	46.4	43.7	21.8	27.9
44R-1, 117	559.37	III	2.13	1.68	2.76	44.2	42.2	21.2	26.9
45R-1, 107	568.77	III	1.96	1.39	2.74	55.4	52.4	29.0	40.8
45R-3, 72	571.42	III	1.88	1.28	2.73	58.1	55.6	31.7	46.3
46R-1, 37	577.77	III	2.12	1.60	2.82	51.0	47.5	24.6	32.7
46R-3, 32	580.72	III	2.10	1.61	2.73	47.6	44.9	23.2	30.3
47R-1, 70	587.70	III	2.16	1.72	2.77	43.3	41.4	20.5	25.9
47R-2, 87	589.37	III	1.93	1.37	2.68	54.2	51.7	28.8	40.5
48R-1, 100	597.70	III	2.05	1.54	2.74	49.7	47.1	24.8	33.0
49R-1, 100	607.40	III	2.13	1.64	2.75	48.0	44.8	23.1	30.0
49R-3, 100	610.40	III	2.00	1.47	2.70	51.5	48.8	26.4	35.9
50R-2, 63	617.27	III	2.04	1.52	2.70	50.8	47.8	25.5	34.3
50R-4, 100	620.62	III	2.24	1.84	2.79	38.7	37.2	17.7	21.5
51R-2, 27	627.47	IV	2.21	1.81	2.42	38.8	34.4	18.0	22.0
51R-4, 75	630.89	IV	2.40	2.10	2.73	29.1	27.6	12.4	14.2
52R-2, 85	637.46	IV	2.66	2.39	2.69	26.0	22.8	10.0	11.1
52R-3, 85	638.78	IV	2.57	2.24	2.69	31.4	27.5	12.5	14.3
52R-6, 85	643.13	IV	2.75	2.46	2.61	28.0	23.1	10.4	11.6
53R-2, 87	647.37	IV	2.44	2.08	2.58	34.5	30.1	14.5	17.0
53R-4, 87	650.37	IV	2.39	2.05	2.55	33.1	29.4	14.2	16.6
53R-6, 87	653.37	IV	3.00	2.24	2.73	74.6	47.9	25.4	34.1
54R-2, 80	657.00	IV	2.21	1.64	2.55	55.4	46.5	25.7	34.6
55R-2, 140	667.30	IV	2.63	2.38	2.71	24.0	21.6	9.3	10.3
55R-4, 140	670.30	IV	2.45	2.17	2.74	27.5	26.0	11.5	13.0
56R-2, 137	675.87	IV	3.31	3.11	3.61	20.0	18.9	6.2	6.6
56R-4, 137	678.84	IV	2.50	2.22	2.75	27.5	25.6	11.3	12.7
57R-2, 67	684.81	IV	2.87	2.78	2.89	9.2	8.8	3.3	3.4
57R-4, 97	687.97	IV	2.67	2.48	2.77	17.8	16.7	6.8	7.3
58R-2, 37	694.17	IV	2.37	2.06	2.62	29.9	27.7	12.9	14.9
59R-2, 120	704.70	V	1.94	1.40	2.68	52.8	50.6	27.9	38.8
59R-4, 120	707.71	V	2.06	1.55	2.73	49.4	46.7	24.6	32.6
59R-6, 120	710.71	V	2.02	1.51	2.70	49.4	47.1	25.1	33.5
60R-1, 140	713.00	V	2.00	1.41	2.77	57.6	53.3	29.5	41.7
60R-3, 140	716.00	V	2.00	1.45	2.76	53.3	50.6	27.3	37.6
60R-5, 127	718.87	V	2.16	1.75	2.67	40.2	38.3	19.1	23.6
61R-1, 147	722.27	V	2.02	1.50	2.74	50.5	48.2	25.6	34.5
61R-3, 147	725.25	V	2.14	1.69	2.77	44.1	42.2	21.1	26.7
61R-6, 147	729.73	V	2.00	1.44	2.83	54.2	51.9	27.8	38.6
62R-2, 25	732.25	V	2.04	1.52	2.75	50.7	48.0	25.4	34.1
62R-4, 25	735.25	V	2.07	1.62	2.70	44.2	42.6	21.8	27.9
63R-2, 22	741.52	V	2.09	1.63	2.71	44.6	42.8	21.9	28
63R-4, 22	744.52	V	2.19	1.79	2.62	39.7	37.1	18.6	22.8
63R-6, 22	747.52	V	2.19	1.78	2.74	39.9	38.2	18.7	22.9
64R-2, 90	751.90	V	2.21	1.79	2.70	40.6	38.1	18.8	23.2
64R-4, 92	754.92	V	2.43	1.97	2.81	45.0	39.3	19.0	23.4

Table 8 (continued).

Sample (cm)	Depth (mbsf)	Unit	Wet-bulk density (Mg/m ³)	Dry-bulk density (Mg/m ³)	Grain density (Mg/m ³)	Porosity		Water content	
						Wet (%)	Dry (%)	Wet (%)	Dry (%)
65R-2, 124	761.94	V	2.69	2.24	2.35	43.6	31.6	16.6	20
65R-4, 124	764.94	V	2.25	1.83	2.6	40.5	36.7	18.5	22.6
65R-6, 124	767.94	V	2.47	2.03	2.67	43.3	36.6	18.0	21.9
66R-1, 119	769.99	V	2.41	2.11	2.64	28.8	26.6	12.2	14
66R-3, 119	772.79	V	2.11	1.63	2.71	46.6	43.8	22.6	29.2
67R-2, 112	781.22	V	2.10	1.64	2.69	44.8	42.6	21.9	28
69R-2, 121	800.51	V	2.30	1.82	2.59	46.7	40.2	20.8	26.3
69R-4, 145	803.75	V	2.28	1.80	2.58	47.3	40.7	21.2	26.9
69R-6, 45	805.75	V	2.01	1.39	2.46	60.5	51.9	30.8	44.5
70R-1, 147	809.17	V	2.24	1.79	2.71	43.8	40.2	20.1	25.1
70R-3, 145	812.15	V	2.32	1.94	2.68	37.1	34.1	16.4	19.6
70R-5, 145	815.15	V	2.39	1.96	2.71	42.1	37.0	18.0	22
71R-2, 125	820.15	V	2.02	1.53	2.66	47.5	45.4	24.1	31.7
71R-5, 105	824.45	V	1.91	1.48	2.32	42.6	40.3	22.8	29.6
72R-2, 22	828.72	V	2.00	1.45	2.71	53.6	50.3	27.4	37.8
72R-4, 29	831.80	V	2.13	1.70	2.67	42.3	40.1	20.3	25.5
72R-6, 22	834.69	V	2.08	1.59	2.68	48.1	45.1	23.7	31
73R-1, 10	836.80	V	2.20	1.77	2.71	41.7	39.1	19.4	24.1
73R-2, 12	838.32	V	2.42	2.05	2.81	35.6	33.0	15.1	17.8
73R-4, 122	842.23	V	2.04	1.56	2.66	47.0	44.7	23.6	30.9
74R-1, 143	847.83	V	2.26	1.87	2.76	37.8	36.0	17.1	20.6
74R-2, 140	849.30	V	2.29	1.96	2.69	31.9	30.6	14.3	16.6
74R-3, 140	850.80	V	2.19	1.78	2.68	39.2	37.3	18.4	22.5
76R-CC, 6	865.76	VI	2.26	1.87	2.77	38.8	36.7	17.5	21.3
77R-CC, 20	875.50	VI	2.38	2.03	2.80	33.5	31.7	14.4	16.9
78R-2, 127	887.77	VI	2.29	1.88	2.74	39.9	37.0	17.9	21.8
78R-4, 122	890.72	VI	2.18	1.76	2.70	41.0	38.7	19.2	23.8
78R-6, 120	893.63	VI	2.11	1.68	2.63	42.7	40.4	20.7	26.1
79R-2, 115	897.35	VI	2.05	1.59	2.61	44.9	42.6	22.4	28.9
79R-4, 110	900.30	VI	2.20	1.77	2.72	42.0	39.4	19.5	24.2
80R-2, 104	906.96	VI	2.23	1.83	2.75	38.8	37.0	17.8	21.7
80R-4, 100	909.92	VI	2.08	1.62	2.63	45.1	42.5	22.2	28.5
81R-2, 134	916.78	VI	2.06	1.60	2.61	45.3	42.8	22.5	29
82R-2, 137	926.57	VI	2.20	1.81	2.63	38.3	36.0	17.8	21.7
82R-5, 137	930.90	VI	2.11	1.66	2.68	43.7	41.5	21.2	26.9
83R-1, 123	934.53	VI	2.26	1.92	2.71	33.0	31.9	15.0	17.6
83R-3, 123	937.53	VI	2.24	1.85	2.67	37.6	35.3	17.2	20.8
85R-1, 92	953.52	VII	2.30	1.94	2.73	34.8	33.1	15.5	18.4
85R-2, 80	954.90	VII	2.12	1.67	2.56	43.7	40.3	21.1	26.8
85R-3, 123	956.83	VII	2.07	1.57	2.64	48.2	45.1	23.9	31.5
85R-4, 88	957.98	VII	2.05	1.54	2.64	49.7	46.2	24.8	33
85R-5, 91	959.51	VII	2.34	1.92	2.68	40.8	36.5	17.9	21.8
86R-1, 72	962.92	VII	2.18	1.71	2.63	45.3	41.3	21.3	27.1
86R-3, 72	965.92	VII	2.41	2.09	2.71	31.2	29.0	13.3	15.3
87R-1, 117	972.97	VII	2.14	1.70	2.63	42.5	39.9	20.4	25.6
87R-3, 118	975.98	VII	2.34	1.94	2.70	39.7	35.8	17.4	21
88R-1, 125	982.35	VII	2.07	1.53	2.77	52.8	49.2	26.2	35.5
88R-2, 130	983.84	VII	2.28	1.87	2.76	39.7	37.2	17.9	21.7
88R-3, 130	985.32	VII	1.98	1.46	2.48	50.8	46.6	26.2	35.6
89R-2, 130	993.60	VII	2.13	1.69	2.62	42.5	39.8	20.4	25.7
89R-4, 131	996.52	VII	2.02	1.53	2.55	48.2	44.9	24.4	32.3
89R-6, 135	999.56	VII	2.13	1.64	2.57	47.2	42.7	22.7	29.4
90R-2, 120	1003.11	VII	2.24	1.88	2.67	35.5	33.8	16.2	19.4
90R-4, 120	1006.11	VII	2.16	1.76	2.58	39.9	37.2	18.9	23.3
90R-6, 120	1009.11	VII	2.13	1.53	2.79	58.9	52.1	28.3	39.5
91R-2, 97	1012.57	VII	2.20	1.77	2.63	41.7	38.5	19.4	24.1
92R-2, 52	1021.46	VII	2.16	1.74	2.73	41.7	39.8	19.7	24.6
93R-2, 15	1030.95	VII	2.19	1.80	2.61	38.1	35.8	17.8	21.7
93R-5, 15	1035.41	VII	2.07	1.63	2.56	43.1	40.6	21.3	27.1
94R-2, 80	1041.27	VII	2.29	1.93	2.45	35.3	31.1	15.8	18.7
95R-2, 132	1051.39	VII	2.29	1.93	2.63	35.9	33.1	16.0	19.1
96R-2, 137	1061.13	VII	2.27	1.96	2.38	30.8	27.4	13.9	16.1
96R-4, 137	1064.03	VII	2.26	1.90	2.43	34.6	30.8	15.7	18.6
97R-2, 133	1070.83	VII	2.11	1.67	2.51	42.8	39.4	20.8	26.3
97R-4, 123	1073.73	VII	2.07	1.63	2.45	43.4	39.8	21.5	27.4
97R-6, 127	1076.77	VII	2.20	1.82	2.37	37.7	33.2	17.5	21.3
98R-2, 120	1080.40	VII	2.23	1.89	2.52	33.5	31.1	15.4	18.2
98R-5, 120	1084.90	VII	2.13	1.72	2.55	40.5	37.8	19.4	24.1
99R-2, 120	1090.01	VII	2.22	1.85	2.51	36.3	33.2	16.8	20.1
99R-4, 118	1092.99	VII	2.06	1.62	2.48	42.8	39.8	21.3	27.0
100R-2, 131	1099.81	VII	2.31	1.95	2.69	35.3	33.0	15.7	18.6
100R-4, 131	1102.82	VII	2.26	1.88	2.64	38.0	35.0	17.2	20.7

Table 9. Hamilton Frame sonic velocity data, Site 832.

Sample (cm)	Depth (mbsf)	Unit	Vertical velocity (m/s)	Wave type ^a	Horizontal velocity (m/s)	Wave type ^a
134-832A-						
1H-2, 80	2.30	IA	1522	C	1526	C
1H-4, 80	5.30	IA	1510	C		
2H-2, 77	8.17	IA	1532	C	1542	C
2H-4, 77	11.17	IA	1525	C	1525	C
2H-6, 80	14.20	IA	1516	C	1524	C
3H-2, 80	17.70	IA	1568	C	1558	C
4H-1, 130	19.80	IA	1910	C	1924	C
4H-3, 115	22.65	IA	2047	S	2093	S
4H-5, 117	25.67	IA	1537	C	1538	C
4H-6, 147	27.47	IA	1639	C	1598	C
5H-1, 130	29.30	IA	1502	C	1490	S
5H-3, 130	32.30	IA	1524	C	1539	C
5H-5, 130	35.30	IA	1692	C		
6H-1, 127	38.77	IA	1539	C	1554	S
6H-3, 132	41.82	IA	1571	C	1749	S
7H-2, 117	49.67	IA	1592	C	1522	C
7H-4, 117	52.67	IA	1592	C	1764	S
7H-6, 117	55.67	IA	1617	S	1847	S
8H-1, 120	57.70	IA	1898	S	1558	C
9H-2, 103	65.53	IA	1524	C	1555	S
9H-5, 103	70.03	IA	1854	S	1867	S
10H-6, 140	81.40	IA	1804	S	1555	S
11H-1, 130	83.30	IA	1618	S	1630	S
11H-4, 130	87.80	IA	1611	C	1612	C
11H-6, 130	90.80	IA	1605	C	1603	C
16H-2, 127	118.77	IA			1896	C
17H-1, 77	126.27	IA	1643	C	1553	C
19H-2, 77	143.27	IB	1826	C	1819	C
21X-CC, 4	151.34	IB			1788	S
24X-2, 132	180.52	IB	1602	C	1592	C
24X-4, 7	182.27	IB	1617	C	1718	C
134-832B-						
2R-CC, 15	154.25	IB			1595	S
3R-1, 27	164.07	IB			1540	C
7R-1, 60	202.80	IB			1899	C
9R-1, 5	221.45	IB	1602	C	1630	S
9R-1, 122	222.62	IB	1534	S	1568	S
9R-2, 100	223.90	IB	1884	S	1628	S
13R-1, 10	260.10	IB	1612	S	1894	C
13R-1, 125	261.25	IB	1649	S	1720	S
14R-1, 87	270.57	IB	1975	C	2084	C
15R-2, 4	280.12	IB	2001	C	1905	C
16R-1, 45	289.45	IB	2375	C	2344	C
16R-2, 16	290.66	IB	1606	S	1603	S
17R-1, 17	298.87	IB	1932	C	1906	C
17R-3, 70	300.90	IB	2124	C	2216	C
18R-2, 72	310.62	IB	2262	C	2257	C
18R-3, 117	312.41	IB	1783	C	1827	C
19R-1, 4	318.14	IB	2678	C	2759	C
19R-1, 105	319.15	IB	3031	C	3072	C
19R-2, 87	320.47	IB	1738	C	1768	C
20R-1, 42	328.12	IB	1861	C	1933	C
20R-3, 26	330.89	IB	3113	C	3192	C
21R-1, 106	338.46	IB	2347	C	2530	C
21R-3, 106	341.46	IB	2373	C	2541	C
22R-1, 58	347.48	IB	1984	C	2062	C
23R-1, 87	357.47	IB	1876	C	1896	C
23R-3, 68	359.09	IB	1852	C	1899	C
26R-1, 66	386.26	II	1887	C	1790	C
26R-1, 114	386.74	II	2773	C	2815	C
27R-1, 102	396.32	II	3364	C	3204	C
28R-1, 17	405.07	II	3073	C	4261	S
28R-2, 50	406.90	II	2736	C	2768	C
28R-3, 147	409.37	II	2912	C	2878	C
28R-5, 70	411.57	II	1961	C	2019	C
29R-1, 37	414.57	II	2809	C	3078	C
29R-3, 37	417.57	II	1915	C	1973	C
29R-5, 37	420.57	II	2538	C	2544	C
30R-2, 83	425.93	II	3140	C	2772	C
30R-3, 88	427.48	II	2816	C	2849	C
30R-4, 92	429.02	II	2211	C	2296	C
30R-6, 92	432.02	II	2499	C	2576	C
31R-1, 127	434.47	II	5082	C	4986	C
31R-3, 127	437.47	II	2215	C	2250	C
32R-1, 137	444.27	II	2195	C	2224	C

Table 9 (continued).

Sample (cm)	Depth (mbsf)	Unit	Vertical velocity (m/s)	Wave type ^a	Horizontal velocity (m/s)	Wave type ^a
32R-3, 137	447.27	II	2211	C	2214	C
33R-1, 122	453.12	II	2967	C	3067	C
34R-2, 60	463.60	III	2025	C	2049	C
35R-2, 110	473.70	III	2395	C	2436	C
36R-2, 75	483.06	III	2555	C	2642	C
37R-2, 96	492.86	III	2653	C	2684	C
38R-1, 84	500.94	III	3016	C	3126	C
39R-2, 85	512.15	III	2281	C	2341	C
40R-1, 95	520.45	III	2464	C	2453	C
41R-1, 94	530.14	III	2449	C	2508	C
42R-2, 84	541.24	III	2324	C	2300	C
43R-1, 47	548.97	III	2147	C	2151	C
43R-3, 44	551.94	III	2652	C	2698	C
44R-1, 117	559.37	III	2528	C	2562	C
45R-1, 107	568.77	III	2315	C	2326	C
45R-3, 72	571.42	III	2255	C	2243	C
46R-1, 37	577.77	III	2812	C	2964	C
46R-3, 32	580.72	III	2218	C	2255	C
47R-1, 70	587.70	III	2593	C	2708	C
47R-2, 87	589.37	III	1983	C	2013	C
48R-1, 100	597.70	III	2427	C	2252	C
49R-1, 100	607.40	III	2515	C	2478	C
49R-3, 100	610.40	III	2213	C	2242	C
50R-2, 63	617.27	III	2495	C	2452	C
50R-4, 100	620.62	III	2701	C	2953	C
51R-2, 27	627.47	IV	3440	C	3389	C
51R-4, 75	630.89	IV	4757	C	3899	C
52R-2, 85	637.46	IV	3996	C	3987	C
52R-3, 85	638.78	IV	4239	C	4239	C
52R-6, 85	643.13	IV	3737	C	3737	C
53R-2, 87	647.37	IV	3647	C	3738	C
53R-4, 87	650.37	IV	3737	C	3845	C
53R-6, 87	653.37	IV	4034	C	4009	C
54R-2, 80	657.00	IV	3449	C	4205	C
54R-4, 80	660.02	IV	5282	C	5337	C
55R-2, 135	667.25	IV	4221	C	4203	C
55R-4, 135	670.25	IV	3740	C	3616	C
56R-2, 137	675.87	IV	4366	C	4283	C
56R-4, 137	678.84	IV	4205	C	4006	C
57R-2, 67	684.81	IV	4882	C	4658	C
57R-4, 97	687.97	IV	4406	C	4435	C
58R-2, 37	694.17	IV	3444	C	3227	C
59R-2, 120	704.70	V	2125	C	2095	C
59R-4, 120	707.71	V	2080	C		
59R-6, 120	710.71	V	2031	C	2011	C
60R-2, 140	714.50	V	2013	C	2077	C
60R-4, 140	717.50	V	2100	C	2186	C
61R-1, 147	722.27	V	2050	C	2170	C
61R-3, 147	725.25	V	2209	C	2370	C
61R-6, 147	729.73	V	2042	C	2080	C
62R-2, 25	732.25	V	2075	C	2180	C
62R-4, 25	735.25	V	2205	C	2427	C
63R-2, 22	741.52	V	2211	C	2323	C
63R-4, 22	744.52	V	2663	C	2830	C
63R-6, 22	747.52	V	2270	C	2482	C
64R-2, 90	751.90	V	2487	C	2804	C
64R-4, 92	754.92	V	2389	C	2776	C
65R-2, 124	761.94	V	2533	C	2844	C
65R-4, 124	764.94	V	2316	C	2634	C
65R-6, 124	767.94	V	2515	C	2804	C
66R-1, 119	769.99	V	2780	C	2954	C
66R-3, 119	772.79	V	1981	C	2017	C
67R-2, 112	781.22	V	2102	C	2129	C
69R-2, 121	800.51	V	2270	C	2436	C
69R-4, 145	803.75	V	2211	C	2371	C
69R-6, 45	805.75	V	2414	C	1891	C
70R-1, 147	809.17	V	2192	C	2455	C
70R-3, 145	812.15	V	2743	C	2430	C
70R-5, 145	815.15	V	2416	C	2720	C
71R-2, 125	820.15	V	2206	C	2349	C
71R-5, 105	824.45	V	2172	C	2408	C
72R-2, 22	828.72	V	2605	C	2653	C
72R-4, 29	831.80	V	2264	C	2679	C
72R-6, 22	834.69	V	2168	C	2295	C
73R-1, 10	836.80	V	2942	C	2868	C
73R-2, 12	838.32	V	3257	C	3282	C
73R-4, 122	842.23	V	2242	C	2296	C

Table 9 (continued).

Sample (cm)	Depth (mbsf)	Unit	Vertical velocity (m/s)	Wave type ^a	Horizontal velocity (m/s)	Wave type ^a
74R-1, 143	847.83	V	2350	C	2381	C
74R-2, 140	849.30	V	2690	C	2679	C
74R-3, 140	850.80	V	2195	C	2164	C
76R-CC, 0	865.70	VI	2618	C		
77R-CC, 20	875.50	VI	3272	C	3436	C
78R-2, 127	887.77	VI	3058	C	3010	C
78R-4, 122	890.72	VI	3141	C	3123	C
78R-6, 120	893.63	VI	3124	C	3149	C
79R-2, 115	897.35	VI	2979	C	3056	C
79R-4, 110	900.30	VI	3002	C	3108	C
80R-2, 104	906.96	VI	3017	C	3126	C
80R-4, 100	909.92	VI	2921	C	2923	C
81R-2, 137	916.81	VI	2992	C	3040	C
82R-2, 137	926.57	VI	3063	C	3068	C
82R-4, 137	929.42	VI	2676	C	2729	C
83R-1, 123	934.53	VI	3529	C	3560	C
83R-3, 123	937.53	VI	3294	C	3235	C
84R-2, 42	944.82	VI	1905	C	1879	C
85R-1, 92	953.52	VII	3682	C	3441	C
85R-2, 80	954.90	VII	2249	C	2224	C
85R-3, 123	956.83	VII	2877	C	2778	C
85R-4, 88	957.98	VII	2304	C	2361	C
85R-5, 91	959.51	VII	3419	C	3394	C
86R-1, 72	962.92	VII	3223	C	3238	C
86R-3, 72	965.92	VII	4074	C	3786	C
87R-1, 117	972.97	VII	3229	C	3227	C
87R-3, 118	975.98	VII	3175	C	3384	C
88R-1, 125	982.35	VII	3125	C	3107	C
88R-2, 130	983.84	VII	3813	C	3477	C
88R-3, 130	985.32	VII	2703	C	2607	C
89R-2, 130	993.60	VII	2940	C	2825	C
89R-4, 131	996.52	VII	2599	C	2522	C
89R-6, 135	999.56	VII	2738	C	2691	C
90R-2, 120	1003.11	VII	2980	C	3101	C
90R-4, 120	1006.11	VII	2908	C	2965	C
90R-6, 120	1009.11	VII	2414	C	2489	C
91R-2, 97	1012.57	VII	3230	C	3191	C
92R-2, 52	1021.46	VII	2935	C	3089	C
93R-2, 15	1030.95	VII	3209	C	3211	C
93R-5, 15	1035.41	VII	2779	C	2784	C
94R-2, 80	1041.27	VII	3729	C	3643	C
95R-2, 132	1051.39	VII	3774	C	3674	C
96R-2, 137	1061.13	VII	3642	C	3532	C
96R-4, 137	1064.03	VII	3900	C	3757	C
97R-2, 133	1070.83	VII	3683	C	3650	C
97R-4, 123	1073.73	VII	3069	C	3115	C
97R-6, 127	1076.77	VII	3350	C	3503	C
98R-2, 120	1080.40	VII	3563	C	3528	C
98R-5, 120	1084.90	VII	3034	C	3222	C
99R-2, 120	1090.01	VII	3608	C	3645	C
99R-4, 118	1092.99	VII	3280	C	3224	C
100R-2, 131	1099.81	VII	3189	C	3199	C
100R-4, 131	1102.82	VII	3332	C	3385	C

^a C = compressional (P-wave) and S = shear (S-wave).

Table 10. Shear-strength data, Site 832.

Sample (cm)	Depth (mbsf)	Unit	Undrained shear strength ^a (kPa)
134-832A-			
1H-2, 85	2.35	IA	12.5
1H-4, 85	5.35	IA	16.1
2H-2, 83	8.23	IA	22.7
2H-2, 122	8.62	IA	28.6
2H-4, 83	11.23	IA	24.2
2H-6, 91	14.31	IA	43.3
3H-2, 90	17.80	IA	20.5
4H-1, 135	19.85	IA	13.2
4H-5, 122	25.72	IA	56.5
5H-1, 16	28.16	IA	22.0
5H-1, 127	29.27	IA	13.2
5H-5, 126	35.26	IA	42.5
5H-7, 46	37.46	IA	58.7
6H-3, 128	41.78	IA	30.8
6H-4, 71	42.71	IA	22.7
6H-7, 36	46.86	IA	35.9
7H-1, 62	47.62	IA	38.9
7H-4, 123	52.73	IA	51.3
8H-1, 115	57.65	IA	31.5
9H-2, 93	65.43	IA	18.3
9H-5, 98	69.98	IA	47.7
9H-7, 46	72.46	IA	13.2
10H-1, 147	73.97	IA	61.6
10H-3, 123	76.73	IA	73.3
10H-6, 146	81.46	IA	55.0
11H-1, 135	83.35	IA	51.3
17H-1, 83	126.33	IA	44.0
19H-2, 84	143.34	IB	35.2
20H-1, 143	146.43	IB	63.8
20H-3, 126	149.26	IB	55.0
24X-2, 126	180.46	IB	14.7
24X-4, 4	182.24	IB	16.9
26X-1, 6	196.76	IB	42.5
134-832B-			
3R-1, 37	164.17	IB	49.1
7R-1, 67	202.87	IB	26.4
8R-1, 68	212.58	IB	38.9
9R-2, 106	223.96	IB	40.9
13R-1, 54	260.54	IB	54.3

^a Values determined by Wykeham-Farrance spring vane-shear apparatus.

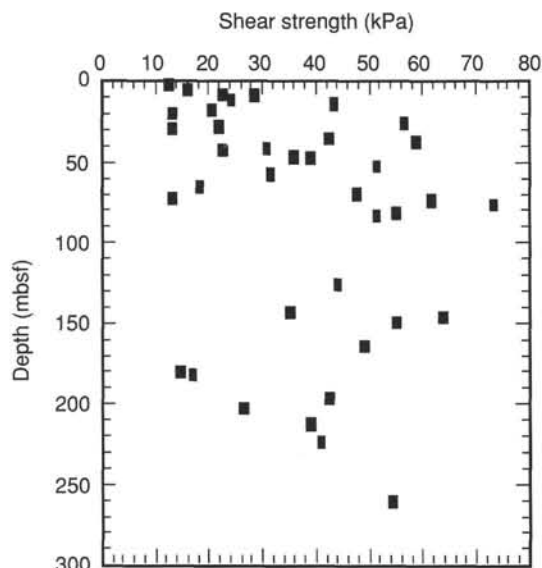


Figure 52. Shear strength vs. depth, Site 832.

Table 11. Thermal conductivity data, Site 832.

Sample (cm)	Depth (mbsf)	Unit	Value (W/[m · K])
134-832A-			
2H-3, 68	9.58	IA	1.1143
2H-4, 68	11.08	IA	0.9439
2H-5, 68	12.58	IA	0.9192
2H-6, 75	14.15	IA	0.8359
3H-1, 75	16.15	IA	0.9635
3H-2, 75	17.65	IA	0.9477
4H-1, 75	19.25	IA	0.8974
4H-2, 75	20.75	IA	0.8379
4H-4, 75	23.75	IA	0.9013
5H-2, 75	30.25	IA	0.9305
5H-6, 75	36.25	IA	0.8682
5H-7, 30	37.30	IA	0.9005
6H-1, 75	38.25	IA	0.9281
6H-2, 75	39.75	IA	0.9325
6H-3, 75	41.25	IA	0.9095
6H-4, 75	42.75	IA	0.9354
7H-1, 75	47.75	IA	0.9177
7H-2, 75	49.25	IA	0.9173
7H-4, 75	52.25	IA	0.7511
7H-6, 75	55.25	IA	0.8929
8H-1, 75	57.25	IA	0.9031
8H-2, 75	58.75	IA	0.9463
8H-3, 75	60.25	IA	1.1296
9H-1, 75	63.75	IA	0.9571
9H-2, 75	65.25	IA	1.0277
9H-3, 75	66.75	IA	1.0745
9H-5, 75	69.75	IA	0.9014
10H-1, 75	73.25	IA	0.9280
10H-2, 75	74.75	IA	0.9325
10H-4, 75	77.75	IA	0.9075
10H-6, 75	80.75	IA	0.9076
11H-1, 75	82.75	IA	0.9876
11H-2, 75	84.25	IA	0.9069
11H-4, 75	87.25	IA	0.9278
11H-6, 75	90.25	IA	0.8767
16H-1, 75	116.75	IA	1.0945
16H-2, 75	118.25	IA	1.0101
17H-1, 75	126.25	IA	0.9754
17H-2, 75	127.75	IA	0.9281
19H-1, 65	141.65	IB	0.9662
19H-2, 65	143.15	IB	0.9668
20H-1, 75	145.75	IB	1.0043
20H-2, 90	147.40	IB	1.0463
20H-3, 75	148.75	IB	0.9132
20H-4, 60	150.10	IB	0.9628
24X-2, 75	179.95	IB	0.8254
24X-3, 75	181.45	IB	0.8992
134-832B-			
52R-6, 48	642.76	IV	1.3768
52R-6, 48	642.76	IV	1.2418
55R-5, 10	670.50	IV	1.4349
55R-5, 10	670.50	IV	1.9213
61R-3, 0	723.78	V	1.3276
61R-3, 0	723.78	V	1.4096
64R-2, 7	751.07	V	1.4968
64R-2, 7	751.07	V	1.4442
82R-3, 69	927.33	VI	1.3094
82R-3, 69	927.33	VI	1.0696
82R-3, 69	927.33	VI	1.1616
97R-3, 50	1071.50	VII	1.2366
97R-3, 50	1071.50	VII	1.1399

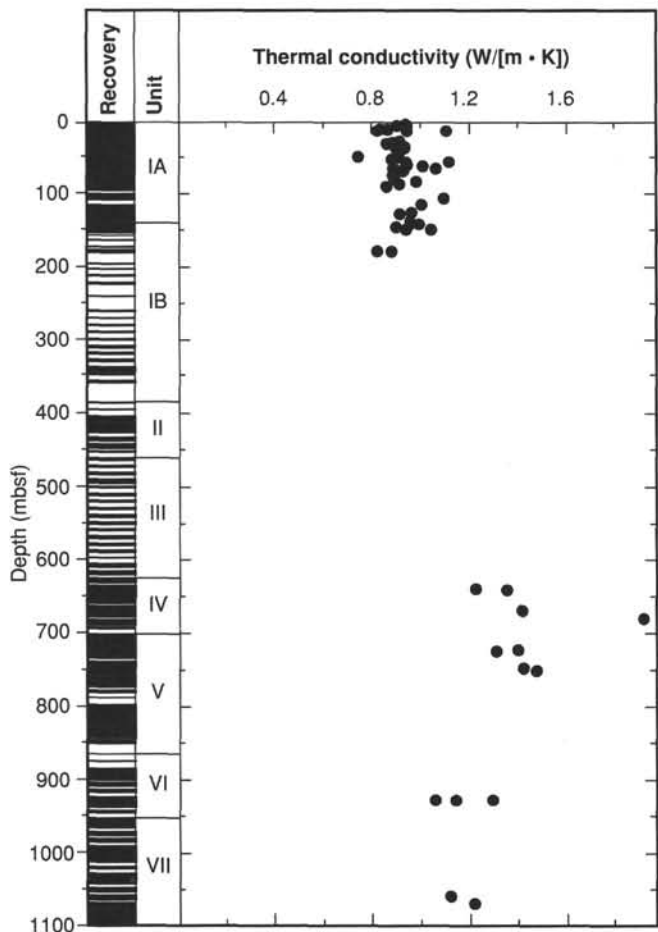


Figure 53. Thermal conductivity vs. depth, Site 832.

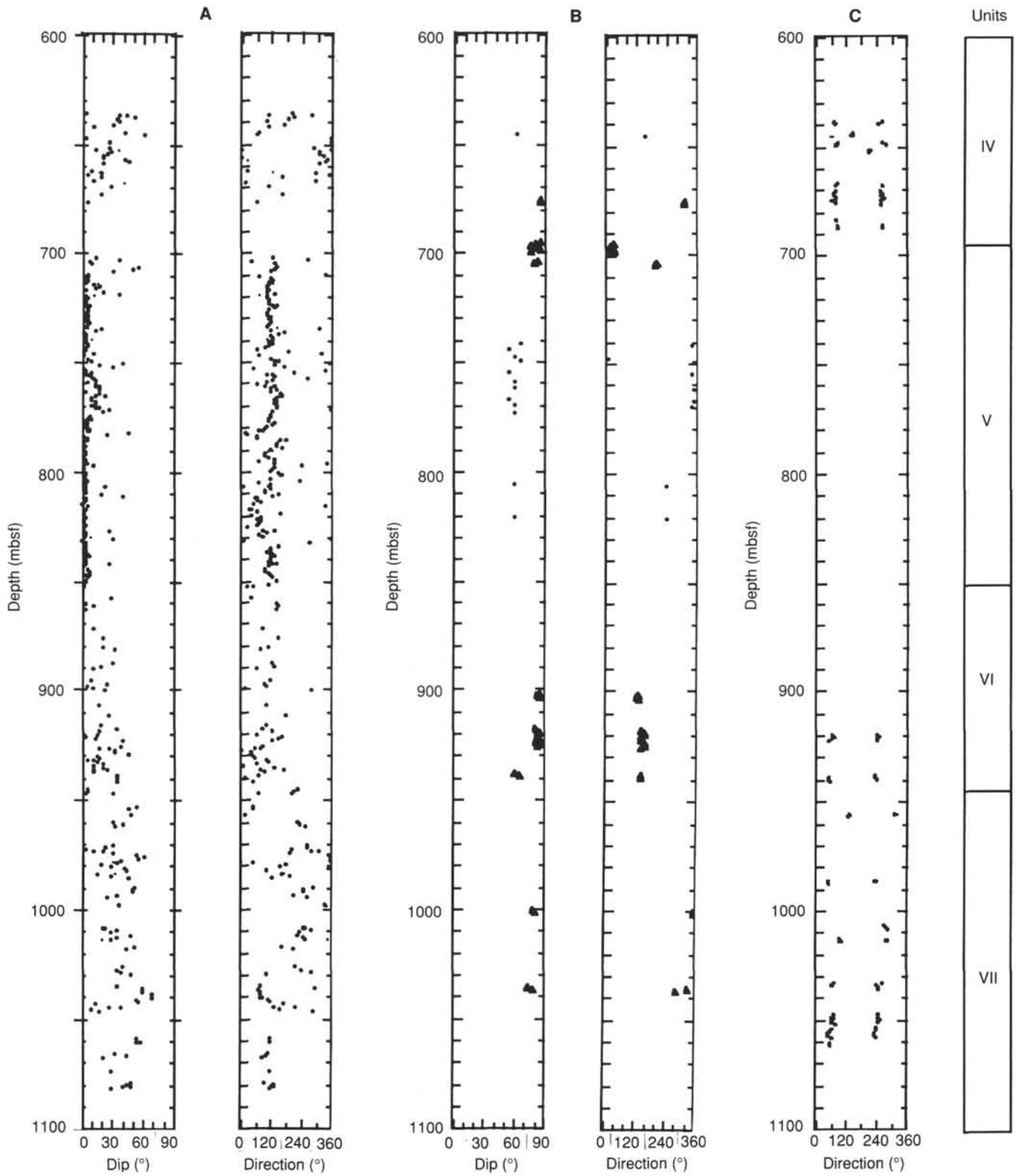


Figure 54. Summary of structures measured from FMS data. A. Bedding. B. Faults (circles) and oblique fractures (triangles). C. Vertical fractures.

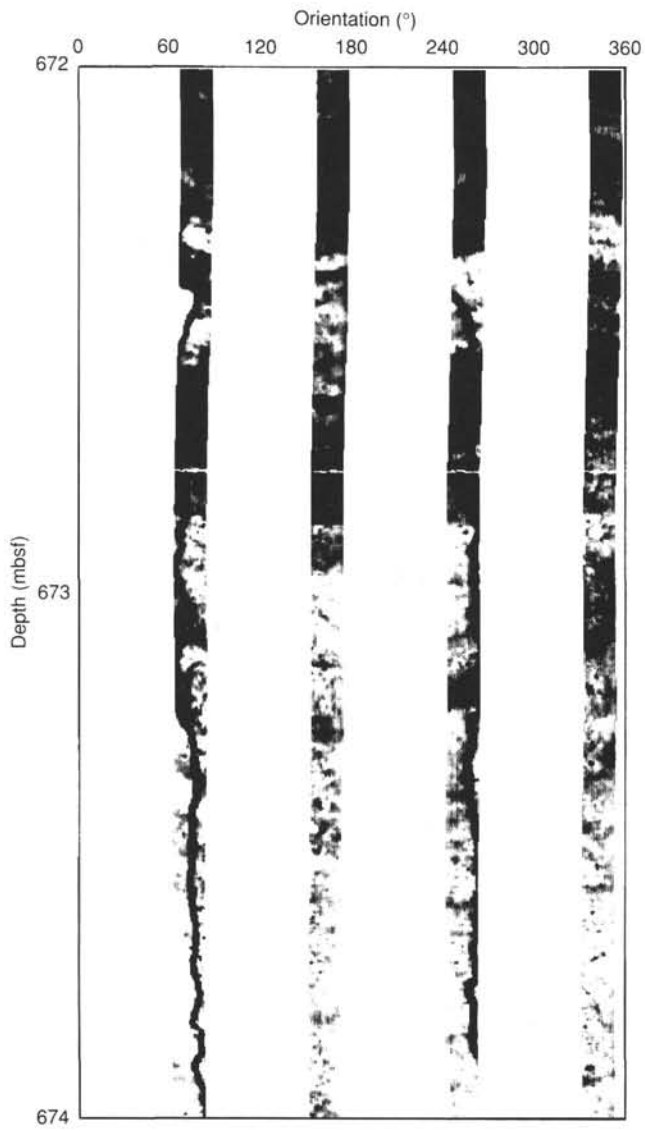


Figure 55. Drilling-induced vertical fracture in sandstone that is parallel to the principal-stress direction. FMS images.

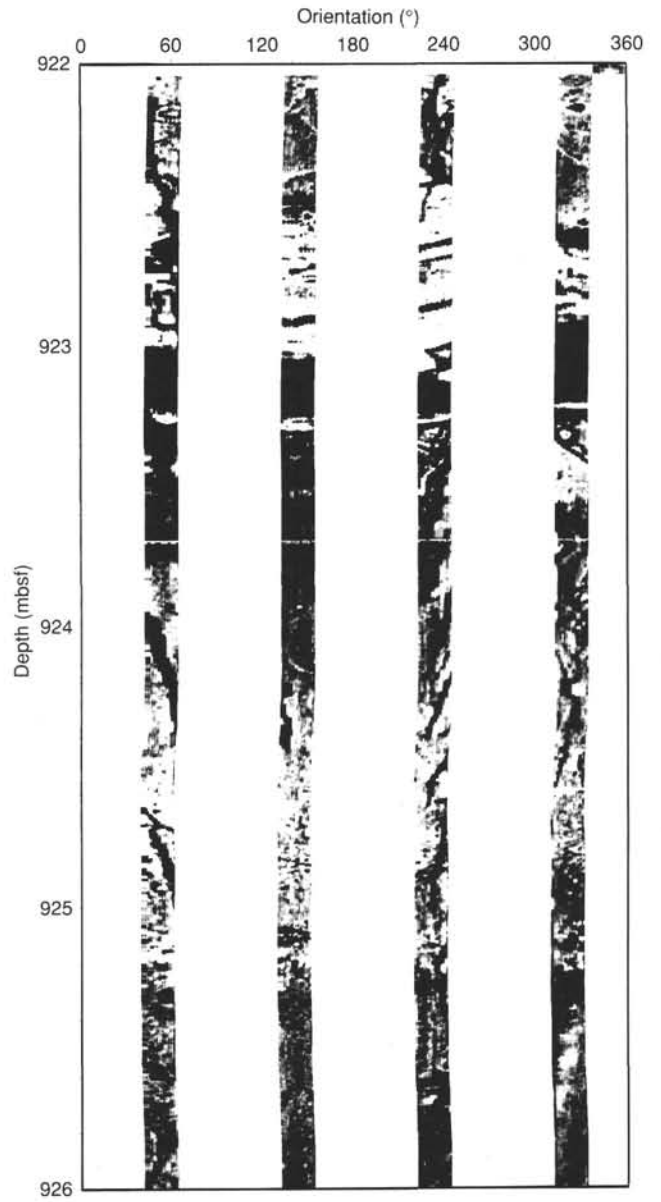


Figure 56. Drilling-enhanced oblique fracture in sandstone. FMS images.



Figure 57. Example of faults that dip 50°–60° in lithostratigraphic Unit V. FMS images.

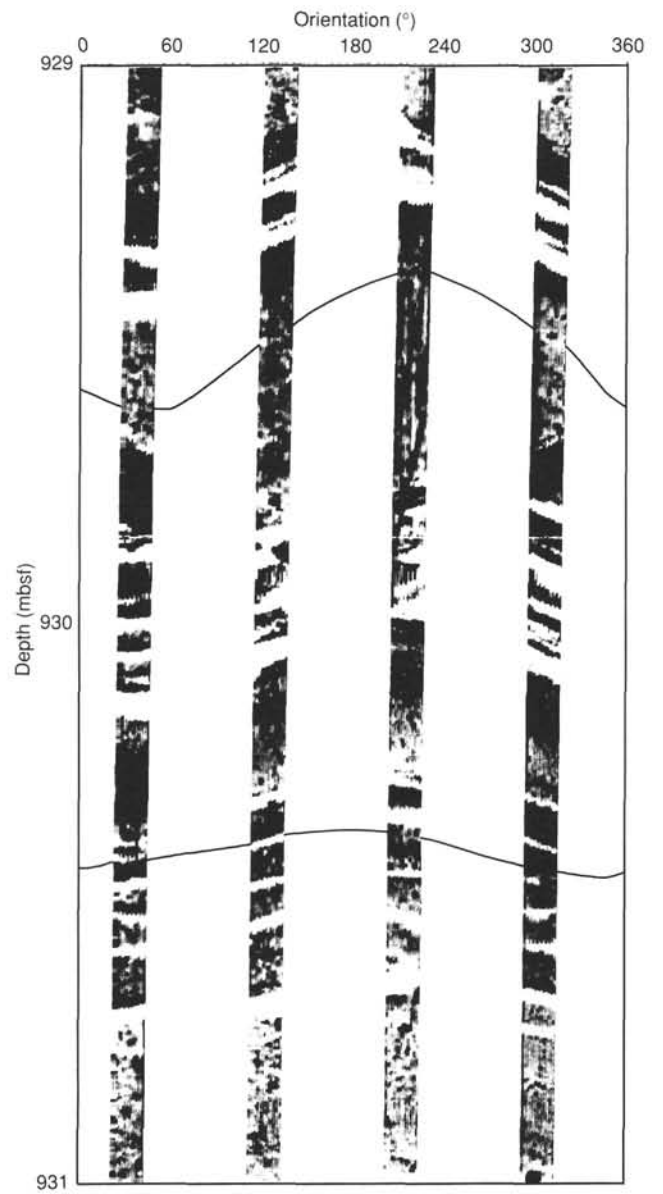


Figure 58. Parallel bedding that dips 45° in volcanic sandstone of lithostratigraphic Unit VI. FMS images.

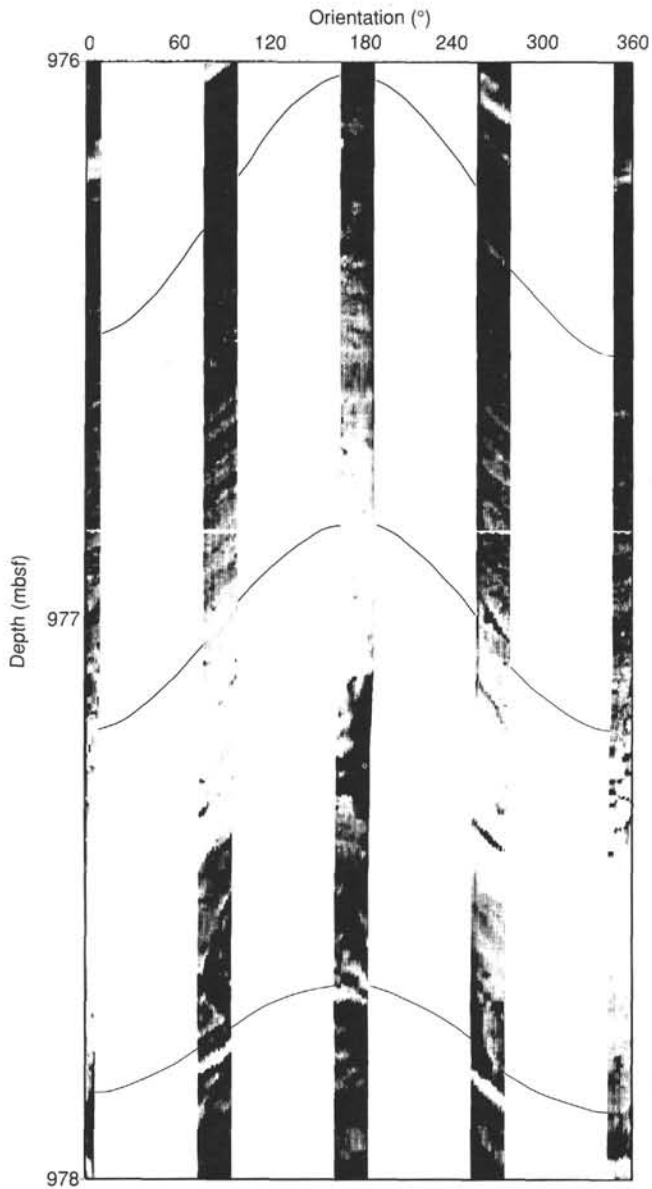


Figure 59. Finely laminated bedding that dips 40° to 60° and has a dip azimuth of 355° in lithostratigraphic Unit VII. FMS images.

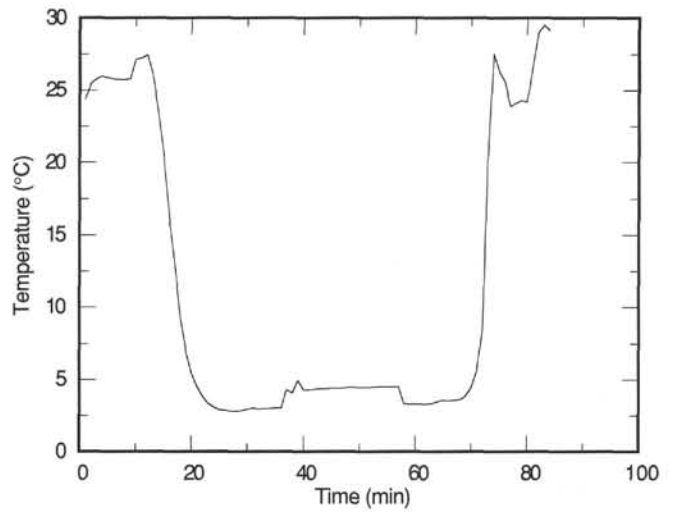


Figure 60. Temperature vs. time for water sampler temperature probe (WSTP) run 4H in Hole 832A at a depth of 18.5 mbsf.

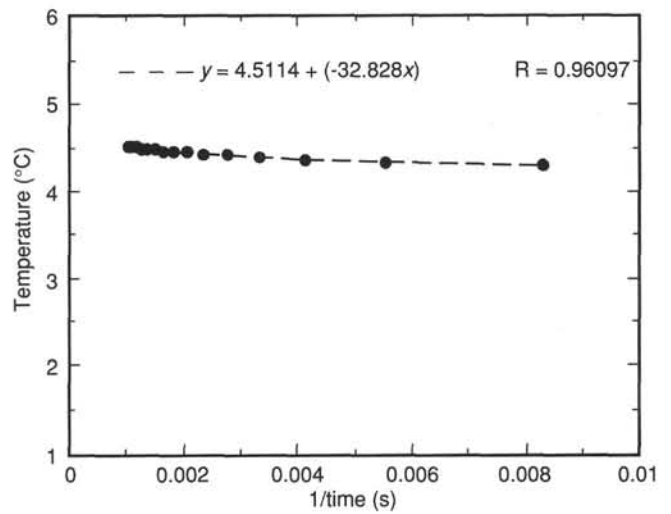


Figure 61. Reduction to equilibrium temperature for WSTP run 4H in Hole 832A. The temperature value at 1/time = 0 is the equilibrium value.

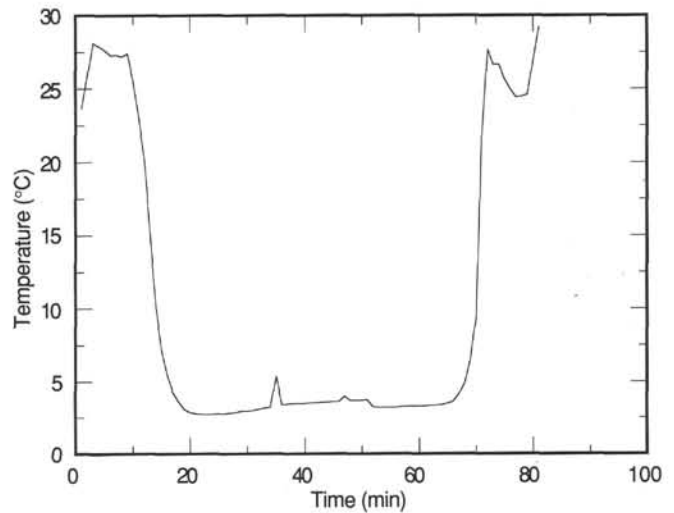


Figure 62. Temperature vs. time for WSTP run 7H in Hole 832A at a depth of 47.0 mbsf.

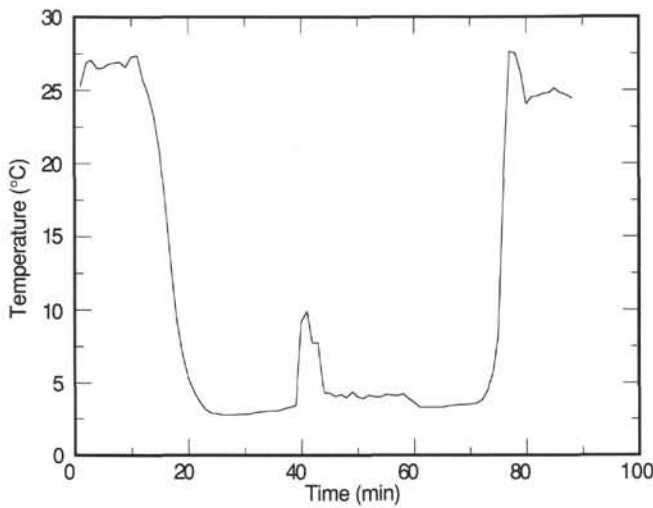


Figure 63. Temperature vs. time for WSTP run 20H in Hole 832A at a depth of 145.0 mbsf.

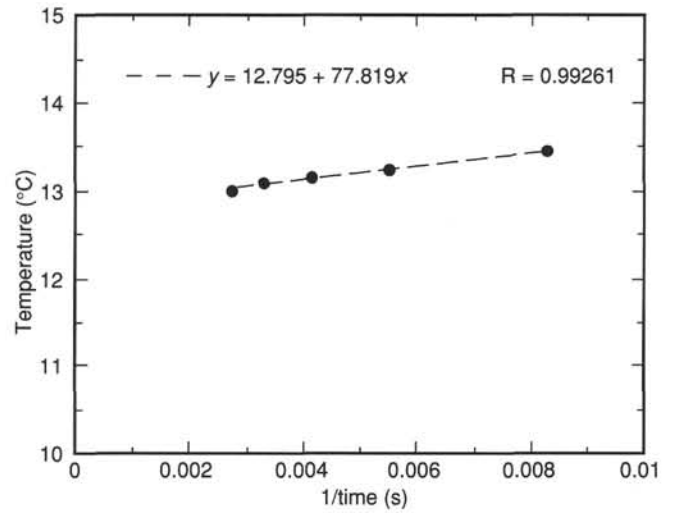


Figure 66. Reduction to equilibrium temperature for WSTP run 28X in Hole 832A. The temperature value at 1/time = 0 is the equilibrium value.

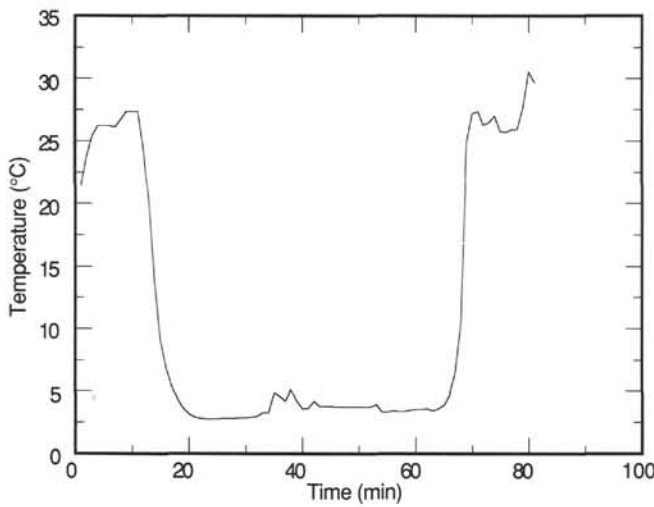


Figure 64. Temperature vs. time for WSTP run 27X in Hole 832A at a depth of 196.7 mbsf.

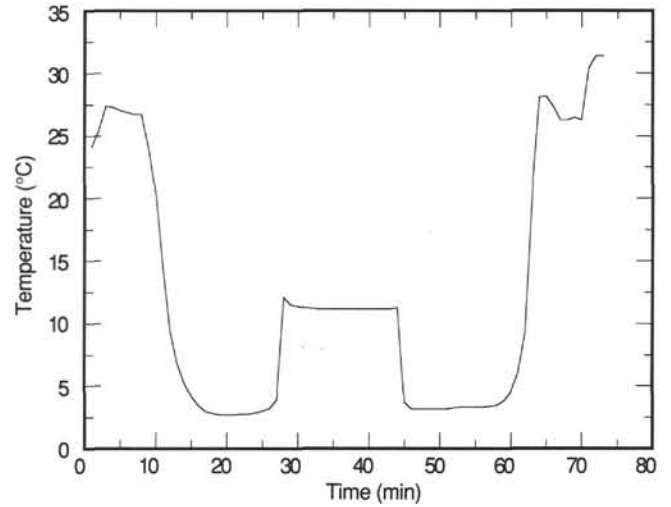


Figure 67. Temperature vs. time for WSTP run 4R in Hole 832B at a depth of 173.3 mbsf.

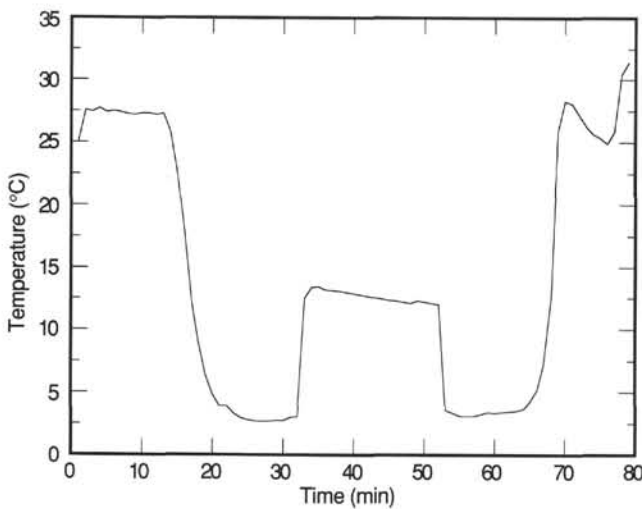


Figure 65. Temperature vs. time for WSTP run 28X in Hole 832A at a depth of 215.9 mbsf.

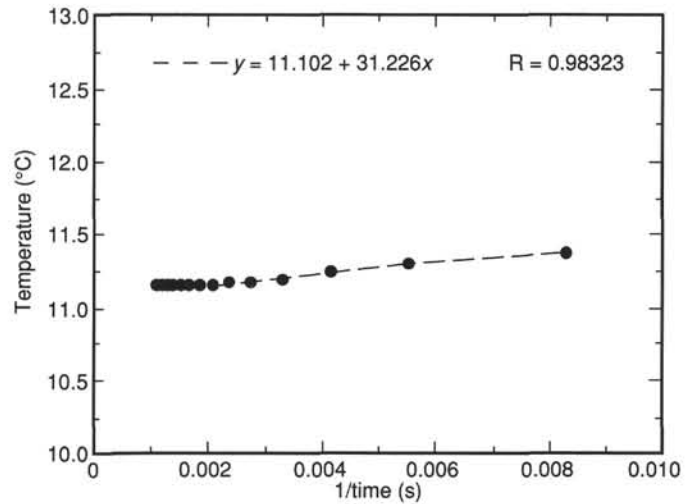


Figure 68. Reduction to equilibrium temperature for WSTP run 4R in Hole 832B. The temperature value at 1/time = 0 is the equilibrium value.

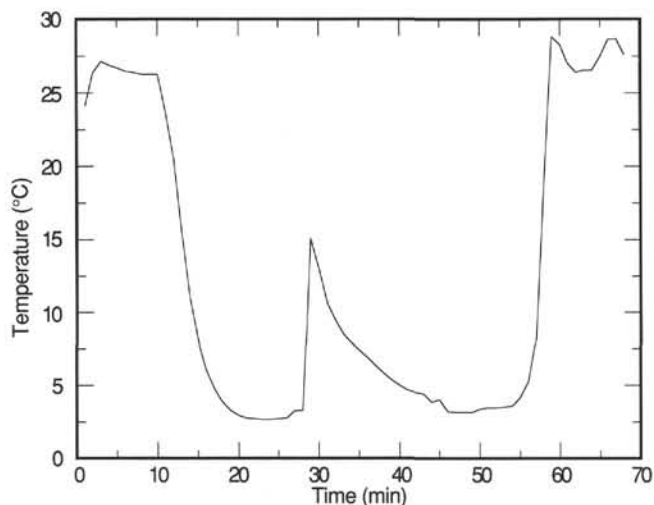


Figure 69. Temperature vs. time for WSTP run 10R in Hole 832B at a depth of 231.0 mbsf.

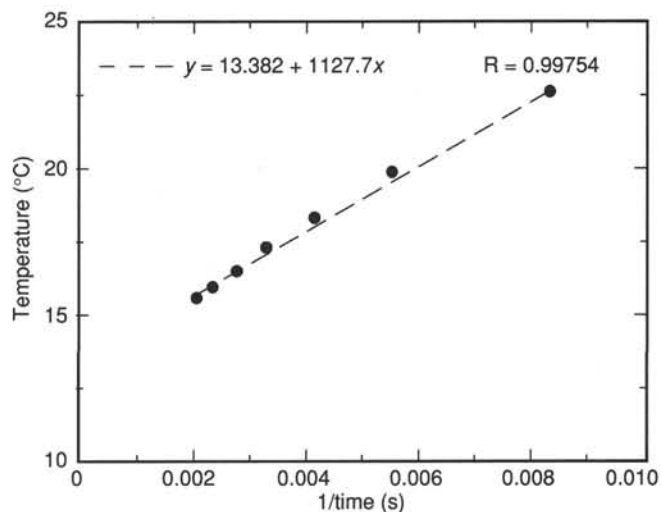


Figure 71. 1/time reduction for WSTP run 19R in Hole 832B. The extreme frictional heating of this measurement causes this approximation to underestimate the equilibrium temperature.

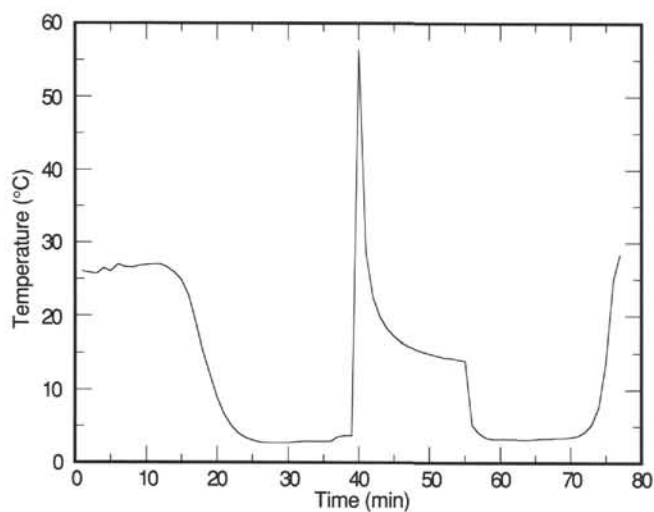


Figure 70. Temperature vs. time for WSTP run 19R in Hole 832B at a depth of 318.1 mbsf.

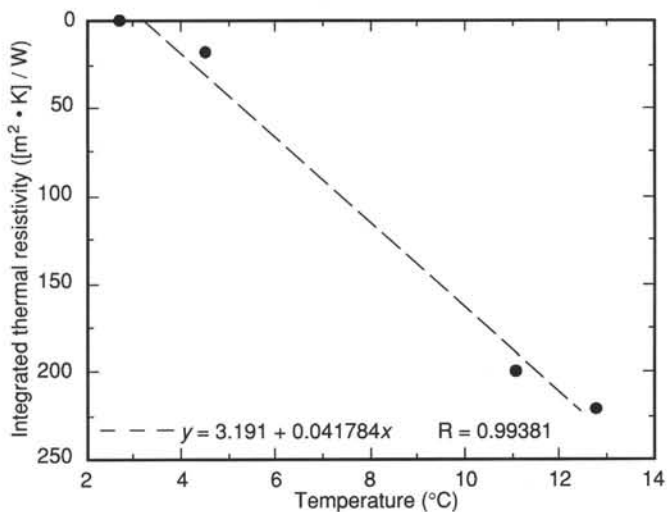


Figure 72. Temperature vs. integrated thermal resistivity at Site 832. The least-squares fit reduction line gives the surficial heat flow of 41.8 mW/m².

Hole 832A (continued)

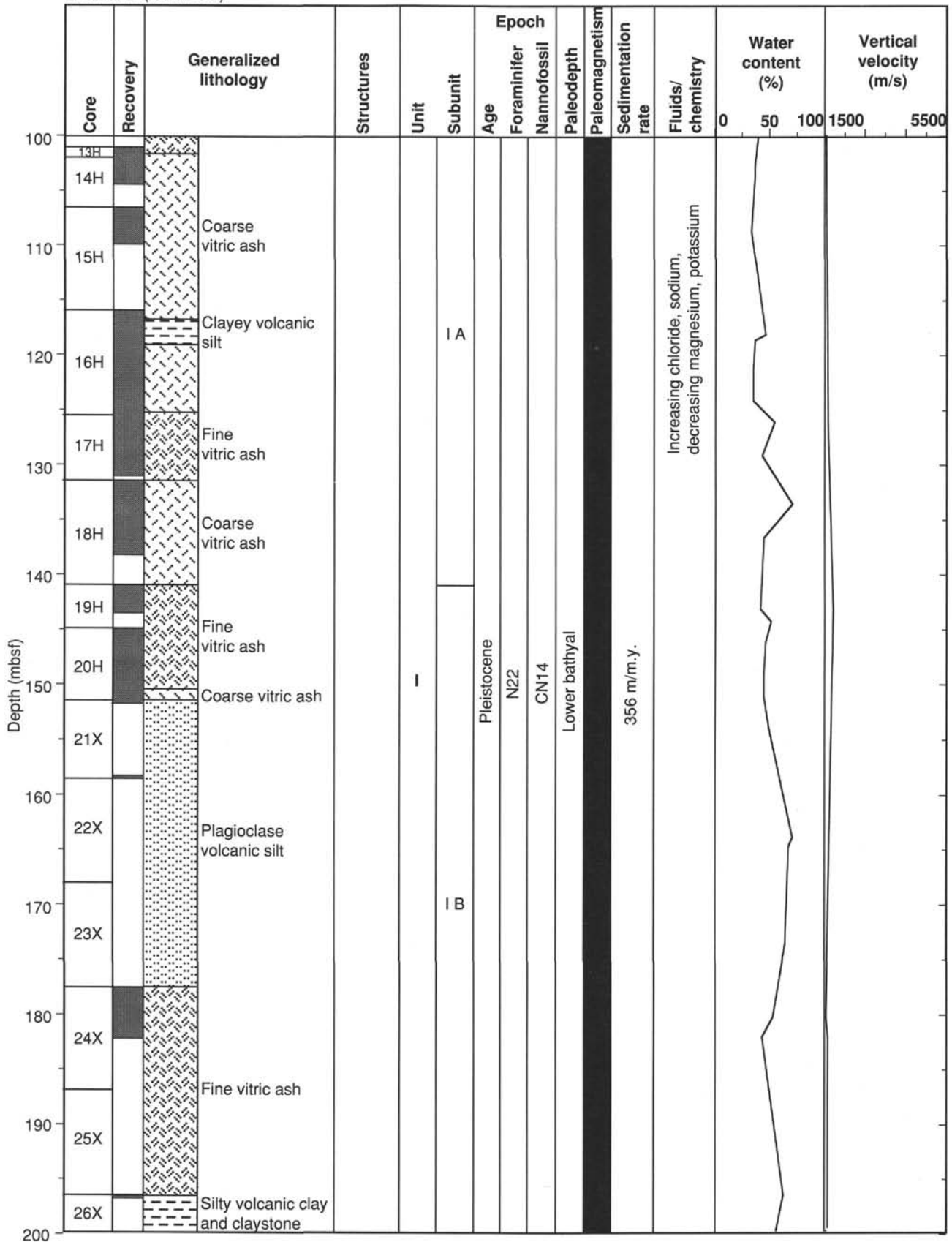


Figure 73 (continued).

Hole 832A (continued)

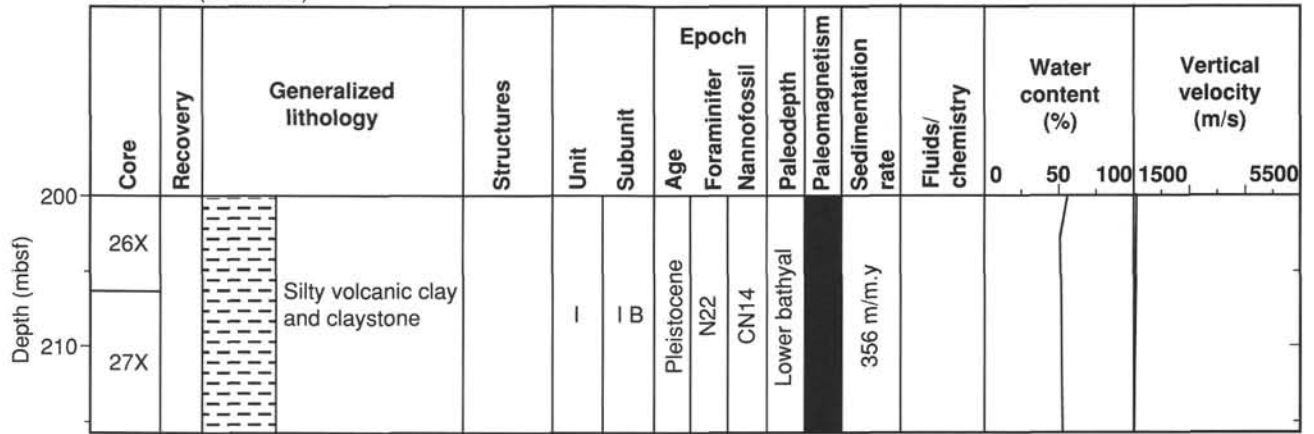


Figure 73 (continued).

Hole 832B

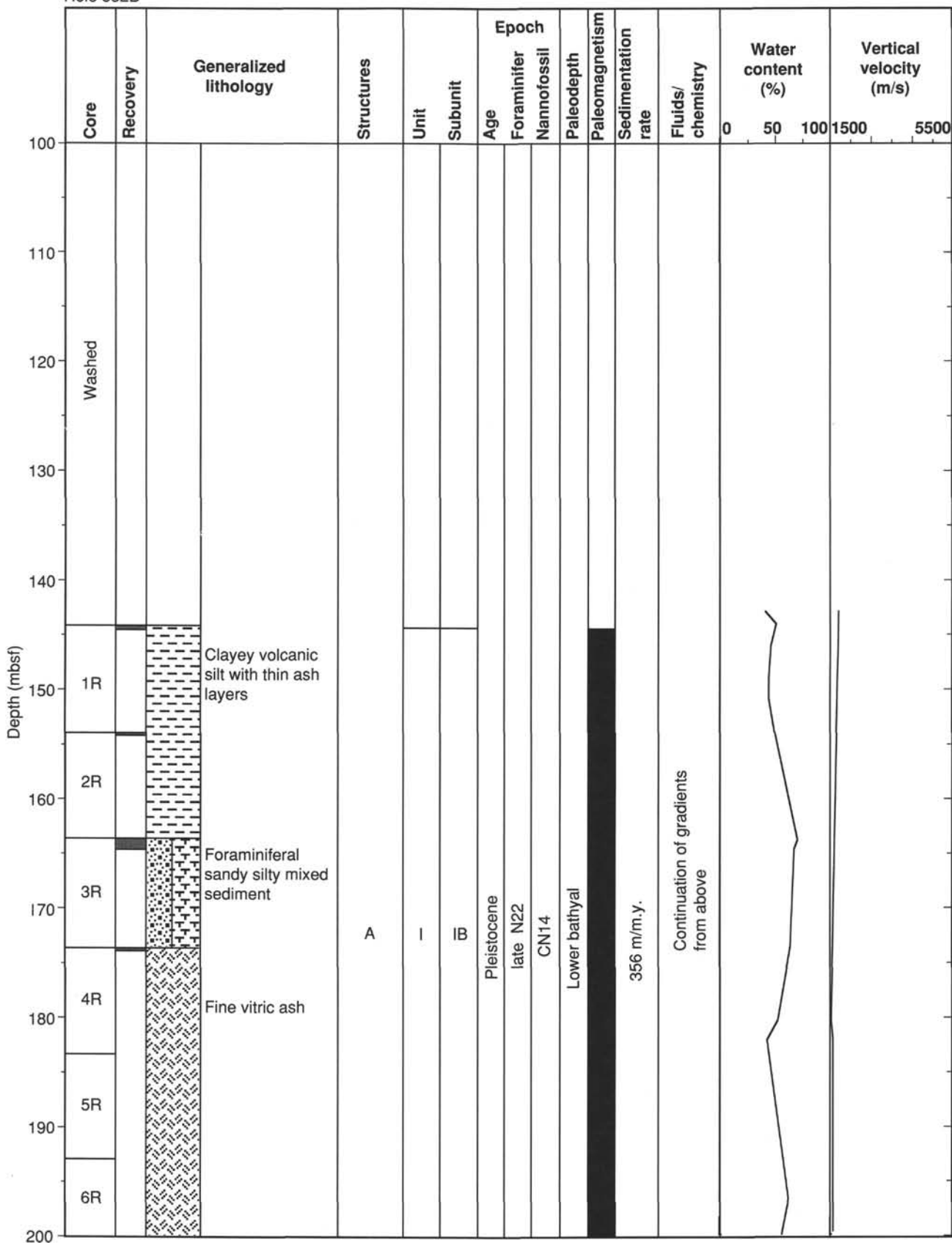


Figure 73 (continued).

Hole 832B (continued)

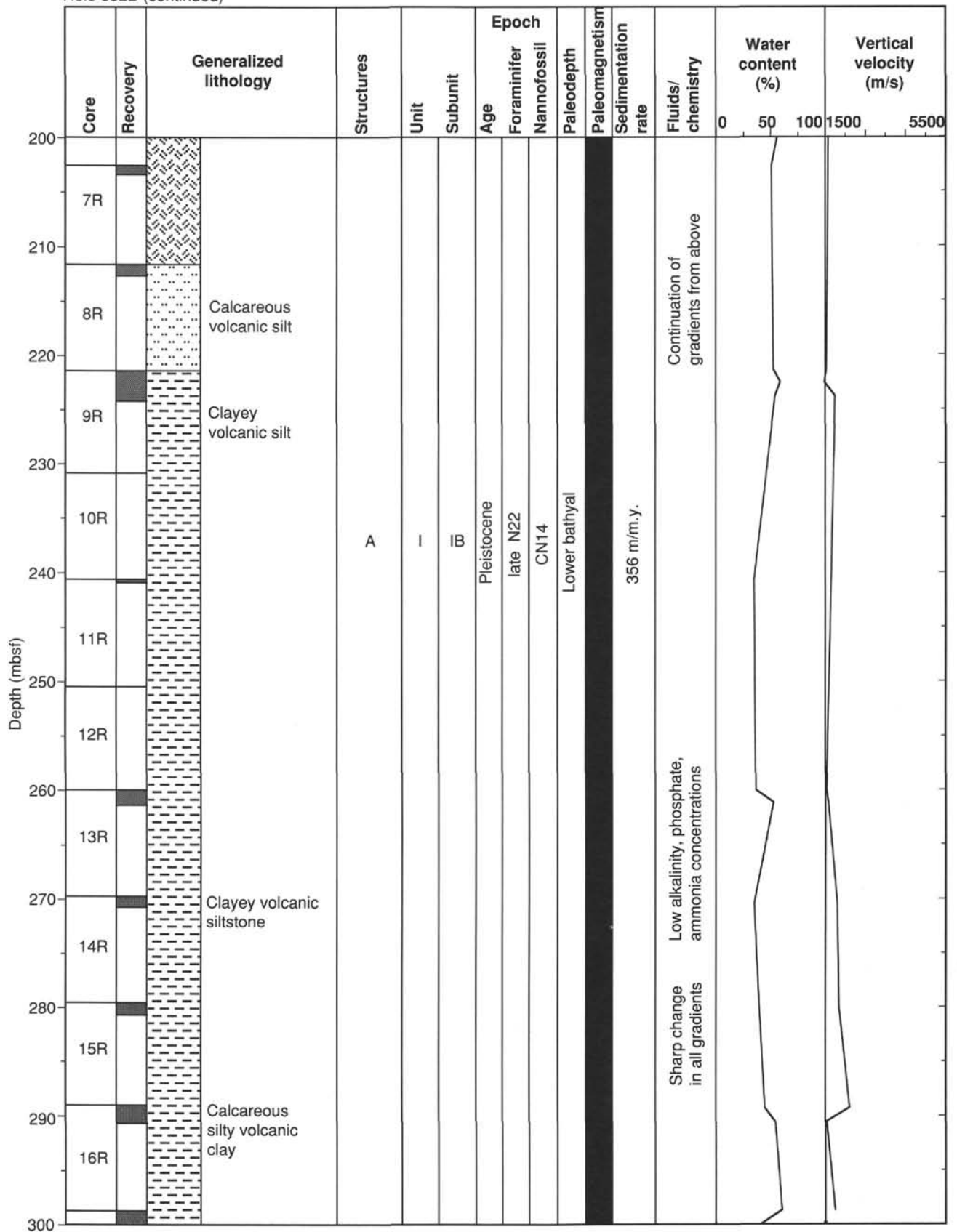


Figure 73 (continued).

Hole 832B (continued)

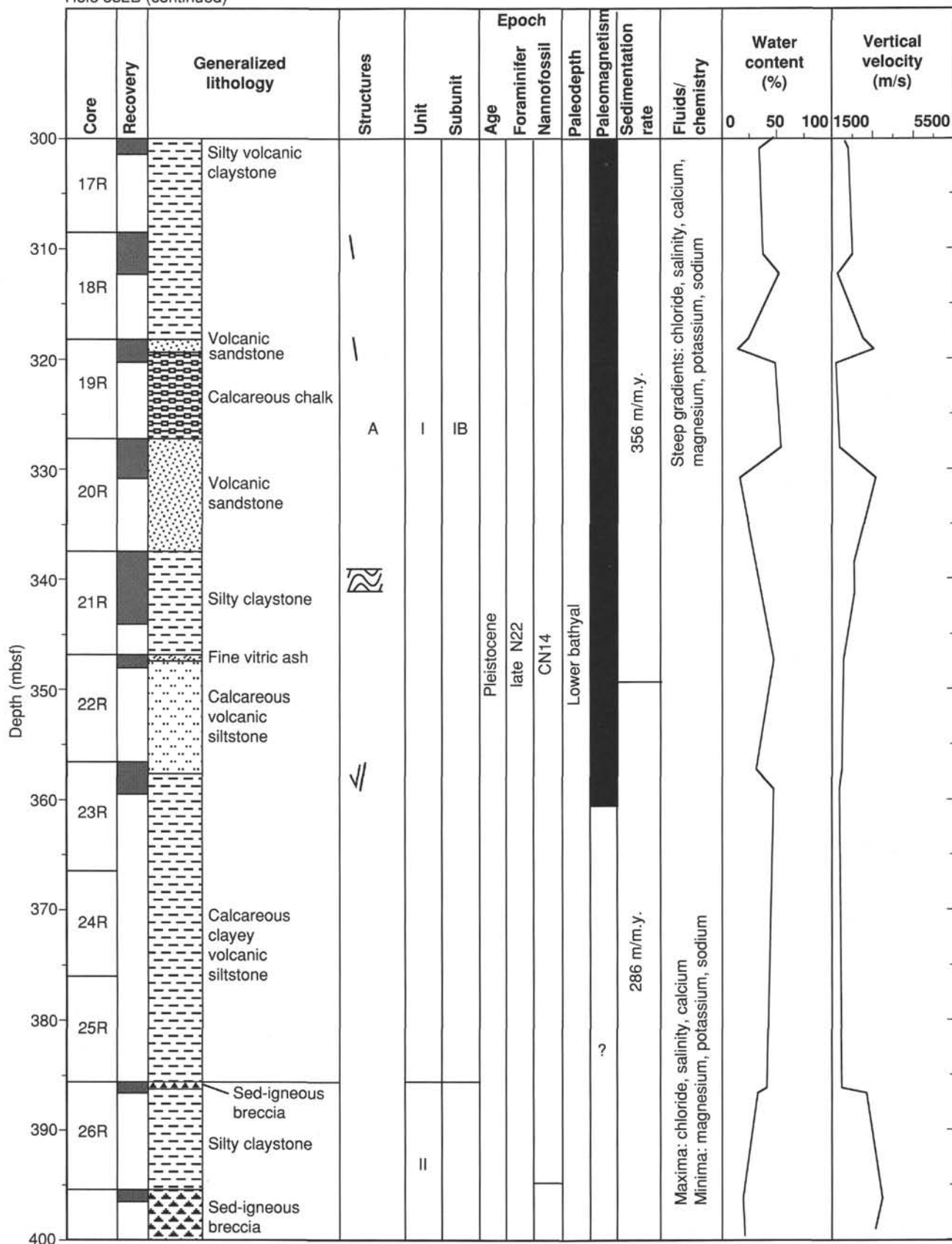


Figure 73 (continued).

Hole 832B (continued)

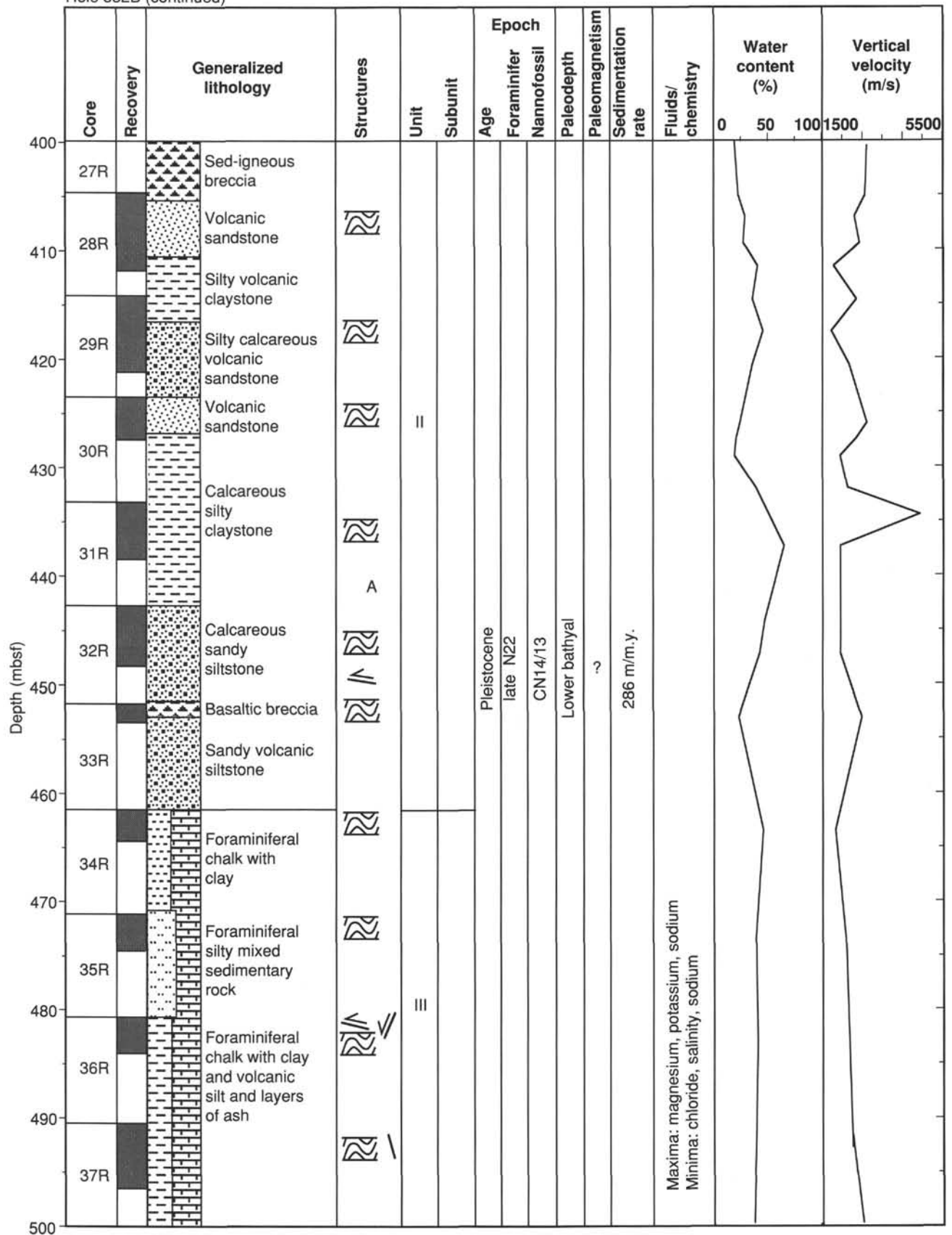


Figure 73 (continued).

Hole 832B (continued)

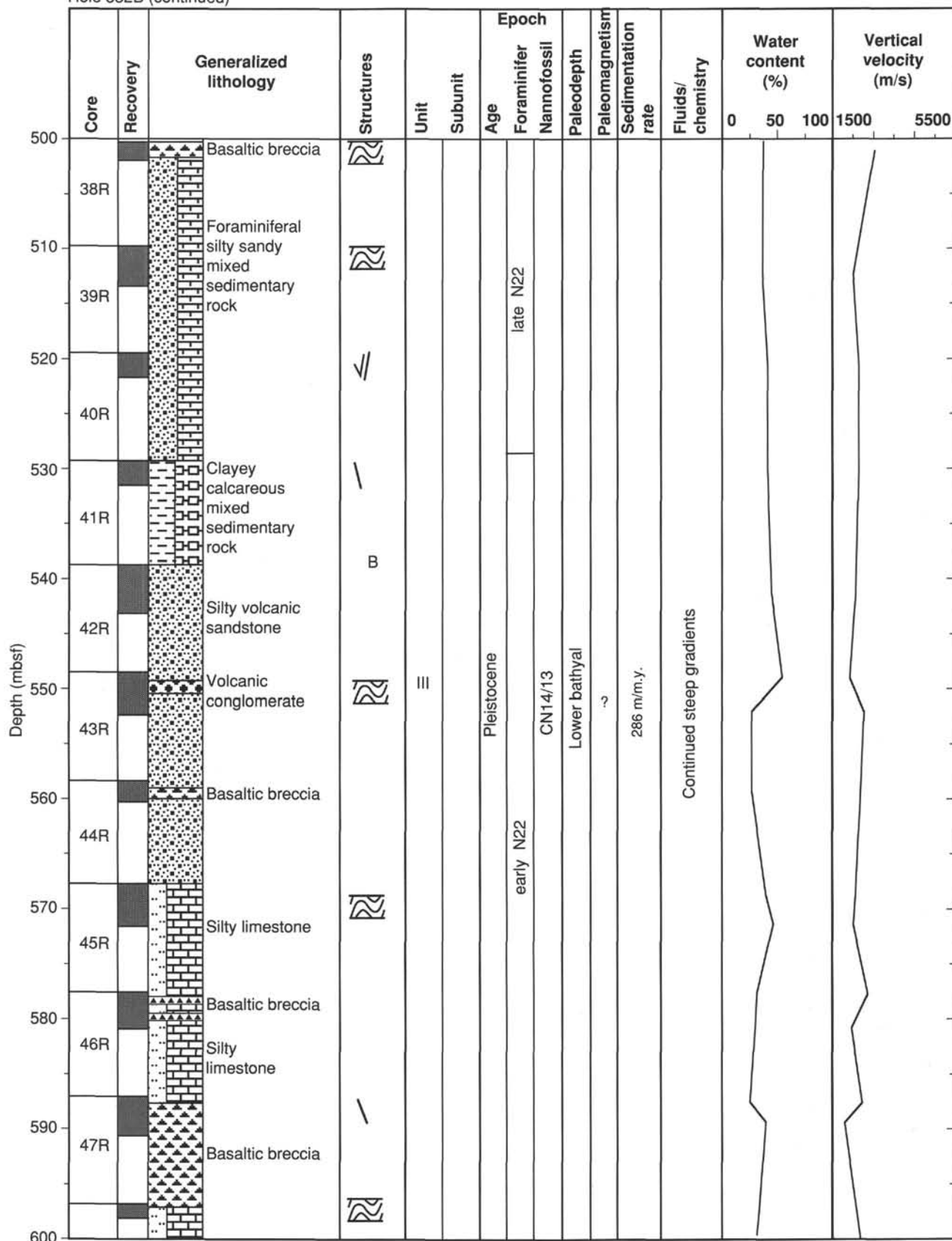


Figure 73 (continued).

Hole 832B (continued)

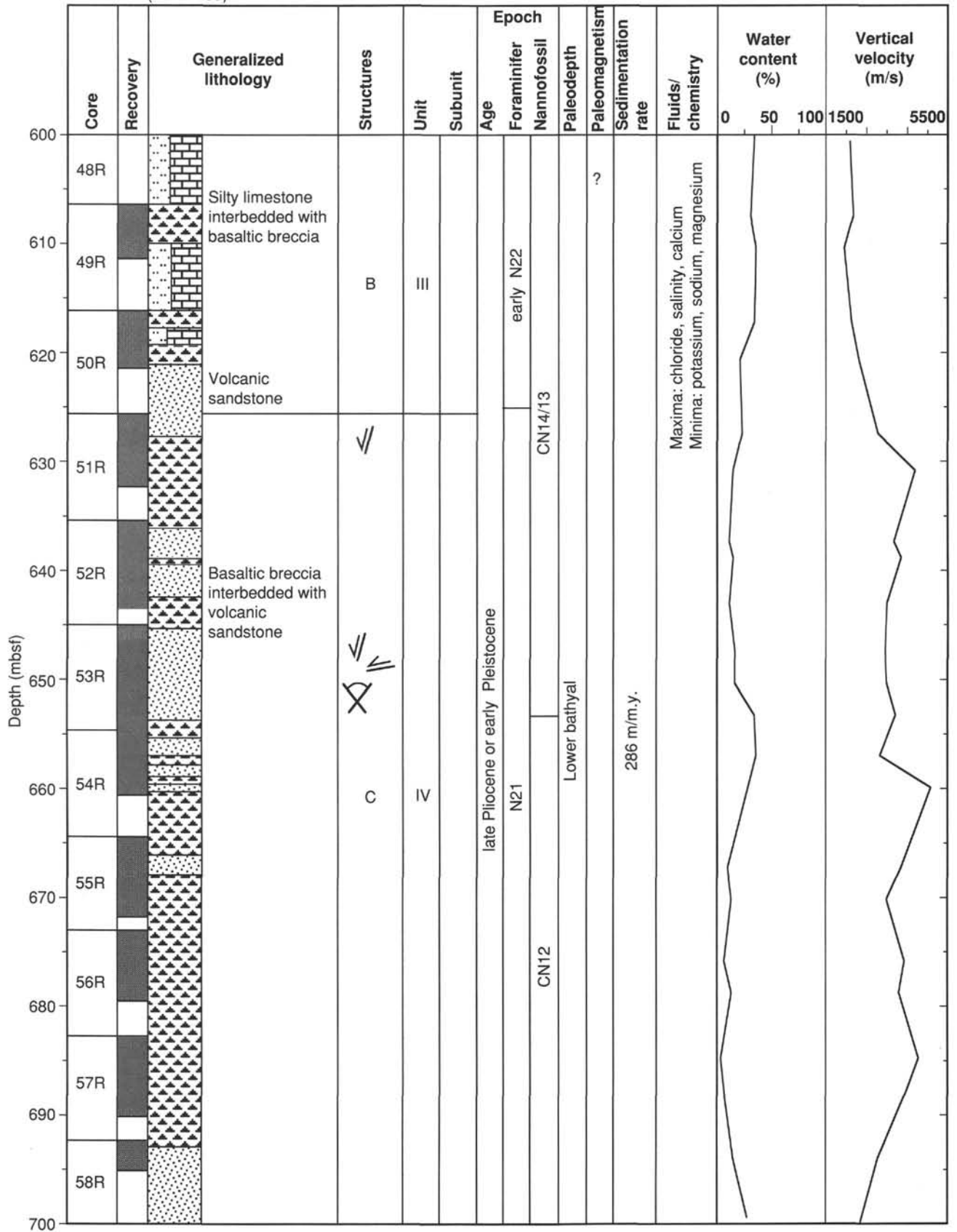


Figure 73 (continued).

Hole 832B (continued)

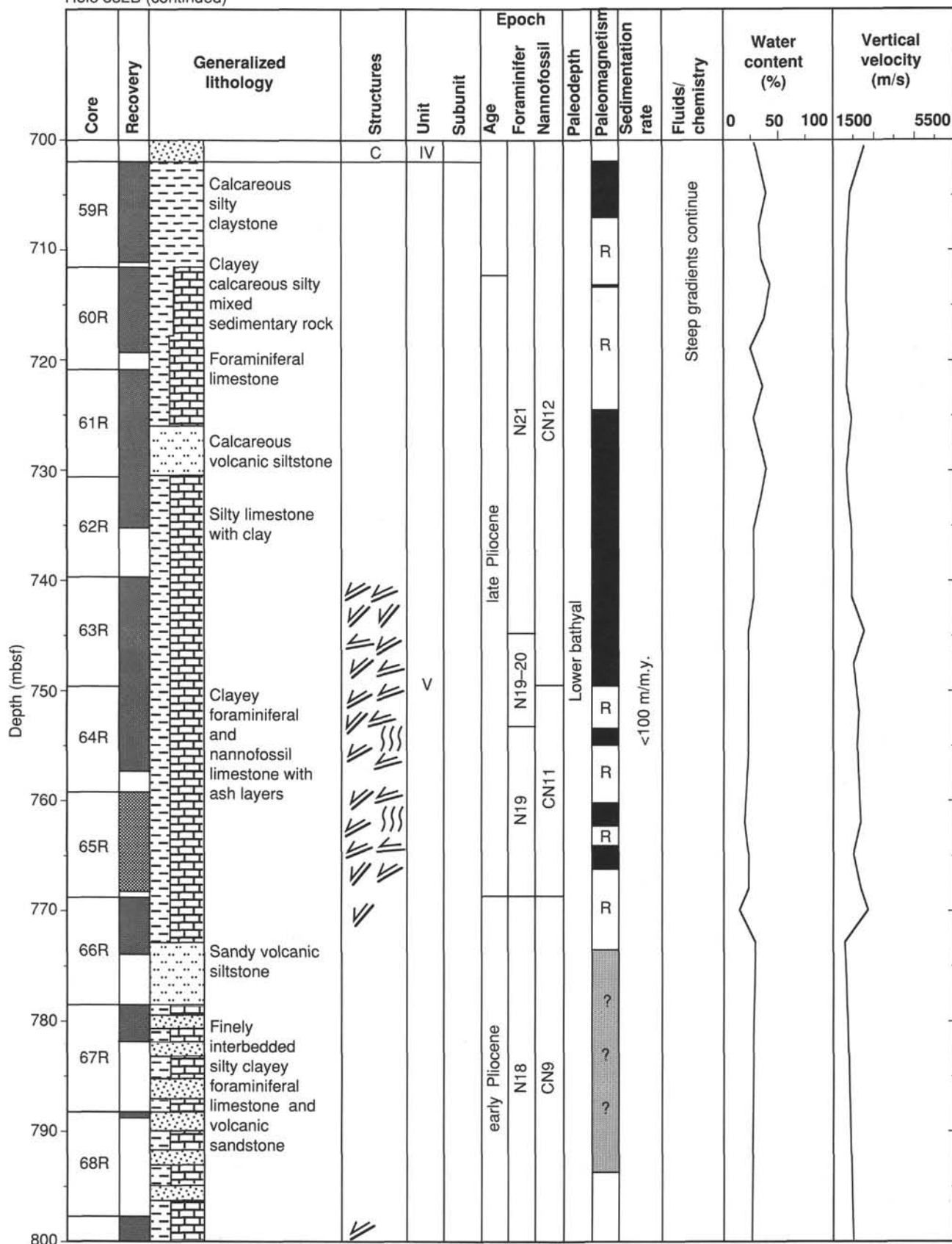


Figure 73 (continued).

Hole 832B (continued)

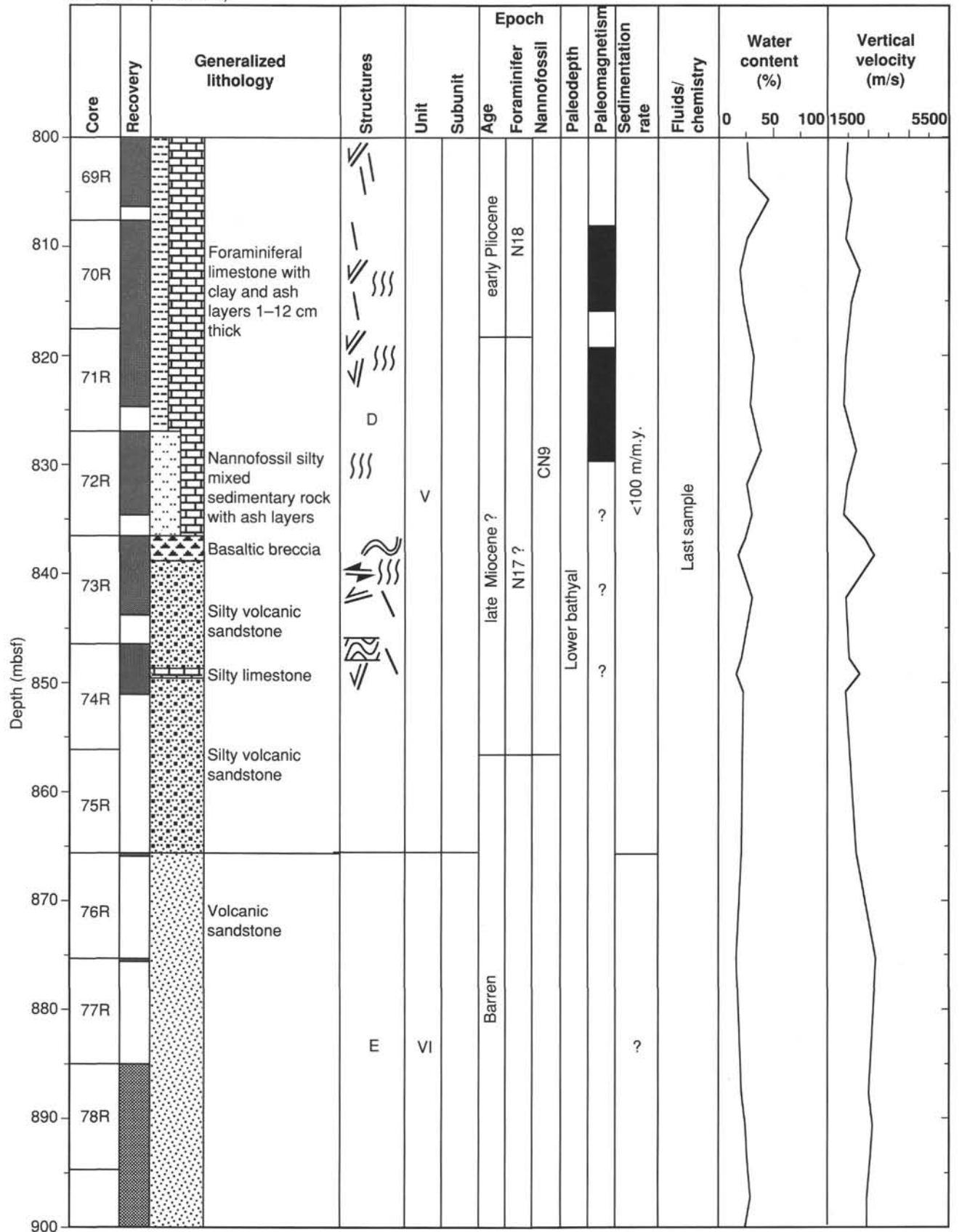


Figure 73 (continued).

Hole 832B (continued)

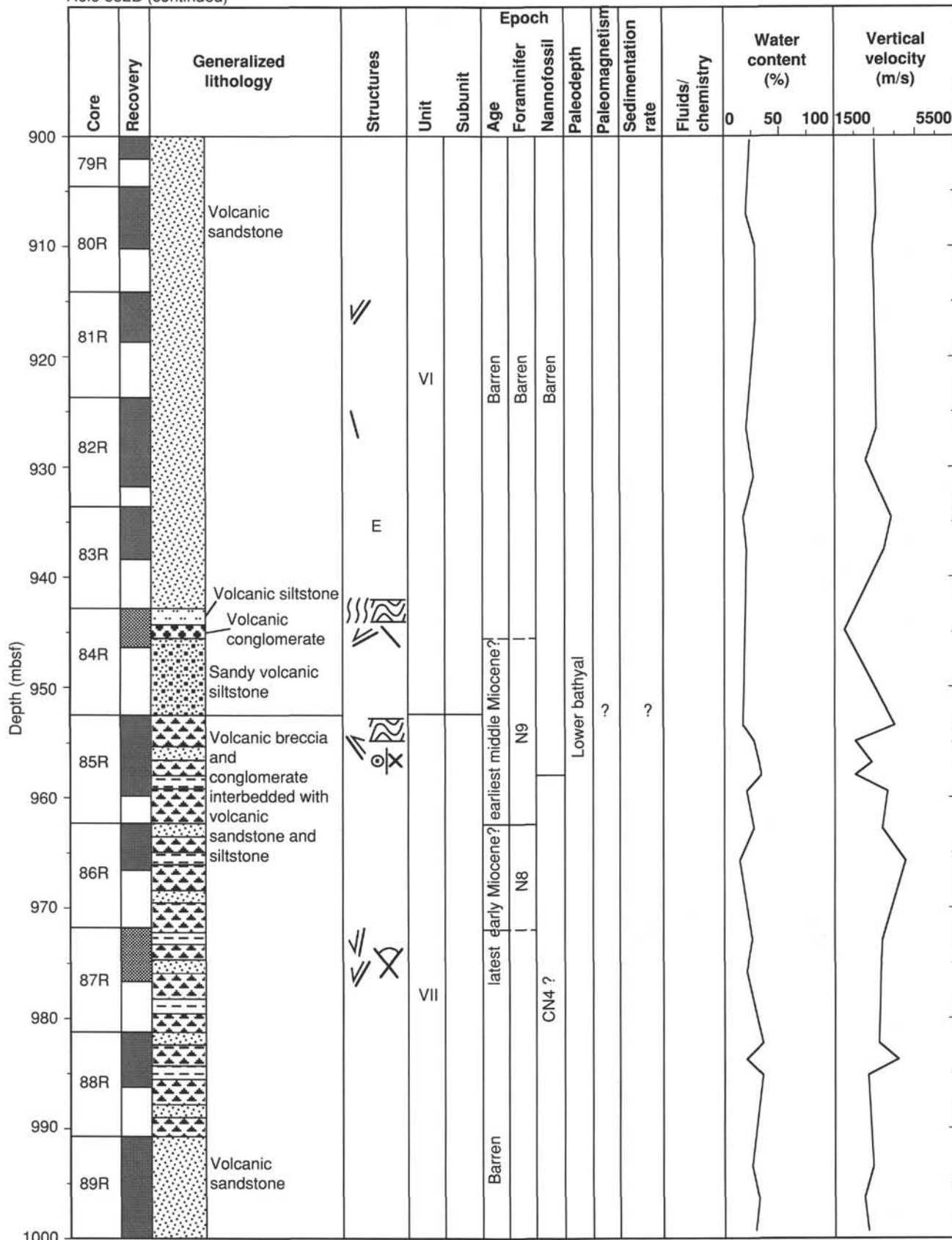


Figure 73 (continued).

Hole 832B (continued)

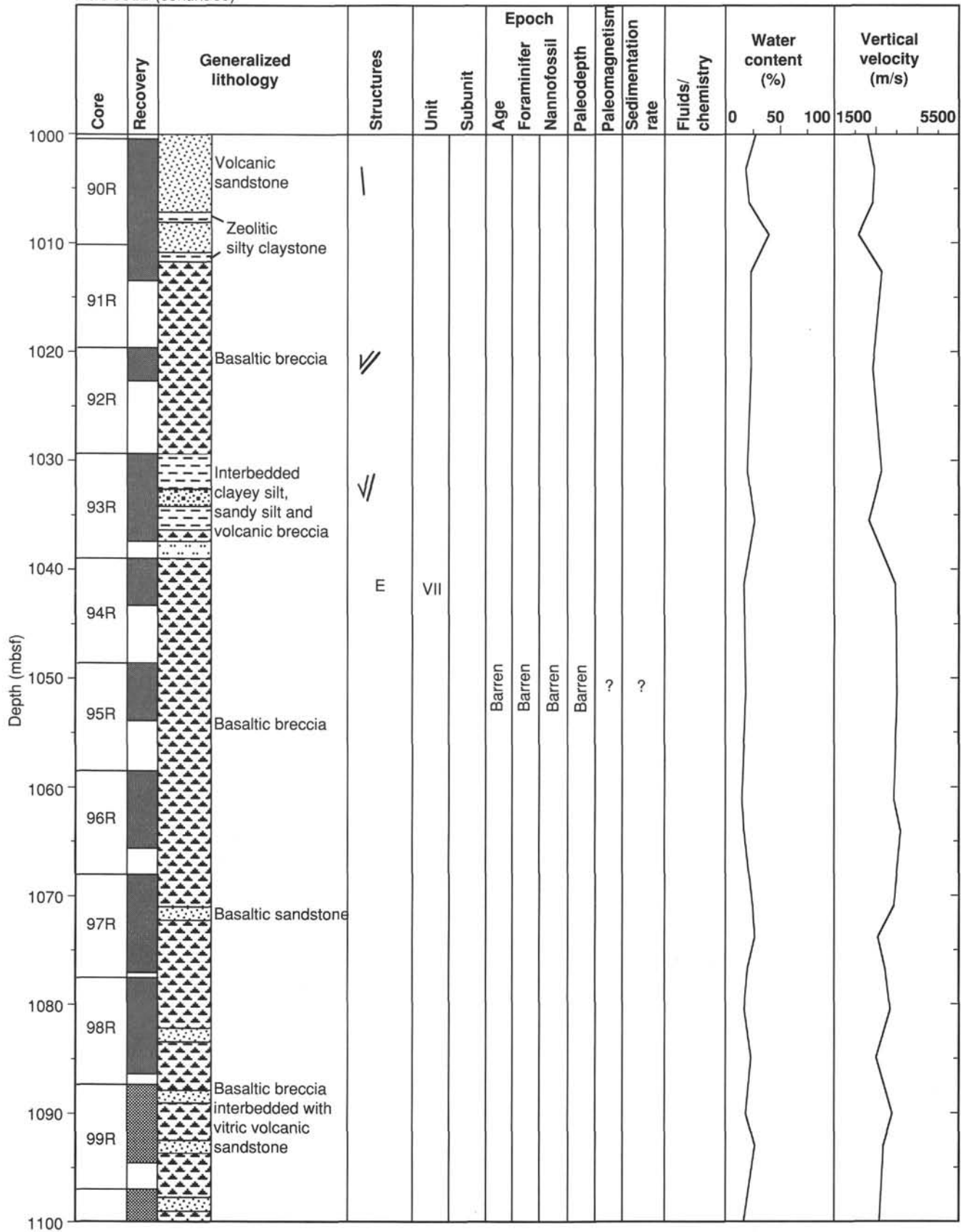


Figure 73 (continued).

Hole 832B (continued)

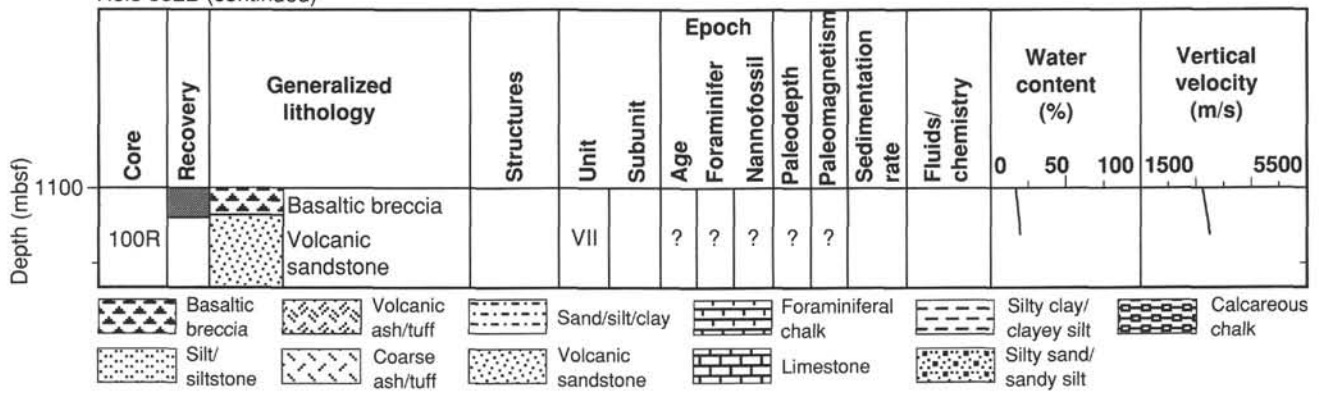
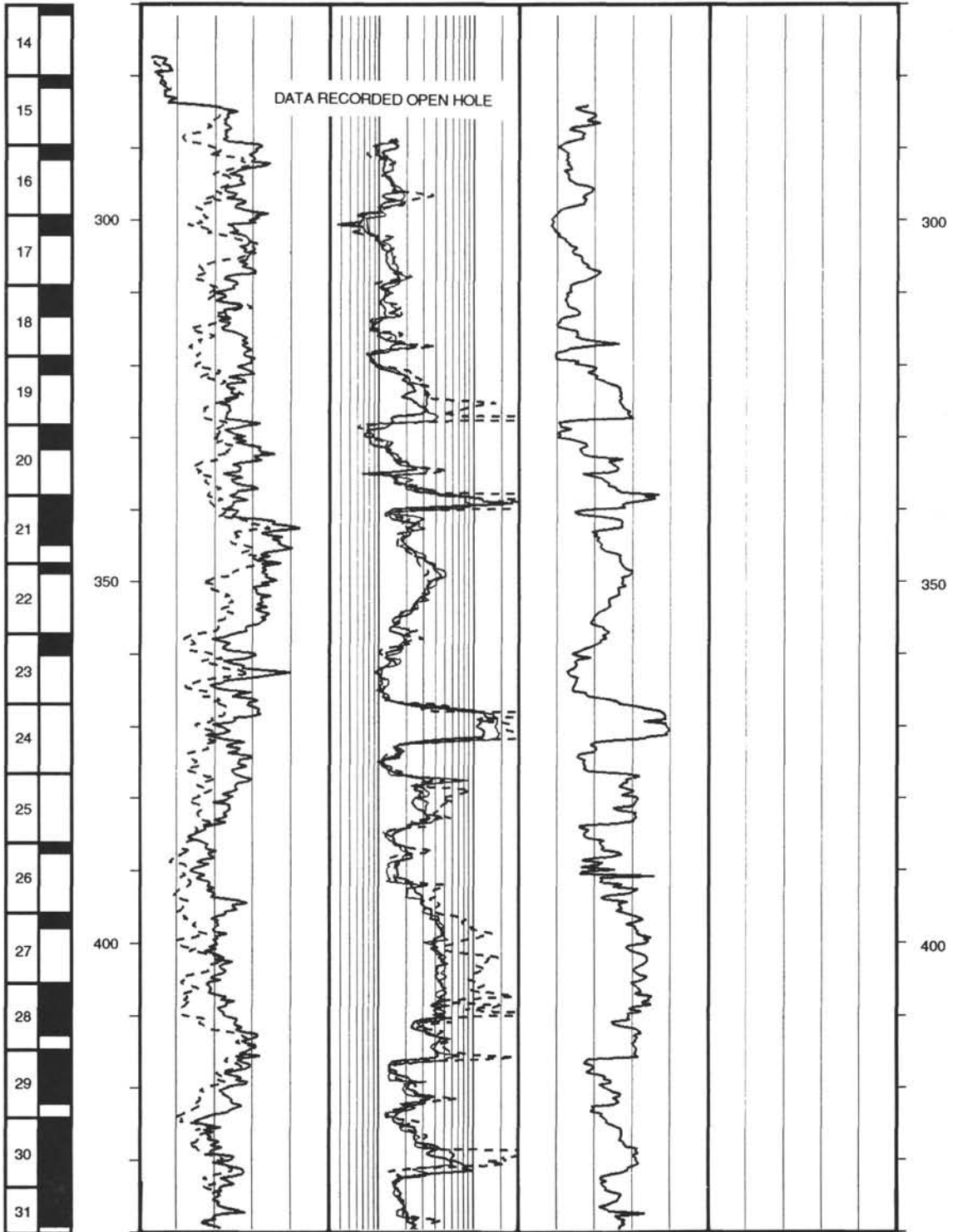


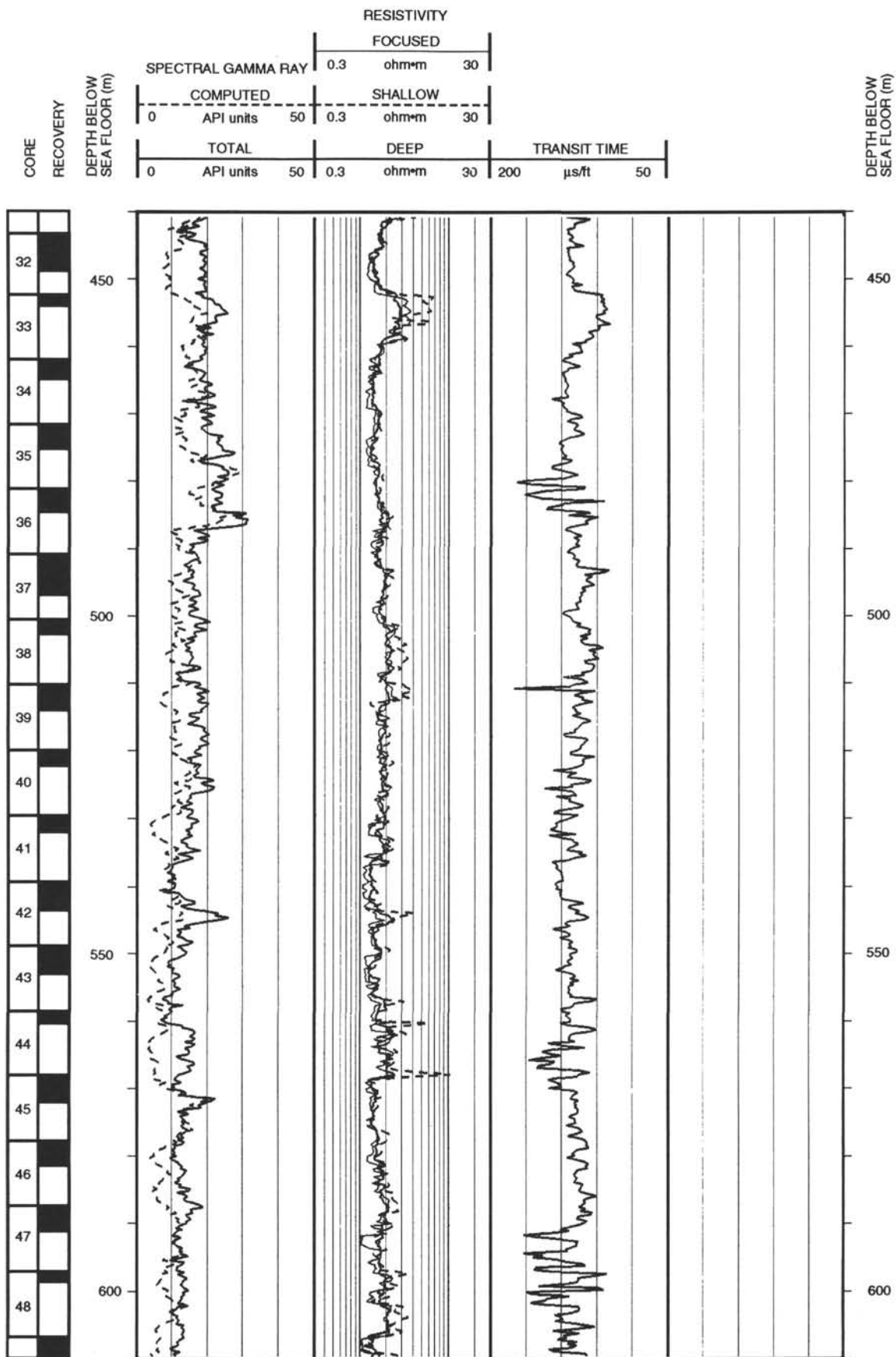
Figure 73 (continued).

Hole 832B: Resistivity-Sonic-Natural Gamma Ray Log Summary

CORE RECOVERY	DEPTH BELOW SEA FLOOR (m)	RESISTIVITY							DEPTH BELOW SEA FLOOR (m)
		SPECTRAL GAMMA RAY		FOCUSED					
		0	50	0.3	ohm·m	30			
		COMPUTED		SHALLOW					
	0	50	0.3	ohm·m	30	TRANSIT TIME			
						200	μs/ft	50	

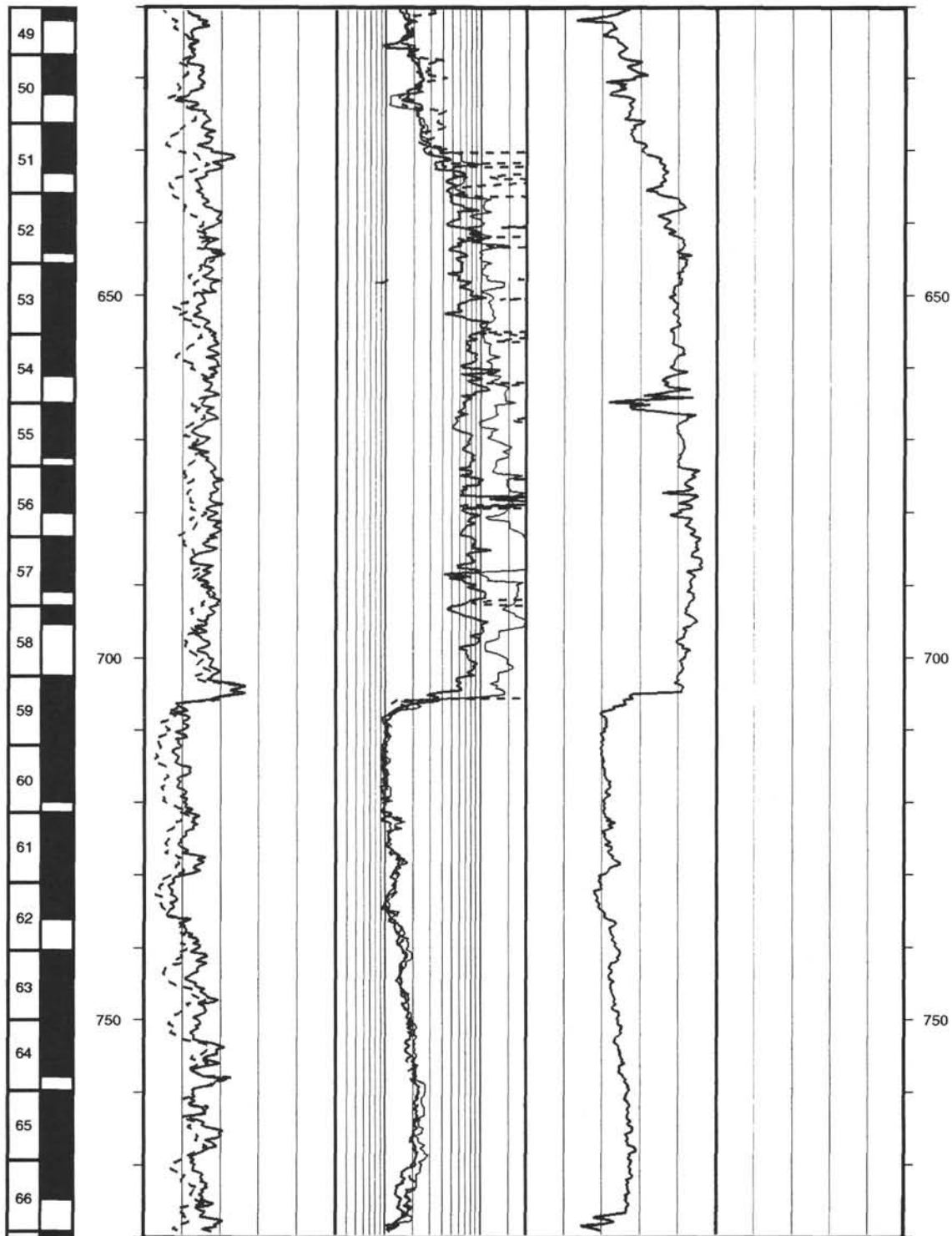


Hole 832B: Resistivity-Sonic-Natural Gamma Ray Log Summary (continued)

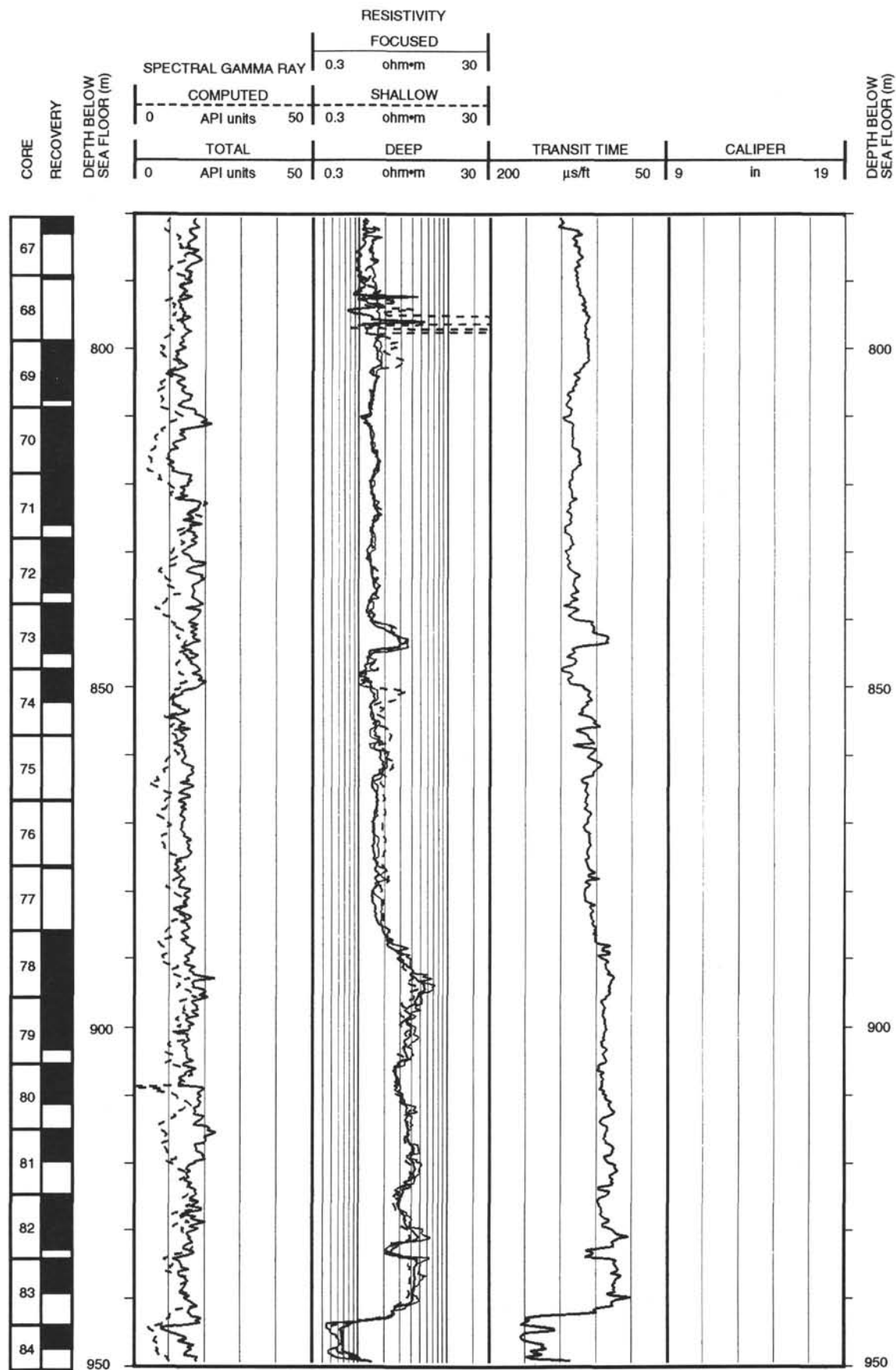


Hole 832B: Resistivity-Sonic-Natural Gamma Ray Log Summary

CORE RECOVERY	DEPTH BELOW SEA FLOOR (m)	RESISTIVITY							DEPTH BELOW SEA FLOOR (m)
		SPECTRAL GAMMA RAY		FOCUSED					
		0	50	0.3	ohm*m	30			
		COMPUTED		SHALLOW					
	0	50	0.3	ohm*m	30				
		TOTAL		DEEP		TRANSIT TIME			
	0	50	0.3	ohm*m	30	200	μs/ft	50	

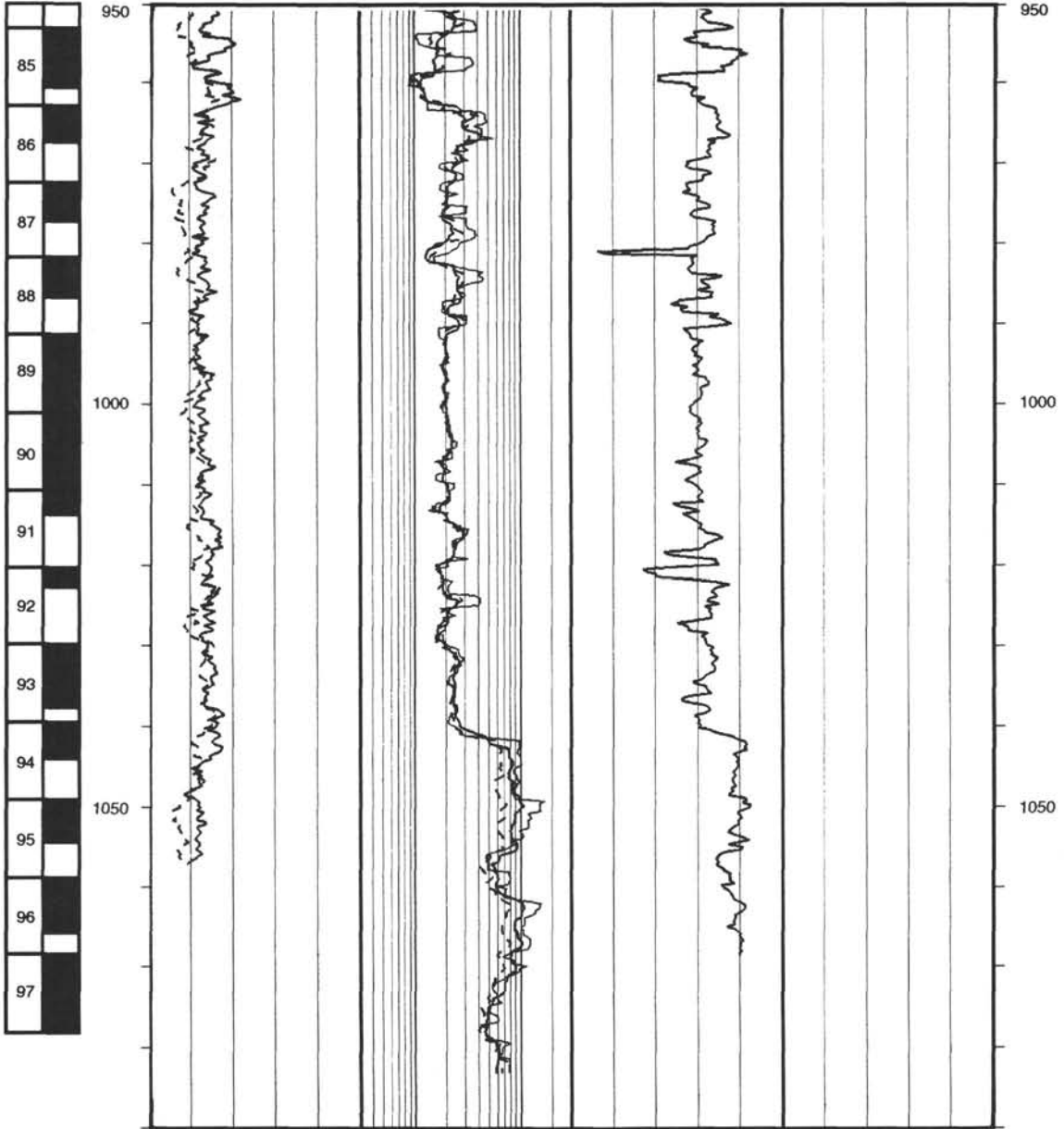


Hole 832B: Resistivity-Sonic-Natural Gamma Ray Log Summary (continued)



Hole 832B: Resistivity-Sonic-Natural Gamma Ray Log Summary (continued)

CORE RECOVERY	DEPTH BELOW SEA FLOOR (m)	RESISTIVITY										DEPTH BELOW SEA FLOOR (m)						
		SPECTRAL GAMMA RAY		FOCUSED		COMPUTED		SHALLOW		TOTAL			DEEP		TRANSIT TIME		CALIPER	
		0	50	0.3	ohm·m	30	0	50	0.3	ohm·m	30		200	μs/ft	50	9	in	19



Hole 832B: Density-Natural Gamma Ray Log Summary

